

3641

**INVESTIGATING RADIONUCLIDE BEARING SUSPENDED  
SEDIMENT TRANSPORT MECHANISMS IN THE RIBBLE ESTUARY  
USING AIRBORNE REMOTE SENSING**

**By**

**Paula Ann Atkin**

Submitted to

The Faculty of Natural Sciences, University of Stirling, October 2000.

For the degree of

Doctor of Philosophy

*This research was undertaken at the Department of Environmental Science,  
University of Stirling.*

*Paula*

## ABSTRACT

BNFL Sellafield has been authorised to discharge radionuclides to the Irish Sea since 1952. In the aquatic environment the radionuclides are adsorbed by sediments and are thus redistributed by sediment transport mechanisms. This sediment is known to accumulate in the estuaries of the Irish Sea. BNFL Springfields is also licensed to discharge isotopically different radionuclides directly to the Ribble estuary. Thus there is a need to understand the sediment dynamics of the Ribble estuary in order to understand the fate of these radionuclides within the Ribble estuary. Estuaries are highly dynamic environments that are difficult to monitor using the conventional sampling techniques. However, remote sensing provides a potentially powerful tool for monitoring the hydrodynamics of the estuarine environment by providing data that are both spatially and temporally representative.

This research develops a methodology for mapping suspended sediment concentration (SSC) in the Ribble estuary using airborne remote sensing. The first hypothesis, that there is a relationship between SSC and  $^{137}\text{Cs}$  concentration is proven *in-situ* ( $R^2=0.94$ ), thus remotely sensed SSC can act as a surrogate for  $^{137}\text{Cs}$  concentration. Initial *in-situ* characterisation of the suspended sediments was investigated to identify spatial and temporal variability in grain size distributions and reflectance characteristics for the Ribble estuary. Laboratory experiments were then performed to clearly define the SSC reflectance relationship, identify the optimum CASI wavelengths for quantifying SSC and to demonstrate the effects on reflectance of the environmental variables of salinity and clay content. Images were corrected for variation in solar elevation and angle to give a ground truth calibration for SSC, with an  $R^2=0.76$ . The remaining scatter in this relationship was attributed to the differences in spatial and temporal representation between sampling techniques and remote sensing.

The second hypothesis assumes that a series of images over a flood tide can be animated to provide information on the hydrodynamic regime, erosion, and deposition. Spatial and temporal data demonstrated the complex controls on sediment transport. The data also showed the importance of microphytobenthos in the stabilisation of intertidal sediments, highlighting their importance in defining sources and sinks of radionuclides in intertidal areas. Water volume data from the VERSE model were combined with SSC from the imagery to calculate the total sediment in suspension for each flight line. This provided the figures used to determine total erosion and deposition, which were then used to derive net suspended sediment and  $^{137}\text{Cs}$  influxes of  $2.01 \times 10^6 \text{kg}$  and  $604 \text{MBq}$  per flood tide.

## ACKNOWLEDGEMENTS

I wish to thank NERC and BNFL, via Westlakes Scientific Consulting, for providing the CASE award (GT19/95/ICS/9) that has made this research possible.

I would particularly like to thank my supervisor, Dr. Andrew Tyler for his support, especially for all those occasions where he cleared the trees so I could see the wood! I would also like to acknowledge the support and advice from my other supervisors, Dr. Dave Gilvear and Dr. Paul McDonald. I am also grateful for the technical help received from within the Department of Environmental Science at the University of Stirling, especially from John McArthur, Bill Jamieson and Stuart Bradley. Thanks also to the NERC Equipment Pool for Spectroscopy for the loan of the spectro-radiometers and to Philippe Gleizon, of Westlakes Scientific Consulting Ltd., for the provision of the VERSE data.

Finally, I would like to say a big thank you to my family, friends and fellow postgraduate students for their patience and support. Particularly to Andy, Mum and Dad, Angie and Tash, Rhiannon, Althea and Caroline, I expect that they are all as glad to see the completion of this as I am!

# CONTENTS

TITLE PAGE.....	i
ABSTRACT.....	ii
ACKNOWLEDGEMENTS.....	iii
CONTENTS.....	iv
INDEX OF FIGURES.....	x
INDEX OF TABLES.....	xiii
INDEX OF PLATES.....	xv
INDEX OF ACRONYMS.....	xv
<b>1</b> <b>CHAPTER 1: INTRODUCTION .....</b>	<b>1</b>
<b>1.1</b> <b>Project overview.....</b>	<b>1</b>
<b>1.2</b> <b>Aims and hypotheses.....</b>	<b>3</b>
<b>1.3</b> <b>Thesis structure.....</b>	<b>4</b>
<b>2</b> <b>CHAPTER 2: LITERATURE REVIEW.....</b>	<b>6</b>
<b>2.1</b> <b>Introduction.....</b>	<b>6</b>
<b>2.2</b> <b>The study area.....</b>	<b>6</b>
2.2.1   The River Ribble.....	6
2.2.2   The Ribble Estuary.....	7
2.2.3   Modelling the Ribble Estuary.....	11
2.2.4   The Irish Sea.....	12
<b>2.3</b> <b>Estuarine characteristics.....</b>	<b>12</b>
2.3.1   Estuary classification.....	14
2.3.2   Estuary circulation and controls on sediment transport.....	16
2.3.3   Estuarine sediments.....	20
2.3.4   The Ribble Estuary: A summary.....	22
<b>2.4</b> <b>Radionuclides in the environment.....</b>	<b>23</b>
2.4.1   Radioactivity and environmental sources.....	23
2.4.2   Geochemistry of radionuclides .....	25
2.4.3   Radionuclides in the coastal environment.....	27
2.4.4   BNFL Sellafield.....	35

	2.4.5 BNFL Springfields.....	37
	2.4.6 Current environmental monitoring.....	38
<b>2.5</b>	<b>Remote Sensing.....</b>	<b>42</b>
	2.5.1 Platforms and sensors.....	43
	2.5.2 The remote sensing of suspended sediment.....	48
	2.5.3 External effects on the sensor.....	56
<b>2.6</b>	<b>Summary.....</b>	<b>60</b>
<b>3</b>	<b>CHAPTER 3: INSTRUMENTATION AND METHODOLOGY.....</b>	<b>62</b>
<b>3.1</b>	<b>Introduction.....</b>	<b>62</b>
<b>3.2</b>	<b><i>In-situ</i> spectrometry.....</b>	<b>63</b>
	3.2.1 <i>In-situ</i> spectrometry instrumentation.....	63
	3.2.2 <i>In-situ</i> spectrometry data processing.....	68
<b>3.3</b>	<b>Airborne remote sensing.....</b>	<b>71</b>
	3.3.1 Airborne remote sensing instrumentation.....	72
	3.3.2 Airborne remote sensing preliminary data processing.....	77
<b>3.4</b>	<b>Global positioning system.....</b>	<b>78</b>
	3.4.1 The principle of the global positioning system.....	78
	3.4.2 GPS data processing.....	80
<b>3.5</b>	<b>Field Methodology.....</b>	<b>82</b>
<b>3.6</b>	<b>Laboratory instrumentation and methodology.....</b>	<b>82</b>
	3.6.1 Suspended sediment.....	83
	3.6.2 Particle size.....	86
	3.6.3 Gamma spectroscopy.....	89
	3.6.4 Turbidity.....	91
	3.6.5 Salinity.....	96
<b>3.7</b>	<b>Summary.....</b>	<b>97</b>
<b>4</b>	<b>CHAPTER 4: SUSPENDED SEDIMENT CHARACTERISTICS.....</b>	<b>98</b>
<b>4.1</b>	<b>Introduction.....</b>	<b>98</b>
<b>4.2</b>	<b>The <i>in-situ</i> properties of the suspended sediment.....</b>	<b>99</b>
	4.2.1 The hypothesis of a relationship between SSC and adsorbed radionuclide concentration.....	100
	4.2.2 Grain size.....	106
	4.2.3 The <i>in-situ</i> reflectance of suspended sediment.....	111
	4.2.4 Summary and conclusions.....	116

4.3	<b>Laboratory analysis of the controls on the SSC reflectance relationship.....</b>	<b>117</b>
4.3.1	Design and testing of the experimental apparatus.....	117
4.3.2	The suspended sediment reflectance relationship.....	123
4.3.3	Variation in the suspended sediment reflectance relationship with variation in clay content.....	127
4.3.4	The suspended sediment reflectance relationship of the 63-125µm size fraction.....	131
4.3.5	The suspended sediment reflectance relationship with variation in salinity.....	134
4.3.6	Comparison of spectrometers and illumination conditions.....	137
4.3.7	Choice of CASI bandset.....	140
4.3.8	Summary and conclusions.....	142
4.4	<b>Chapter summary.....</b>	<b>143</b>
5	<b>CHAPTER 5: ACQUISITION AND PROCESSING OF REMOTE SENSING DATA.....</b>	<b>144</b>
5.1	<b>Introduction.....</b>	<b>144</b>
5.2	<b>Data acquisition.....</b>	<b>144</b>
5.2.1	Choice of flight line.....	145
5.3	<b>Ground truth data collection.....</b>	<b>146</b>
5.3.1	Sampling strategy.....	146
5.3.2	Processing of the ground truth data.....	148
5.3.3	Ground truth results.....	148
5.4	<b>Image pre-processing.....</b>	<b>153</b>
5.4.1	NERC geometric correction.....	153
5.4.2	Manual geometric correction.....	156
5.4.3	Atmospheric corrections.....	157
5.4.4	Summary and conclusions.....	170
5.5	<b>Image calibration.....</b>	<b>171</b>
5.5.1	Validation of the radiance SSC relationship.....	174
5.6	<b>Chapter summary.....</b>	<b>174</b>
6	<b>CHAPTER 6: AIRBORNE REMOTE SENSING OF SEDIMENT TRANSPORT OVER A FLOOD TIDE IN THE RIBBLE ESTUARY.....</b>	<b>176</b>
6.1	<b>Introduction.....</b>	<b>176</b>
6.2	<b>The outer estuary: Warton Bank.....</b>	<b>176</b>
6.2.1	Introduction.....	176
6.2.2	08:11 GMT, Figure 6.1a.....	177
6.2.3	08:30 GMT, Figure 6.1b.....	178

6.2.4	08:45 GMT, Figure 6.1c.....	179
6.2.5	09:02 GMT, Figure 6.1d.....	179
6.2.6	09:20 GMT, Figure 6.1e.....	180
6.2.7	09:37 GMT, Figure 6.1f.....	181
6.2.8	09:55 GMT, Figure 6.1g.....	182
6.2.9	11:11 GMT, Figure 6.1h.....	182
6.2.10	11:25 GMT, Figure 6.1i.....	183
6.2.11	Warton Bank summary.....	184
<b>6.3</b>	<b>The Ribble/Douglas confluence.....</b>	<b>203</b>
6.3.1	Introduction.....	203
6.3.2	08:11 GMT, Figure 6.2a.....	203
6.3.3	08:30 GMT, Figure 6.2b.....	204
6.3.4	08:45 GMT, Figure 6.2c.....	205
6.3.5	09:02 GMT, Figure 6.2d.....	205
6.3.6	09:20 GMT, Figure 6.2e.....	206
6.3.7	09:37 GMT, Figure 6.2f.....	207
6.3.8	09:55 GMT, Figure 6.2g.....	208
6.3.9	11:11 GMT, Figure 6.2h.....	209
6.3.10	11:25 GMT, Figure 6.2i.....	210
6.3.11	Confluence summary.....	211
<b>6.4</b>	<b>The Springfields discharge area; Savick Brook.....</b>	<b>229</b>
6.4.1	Introduction.....	229
6.4.2	08:11 GMT, Figure 6.3a.....	229
6.4.3	08:30 GMT, Figure 6.3b.....	230
6.4.4	08:45 GMT, Figure 6.3c.....	230
6.4.5	09:02 GMT, Figure 6.3d.....	230
6.4.6	09:20 GMT, Figure 6.3e.....	231
6.4.7	09:37 GMT, Figure 6.3f.....	232
6.4.8	09:55 GMT, Figure 6.3g.....	233
6.4.9	11:11 GMT, Figure 6.3h.....	234
6.4.10	Savick Brook summary.....	235
<b>6.5</b>	<b>The docks.....</b>	<b>252</b>
6.5.1	Introduction.....	252
6.5.2	08:11 GMT, Figure 6.4a.....	252
6.5.3	08:30 GMT, Figure 6.4b.....	253
6.5.4	08:45 GMT, Figure 6.4c.....	253
6.5.5	09:02 GMT, Figure 6.4d.....	254
6.5.6	09:20 GMT, Figure 6.4e.....	255
6.5.7	09:37 GMT, Figure 6.4f.....	255
6.5.8	09:55 GMT, Figure 6.4g.....	256
6.5.9	11:11 GMT, Figure 6.4h.....	257
6.5.10	11:25 GMT, Figure 6.4i.....	258
6.5.11	The docks summary.....	258
<b>6.6</b>	<b>Chapter summary.....</b>	<b>278</b>

<b>7</b>	<b>CHAPTER 7: AIRBORNE REMOTE SENSING OF SEDIMENT TRANSPORT OVER A FLOOD TIDE IN THE RIBBLE ESTUARY.....</b>	<b>280</b>
<b>7.1</b>	<b>Introduction.....</b>	<b>280</b>
<b>7.2</b>	<b>Erosion of intertidal areas.....</b>	<b>281</b>
	7.2.1 Identification of sources of sediment supply.....	283
	7.2.2 Controls on sediment supply.....	293
<b>7.3</b>	<b>Transport of suspended sediment.....</b>	<b>296</b>
	7.3.1 The importance of the tidal bore in sediment suspension.....	296
	7.3.2 Formation and strength of the axial convergence.....	300
	7.3.3 Variation in SSC across the convergence front.....	303
	7.3.4 The controls of axial convergence and sediment availability on SSC.....	307
<b>7.4</b>	<b>Comparison of remote sensing data with a sediment transport model.....</b>	<b>308</b>
	7.4.1 The model.....	309
	7.4.2 Comparability of remote sensing and model data.....	310
<b>7.5</b>	<b>Calculation of total sediment and <sup>137</sup>Cs loading and net budgets...313</b>	
	7.5.1 Assumptions.....	313
	7.5.2 Budget of suspended sediment and <sup>137</sup> Cs in suspension.....	314
	7.5.3 Interpretation and validity.....	316
<b>7.6</b>	<b>Summary.....</b>	<b>319</b>
<b>8</b>	<b>CHAPTER 8: DISCUSSION AND CONCLUSIONS.....</b>	<b>321</b>
<b>8.1</b>	<b>The need for a spatial and temporal approach to monitoring radionuclides in the Ribble estuary.....</b>	<b>321</b>
<b>8.2</b>	<b>Development of a time series approach to flood tide monitoring.....</b>	<b>322</b>
	8.2.1 Characterisation of SSC.....	323
	8.2.2 Processing of time series image data.....	326
<b>8.3</b>	<b>Application of image data to the Ribble estuary.....</b>	<b>329</b>
	8.3.1 Identification of sediment sources.....	329
	8.3.2 Hydrodynamic controls on sediment transport.....	331
	8.3.3 Model validation.....	324
	8.3.4 Sediment and radionuclide budgets.....	336
<b>8.4</b>	<b>Main contributions of this thesis.....</b>	<b>337</b>

<b>8.5</b>	<b>Refinements in methodology.....</b>	<b>338</b>
<b>8.6</b>	<b>Final conclusions of this research.....</b>	<b>340</b>
<b>8.7</b>	<b>Further work.....</b>	<b>342</b>
	<b>REFERENCES.....</b>	<b>344</b>
	<b>APPENDIX A.....</b>	<b>353</b>
	<b>APPENDIX B.....</b>	<b>356</b>
	<b>APPENDIX C.....</b>	<b>359</b>

## INDEX OF FIGURES

<b>Figure 2.1</b> The Ribble estuary.....	8
<b>Figure 2.2</b> The mechanism of tidal intrusion (Simpson and Turrell, 1989).....	18
<b>Figure 2.3</b> The decay of $^{137}\text{Cs}$ (Knoll 1989) .....	27
<b>Figure 2.4</b> $^{137}\text{Cs}$ distribution of the intertidal sediment on Warton Bank (Rainey 1999).....	40
<b>Figure 2.5</b> The effects of chlorophyll and Gelbstoff on the reflectance spectra of suspended sediment (Hudson <i>et al.</i> , 1994).....	55
<b>Figure 3.1</b> The ASD FR fieldspec® spectroradiometer (Wilson, 1995).....	63
<b>Figure 3.2</b> The GER 1500 spectroradiometer.....	67
<b>Figure 3.3</b> The normalised response of the ATM sensor, channels 1 to 8 (Wilson, 1995).....	69
<b>Figure 3.4</b> The filter function matrix for the ATM data (Wilson, 1995).....	70
<b>Figure 3.5</b> The normalised response of the CASI sensor (Wilson, 1995).....	70
<b>Figure 3.6</b> The equipment layout with the NERC aircraft (Wilson, 1995).....	71
<b>Figure 3.7</b> The internal set-up of the CASI.....	73
<b>Figure 3.8</b> The internal optics and detectors of the Daedalus ATM (Wilson, 1995).....	76
<b>Figure 3.9</b> The NERC integrated data systems (Wilson, 1995).....	77
<b>Figure 3.10</b> The velocity plot of the GPS data, Warton Bank, 6 <sup>th</sup> June 1996.....	81
<b>Figure 3.11</b> The GPS plot over a 30 second sampling period, showing the movement and mean position.....	81
<b>Figure 3.12</b> The filter assembly used for radionuclide sample preparation.....	91
<b>Figure 3.13</b> The variation in the turbidity SSC relationship with grain size.....	92
<b>Figure 4.1</b> The location of the 6 <sup>th</sup> June 1996 samples sites relative to the training wall.....	102
<b>Figure 4.2</b> The environmentally derived SSC- $^{137}\text{Cs}$ relationship and its temporal stability.....	104
<b>Figure 4.3</b> The longitudinal sampling regime used on the 3 <sup>rd</sup> & 4 <sup>th</sup> August 1996.....	107

<b>Figure 4.4</b> The sediment grain size distribution for the Ribble estuary.....	110
<b>Figure 4.5</b> The <i>in-situ</i> continuous reflectance spectra.....	112
<b>Figure 4.6</b> The variation in Pearson Product Momentum Correlation Coefficient, R, of SSC and <i>in-situ</i> reflectance with wavelength.....	113
<b>Figure 4.7</b> The <i>in-situ</i> relationship between lnSSC and reflectance.....	114
<b>Figure 4.8</b> The arrangement of the laboratory apparatus.....	118
<b>Figure 4.9</b> Laboratory derived continuous reflectance spectra.....	125
<b>Figure 4.10</b> The Pearson Product Momentum Correlation Coefficient, R, for the laboratory derived SSC reflectance relationship.....	126
<b>Figure 4.11</b> An example of the linear and ln-linear SSC reflectance relationship for 20nm CASI bands.....	127
<b>Figure 4.12</b> The variation in the SSC reflectance relationship at 720-740nm with <2 $\mu$ m content.....	129
<b>Figure 4.13</b> The variation in the SSC reflectance relationship at 720-740nm with <2 $\mu$ m content using ground sediment.....	130
<b>Figure 4.14</b> The effect of the >63 $\mu$ m content on the reflectance spectra.....	133
<b>Figure 4.15</b> The effect of salinity on the reflectance of SSC with wavelength.....	136
<b>Figure 4.16</b> The variation in laboratory reflectance with salinity at various SSC.....	137
<b>Figure 4.17</b> The SSC reflectance relationship using different spectrometers and environments.....	138
<b>Figure 5.1</b> The area of the proposed CASI flight line.....	145
<b>Figure 5.2</b> An example of raw and NERC GCORR corrected CASI data.....	155
<b>Figure 5.3</b> A diagrammatic representation of the path length correction method.....	159
<b>Figure 5.4</b> An example of mean radiance verses pixel number illustrating path length effects.....	160
<b>Figure 5.5</b> An example of a path length corrected image.....	164
<b>Figure 5.6</b> The variation in radiance with time for different surface types.....	167
<b>Figure 5.7</b> The percentage change in radiance, relative to the first image, with time, for different surface types.....	167

<b>Figure 5.8</b> The percentage change in radiance with time for the combined surface types.....	168
<b>Figure 5.9</b> The SSC reflectance calibration for CASI band 9 before and after solar elevation angle correction.....	173
<b>Figure 6.1</b> CASI SSC and ATM thermal images of Lytham to Warton Bank.....	186
<b>Figure 6.2</b> CASI SSC and ATM thermal images of the confluence area.....	213
<b>Figure 6.3</b> CASI SSC and ATM thermal images of the Springfields discharge area, Savick Brook.....	237
<b>Figure 6.4</b> CASI SSC and ATM thermal images of the docks.....	261
<b>Figure 7.1</b> CASI SSC images of Lytham Creek, 0811 to 1111 GMT.....	284
<b>Figure 7.2</b> CASI SSC images of Longton Bank, 0902 to 1111 GMT.....	289
<b>Figure 7.3</b> A map of percentage clay abundance, Lytham, 31 <sup>st</sup> May 1997 (Rainey, 1999).....	293
<b>Figure 7.4</b> Uncalibrated microphytobenthos image of Lytham, 31 <sup>st</sup> May 1997 (Rainey, 1999).....	295
<b>Figure 7.5</b> A map of percentage clay abundance, Longton Bank, 31 <sup>st</sup> May 1997 (Rainey, 1999).....	296
<b>Figure 7.6</b> The locations of the tidal bore in the first four images.....	297
<b>Figure 7.7</b> The variation in SSC with time as the tidal bore passes.....	299
<b>Figure 7.8</b> How the angle at which the SSC is transported can be used to infer the relative strength of the convergence.....	302
<b>Figure 7.9</b> The location of the transects used in Figure 7.10 and 7.11.....	304
<b>Figure 7.10</b> The SSC of a transect across the estuary at 344000E, for the first eight images.....	305
<b>Figure 7.11</b> The SSC of a transect across the estuary at 347000E, for the first eight images.....	306
<b>Figure 7.12</b> A comparison of the CASI SSC with the model predicted SSC.....	312
<b>Figure 7.13</b> The variation in SSC and <sup>137</sup> Cs with time for each flight line.....	317

<b>Figure 7.14</b> A schematic representation of the trapeziums, areas and gradients used to calculate SSC and $^{137}\text{Cs}$ budgets.....	318
---	-----

## INDEX OF TABLES

<b>Table 2.1</b> A summary of hydrodynamic estuarine classification (Open University 1991).....	15
<b>Table 2.2</b> The concentrations of radionuclides in the deposited sediments of the Ribble estuary (BNFL 1993).....	29
<b>Table 2.3</b> Variation in the BNFL Sellafield critical groups and their peak doses (BNFL 1993).....	38
<b>Table 2.4</b> Natural background radiation levels (BNFL 1993).....	38
<b>Table 2.5</b> A summary of earth observation satellites.....	45
<b>Table 2.6</b> A summary of airborne sensors.....	46
<b>Table 3.1</b> The technical specifications of the ASD FR detectors.....	65
<b>Table 3.2</b> The ATM bandset.....	75
<b>Table 3.3</b> The preparation of the formazine turbidity standard.....	94
<b>Table 4.1</b> The co-ordinates of the sample sites, 6 <sup>th</sup> June 1996.....	100
<b>Table 4.2</b> The SSC and $^{137}\text{Cs}$ activities, 6 <sup>th</sup> June 1996.....	102
<b>Table 4.3</b> The equations of the relationship between SSC and $^{137}\text{Cs}$ .....	104
<b>Table 4.4</b> The descriptive statistics for the <2 $\mu\text{m}$ grain size fraction.....	106
<b>Table 4.5</b> The errors introduced into SSC by measuring 40 $\pm$ 0.01cm depth.....	117
<b>Table 4.6</b> The surface variability in turbidity of the experimental apparatus.....	119
<b>Table 4.7</b> The variability in turbidity with depth of the experimental apparatus.....	120
<b>Table 4.8</b> The settlement of SSC with time in the experimental apparatus.....	120
<b>Table 4.9</b> The grain size distribution of the sediments used to assess variability in reflectance with clay content.....	126

<b>Table 4.10</b>	The percentage of sediment composition $>63\mu\text{m}$ , the daily mean.....	130
<b>Table 4.11</b>	The salinity values used in the laboratory experiments.....	134
<b>Table 4.12</b>	The areas viewed by the different spectrometers.....	137
<b>Table 4.13</b>	The CASI bandset used for airborne remote sensing data acquisition.....	139
<b>Table 5.1</b>	The ground truth data for electronically measured parameters.....	149
<b>Table 5.2</b>	The ground truth data for laboratory analysed parameters.....	151
<b>Table 5.3</b>	The details of the errors of manual geo-correction.....	156
<b>Table 5.4</b>	The significance of the relationship between radiance and pixels number for each CASI band.....	161
<b>Table 5.5</b>	The location of the four surfaces used in the derivation of the solar elevation angle correction.....	166
<b>Table 5.6</b>	The empirically derived equations for the correction for variation in solar elevation angle.....	170
<b>Table 6.1</b>	The location of the four geographical areas used in chapter six.....	176
<b>Table 6.2</b>	The positions of the sandbanks in the confluence area.....	204
<b>Table 7.1</b>	The location of the tidal bore and the point 100m west of the tidal bore in the first four images.....	297
<b>Table 7.2</b>	The times and distances used to calculate the velocity of the tidal bore....	298
<b>Table 7.3</b>	The distance the axial convergence front forms behind the tidal bore.....	301
<b>Table 7.4</b>	The comparative velocity of the convergence current relative to the longitudinal velocity.....	302
<b>Table 7.5</b>	The information used to calculate the total SSC and $^{137}\text{Cs}$ in suspension for each flight line.....	314
<b>Table 7.6</b>	The total SSC and $^{137}\text{Cs}$ load for each image.....	316
<b>Table 7.7</b>	The image derived erosion and deposition.....	317

## INDEX OF PLATES

<b>Plate 4.1</b> The boat used for fieldwork.....	99
---	----

## INDEX OF ACRONYMS

<b>ADCP</b>	Acoustic Doppler Current Profiler
<b>AEA</b>	Atomic Energy Authority
<b>ASD</b>	Analytical Spectral Devices
<b>ATM</b>	Airborne Thematic Mapper
<b>AVHRR</b>	Advanced Very High Resolution Radiometer
<b>BNFL</b>	British Nuclear Fuels plc.
<b>BST</b>	British Summer Time
<b>CASI</b>	Compact Airborne Spectrographic Imager
<b>CCD</b>	Charge Coupled Devices
<b>CEC</b>	Cation Exchange Capacity
<b>CZCS</b>	Coastal Zone Colour Scanner
<b>DGPS</b>	Differential Global Positioning System
<b>DOM</b>	Dissolved organic matter
<b>DTM</b>	Digital Terrain Model
<b>EA</b>	Environment Agency
<b>EARP</b>	Enhanced Actinide Removal Plant
<b>EPFS</b>	Equipment Pool For Spectroscopy
<b>FOV</b>	Field Of View
<b>FTU</b>	Formazine Turbidity Unit
<b>GCP</b>	Ground Control Point
<b>GER</b>	Geophysical Environmental Research
<b>GMT</b>	Greenwich Mean Time
<b>GPS</b>	Global Positioning System
<b>IAEA</b>	International Atomic Energy Authority
<b>IDS</b>	Integrated Data System
<b>IFOV</b>	Instantaneous Field Of View

<b>LIDAR</b>	Light Detection And Ranging
<b>MAFF</b>	Ministry of Agriculture Fisheries and Food
<b>MSS</b>	Multi-Spectral Scanner
<b>NERC</b>	Natural Environment Research Council
<b>ODN</b>	Ordnance Datum Newlyn
<b>RMS</b>	Root Mean Square
<b>SAR</b>	Synthetic Aperture Radar
<b>SIXEP</b>	Site Ion eXchange Effluent Plant
<b>SPOT</b>	Satellite Pour l'Observation de la Terre
<b>SSC</b>	Suspended Sediment Concentration
<b>SURRC</b>	Scottish Universities Research and Reactor Centre
<b>SWIR</b>	Short Wave Infra-Red
<b>THORP</b>	Thermal Oxidising Re-processing Plant
<b>TM</b>	Thematic Mapper
<b>VNIR</b>	Very Near Infra-Red

# **CHAPTER 1: INTRODUCTION**

## **1.1 PROJECT OVERVIEW**

Estuaries are important natural environments that are often nuclei for human leisure activity, such as water-sports, fishing, bird watching and walking. As such, the impact of industrial discharges into estuaries has been a problem in the past and is still a concern for scientific research and coastal zone management. Radionuclide concentrations in the marine and estuarine environments are one such case. To date, detailed scientific understanding of radionuclides in estuarine environments has been hampered by the inability to gain high spatial resolution data with regard to the transport of the sediment and the adsorbed radionuclides. This research addresses the feasibility of using airborne remote sensing to examine the suspended sediment dynamics of estuaries and radionuclide erosion, transport and deposition within estuarine environments. The work is undertaken using the Ribble estuary as a case study

The Ribble estuary is located 85km south of BNFL Sellafield, a nuclear fuel reprocessing plant located on the Cumbrian coast. The radionuclides discharged under license from BNFL Sellafield since 1952 have adsorbed on to the fine sediments of the Irish Sea, where their fate is controlled by the hydrodynamic regime. The tidal asymmetry of estuarine environments results in a net inland transportation of sediment and the accumulation of radionuclides in the intertidal areas. In addition to the BNFL Sellafield discharge, the Ribble estuary is subject to a second authorised discharge of isotopically different radionuclides from the uranium fuel fabrication plant of BNFL Springfields. These are discharged directly into the estuary near Savick Brook. Whilst

levels of the accumulated radionuclides are far below those that would raise health concerns, there is a necessary requirement to check the possible levels of radiation exposure to the general public. For this reason BNFL regularly monitor the Ribble estuary for radionuclide concentrations with respect to the anthropogenic radiation dose to the public (BNFL, 1998). Thus it is of primary importance to BNFL, and other organisations such as the Environment Agency, that spatial and temporally accurate data can be obtained for the estuarine environment.

Estuarine monitoring usually consists of the removal of sediment or water for laboratory analysis. This collection of spot sample data is a well-established technique, but it is also labour intensive, time consuming and expensive. Replicate samples are used to assess the magnitude of sampling errors but also increase the cost of sample collection and analysis. In addition to this, the data from sparsely spaced samples require spatial interpolation, which can introduce many errors, especially when the environment is spatially heterogeneous, such as an estuary. Spot sample data also take time to collect, which is unsuitable for use in highly dynamic environments such as an estuary. The result is data that can only provide limited information, as it is a time-averaged data set. Another method of investigating the estuarine environment is to use mathematical modelling. This is primarily a predictive technique and is often used in studies predicting the fate of chemicals in the environment. There are two problems particular to modelling. Firstly, the models are often over-simplified in order to reduce the computing time and secondly, the models are usually built, calibrated and validated using spot sample data. Thus, the potential for errors is even greater than for spot samples as there are the additional errors introduced by the assumptions of the model.

These problems illustrate a definite need for a tool that can provide spatially and temporally representative data in a dynamic environment at a comparatively low cost.

One method that has the potential to meet the need for accurate spatial and temporal representation of the estuary is remote sensing. The technique uses digital images of the estuary obtained from sensors detecting reflected electromagnetic radiation. The data produced are gathered rapidly giving temporally representative data and, because the images are collected from above, either by aircraft or satellite, they provide a continuous spatial overview of the target. An image is composed of picture elements, or pixels, each one being equivalent to a single spot sample. This size of the pixel, or spatial resolution, is dependent on the type of sensor and/or altitude, however, even an image with a relatively coarse spatial resolution image, (10m), will provide far superior data to spot samples and interpolation.

## **1.2 AIMS AND HYPOTHESES**

This investigation aims to develop a method to use airborne remote sensing to quantify suspended sediment concentration (SSC) and to use the image data to assess sediment transport mechanisms in the Ribble estuary.

There are many previous studies indicating the existence of a relationship between SSC and the reflectance of the water, and these are discussed in detail in section 2.5.2. However, the relationships are site specific and thus will need to be developed from first principles for the Ribble estuary. It is also known that there is a systematic relationship between the grain size of sediment and the associated radionuclide concentration, derived from deposited intertidal sediment. Therefore, this study hypothesises that there

is a systematic relationship between SSC and the adsorbed radionuclide concentration. This has not yet been shown to be true for suspended sediment and needs to be defined and characterised. Assuming this first hypothesis is true, the SSC predicted from reflectance can then be used as a surrogate for radionuclide concentration and SSC images can be calibrated to suspended radionuclide images.

The second hypothesis states that a series of sequential remote sensing images can be used to derive information behaviour of the estuary over a flood tide. Images calibrated for SSC can be used to:

1. Identify sources of sediment and radionuclide resuspension.
2. Calculate budgets of sediment and radionuclides estuary wide for the flood tide.

This should provide useful information to a sector of users to whom remote sensing data are generally considered inaccessible or too technical to be of use.

### **1.3 THESIS STRUCTURE**

The thesis is structured to guide the reader through the development of the method used to define the relationships between SSC, reflectance and radionuclides, after which a general assessment of the imagery results and the potential uses of the data will follow.

The thesis provides an introduction to the study area, an overview of previous studies and some background information on subjects relevant to this study. Chapter three follows this, containing a detailed description of all the instrumentation and laboratory methods used throughout the study. This information is provided within a single chapter so the flow of subsequent chapters is not impeded by excessive technical information. Prior to the remote sensing image acquisition it is fundamental that SSC

reflectance characteristics are established. *In-situ* characterisation of the SSC was performed and the results of this are presented in chapter four. Subsequent laboratory work, investigating the possible variables of the SSC reflectance relationship, follows the *in-situ* work.

The rationale behind the collection of the image data and the details of the image processing techniques used are presented in chapter five, which ends with the final image calibration used to produce calibrated SSC images. The actual SSC images are introduced in a descriptive format in chapter six. This aims to introduce the reader to image interpretation and to highlight the main features of the estuarine flood tide. Chapter seven will then bring the image data into the realm of estuarine management by using the results to identify the sediment sources and the controls on erosion and hydrodynamics. The image data are also compared to the latest model of the Ribble estuary, VERSE, in an attempt to assess the potential of using image data to validate or enhance the model data. The two data sources are combined to produce figures for the total SSC for each flight line and subsequent sediment budgets. The final discussion chapter brings together all aspects of the project to assess the potential contributions and problems of the data in context with other people's work. The potential for the use of this technique in future studies is then considered. The final conclusions are presented in a bullet point format as a final summary to the findings of the investigation.

## **CHAPTER 2: LITERATURE REVIEW**

### **2.1 INTRODUCTION**

The following chapter aims to give an over view of published literature relevant to this project. The subjects reviewed are split into three broad areas, the Ribble estuary and estuarine characteristics, the sources and behaviour of radionuclides in the environment and remote sensing platforms and their application to estuarine systems. The key points resulting from this literature review are summarised at the end of this chapter.

### **2.2 THE STUDY AREA**

#### **2.2.1 The River Ribble**

The river Ribble rises at Newby Head Moss (422m) in North Yorkshire, from where it flows South before turning West through Preston and out into the Irish Sea. The solid geology around Newby Head Moss is mainly Carboniferous limestones (Mudge *et al.*, 1994) which provide alkaline headwaters with a pH of approximately eight (EA, 1997). As the river approaches the coast Permian sandstones (Mudge *et al.*, 1994) over-lie the limestone geology. The river Ribble is one of the largest in Northwest England covering a distance of 110 km through a catchment area of 2182 km<sup>2</sup> (EA, 1997). The average annual rainfall varies from 1775 mm at Newby Head Moss to 890 mm at the coast (EA, 1997). There are four tributaries of the river Ribble:

1. The river Calder, which having run through industrial areas reduces the water quality of the Ribble.
2. The river Hodder, which has an exceptionally high water quality.
3. The river Darwen, which flows into the estuary at Penwortham.
4. The river Douglas, which flows into the estuary west of Longton Marsh.

### **2.2.2 The Ribble Estuary**

The estuary (Figure 2.1) is approximately 30km in length, from Lytham to the tidal limit at the M6 motorway bridge and 15km wide at the mouth at Lytham and lies in approximately an East-West orientation. The tidal range can be up to 10m at Lytham (Mudge *et al.*, 1994) and the average influx of water on an incoming tide is estimated to be  $12,000 \text{ m}^3 \text{ s}^{-1}$  (Brown, 1996). The estuary is known to exhibit an asymmetrical tidal regime, which leads to a net landward transportation of sediment, and the position of the turbidity maximum in the estuary is known to depend primarily on freshwater flow rather than tidal magnitude (Burton *et al.*, 1995). Salinity data obtained by Burton *et al.* (1995) also suggest that the estuary is well mixed on a flood tide but stratified on the ebb. The dominant mechanisms controlling the flux of sediment in the estuary vary both spatially and temporally, however, on a spring flood tide the landward transportation of sediment is controlled predominantly by tidal pumping (Lyons, 1997).

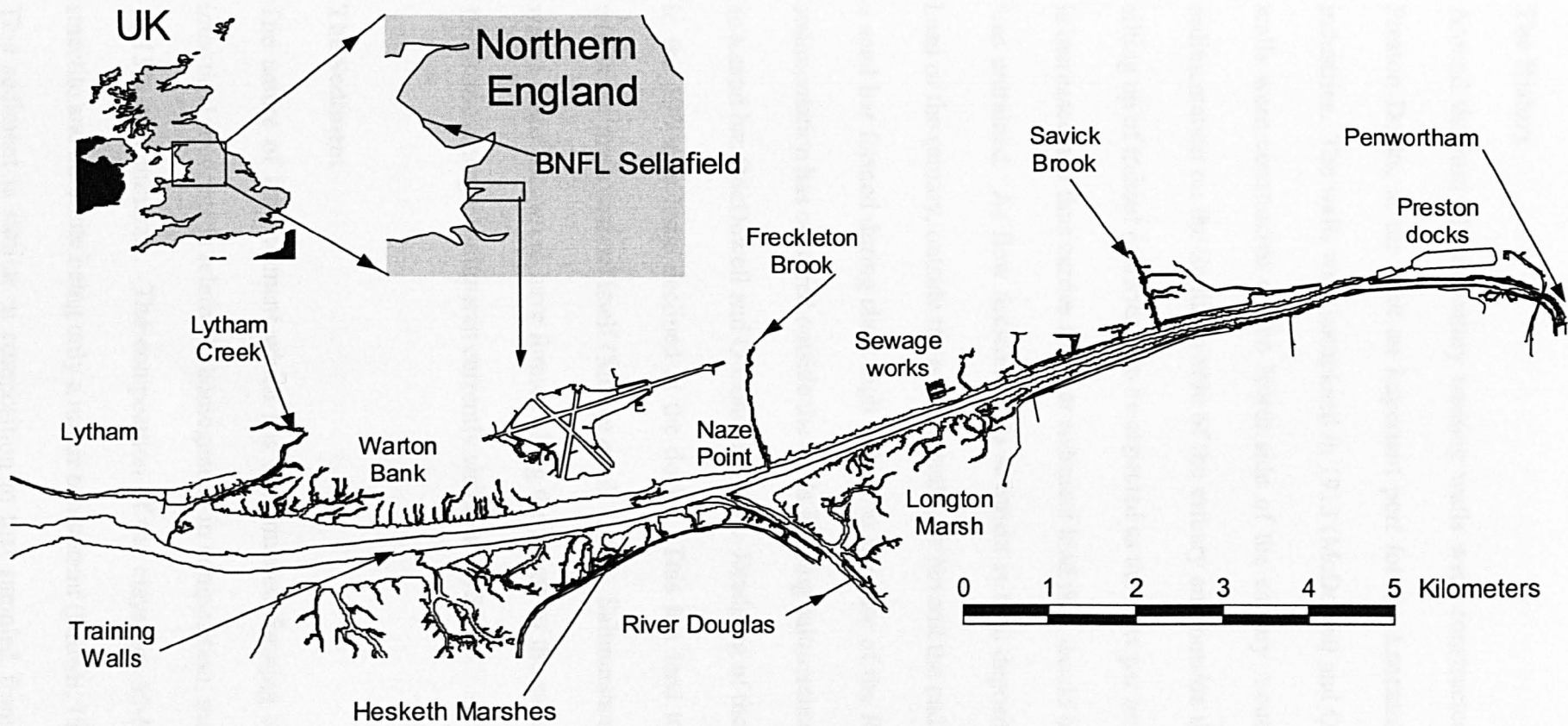


**Figure 2.1** The Ribble Estuary

## **The History**

Around the turn of the century training walls were constructed to ease navigation to Preston Docks, at the time an important port for the Lancashire cotton and woollen industries. The walls were completed in 1913 (McDowell and O'Connor, 1977). These walls were constructed on the North side of the estuary mouth and led to increased sedimentation on the Southern side of the estuary and outside the training walls. This silting up of trained estuaries is to be expected as the flow per unit width in trained areas is increased and thus carries a higher sediment load than would be the case if the estuary was untrained. As flow decreases this sediment is then deposited. This occurs at the head of the estuary, outside the training walls, or beyond the end of the training walls as a sand bar formed during slack high water. In the case of the Ribble estuary extensive sedimentation has occurred outside the walls forming saltmarshes and outside the mouth as a sand bar (McDowell and O'Connor, 1977). Dredging of the trained channel ceased in the 1980s as trade declined at the docks. This has led to further sedimentation within the main channel itself (Mudge *et al.*, 1994). Saltmarshes are continuing to form with 5.5 km<sup>2</sup> known to have formed along the length of the estuary since 1949 (Brown, 1996) and emergent saltmarsh currently visible at Lytham.

## **The Sediment**

The nature of the sediment which has accumulated forming the saltmarshes and the inter-tidal mudflats is relatively homogenous in composition, that is 50-70% quartz and 10-15% clay minerals. The composition of the clays are 50-60% illite with 20-30% smectite and kaolinite being only a minor component (Brown, 1996 Bryant *et al.*, 1996). This sediment is similar in composition to that sampled from a marine location but

markedly different from that of an alluvial source which was higher in quartz and the clay component was much higher in kaolinite. This indicates that the sediment accumulating in the Ribble estuary is almost purely of a marine origin (Brown, 1996). Sedimentation rates in the estuary have been estimated at between 15-120 mm yr<sup>-1</sup>, varying both spatially and temporally. These values are considered well within the normal range for a UK estuary (Mamas *et al.*, 1995). Some areas of sediment in the Ribble are known to be more dynamic than other areas. A study by Mudge *et al.* (1997) found that the Freckleton, Savick Brook and Penwortham areas acted as a sink for fine-grained sediments carried up on spring tides. At high river-flow these fine sediments are remobilised and deposited at Lytham. However, there tends to be no net loss of sediment from the estuary as a whole. The results of the study split the estuary into three sections:

1. The upper estuary where fine sediment is stored during low river flows.
2. The middle estuary where sediment is deposited and removed on a regular tidal basis.
3. The lower estuary where fine sediment accumulates during high river flows.

One of the key consequences of the accumulation of the sediment in the Ribble estuary is in the associated radionuclide originating from both BNFL Sellafield via the Irish Sea and BNFL Springfields which discharges directly to the estuary. This is discussed more fully in section 2.3.1. However, in a general context the Ribble estuary has other key environmental characteristics that make it a Site of Special Scientific Interest, (SSSI). The accumulated saltmarsh has undergone extensive reclamation to provide agricultural land, approximately 152 km<sup>2</sup> in total (Mudge *et al.*, 1994). The saltmarshes on the south of the estuary form England's largest National Nature Reserve which is

internationally significant for species such as whooper swan, wigeon, and the knot- and black tailed godwits. The lower Ribble and Hodder are important salmon rivers. Commercial fisheries for mullet, bass, elvers and shellfish are also active in the area however, the estuary itself has been over-fished of shellfish, which are now absent from this part of the Ribble (EA, 1997).

### **2.2.3 Modelling the Ribble Estuary**

Thus far, attempts to model the Ribble have tended to be unsuccessful and there maybe many reasons for this. One reason is likely to be the difficulty in collecting precise and accurate data in such a dynamic environment with which to build and validate the model, an example of this can be seen in the 2-D model produced by Burton *et al.* (1995). Data were collected from just three ground stations and the presence of the river Douglas was omitted completely. Other reasons may lie in the fact that the models are over simplified as in the one-dimensional MIKE11 model (Atkins, 1993).

The latest attempt to model the Ribble estuary, by Westlakes Scientific Consulting Ltd for BNFL, is nearing completion. The model is a two-dimensional model with a longitudinal resolution of 250m and a depth resolution of 0.2m, comprising computational modules for non-cohesive sediment transport, cohesive sediment transport and hydrodynamics (elevation and velocities) (Gleison 1999). This model will be unable to reproduce the physical phenomena of axial convergence and lateral variations in sediment supply.

## **2.2.4 The Irish Sea**

The source of sediment accumulating in the Ribble estuary is the Irish Sea. The Irish Sea consists of several sedimentary basins resulting from the faulting of the Carboniferous, and Permo-Triassic rocks (Brown, 1996). These rocks have been glacially eroded and are overlain with tills. The changes in composition of the sea bed sediment are much more abrupt than in the North Sea. The muds in the Irish Sea are confined to two distinct areas, a belt parallel to the Cumbrian coast and in the deeper channel between the Isle of Man and Ireland. It is the mud banks off the Cumbrian coast that are thought to store a large proportion of the radionuclides discharged from Sellafield over the last forty five years (Cook *et al.*, 1997). Atlantic waters enter the Irish Sea mainly via St. George's Channel in the south with only a small amount entering via the Northern channel. The circulation is tidally driven and the water leaves through the North Channel via the south or north of the Isle of Man (Kershaw *et al.*, 1992). The Eastern Irish Sea is markedly affected by freshwater input and this may lead to a weak stratification whereas the Western side is generally well mixed but contains a summer density driven gyre (Hill *et al.*, 1997).

## **2.3 ESTUARINE CHARACTERISTICS**

This section gives a brief review of the basic characteristics of estuaries, which have a direct relevance to the Ribble. Further information on these subjects can be found in most textbooks relating to the estuarine environment, such as Dyer (1979) and Olausson and Cato (1980).

The estuary is difficult to define in a global context, as there are limitless variations in external parameters such as geographical location, climate, river flow and tidal range. The common perception of an estuary is where a river flows into the sea but an estuary could also be considered as a river valley drowned by a sea level rise. The problem is complicated further depending on the temporal framework in which an estuary is considered, for example in geological terms an estuary is merely an ephemeral feature that develops, silts up and disappears in a very short geological time span. However, when considered on a short time scale, for example when modelling an estuary, it is generally considered as a steady state system that changes very little. For this reason the definition given by Fairbridge (1980) is somewhat convoluted. "An estuary is an inlet of the sea reaching into a river valley as far as the upper limit of tidal rise, usually being divisible into three sectors:

1. A marine or lower estuary, in free connection with the open sea;
2. A middle estuary, subject to strong salt and freshwater mixing; and
3. An upper or fluvial estuary, characterised by fresh water but subject to daily tidal action."

For the purpose of this project, which uses one rising tide as its temporal framework, we will define the estuary as the area of the River Ribble where fresh water/saltwater mixing takes place and tidal influence is apparent. This distance will actually depend on fresh water flow and tidal range, but with regard to the aerial data, will cover the stretch from Preston to Lytham St Annes.

### **2.3.1 Estuary Classification**

The classification of an estuary is as ambiguous as its definition and for all the same reasons. However, there are two methods that have come into common use. The choice of classification method depends whether one is describing an estuary as a physical geographical feature by physiographic classification or with regard to the circulation patterns and water body structures by hydrodynamic classification.

The simplest method of estuarine classification is by physiographical description, that is a description of the shape of the estuary and its surrounding landscape. Although the physiographic classification method is very simple, it provides little information about the hydrodynamic behaviour of the estuary. The hydrodynamic method of classification of an estuary is more specific and requires field data for salinity. Details of the classifications are found in most estuarine textbooks, for example Dyer (1979). This classification technique has three main classes, 1-3, in addition to two further classes, 4-5, representing the more exceptional circumstances, these are;

1. The Salt Wedge Estuary
2. The Partially Mixed Estuary
3. The Well Mixed Estuary
4. The Fjord
5. The Negative Estuary

Table 2.1 summarises the characteristics of the three key classes of estuary.

<b>The Salt Wedge</b>	<b>Partially Mixed</b>	<b>Well Mixed</b>
River flow $\geq$ Tidal flow	River flow $\cong$ Tidal flow	River flow $\leq$ Tidal flow
Minimal mixing: by saline entrainment	Some mixing: at interface and bed	Free mixing
Large variation in salinity with depth. (~30 ‰ in 0.5m) [Pronounced halocline]	Some variation in salinity with depth. [Halocline]	No variation in salinity with depth. (large lateral variation) [No halocline]
e.g. Mediterranean Sea: Nile Black Sea: Po, Danube	e.g. NW Europe: Thames and Mersey	e.g. Wide shallow estuaries: Exe

**Table 2.1** A summary of features of hydrodynamic estuarine classification. (Open University 1991).

This classification is purely qualitative and no estuary class is discrete. There is a continuous progression of estuarine features producing ambiguous estuaries that are difficult to classify. A common example of this ambiguity is where one estuary will exhibit different behaviour in flood and ebb or spring and neap conditions.

A useful discussion on whether this method of qualitative classification is actually useful can be found in Pritchard (1989) which concludes that there is still some value to be gained from using these very simplistic approaches to classification, provided that caution is exercised.

The Ribble can be physiographically classified as a coastal plain estuary. This is an estuary that is situated in a low relief landscape. It is shallow with a wide mouth and

generally funnel shaped. However, using the hydrodynamic classification, the classification of the Ribble estuary is more ambiguous. It is known to be well mixed on the flood tide and partially mixed, showing some stratification on the ebb tide (Burton *et al.*, 1995). Throughout this study the Ribble estuary will be considered a well-mixed coastal plain estuary, as data are collected over a spring flood tide when no partially mixed characteristics are seen.

### **2.3.2 Estuary Circulation and Controls on Sediment Transport**

Estuary circulation is a complex process governed predominantly by the tides, but freshwater-saltwater mixing also creates secondary density driven circulation patterns called residual currents (Dyer, 1973). These circulation patterns control the sediment transport within the estuary. The following sections provide an overview of some of the main influences on sediment transport that are of importance in an estuary such as the Ribble.

#### **Tides**

In an estuarine environment the symmetrical sinusoidal wave of the high and low tide is distorted to form an asymmetrical tide. This is evident as a short fast flood tide and longer, gentler ebb tide. This distortion appears because the speed of a shallow water wave is directly related to the square root of the depth of the water, thus the crest of the progressive tide wave (high water) travels faster than the trough (low water). The tides are further distorted by the shallowing of an estuary towards the tidal limit, hence the asymmetry is more pronounced in the upper reaches of an estuary than at an estuary mouth (Uncles, 1981).

This tidal asymmetry is particularly evident in the Ribble estuary where the flood tide is especially rapid, lasting less than three hours, followed by much longer periods of slack and ebbing water.

### **Mixing**

Turbulence is the main mechanism by which heat, salt and momentum are transferred, heat and salt being transferred to a far lesser extent than momentum. Turbulence is produced when the flow interacts with either the bed or another flow. Where there is minimal turbulence, mixing can occur by the process of entrainment, a process found in salt wedge type estuaries. Shear stress between adjacent water bodies moving in opposite directions cause small internal waves. When these waves break, small quantities of salt are ejected into the overlying freshwater. Other forms of mixing processes include convection and advection, where buoyancy forces drive vertical and horizontal circulations, (Bowden, 1980). Mixing can also occur due to molecular diffusion and dispersion which are both much more applicable to point source pollution modelling and monitoring.

### **Tidal Intrusion Fronts.**

Despite the numerous mixing processes within an estuary, there are distinct areas of unmixed water with a definite boundary between water bodies, this boundary is known as a front (Largier, 1992). In a stricter sense, a front can be defined as the positions where the halocline (or thermocline) of stratified water touches the surface (Open University, 1991). This frontal zone is a region where turbulent mixing is present and yet the distinct identity of each water mass is maintained, for example a river plume spreading out over saline water. The velocity of propagation of the front is

approximately proportional to the square root of the depth of the freshwater layer. However, the actual propagation velocity is generally less than that given by theoretical calculations due to partial mixing at the freshwater/saline interface. On a fast flood tide an outward spreading freshwater front is swept back into the estuary forming the characteristic V-shape of the tidal intrusion front, this V-shape being subject to deformation by estuary bottom topography.

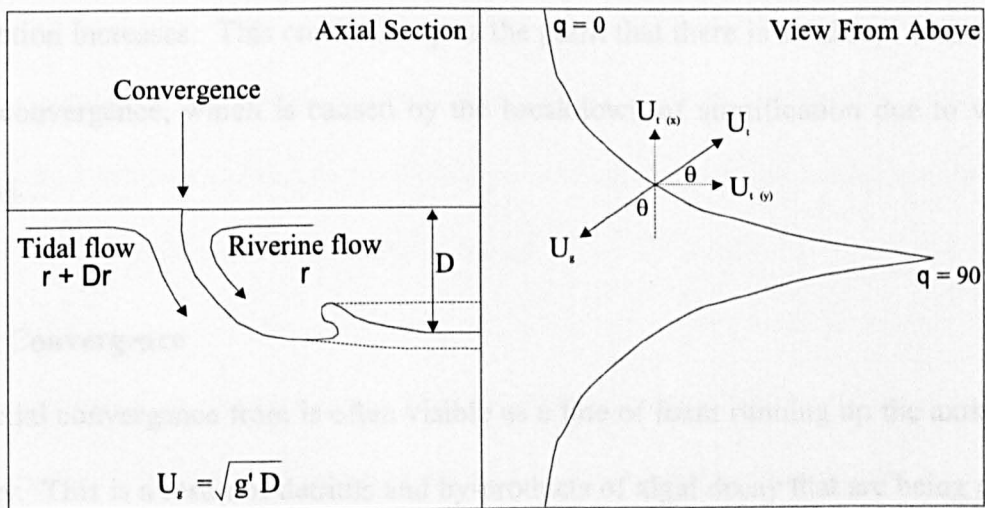


**Figure 2.2** The mechanism of tidal intrusion. (Simpson and Turrell, 1986)

Figure 2.2 demonstrates why the shape of the tidal intrusion takes the form of a V. At the front, the density current outflow is in equilibrium with tidal inflow, that is fresh water outflow ( $U_g$ ) is balanced by the local component of the tidal flow ( $U_t$ ) perpendicular to the front.

$$U_g = U_{t(y)} \cos\theta \quad [2.1]$$

Thus, the angle between the front and a line across the estuary,  $\theta$  is given as

$$\theta = \cos^{-1} (U_g / U_{t(y)}) \quad [2.2]$$

If  $U_g$  is assumed to be constant  $\theta$  is proportional to  $U_{t(y)}$ . Thus, where  $U_{t(y)} = U_g$ ,  $\theta$  will be zero degrees. This is the situation at the banks of the estuary and as the front approaches the centre,  $\theta$  approaches  $90^\circ$ . Density currents produced by stratification maintain the tidal intrusion front. As the flood currents increase the angle of the V of the intrusion becomes increasingly acute and the transverse component of the density circulation increases. This continues up to the point that there is an abrupt transition to axial convergence, which is caused by the breakdown of stratification due to vertical mixing.

### **Axial Convergence**

The axial convergence front is often visible as a line of foam running up the axis of the estuary. This is a result of detritus and by-products of algal decay that are being pushed together by residual currents. However, the foam line can be dispersed under severe wind stresses and is not always well defined. West and Cotton (1981) observed the first direct evidence of this convergence in mid-channel by releasing rhodamine dye into mid-channel surface waters. Traces of the dye were found in upstream bottom water samples but not upstream surface water samples. Nunes and Simpson (1985) hypothesised that the axial convergence was caused by the distortion of vertical isohalines, by incoming saline flow allowing denser water to overly less dense water. This would lead to plunging at the centre of the v-shape intrusion and the subsequent establishment of a density driven, two cell transverse circulation. Evidence to support this hypothesis was observed directly during a study of the estuary of the river Conwy in North Wales. Measurements made using an inter-calibrated bridge of salinity probes

showed that salinity was consistently higher at the centre of the channel and small drogues released from a transect across the estuary ended up in a line along the centre of the estuary demonstrating the existence transverse currents. The data from the drogues implied that the transverse current velocities were only 20% of the axial current velocities. Further evidence of the details of the two-cell circulation was provided by Acoustic Doppler Current Profiler (ADCP) data (Robinson-Swift *et al.*, 1996) which were subsequently reproduced by modelling. Aerial survey of spring flood tides in 26 UK estuaries (Brown *et al.*, 1991) revealed that in 15 cases axial convergence was found to be present with a further 6 cases identified through field observation. Thus axial convergence was considered to be typical of well-mixed shallow macrotidal estuaries and far more widespread than previously thought.

Other sources of convergence include flow separation by obstacles where a boundary forms between the uninterrupted flow and a stationary horizontal eddy but axial convergence is distinctly along the axis of the estuary. The axial convergence front foam line is modified by shear stresses often producing a sinusoidal distortion and by bottom topography and bends (Nunes and Simpson, 1985). On an ebb tide in the Conwy estuary a weak divergence is observed (Turrell *et al.*, 1996) where axial gradients are only a quarter of those on the flood.

### **2.3.3 Estuarine Sediments**

The circulation patterns of water in an estuary are the governing factor in the distribution of sediment and associated pollutants but the properties of the sediment are also very important. It is essential to understand both the sediment behaviour and the

complex circulation patterns if the environment is to be managed effectively as a recreational resource or as a means for the disposal of effluent.

### **Sediment Erosion**

Erosion of non-cohesive and cohesive sediment occurs differently. The flow required to transport sediment, the critical shear velocity, is related to the mass of the grains and the interacting forces with other grains, such as cohesion. Non cohesive sediments are transported individually by the flow. At lower flows they will slide and bounce along as bed load but as the flow increases they are lifted into suspension.

Cohesion is an electrostatic attraction between individual grains that binds them together very strongly. This electrostatic attraction causes cohesive particles to form clumps when in solution, a process known as flocculation. Clay minerals present in only a small amount (5% -10%  $w/w$ ) mixed in non-cohesive sand will alter the sediment properties significantly (Open University, 1991). The presence of biogenic films also increases cohesive properties of sediment by the production of extracellular polymeric substances that bind the sediment grains together (Paterson *et al.*, 1998, Paterson, 1999). Thus, rather than transport of individual grains, the sediment forms flocs. If the sediment has been compacted in any way, for example by exposure of mud flats at low tide, then the flocs can no longer just lift away at the appropriate shear velocity. Instead erosion tends to take the form of mass failure where large chunks of sediment are torn away. This requires very high shear velocities, therefore once deposited cohesive sediments are more difficult to erode, despite their small grain sizes. In an estuary, it is the cohesive muds that are particularly plentiful and the abundance of ions in the saline water, further increase cohesive strength and flocculation.

## **Deposition**

Deposition starts to occur when the velocity of flow decreases enough for the sediment to start to settle, with the heavier grains settling first. The suspended grains will start to settle once the shear stresses fall below the critical level, however it then takes time for each grain to reach the bed, the settling lag, which is larger for smaller grain sizes (Dyer, 1979). Water in an estuary is very rarely static. As this is the case it is surprising that deposition of the smaller grains occurs at all. The smallest grains can only settle at the lowest flow velocities but the ability of clays to flocculate decreases the settling time, aiding deposition. There is also evidence that the presence of bio-films on the underlying mud increase the rate of deposition by sequestering clay minerals, (Black *et al.*, 1998, Paterson, 1999).

Temporally, deposition is also aided by the long-term variations in the tidal system. As the tides decrease in size from springs to neaps, deposition will occur at the tidal limits of the channel and tributaries. The position of the tidal limit will change with each tide, allowing substantial deposition and compaction to occur until the situation reverses and the magnitude of the tides increase, becoming an erosive environment. In flood conditions deposition also occurs on a saltmarsh environment where the vegetation substantially aids deposition by trapping sediment.

### **2.3.4 The Ribble Estuary: A Summary**

It can be concluded that the Ribble estuary can be physiographically classified as a coastal plain estuary. Hydrodynamically, salinity and flow data (Burton *et al.*, 1995) show that the estuary is well mixed on a flood tide and stratified and thus partially

mixed on an ebb tide. However, this variation between well mixed and partially mixed is also due to the asymmetry between flood and ebb tide flows, in addition to other factors such as tidal range and river-flow. It is known that the Ribble does exhibit a turbidity maximum (Burton *et al.*, 1995). This is a feature common to partially mixed estuaries, therefore it is possible that this is an occasional feature dependent on the magnitude of the tide and river flow. Lateral circulations due to Coriolis force, particularly the use of separate flood and ebb channels characteristic of well-mixed estuaries, are restricted in the Ribble by the construction of the training wall. For the purpose of this study, where the estuary is studied over the course of a single spring flood tide, it is assumed to be a well-mixed estuary. Sedimentation rates in the Ribble are estimated to be between 15 and 120 mm yr<sup>-1</sup> (Mamas *et al.*, 1995) which are typical of a UK estuary. Accretion rates for the Freckleton Brook area have been quoted to be >600mm yr<sup>-1</sup> (Beresford-Hartwell *et al.*, 1995) but this information was based on the lack of a maximum in the caesium profile at this location. Thus, the maximum caesium concentration from the peak Sellafield discharge was assumed to be at a greater depth. No consideration was given to the possible disturbance of the profile by sediment reworking.

## **2.4 RADIONUCLIDES IN THE ENVIRONMENT**

### **2.4.1 Radioactivity and Environmental Sources**

#### **Radioactivity**

The radioactive decay of an atomic nucleus is the result of the atom trying to achieve a more stable energetic state, this emission of energy can take three forms, alpha ( $\alpha$ ), beta ( $\beta$ ) and gamma ( $\gamma$ ).

Alpha decay is the emission of a helium nucleus from the nucleus of the atom and is sometimes known as heavy charged particle emission, however, heavy charged particle emission also includes fission products. Examples of typical alpha emitters in the Ribble environment are  $^{230}\text{Th}$ ,  $^{232}\text{Th}$ ,  $^{238}\text{U}$ ,  $^{239+240}\text{Pu}$  and  $^{241}\text{Am}$  (Brown, 1996). Beta decay is the emission of a fast electron, negative or positive from the nucleus of the atom. Gamma radiation is the emission of a photon of electromagnetic radiation from the nucleus of the atom. This is necessary for the atom to stabilise itself after the ejection of an  $\alpha$  particle or  $\beta$  electron. An ejection of gamma radiation will always be preceded by either an  $\alpha$  or  $\beta$  decay, however, an  $\alpha$  or  $\beta$  decay is not always followed by gamma emission if no further energy stabilisation is necessary. Gamma radiation is emitted at distinct energies specific to the atom from which it is emitted, (Knoll, 1989). It is this property which gamma spectroscopy uses to identify which radionuclides are present in a given sample. For example, gamma rays with energy of 0.622 MeV would indicate the presence of  $^{137}\text{Cs}$ .

### **Sources of Radioactivity in the Environment**

Radioactive decay is common to many naturally occurring elements, both in bio-systems and minerals, such as  $^{14}\text{C}$ ,  $^{40}\text{K}$  and  $^{238}\text{U}$ . Anthropogenic additions to the natural background radioactivity can occur via some industrial processes or as the release of anthropogenic isotopes from the nuclear power industry or atomic weapons testing. With respect to the Ribble estuary the focus of interest is the authorised discharge of radionuclides originating from BNFL Sellafield, 85 km North of the Ribble estuary and BNFL Springfields, which discharges directly to the estuary.

## **2.4.2 Geochemistry of radionuclides**

To assess the behaviour of a radionuclide once it is discharged to the marine environment one must understand the reactions and interactions that are likely to take place and any external factors causing variation in the reactions and interactions. For example, we need to know whether a radionuclide will remain in solution or adhere to suspended particulates and what the controlling factors are, such as sediment composition or solution composition. The following discussion examines the basics of these environmental interactions and the known geochemistry of some of the important radionuclides in the Irish Sea.

### **The solid-water interface**

Small electronic charges on the surface of suspended particles leads to an accumulation of oppositely charged ions in a bid to conserve electrical neutrality. The interactions of these ions at the solid-water interface are a complex function of charged surface sites on the particle and the composition and pH of the surrounding solution. The chemical interactions are termed sorption of which there are three types (Krauskopf and Bird, 1995).

1. Surface precipitation, where the sorbed ions form a surface precipitate with a structure and composition different to that of the host mineral particle.
2. Absorption, or co-precipitation, where solute species are incorporated into the mineral structure by diffusion or dissolution and re-precipitation.
3. Adsorption, where there is an accumulation of aqueous ions on the mineral surface without a 3D molecular structure typical of a mineral.

Adsorption depends on the absolute and relative concentrations of both adsorbate (mineral) and adsorbant (aqueous ions) in addition to the ionic strength of the solution. Elements of the different chemical groups exhibit different adsorption behaviour. For the alkali metals, sorbability decreases from caesium to lithium, probably because lithium, although it is smaller in size, is such a strongly hydrated ion it is effectively larger than caesium.

### **Clay minerals**

The term clay can be used in two contexts:

1. To describe the grain size fraction of a sediment,  $<4\mu\text{m}$  on the Wentworth scale (Open University, 1991), or  $<2\mu\text{m}$  in some older scales
2. To describe a range of aluminosilicate minerals of specific composition and crystal structure.

The two uses effectively overlap, as the clay mineral structures do tend to form the smaller particles of sediment. The structure of clay minerals are generally phyllosilicates which are sheets made up of silicate tetra- and octa-hedra with combinations of other ions. There are a few exceptions but these are rare. Examples of the various clay mineral structures can be found in most geochemistry textbooks, for example, Ellis and Mellor (1995).

### 2.4.3 Radionuclides in the Coastal Environment

This project focuses on the behaviour of caesium due to its abundance and ease of detection. However, a summary of the geochemical behaviour of caesium in addition to some of the other key radionuclides found in the Ribble estuary is given below.

#### Caesium

Caesium is found in the environment in two isotopic forms,  $^{134}\text{Cs}$  and  $^{137}\text{Cs}$  with the latter form predominating. The following information relates to the  $^{137}\text{Cs}$  isotope on which this project will focus.  $^{137}\text{Cs}$  is a fission product, it is a normal trace element found in low-level waste from commercial reactors and is also released from weapons testing (Eisenbud and Gesell, 1997). The half-life of  $^{137}\text{Cs}$  is 30.17 years and radioactive decay is via a beta and gamma route as shown in Figure 2.3, showing 93.5% of caesium decay results in the emission of a gamma ray.

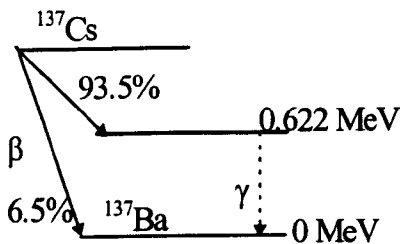


**Figure 2.3** Decay of  $^{137}\text{Cs}$ , (Knoll 1989).

In an aquatic environment caesium exists in a single oxidation state,  $\text{Cs}^+$  and exhibits conservative behaviour, i.e. it is soluble and transport is controlled by water flow. Concentrations within the water tend to parallel salinity (Assinder *et al.*, 1985), another indication of conservative behaviour. Caesium has a higher solubility in saline water than in fresh water (Eisenbud and Gesell, 1997). However, there is also evidence that

once bound to a particle, caesium is effectively fixed (Hird *et al.*, 1995) and consequently exhibits a less conservative behaviour.  $^{137}\text{Cs}$  distribution within the Irish Sea has been determined annually since 1979 (Kershaw *et al.*, 1992) and samples of deposited sediment from the Ribble estuary are analysed quarterly by BNFL (BNFL, 1993). Details of these values for  $^{137}\text{Cs}$  and other radionuclides found in the Ribble estuary and discussed later are given below in table 2.2.

Concentrations of  $^{137}\text{Cs}$  in filtered seawater from the Irish Sea were found to be 0.62-0.66 Bq l<sup>-1</sup> and the concentration of caesium on associated suspended sediments was approximately 0.12 Bq l<sup>-1</sup> (BNFL, 1993). Another survey (Cook *et al.*, 1997) found that caesium concentrations in filtered seawater from the Irish Sea were 0.2-0.343 Bq l<sup>-1</sup> with the higher values being located along the coast in close proximity to BNFL Sellafield. The same survey found that all values for the associated suspended sediments were below the limit of detection and estimated that the loss of caesium from the Irish Sea via the North Channel was 86TBq yr<sup>-1</sup>.

On discharge from Sellafield it is estimated that 10% of the  $^{137}\text{Cs}$  becomes immediately associated with the sediments. Many studies have utilised sequential extraction techniques to establish the phase associations of  $^{137}\text{Cs}$  within various sediments and soils. There is overall agreement that  $^{137}\text{Cs}$  becomes irreversibly associated with the residual phase (Livens and Baxter, 1988a), which contains the clay minerals. The percentage of  $^{137}\text{Cs}$  in the residual phase has been found to range from 81-86% in Solway Firth cores (McDonald and Jones, 1995) and up to 100% in Ribble intertidal sediment, (Brown, 1996). The Solway Firth core data showed little variation in association of caesium with depth.

Location	<sup>137</sup> Cs	<sup>241</sup> Am	<sup>234m</sup> Pa	<sup>228</sup> Th*	<sup>230</sup> Th	<sup>232</sup> Th
Lytham Boatyard	795	299	16475	52.5	175	46
BNFL Outfall	373	198	14402	37	110	35
Penwortham Bridge	445	171	30215	37	110	33.5
River Douglas	464	180	17390	42.5	114	37.5
Hesketh Outmarsh (3/4)	585	279	78477	44.6	82	34.7
Savick Brook	548	240	95030	60	256	49.5
Warton Bank Msh. (1/4)	940	342	5000	60	200	60
Freckleton	735	286	31650	54	212	40
Penwortham Park	703	336	116726	66	237	47

**Table 2.2** The concentrations of radionuclides in the deposited sediments of the Ribble estuary, given in Bq kg<sup>-1</sup>, dry weight. Average value of samples taken at quarterly intervals in 1992. Sample site switched from Hesketh Outmarsh to Warton Bank in last quarter (\* = naturally occurring), (BNFL, 1993).

In addition to sequential extraction, the association of <sup>137</sup>Cs with respect to sediment grain size has also been thoroughly investigated. Livens and Baxter (1988b) found over 47% of caesium was associated with the sediment fraction <2µm in Cumbrian intertidal sediments. In the Ribble estuary a good correlation was found between caesium concentration and the percentage of sediment less than 63µm over the whole length of the estuary (Mudge *et al.*, 1994, Assinder *et al.*, 1997 and Rainey *et al.*, 1999).

The above studies are consistent with the fixation of caesium on clays. Laboratory experiments have shown that minerals other than kaolinite are responsible for this caesium fixation concluding that fixation must be due to illite or micas (Francis and Brinkley, 1976). It is worth noting that in Europe illite is the dominant clay mineral (Tyler, 1994) and as the release of caesium from kaolinite is eight times greater than that for illite, therefore, illite must be the fixing mineral. In the intertidal sediments of the Ribble estuary the main clay mineral is also illite with some smectite and only minor proportions of kaolinite and chlorite (Brown, 1996). This suggests a high potential for

caesium fixation in the Ribble estuary. A suggested mechanism for caesium fixing can be found in Hird *et al.*, (1995), and is briefly summarised here.

On external or internal expanded sites, strongly hydrated, di- and tri-valent ions are sorbed in preference to caesium, which has a small hydrated radius. However, the larger hydrated ions are physically prevented from sorbing onto the internal sites due to their size leaving wedge sites specifically for caesium. Once caesium has sorbed onto an internal site the repulsive forces between the layers are neutralised and, as the internal solution is more dilute than the bulk solution, water is osmotically expelled. The combination of these effects causes interlayer collapse. This collapse creates new wedge zones and the process is repeated. If enough caesium is present there can be total interlayer collapse, which prevents diffusion of the larger hydrated ions, effectively fixing the caesium. Davis and Shaw (1993) used Langmuir isotherms to infer that there were in fact two distinct sorption mechanisms, one for general non-specific sorption sites and one for the internal caesium specific sites discussed by Hird *et al.*, (1995).

The behaviour of a radionuclide in an aquatic environment is often described in terms of  $K_d$ , the distribution coefficient. There are in fact two different expressions of  $K_d$ ,  $K_{d(\text{mass})}$  and  $K_{d(\text{volume})}$  the volume distribution coefficient.  $K_{d(\text{mass})}$  is the ratio of “the activity of the radionuclide per unit mass of particulate fraction” to “the activity of the radionuclide per unit mass of dissolved fraction”.  $K_{d(\text{vol})}$  is the ratio of “the activity of the radionuclide per unit volume of particulate fraction” to “the activity of the radionuclide per unit volume of dissolved fraction”. Both will give different values but are related as  $K_{d(\text{volume})}$  equals approximately two and a half times the  $K_{d(\text{mass})}$  (Assinder *et al.*, 1985). To ease the calculation from field data, a hybrid form tends to be used

which uses the mass of the particulate fraction but the volume of the dissolved fraction, a far more practical approach giving units of litres per kilogram. The higher the  $K_d$  of a radionuclide the less conservative the behaviour.

A range of values has been quoted for the  $K_d$  of  $^{137}\text{Cs}$ . The International Atomic Energy Agency (IAEA, 1985) quote a  $K_d$  of  $3 \times 10^3$  for  $^{137}\text{Cs}$  in coastal waters. Turner *et al.* (1994) gives a  $K_d$  of  $2.5 \times 10^2$  for the Dee estuary, running along the South coast of the Wirral. In the Ribble the  $K_d$  of caesium was proportional to pH, indicating negatively charged adsorption sites and was also inversely proportional to sediment grain size. However, Gillham *et al.*, (1980) performed laboratory experiments on a range of unconsolidated geological materials and found that  $K_d$ , whose values ranged over three orders of magnitude, does not correlate to sediment properties such as cation exchange capacity (CEC), cation concentrations, clay composition, organic content and pH. They concluded that the caesium  $K_d$  is influenced by the chemistry of the solution and not the solid phase. It is competition from other ions in solution that determine the  $K_d$  value. The main competitors for  $\text{Cs}^+$  adsorption sites are  $\text{NH}_4^+$  and  $\text{K}^+$ . In other laboratory studies, solutions of these ions were shaken with sediment and were found to remobilise up to 80% of the caesium adsorbed onto the sediment (Schulz, 1965). In the Esk estuary in Cumbria, ammonium and potassium ions were found to remobilise 50% of the caesium bound to the residual phase. Other ions that are less likely to compete for the same adsorption sites are  $\text{Na}^+$ ,  $\text{Ca}^{2+}$ ,  $\text{Mg}^{2+}$ , and  $\text{Ba}^{2+}$ . These ions were found to remobilise less than 10% of adsorbed caesium (Schulz 1965).

## Thorium

There are six naturally occurring isotopes of thorium,  $^{227}\text{Th}$ ,  $^{232}\text{Th}$ ,  $^{228}\text{Th}$ ,  $^{230}\text{Th}$ ,  $^{231}\text{Th}$  and  $^{234}\text{Th}$  of which the latter four are the most abundant in the environment. The isotopes have half-lives ranging from 18.2 days ( $^{227}\text{Th}$ ) to  $1.4 \times 10^{10}$  years ( $^{232}\text{Th}$ ). In the environment all thorium isotopes exist in an oxidation state of  $\text{Th}^{4+}$  and form relatively insoluble compounds (Bowie and Plant, 1983). Concentrations for some of the thorium isotopes in the Ribble estuary are shown in table 2.2, (BNFL, 1993). Due to the low solubility and non-conservative behaviour, the  $K_d$  is high at  $2 \times 10^6$  (IAEA, 1985). Sequential extractions performed on Ribble sediments (Brown, 1996) show that thorium is mainly associated with the organic phase of the sediment. For most of the thorium isotopes discharged from BNFL Springfields the correlated association with grain size was found only in the upper Ribble estuary (Mudge *et al.*, 1994), above the Springfields discharge point. However, for  $^{234}\text{Th}$  no correlation with grain size was found. It was suggested that this was due to there being two sources, discharge and ingrowth from the decay of  $^{234}\text{U}$ .

## Protactinium

Protactinium exists in two isotopic forms,  $^{231}\text{Pa}$ , daughter of  $^{231}\text{Th}$  in the actinium decay series with a half life of  $3.4 \times 10^4$  years and  $^{234}\text{Pa}$  daughter of  $^{234}\text{Th}$  in the uranium decay series with a half life of 1.18 minutes (Ivanovich and Harman, 1982). Like thorium, protactinium exists only in a single oxidation state,  $\text{Pa}^{5+}$  and is insoluble (Scott, 1982). Concentrations of  $^{234\text{m}}\text{Pa}$  for the Ribble estuary are given in table 2.2. Although the concentrations may seem large the short half-life must be taken into account. This short half-life and the local nature of the discharge are the reasons for a poor correlation with grain size in the Ribble estuary (Mudge *et al.*, 1994) and that accumulation within the

sediment is spatially and temporally unstable (Sanderson *et al.*, 1993a).  $K_d$  for protactinium in coastal waters is  $1 \times 10^6$ , indicating non-conservative behaviour (IAEA, 1985).

### Neptunium

In a study on West Cumbrian soils and sediments,  $^{237}\text{Np}$  exists as  $\text{Np}^{5+}$  in oxidising conditions, usually as  $\text{NpO}_2^+$  but reduces to  $\text{Np}^{4+}$  (Hursthouse *et al.*, 1991). Concentrations of  $^{237}\text{Np}$  in the Irish Sea are generally in the range  $0.01 - 4.5 \text{ Bq kg}^{-1}$ , however, in the Ribble estuary concentrations of upto  $13.3 \text{ Bq kg}^{-1}$  have been recorded (Assinder *et al.*, 1991). This was believed to be the highest recorded environmental levels. Further work in the tidal limit region recorded concentrations of  $5-8 \text{ Bq kg}^{-1}$  suggesting the  $^{237}\text{Np}$  had a non-marine source.  $^{237}\text{Np}$  is far more soluble than radionuclides such as plutonium and americium and it behaves much more like caesium than other transuranic elements (Hursthouse *et al.*, 1991). The  $K_d$  for coastal water is given as  $5 \times 10^3$  (IAEA, 1985), much more comparable to the  $K_d$  of caesium as suggested by Hursthouse *et al.* (1991).

### Plutonium

Plutonium is an anthropogenic radionuclide. The four isotopes with environmental significance are,  $^{238}\text{Pu}$ ,  $^{239}\text{Pu}$ ,  $^{240}\text{Pu}$  and  $^{241}\text{Pu}$ , with half lives of 87.7 years, 24130 years, 6570 years and 14 years respectively (Eisenbud and Gesell, 1997). Of the four isotopes  $^{239}\text{Pu}$  and  $^{240}\text{Pu}$  are the most abundant. These cannot be separated by alpha spectrometry and are usually combined as  $^{239, 240}\text{Pu}$ . It is these isotopes which are generally being referred to when publications refer to "plutonium". In the environment plutonium is stable as  $\text{Pu}^{3+}$ ,  $\text{Pu}^{4+}$ ,  $\text{Pu}^{5+}$  and  $\text{Pu}^{6+}$  (Kershaw *et al.*, 1992), but in the

sediments of the aquatic environment exists mainly as  $\text{Pu}^{3+}$  and  $\text{Pu}^{4+}$  (Hamilton-Taylor *et al.*, 1987).  $^{239, 240}\text{Pu}$  concentrations associated with suspended sediment in the Irish Sea has been found to be in the range 7.2-62.3 Bq  $\text{kg}^{-1}$  (Cook *et al.*, 1997). Sequential extraction studies have revealed that plutonium associates with the insoluble organic phase of soils and sediments (Cook *et al.* 1984a and Cook *et al.*, 1984b). This is in agreement with the good spatial correlation of plutonium with percentage total organic carbon found in the Wyre estuary (Aston *et al.*, 1981). If the organic content of the sediment is low, as is often the case with marine sediments, plutonium will be mainly associated with the iron and manganese sesquioxide phase (McDonald and Jones, 1995). The grain size associations of plutonium are as for other radionuclides and in the Ribble, good correlations with percentage of the sediment less than 63 microns was obtained over the whole estuary (Mudge *et al.*, 1994). The solubility of plutonium is low, the International Atomic Energy Agency quote a  $K_d$  for coastal waters of  $1 \times 10^5$  (IAEA 1985). However, this value does vary depending on the oxidation state of the plutonium.  $\text{Pu}^{3+}$  and  $\text{Pu}^{4+}$  both have a  $K_d$  of around  $1 \times 10^6$  and  $\text{Pu}^{5+}$  and  $\text{Pu}^{6+}$  both have a  $K_d$  of around  $1 \times 10^4$  (Kershaw *et al.*, 1992) thus the IAEA is an average  $K_d$ . At low salinities plutonium has a slightly higher solubility and therefore a lower  $K_d$  (McDonald and Jones, 1995, Sholkovitz, 1983).

### **Americium**

$^{241}\text{Am}$  concentrations in the Ribble estuary sediments can be seen in table 2.2. In the environment americium is of the form  $\text{Am}^{3+}$  (McDonald and Jones, 1995) and forms stable organic complexes (Bondietti, 1981) and oxy-hydroxides (Turner *et al.*, 1994). On discharge from Sellafield it is estimated the 95% of the  $^{241}\text{Am}$  binds to sediments (McDonald and Jones, 1995) as it is highly particle reactive. This is indicated by the

excellent correlations between  $^{241}\text{Am}$  concentrations and small grain sizes in the Ribble estuary (Mudge *et al.*, 1994, Rainey, 1999). The  $K_d$  for  $^{241}\text{Am}$  in coastal waters is  $2 \times 10^6$  (IAEA, 1985) but has also been found as  $5 \times 10^5$  in the Dee estuary (Turner *et al.*, 1994). Both values are relatively high due to the non-conservative behaviour of  $^{241}\text{Am}$ . A particularly interesting feature of  $^{241}\text{Am}$  is that as a decay product of the more mobile  $^{241}\text{Pu}$  (MacKenzie *et al.*, 1994), the inventory of americium in the Irish Sea sediments is increasing by  $12 \text{ TBq yr}^{-1}$  due to ingrowth (McDonald and Jones, 1995).

#### **2.4.4 BNFL Sellafield**

Sellafield is located on the Cumbrian coast approximately 85km North of the Ribble estuary. BNFL are authorised to discharge from Sellafield low level radioactive liquid waste by pipeline to the Irish Sea in addition to radioactivity in the form of dust, gases and mists via stacks to the atmosphere. There is also authorisation to discharge potentially contaminated liquid effluent via the factory sewer (Seaburn sewer) such as surface water run-off. Sellafield is a reprocessing plant for spent nuclear fuel but also contained on the site is the Calder Hall nuclear power station with four magnox reactors and the Windscale laboratories of the Atomic Energy Authority (AEA) Technology. The thermal oxide reprocessing plant (THORP) was completed in 1992 and meets very stringent discharge limits. Waste treatment plants on site are the site ion exchange effluent plant (SIXEP), which consists of an array of sand filters and clinoptilolite ion exchangers and came on-line in 1985. The enhanced actinide removal plant (EARP) came on-line in 1993. Both have substantially reduced waste inputs to the Irish Sea. Current radioactive discharges are less than one percent of the peak levels of the mid-seventies. The handling of the liquid waste streams is dependent on the radioactivity levels. High level liquid waste is placed in interim storage and the vitrification plant

converts the waste into solid glass blocks that are stored on site. Medium level waste streams are routed to a salt evaporator and then treated by EARP prior to discharge. The low-level waste is discharged direct to the Irish Sea via pipeline from the following sources.

1. Storage pond water from magnox decanning, principally contaminated with caesium and strontium. The pond water is continually replaced and passed through SIXEP, before being analysed for radionuclide content and discharged.
2. Storage pond water from THORP has very low contamination levels and this is determined prior to discharge.
3. Other liquors are held in tanks for determination of radioactivity levels and composition before discharge.
4. Minor streams such as laundry effluent and surface drainage are monitored and discharged but contain little contamination.

Daily monitoring of effluents consists of measurements on the THORP receipt and storage tanks and SIXEP waste and laundry and run-off for total alpha and beta activity. More detailed analyses of bulked samples are carried out fortnightly or monthly. Consumption of local produce, such as seafood and milk are continually monitored and consumption habits are kept under review. There is also regular monitoring of external radiation exposure from mudflats. BNFL routinely collect samples of seawater from shore locations near Sellafield and from a line parallel to the coast 1.5 miles offshore. Beta and gamma surveys are carried out on tide lines of the local beaches with extra surveillance after exceptionally high tides and severe storms. No solid waste has been disposed of at sea since 1982, however the option of sea disposal has been retained should it be required for disposal of large items as a result of decommissioning.

### 2.4.5 BNFL Springfields

BNFL Springfields is situated close to the North shore of the Ribble estuary and discharges liquid waste to the estuary via an outfall near Savick Brook (Figure 2.1). The main function of BNFL Springfields is to produce uranium fuel and intermediate fuel products for the nuclear industry in the UK and abroad. Uranium is processed to uranium metal for use in magnox reactors or to UF<sub>6</sub> which is then enriched at BNFL's Capenhurst site. The enriched UF<sub>6</sub> is received back at Springfields for processing to oxide fuel for advanced gas cooled reactors (AGR) or light water reactors (LWR). Depleted uranium tri-oxide from the reprocessing at Sellafield is also received at Springfields for processing into UF<sub>6</sub> for enrichment and tri-oxide fuel. Liquid waste from these processes is discharged to the Ribble estuary. Prior to discharge the effluent is sampled to check compliance and acidity adjusted. Although <sup>234m</sup>Pa can reach elevated levels in the estuary muds (Mudge *et al.*, 1994) the majority of the dose is a result of <sup>137</sup>Cs originating from Sellafield. Indeed, only ten percent of the dose received from Ribble muds is due to BNFL Springfields discharges (BNFL, 1993).

The group of people most at risk of receiving an elevated dose of radiation from anthropogenic sources is referred to as the critical group. The critical group will change over the years as consumer and leisure habits vary and the abundance of radioisotopes in the environment change. For example the critical groups for BNFL Sellafield derived radiation are shown in table 2.3. It can be seen that the dose to the current critical group is an order of magnitude lower than the average annual dose from natural sources as given in table 2.4. For the Ribble estuary the most significant pathways for radiation exposure to the general public is via external exposure to the intertidal mudflats with the

critical group being houseboat dwellers on the River Douglas as shown in table 2.3. It is calculated that  $^{137}\text{Cs}$  dominates this external dose, (Tyler, 1999).

Dates	Critical Group	Approximate Dose
1952-1970	Laverbread Consumers - (Porphyra Seaweed)	1 mSv yr <sup>-1</sup>
1970-1985	Fish/Shellfish Consumers - (From Irish Sea)	2 mSv yr <sup>-1</sup> (Peak dose)
1985-	Houseboat Dwellers - (Ribble)	0.3 mSv yr <sup>-1</sup>

**Table 2.3** Variation in Sellafield critical groups and approximate peak dose, (BNFL 1993).

Radiation Source	Dose Equivalent for 1992 (μSv)
Cosmic	260
Earth Gamma Rays	350
Radon Decay	1300
Other Internal Radiation	300
Total	2210 (=2.2mSvyr <sup>-1</sup> )

**Table 2.4** Natural background radiation sources and levels, (BNFL 1993).

## 2.4.6 Current environmental monitoring

Traditional monitoring techniques for radioactivity in the environment involve either collecting a sample for removal to a laboratory for processing and analysis or occasionally, in-situ measurement with a portable detector. The choice of method will depend on what is required, a complete inventory of the concentrations of individual radionuclides present or a general alpha, beta or gamma count rate. As with most ground based environmental surveys, the main concern is gaining a result that is spatially representative of the area studied. This requires multiple samples to be taken, increasing the workload and cost. Samples are regularly taken of soil, vegetation, water and sediments, all of which are spatially heterogeneous. Thus environmental monitoring programs must be both spatially representative and consistent in location and methodology, thus being temporally comparable.

A relatively recent environmental monitoring technique is airborne gamma spectrometry, which has been successfully applied by the Scottish Universities Research and Reactor Centre (SURRC), (Sanderson *et al.*, 1993a, Sanderson *et al.*, 1993b, Sanderson *et al.*, 1993c). This technique is relatively rapid and spatially representative with a ground resolution of between 200m and 500m approximately, depending on the flying altitude. This technique is ideal for purposes such as incident response. However, gamma rays within the water column are rapidly attenuated. This attenuation, coupled with the large spatial resolution of airborne gamma spectroscopy and the time taken to collect the data, make the technique less suitable for use in an aquatic area that is highly dynamic, such as the Ribble estuary.

Further innovative research has shown the capability of remote sensing to successfully map the grain size of the intertidal sediment of the Ribble estuary at high spatial resolution using airborne Daedalus ATM (Rainey 1999, Rainey *et al.*, 1999). This technique has been extended to radionuclide mapping by using the well-established relationship between sediment grain size and the associated radionuclide concentration of the sediment. As a means of monitoring radionuclide distribution this technique is unsurpassed in spatial detail as no interpolation between spot samples is necessary. The general trends of radionuclide activities in the intertidal sediments of the Ribble estuary show a west to east increase in radionuclide activity in addition to the activity being inversely related to the proximity of the sediment to the main channel.

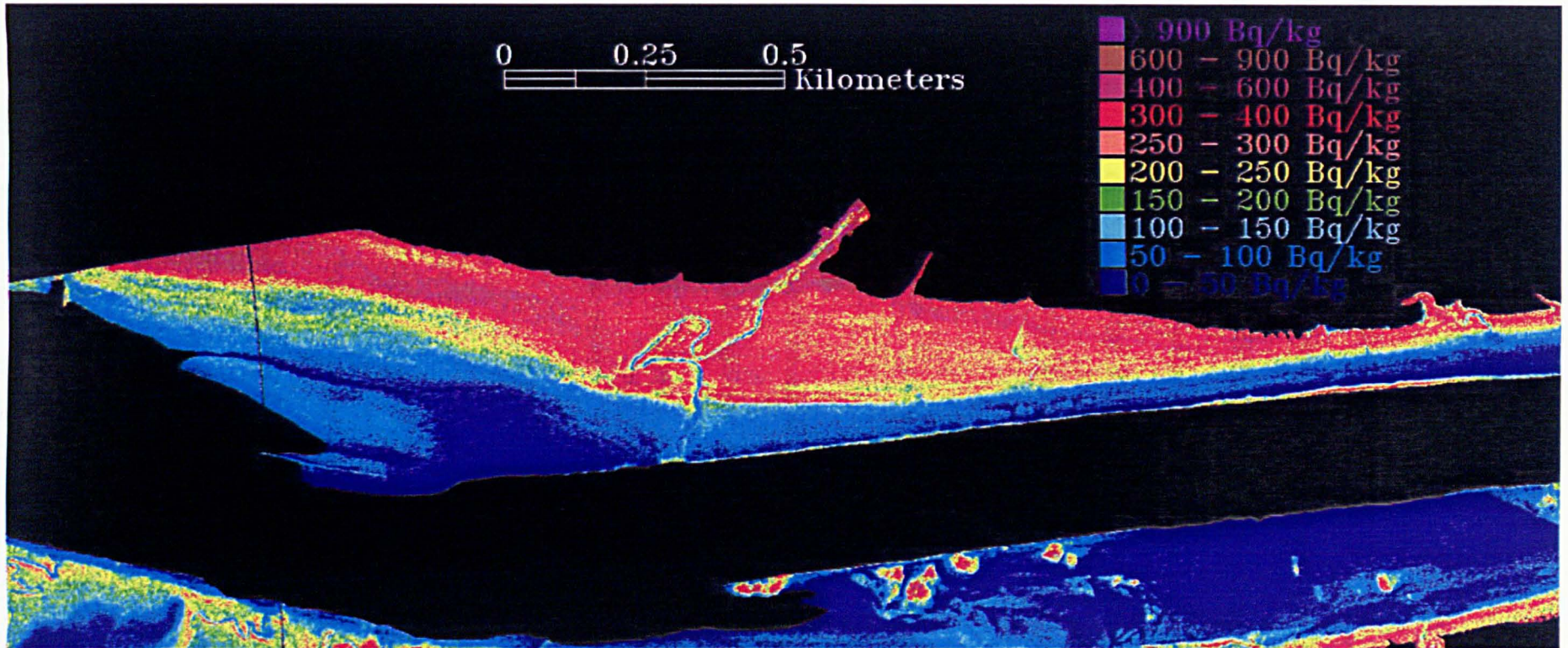


Figure 2.4.  $^{137}\text{Cs}$  distribution of the intertidal sediment of Warton Bank, (Rainey 1999).

The results of the intertidal mapping of the outer estuary are shown in Figure 2.4.

### **Statutory Monitoring of the Ribble Estuary**

BNFL, MAFF and the Environment Agency each implement environmental monitoring programs in addition to other university based studies which may be carried out sporadically. Details of the sampling programs can be obtained from the organisations concerned but a brief overview of the BNFL statutory monitoring program for the Ribble estuary is given here. The sample sites used by BNFL are listed below.

1. Lytham
2. Freckleton
3. BNFL Springfields outfall
4. 460m upstream of BNFL Springfields outfall
5. Savick Brook (old vehicle crossing point)
6. Penwortham Bridge (boat mooring area)
7. River Douglas (Beconsall boat yard)
8. Hesketh Outmarsh

Gamma dose is measured quarterly at sites 1-8. The measurement is taken 1m above the surface of the intertidal silt, halfway between the waterline and the high water mark at low water. At the same sites the beta dose is measured in contact with the silt. Gamma and beta contact monitoring is also carried out quarterly, between the high water mark and the waterline at low water, where flotsam and jetsam are monitored 100m either side of the BNFL Springfields outfall and the confluence of Savick Brook and the river Ribble. Any item with a count greater than 1000 counts per second on a

1828B probe is removed for further investigation, any item with a count greater than 500 cps is recorded. Fishing nets used in the Ribble are also monitored bi-annually using the same method.

Sediment samples are taken quarterly from sites 1, 3, 6 and 7. These are analysed for  $^{241}\text{Am}$ , U,  $^{234\text{m}}\text{Pa}$ ,  $^{233}\text{Pa}$ ,  $^{232}\text{Th}$ ,  $^{230}\text{Th}$ ,  $^{228}\text{Th}$ ,  $^{214}\text{Bi}$ ,  $^{212}\text{Pb}$ ,  $^{155}\text{Eu}$ ,  $^{154}\text{Eu}$ ,  $^{144}\text{Ce}$ ,  $^{137}\text{Cs}$ ,  $^{134}\text{Cs}$ ,  $^{125}\text{Sb}$ ,  $^{110\text{m}}\text{Ag}$ ,  $^{106}\text{Ru}$ ,  $^{103}\text{Ru}$ ,  $^{95}\text{Zr}$ ,  $^{60}\text{Co}$  and  $^{40}\text{K}$ . Any other gamma emitting radionuclide is noted. After a six month period the sample is re-analysed for  $^{241}\text{Am}$  as  $^{234}\text{Th}$  will have decayed thus reducing interference.

Twice a year cockles from the Ribble are sampled to yield 1 kg of flesh. These are cooked and shucked but not cleaned and analysed for the radionuclides mentioned above in addition to  $^{228}\text{Ac}$ . An annual bulked cockle sample is analysed for  $^{237}\text{Np}$  and other gamma emitting radionuclides present are noted. In addition to the monitoring of the estuary other analyses are performed inland on foodstuffs, grass, soil, ovine and bovine faeces, water and air quality.

## **2.5 REMOTE SENSING**

Remote sensing is the technique of retrieving information about an object without contact. Generally, remote sensing is the acquisition of information from the electromagnetic radiation reflected or emitted from a surface. The theory on which remote sensing is based is that a resulting reflectance spectrum will contain information on all the interactions between the incident radiation, the surface from which it is reflected and the atmosphere through which it has passed. As many of these interactions are wavelength specific, the required information can be isolated or unmixed by careful

selection of wavelengths, or the combinations of wavelengths being measured. This optimisation to a particular application is often gained through laboratory based spectral studies.

The advantage of remote sensing is the ability to obtain information over a large area instantaneously, this is beneficial with regard to both cost and data quality. For example, an image consisting of pixels with a ground resolution of 10m x 10m will have data equivalent to a sample taken every 10m on a grid. If the study area is tidal the temporal aspect becomes far more important. An image whose collection takes five minutes to cover an entire estuary will give spatial information on features that cannot be detected from a grid of water samples, which may take hours to collect and thus be temporally incompatible.

### **2.5.1 Platforms and Sensors**

Remotely sensed data are obtained from a variety of platforms and sensors, each with associated advantages and disadvantages. The most familiar platform on which to mount a sensor would be the satellite. Details of the most commonly used satellites are given in table 2.5. By browsing table 2.5, the development of the satellite sensor is evident. Over time the availability of bands, the spatial and spectral resolutions have improved. The latest generation of satellite sensors has a greater flexibility by either having a large number of bands (e.g. MODIS) or full user programmability (e.g. MERIS). The advantage of satellite remote sensing is the large spatial coverage obtained for relatively little cost and a large archive of data. However, two main disadvantages of satellite imagery are the fixed and often poor spatial resolution and the temporal coverage. Satellite overpasses range from every six hours (AVHRR) to every

26 days (SPOT) with no flexibility regarding time or weather conditions. This is probably the most limiting factor for satellite data, especially in a temperate climate with a high probability of cloud cover such as in the UK.

Table 2.6 shows the general specifications of the two most commonly used airborne spectrometers in the UK, both of which are flown by NERC Airborne Remote Sensing. The Environment Agency also regularly uses the CASI. More detailed descriptions of the technical specifications will be given in chapter three, however the advantages of airborne remote sensing over satellite remote sensing are in the total flexibility offered by the airborne technique, both in spatial, spectral and temporal resolution.

Sensor	Res. (m)	Bandset (nm)	Repeat	Notes
Landsat MSS	80m	500-600 (g) 600-700 (r) 700-800 (r-nir) 800-1100 (nir)	16 Days	Launched 1972 Scene Size = 185km x 185km
CZCS	825m	430-450 510-530 540-560 660-680 700-800 10.5-12.5 $\mu$ m		Launched 1978 Swath width = 1566km Bands 1,2 & 4 = chlorophyll Band 3 = DOM Band 5 = vegetation Band 6 = Sea surface temp.
Landsat TM	30m  120m	450-520 (b) 520-600 (g) 630-690 (r) 760-900 (nir) 1.55-1.75 $\mu$ m (ir) 2.08-2.35 $\mu$ m (ir) 10.4-12.5 $\mu$ m (t)	16 Days	Launched 1982 Scene Size = 185km x 185km 1/4 Scene = 98km x 98km
SPOT 1-3	20m  10m	500-590 (g) 610-680 (r) 790-890 (nir) 510-730 (PAN)	26 Days	Launched 1986. Scene = 60km x 60km Repeat frequency can be programmed for change. Stereoscopic capabilities.
SPOT 4	20m  10m 1.15km	500-590 (g) 610-680 (r) 790-890 (nir) 510-730 (PAN) 1.58-1.75 $\mu$ m (ir)	26 Days	Launched 1997. Scene = 60km x 60km Repeat frequency can be programmed Stereoscopic capabilities. Veg. sensor (ir) swath 2200km wide.
AVHRR	local = 1.1km  Global = 4km	580-680 (r) 725-1100 (nir) 3.55-3.93 $\mu$ m 10.3-11.3 $\mu$ m 10.3-12.5 $\mu$ m	4 Per Day (2 Sat.)	Launched 1970. Local scene =3000 x 3000km Global scene =25000 x 6000km Network of 14 US weather satellites - NOAA.
SeaWiFS	Low = 4km  High = 1.1km	402-422 433-453 480-500 500-520 545-565 660-680 745-785 845-885	1 Day	Launched late 1997.

**Table 2.5** Summary of Earth Observation Satellites.

Sensor Name	Spatial Resolution	Bands (nm)	Notes
Daedalus AADS 1268 ATM	1.3m at 1000m altitude	420-450 450-520 520-600 605-625 630-690 695-750 760-900 910-1050 1.55-1.75 $\mu$ m 2.08-2.35 $\mu$ m 8.5-13.0 $\mu$ m	Swath at 1000m = 1.4km 716 pixel swath IFOV = 0.14° FOV = 85.92° 3 scan rates Bands 1-8 on 1 detector array. Bands 9-11 on three separate detectors (N <sub>2</sub> cooled).
CASI (spatial mode)	Dependent on speed, focal length, integration time and altitude.	400-915 Upto 18 bands, position and width programmable at 1.8nm intervals	FOV = 42° Swath dependent on altitude, 512 pixels. Variable integration times and auto-adjusted iris.

**Table 2.6** Summary of Airborne Sensors.

Spatially, satellite data are often inadequate when the study area is relatively small or very heterogeneous because the finer details are lost in the coarse resolution. Airborne remote sensing offers the ability to map an area with a much smaller pixel size. The larger file sizes generated by finer ground resolution can be offset by targeting data collection so there is no coverage of areas outside the immediate study site and data are not collected under cloudy conditions, as is often the case with large satellite images.

Spectrally, the Daedalus ATM is comparable to Landsat TM with relatively broad bandwidths but has the advantage of a thermal infrared channel. However, the CASI is far more flexible with four modes of operation and user programmable bandwidths and position. This allows the user to select the optimum wavelengths for the application and use pre-defined narrow bands, which enable the finer spectral details to be seen without losing the feature through averaging out across many wavelengths. This is possible with

the CASI as the internal optical mechanism is not a scanning detector coupled with a prism and diffraction grating as in many other spectrometers but an array of charge coupled devices (CCDs) each one sensitive to a particular wavelength at 1.8nm intervals. The instrument is then programmed by selection of the individual CCDs to form a band-width. Temporally, the timing of data collection is of particular importance in tidal areas and the flexibility of the repeat frequency allows studies of changes over the short term such as tides in addition to other aspects such as spring/neap cycles and seasonal variability.

### **The Choice for This Study**

The factors affecting choice of data source for this project are:

1. The need for a bandset that is suitable for the remote sensing of water quality parameters such as suspended sediment, chlorophyll and dissolved organic matter, sometimes referred to as Gelbstoff.
2. The flexibility of specifying the data collection times to coincide with the start of the incoming tide with the high water shortly after noon in as near perfect weather conditions as possible
3. The need for a rapid repeat sequence to allow the study of sediment transport and the development and movement of tidal fronts.
4. A high signal to noise ratio due to the low reflectance of water.

Airborne remote sensing was chosen for the temporal flexibility offered with respect to flight timing and location. NERC airborne remote sensing facility offers both CASI and ATM sensors and it was decided to combine the advantages of these sensors, the fully programmable bandset of the CASI and digital thermal channel of the ATM.

## **2.5.2 The Remote Sensing of Suspended Sediment**

Prior to the design of the laboratory and fieldwork a thorough literature search was necessary to assess the previous work regarding remote sensing of suspended sediment in coastal and estuarine waters.

### **Suspended Sediment Concentration**

The one feature of the suspended sediment reflectance relationship on which all studies agree is the observation that reflectance always increases as suspended sediment concentration (SSC) increases (Bhargava and Mariam, 1991a, Chen *et al.*, 1991), however, this appears to be the only area of agreement.

The nature of the relationship used for the retrieval of SSC from reflectance varies. The most common relationship type appears to be the linear relationship (Novo *et al.*, 1991, Choubey and Subramanian, 1992 and Han, 1997) but some studies required the data for SSC to be logarithmically transformed prior to linear regression (Chen *et al.*, 1991). Multiple linear regression techniques gave better results than single band linear regression in a Severn estuary study using ATM data (Collins and Pattiaratchi, 1984). However, other studies have found using ratios of near infra-red reflectances (Hudson *et al.*, 1994) or combining pairs of ratios (Topliss *et al.*, 1990) reduces retrieval errors. Differentiation of spectra has also been used to quantify suspended sediment as there has been shown to be a strong negative correlation between the derivative spectra and SSC (Chen *et al.*, 1992). Goodin *et al.*, (1993) stated that the first differential removes the reflectance due to water, the second removes reflectance due to sediment leaving the

reflectance due to chlorophyll and thus used the derivative spectra as part of a three-component model.

There are many reasons why so few of the studies agree, as each study uses a different range of suspended sediment concentration, sediment type and wavelengths to correlate to SSC. Each of these factors affects the shape of the suspended sediment reflectance relationship. In general, the studies that use a low SSC range find the relationship to be linear such as Aranuvachapun and Le Bond, (1981) who used a 0-25 mg l<sup>-1</sup> range and Choubey and Subramanian (1992) who used 11-45 mg l<sup>-1</sup> but, as with all generalities there is the exception. Bhargava and Mariam (1991a and 199b) used linear correlations with a concentration range of 0-1280 mg l<sup>-1</sup>. Most studies find that the best wavelengths for retrieval of SSC data are those in the red and near infra-red for example, Harrington *et al.*, (1992) used Landsat MSS band 3 (700-800nm) and Topliss (1986) found the best correlations with Landsat MSS band 4 (800-1100nm). The laboratory-based studies have been able to select optimum wavelengths in more narrow bands than the studies using satellite data. However, the majority of the wavelengths chosen were still in the red near infrared region. For example 720-740nm and 820-830nm (Chen *et al.*, 1992), anywhere between 700nm and 900nm (Bhargava and Mariam, 1991a), 675nm (Topliss *et al.*, 1990) and either 827, 830 or 847nm for clear water or 767, 769 or 770nm for algal laden water (Han, 1997). The reason most of the wavelengths chosen are greater than 700nm is because at 700nm interference from dissolved constituents such as dissolved organic matter and chlorophyll decreases to zero, (Hudson *et al.*, 1994). Hence, selecting wavelengths greater than 700nm removes any reflectance due to dissolved organic matter and chlorophyll correlations would be expected to improve.

Other features of the suspended sediment reflectance relationship on which several studies agree is the way in which the spectra increase in the shorter wavelengths first, and when these wavelengths become saturated, that is stop increasing as SSC increases, the longer wavelengths will continue to increase (Harrington *et al* 1992, Novo *et al.*, 1991 and Choubey and Subramanian, 1991). This shift in sensitivity of the relationship from the shorter to the longer wavelengths as the SSC range increases is demonstrated by a shift in the wavelength at which the maximum reflectance occurs. This is evident in studies by Chen *et al.*, (1991), Topliss *et al.*, (1990) and Han and Rundquist (1996). Han (1997) demonstrated that this shift occurred for sediment free water but was not detected when the experiment was repeated using water containing a quantity of algal material.

Within the concluding paragraphs of many of the papers whose data were obtained in a field situation the discrepancies between the predicted SSC and gravimetrically determined SSC is attributed to variations in sediment grain size distribution (Choubey and Subramanian, 1992) or sediment type (Collins and Pattiaratchi, 1984). This implied that the laboratory studies needed to incorporate experimental data to assess the magnitude of these effects.

### **Grain Size**

Experiments incorporating sediment of different grain size fractions revealed, that for a given SSC, the reflectance is inversely proportional to the grain size, (Novo *et al.*, 1989, Bhargava and Mariam, 1991a and 1991b). There was found to be a ten-fold increase in reflectance when using a range of sediments ranging from coarse to fine (Bale *et al.*, 1994). One reason suggested for this increase in reflectance with decrease in grain size

(Ferrier, 1995) was that the smaller particles tend to be sheet-like clay minerals which align with least resistance to the flow which leaves the largest surface as the reflecting surface. One study, (Bhargava and Mariam, 1991a) found the effects due to grain size to be equally effective over the entire 500-1000nm range and yet in another paper Bhargava and Mariam, (1991b) stated that the effects are most pronounced in the 700-900nm wavelength range. Topliss (1986) and Bale *et al.* (1994) both state that it is the particle size which is dominant and thus affects the spectral shape to a greater extent than SSC. However, only one study (Bhargava and Mariam, 1991a) actually produces a multiple linear regression equation which has both SSC and mean grain size as independent variables despite the general acknowledgement of the importance of the grain size. Bale *et al.*, (1994) attempted to predict the grain size from reflectance using the target area calculated assuming a spherical particle, at 804nm. A plot of reflectance verses target area put all grain size fractions on the same line with an  $R^2 = 0.89$ , indicating that 804nm could be used to retrieve information on grain size. Unfortunately when the equation was used in reverse to predict grain size the results were less accurate than expected. Rimmer *et al.*, (1987) also examined mean grain size as a parameter in the field but failed to find a correlation with ATM bands 2 and 3. Han and Rundquist (1996) highlighted other differences in spectral behaviour between fine and coarser sediments, they showed that the correlations were consistently higher for finer sediments. From this they concluded that the finer sediments were the primary scatterers.

### **Sediment Type**

The effect of the sediment type, that is the overall colour of sediment, is more difficult to quantify due to the range of possibilities. Although it is known that sediment colour

does affect the spectral reflectance (Bhargava and Mariam, 1990, Chen *et al.*, 1991) quantifying the effect proved problematic. The conclusions regarding the magnitude of these effects may depend on the sediments used during the comparison experiments. Bhargava and Mariam (1991b) found that both grain size and sediment type were more dominant in controlling the spectra than SSC but they used highly contrasting sediments, white kaolinite and black cotton soil. Choubey and Subramanian (1991) also concluded that sediment type was the dominant factor controlling spectral shape. However, Bale *et al.*, (1994) found that a red sediment from the river Exe and a grey/brown sediment from the river Tamar give very similar spectral shape when similar grain size fractions were used and concluded that the spectral shape was controlled by grain size and not sediment type. A further study (Hudson *et al.*, 1994) combined the sediments of the Exe and the Tamar with sediment from the river Humber and concluded that reflectance in the near infrared was dependent only on SSC and not sediment type.

From the above discussion it can be seen that the reflectance spectra resulting from suspended sediment is far more complex than would be initially anticipated and that the spectral shape and magnitude is dependent on the suspended sediment concentration, grain size distribution and overall sediment colour. To be able to retrieve reliable quantitative information on the concentration of suspended sediment, the sediment type and grain size distribution must be constant or included as an independent variable.

### **Salinity**

One of the most obvious components of the water column that will vary over the length of an estuary is the salt concentration or salinity. The standard range which can be

expected along a UK estuary is approximately 33 practical salinity units or parts per thousand (‰) (Open University, 1989). A solution of salt water is colourless, however, an increase in density with salt concentration may alter the optical property of the water. This possibility suggests that the salinity component cannot be ignored. Khorram (1982) for example successfully mapped salinity in the San Francisco Bay Delta using Landsat MSS. Errors in the relationship were blamed on bathymetry implying that very low suspended sediment waters, called CASE 1 waters, were used for this study. At no point in this paper are the possible effects of suspended sediment mentioned. In addition to this, the paper states that no visual judgement could be made and yet the MSS bands used were mainly in the visible part of the spectrum. It is known that salinity is often inversely correlated with dissolved organic matter (or Gelbstoff) (Rimmer *et al.*, 1987). Perhaps this was the parameter that was actually being defined? The study by Rimmer *et al.*, (1987) also found high correlations between ATM bands 7 and 8 and salinity in Swansea Bay but this was over a salinity range of just 0.6 parts per thousand. One other study mapped salinity with some success using SAR (Muller-Karger, 1992) but the ground resolution of the SAR is very low making it more suitable for use in the open ocean environment. None of the published studies has produced controlled laboratory experiments to validate that the relationships found were actually representing salinity, thus further work is required in this area.

### **Chlorophyll and Dissolved Organic Matter**

Chlorophyll is the main feature of many studies as primary productivity of a water body can be used to assess the overall water quality and lead to the possibility of monitoring blooms of algae, of which some species have toxic effects. Chlorophyll concentrations have been retrieved using a variety of techniques. Gower *et al.*, (1984) used eigenvector

analysis to improve on previous studies using blue/green ratios. Goodin *et al.*, (1993) found that derivative spectra could be used with the value remaining after the second derivative of continuous spectra being correlated to chlorophyll concentration. Chlorophyll exhibits a solar stimulated fluorescence at 685nm. This feature of the chlorophyll spectra was exploited by Gower and Borstad, (1990), to quantify chlorophyll concentration. This technique uses triangulation methods to measure the height of the solar stimulated fluorescence peak at 685nm above a base line interpolated from surrounding wavelengths. The height of this peak is then correlated to chlorophyll concentration.

In relation to the retrieval of suspended sediment concentration data, the reflectance of chlorophyll must be considered. Chlorophyll absorbs strongly at 450nm and 670nm, decreasing reflectance in the blue and red giving a green appearance (Lillesand and Kiefer, 1994). If green wavelengths were used to retrieve suspended sediment concentrations additional reflectance from chlorophyll would lead to an over-estimation of sediment (Bhargava and Mariam, 1991a). The presence of chlorophyll does not alter the nature of the suspended sediment reflectance relationship but does affect the locations of the wavelengths of best correlation (Han, 1997). Han (1997) found that the wavelengths of best correlation for clear and algal-laden waters were around 830nm and 770nm respectively, a shift of 60nm in wavelength. Studies have shown that to retrieve suspended sediment concentration without any interference from chlorophyll, one must use wavelengths greater than 700nm and 750nm (Hudson *et al.*, 1994, Bale *et al.*, 1994). This is clearly demonstrated by Hudson *et al.* (1994) as can be seen in Figure 2.5

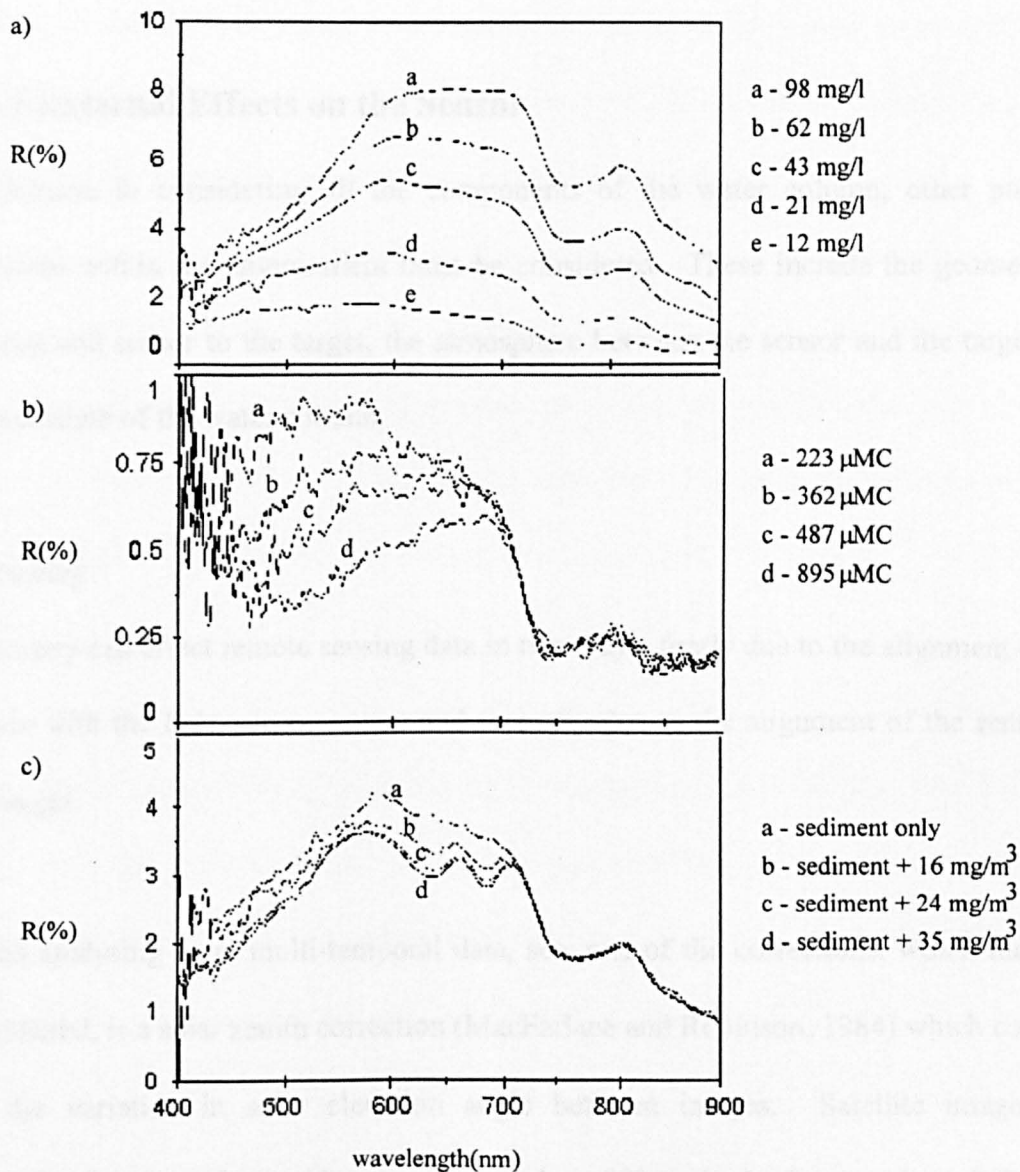


**Figure 2.5** The effects of chlorophyll and dissolved organic matter on the reflectance spectra of SSC, a) Varying SSC, b) Varying dissolved organic matter with constant SSC and c) Varying chlorophyll with constant SSC. (Hudson *et al.*, 1994).

Dissolved organic matter will also interfere with the reflectance spectra from suspended sediment but like chlorophyll, interference can be avoided by selecting wavelengths for suspended sediment concentration retrieval above 750nm (Bale *et al.*, 1994, Hudson *et al.*, 1994), see figure 2.5. Dissolved organic matter absorbs strongly at shorter wavelengths and is normally measured using ultra-violet wavelengths or at higher concentrations in a laboratory using fluorescence (Bricaud *et al.*, 1981).

### **2.5.3 External Effects on the Sensor**

In addition to considering all the components of the water column, other possible variables within the environment must be considered. These include the geometry of the sun and sensor to the target, the atmosphere between the sensor and the target and the substrate of the water column.

#### **Geometry**

Geometry can effect remote sensing data in two ways, firstly due to the alignment of the sensor with the light-source or sun and secondly due to the alignment of the sensor to the target.

When analysing large multi-temporal data, sets one of the corrections, which must be considered, is a solar zenith correction (MacFarlane and Robinson, 1984) which corrects for the variation in solar elevation angle between images. Satellite images are normalised to the solar zenith, when the sun is at  $90^\circ$  to the horizontal plane (Lillesand and Kiefer, 1994). This is achieved by dividing the radiance value by the cosine of the angle of the sun from the solar zenith, or by the sine of the angle above the horizontal plane (Lillesand and Kiefer, 1994), both of which give identical results. Laboratory results (Novo *et al.*, 1989) showed that in a laboratory experiment water reflectance was partly a function of solar zenith and a variation in solar zenith between  $0^\circ$  and  $70^\circ$  produced a 9% increase in reflectance.

The viewer geometry also affects remotely sensed data particularly the sensitivity of the suspended sediment reflectance relationship (Novo *et al.*, 1989). The strength of the

suspended sediment reflectance relationship decreases as the sensor moves off nadir. In-situ studies on the River Tay estuary (Ferrier, 1995) found that for turbid water, as the viewing angle moves off the nadir, the reflectance increases.

The implications of this are that for laboratory and field studies within this project the sensor-viewing angle must be kept constant, preferably at nadir in order to achieve the strongest suspended sediment reflectance relationship. The solar zenith angle variation must be kept to a minimum or corrections must be applied.

### **The Atmosphere**

The radiance recorded by a sensor is a function of the incident radiation, the reflectance from the target surface and the atmosphere between the sensor and the target. The atmosphere affects what the sensor sees in two ways, increasing brightness by scattering and reducing brightness by attenuation (Lillesand and Kiefer, 1994).

There are three types of scatter, Rayleigh, Mie and non-selective. Rayleigh scatter is the primary source of haze and is dominant at the shorter wavelengths with the effects being proportional to  $\lambda^{-4}$ , resulting in a blue sky. The incident radiation interacts with the atmospheric molecules that have a diameter less than the wavelength of the incident radiation. Mie scatter occurs when radiation interacts with particles that have a diameter similar to the wavelength of the incident radiation such as dust and water vapour. Mie scatter becomes more significant in overcast conditions. There is also a non-selective scatter that occurs due to interactions of radiation with particles greater in size than the wavelength of the incident radiation. This is non-selective with respect to wavelength, which is why fog appears white. All types of scatter add brightness to

remotely sensed radiance values. In addition, there are constituents within the atmosphere which act as absorbers, thus reducing the brightness of remotely sensed radiance. The most efficient absorbers are water vapour, carbon dioxide and ozone. All of these occur at very specific wavelengths.

### **Atmospheric Correction**

The atmosphere has a considerable effect on remotely sensed data, thus ideally an atmospheric correction technique that would produce the actual target surface reflectance should be used. As yet there is no universally used atmospheric correction technique applied routinely to remote sensing data. There are three main methods of atmospheric correction that are frequently used, the histogram minimum method, regression and radiative transfer models, (Campbell, 1996). Essentially all techniques rely on the fact that the near infrared wavelengths are largely free of atmospheric effects, (Jensen, 1986).

The histogram minimum method is more commonly referred to as dark pixel subtraction, in which dark pixels are usually selected from an inland waterbody where there is little reflectance in the near infrared. Any reflectance from these pixels is assumed to be due to atmospheric effects and the histograms are adjusted to zero accordingly.

Regression is a more complex variation of the dark pixel subtraction method, which involves the calculation of a bias by plotting each band against the near infra-red band (Jensen, 1986). The intercept is then taken as the bias, this method assesses the contribution of the atmosphere to each band and takes account of the wavelength

dependence of atmospheric effects. A good example of this can be seen in Chavez, (1988). Jensen (1986) states that despite being more complex this method is not necessarily better than the basic dark pixel subtraction as both methods are only first order corrections.

The most complex atmospheric correction method involves producing models of the physical behaviour of radiation as it travels through the atmosphere. These are the radiative transfer models. The radiative transfer model is generally more accurate (Jensen 1986) but has the disadvantage of being computationally complex and requires atmospheric input parameters from other sources such as meteorological radiosondes (Richter, 1990). Examples of the models are LOWTRAN, MODTRAN, 5S and 6S. Many publications on atmospheric correction are simplifications of the above models (Rahman and Dedieu, 1994, Singh, 1994). This normally involves the estimation of the required input parameters from the imagery itself as in Gilabert *et al.* (1994).

It should be noted here that the majority of the papers reviewed on remote sensing of suspended sediment concentration use no atmospheric correction as the radiance is usually related to ground truth data. This assumes that the atmosphere is spatially uniform and temporally stable.

### **Bathymetry**

There are many studies which used remote sensing to map bathymetry in coastal waters, (e.g. Lyon *et al.*, 1992, Bierwirth *et al.*, 1993), thus the possibility of a contribution to the reflectance signal from the substrate cannot be ignored. However all the papers examined are studies in CASE 1 waters, which have low suspended sediment and

chlorophyll (Campbell, 1996). The only paper which looked promising in the provision of information on contribution of bed reflectance in turbid waters (Bagheri *et al.*, 1998) used the phrase “turbid waters” in the paper title and then stated in the text that concentrations of suspended sediment and chlorophyll were insignificant and spatially uniform. This lack of literature on the subject implies that the reflectance contribution from the bed can be considered to be negligible, but this needs to be supported by Secchi-disc depth data.

## **2.6 SUMMARY**

The extensive literature search has revealed that the Ribble estuary has a history of siltation after the construction of the training walls. It is also known that this silt is of a marine origin evident from the mineralogy and the associated Sellafield derived radionuclide concentrations. This silt is brought into the estuary via an asymmetrical tidal system, which is common in the UK. The estuary is a coastal plain estuary which is well mixed on a flood tide but can exhibit some stratification on the ebb tide. There is an axial convergence that is known to develop during the flood tide, after tidal intrusion. The Sellafield radionuclides bound to the estuarine sediment show an inverse grain size association over the whole of the estuary. The Springfields radionuclides show this association only in the upper section of the estuary and tend to be temporally unstable. Of the remote sensing platforms available, airborne instruments would be more suitable due to spatial resolution and temporal flexibility. It is known that there is a relationship between suspended sediment and reflectance, however the exact nature of the relationship is extremely site specific. Variations are caused by sediment type, suspended sediment concentration range, grain size distribution and other constituents within the water column such as salinity, chlorophyll and dissolved organic matter.

Geometric changes and atmosphere can be corrected for if the sensor viewing angle remains constant. All these variables must be either eliminated or included in the final algorithm. Also, it is known that the geometry of the sensor with the target and illumination source does affect the sensitivity of the suspended sediment reflectance relationship. This suggests that errors may be introduced due to a variation in the suspended sediment reflectance relationship caused by the roll, pitch and yaw of the aircraft. This particular source of error cannot be removed or accounted for by a variable in a regression equation. In the absence of complex atmospheric modelling this may introduce a source of error into the data.

## **CHAPTER 3: INSTRUMENTATION AND METHODOLOGY**

### **3.1 INTRODUCTION**

This thesis represents a development in methodology itself, but relies on the understanding of a variety of primary techniques and methodologies ranging from gamma spectroscopy to *in-situ* and airborne remote sensing instrumentation. It is therefore necessary to present the details of these instruments and methods in such a way as not to detract from the main purpose of the study. For this reason, the details of each method, in addition to some possible alternatives and the avoidable pitfalls are presented together within a single chapter.

The layout of the chapter describes the following equipment and associated methodologies:

1. Field equipment used in *in-situ* spectral data collection and the methods used to process these data.
2. Airborne remote sensing instrumentation and the preliminary processing techniques developed by NERC.
3. Global Positioning System and application to this study.
4. Electrochemical field and laboratory instrumentation.
5. Laboratory analysis of samples.

## 3.2 *IN-SITU* SPECTROMETRY

### 3.2.1 *In-situ* spectrometry Instrumentation

The *in-situ* spectrometers were provided on loan from the Natural Environment Research Council's Equipment Pool for Spectroscopy (NERC EPFS) based in the Department of Geography at the University of Southampton.

#### **The ASD Fieldspec<sup>®</sup> FR portable spectroradiometer**

The Analytical Spectral Devices (ASD) Fieldspec<sup>®</sup> FR, as shown in Figure 3.1, is a 16-bit, single beam radiometer capable of measuring visible to short-wave infrared (SWIR) wavelengths, 350 nm-2500 nm using three separate detectors.



**Figure 3.1** The ASD FR Fieldspec spectroradiometer.

The visible and near infrared wavelengths (VNIR), 350-1100 nm, are detected using a 512 element silicon photo-diode array. Two scanning spectrometers are used to measure the short-wave infrared wavelengths. These consist of a holographic grating and a thermo-electrically-cooled indium-gallium-arsenide detector, (InGAs), spanning 1100-1800 nm and 1800-2500 nm respectively. Details of the technical specifications of the detectors are given in table 3.1.

Light input to the detectors is via pistol-grip style handle and a single fibre-optic cable, which trifurcates inside the detector housing to deliver the light signal to each of the three detectors. There are various fore-optics which attach to the pistol-grip, for example 8° reduction tube, 1° mirror with integral rifle sight or a cosine receptor. There are also fibre-optic cable extensions, however their use can result in up to a 70% loss of signal, making them useful only in situations where there is a large reflectance. This is not the case with natural waters where even high concentrations of suspended sediment produce low reflectances, usually less than 15%.

The ASD FR Fieldspec® operates in both raw data mode and reflectance/white reference mode. Raw data mode measures the raw digital data and is used for measurement of radiance/irradiance and for bi-directional reflectance factors. In reflectance or white reference mode the spectra are normalised against a reference panel spectrum to give units of percentage relative reflectance. The spectroradiometer was used in the reflectance mode throughout this project.

<b>Detector</b>	<b>VNIR</b>	<b>SWIR 1</b>	<b>SWIR 2</b>
<b>λ Range</b>	350-1020 nm	1020-1800 nm	1800-2500 nm
<b>Detector</b>	512 photo-diode array overlaid with order separating filters	Scanning spectrometer, concave holographic grating, thermo-electrically cooled InGA detector	Scanning spectrometer, concave holographic grating, thermo-electrically cooled InGA detector
<b>Sampling resolution</b>	1.5 nm	2 nm	2 nm
<b>Bandwidth</b>	3 nm (FWHM)	10-11 nm (FWHM)	10-11 nm (FWHM)
<b>Measurement</b>	All simultaneously	Sequential scanning	Sequential scanning
<b>Dark current</b>	Operator measured via mechanical shutter	Automatically measured every scan via shutter and reference channels	Automatically measured every scan via shutter and reference channels
<b>Signal amplification</b>	Integration time	Gain	Gain

**Table 3.1** The technical specifications of the three ASD FR detectors, (Wilson 1995).

Above the detectors, a sub-notebook computer is mounted, used to control the instrument. The dark current from the SWIR detectors is automatically measured and subtracted from each spectrum, however, the dark current from the visible-near infrared needs to be taken manually after approximately 15 minutes once the instrument has

stabilised. The spectroradiometer is configured prior to use for integration time and scan averaging. The integration times for the SWIR wavelengths are set at 100 milliseconds but the VNIR wavelengths integration time must be set manually using the choice of four settings, 17, 34, 68 and 168 ms depending on the intensity of the incoming signal. This is set using the spectrum from the brightest object to be measured, which is the barium sulphate reference panel. The spectroradiometer will use an average spectrum of multiple scans as a method of reducing random noise effects. This is user selected but a scan average of ten is appropriate for clear UK conditions.

The whole spectrometer assembly measures 35 x 31 x 18 cm and weighs 5.7 kg, the nickel- cadmium rechargeable battery pack used to power the detectors weighs a further 2.5 kg. The spectrometer is carried in the field within a harness strapped to the front of the user with the batteries fitted into the small of the back. The pistol-grip sensor head can be pointed at a target by hand or fixed onto a standard photographic tripod. The battery life of the external battery pack is approximately 3 hours but the limiting power source is the rechargeable batteries for the sub-notebook PC which have a life of approximately 2-2.5 hours and have a power failure warning sound to prevent data loss. Details of the operation procedure for the ASD FR spectroradiometer can be found in Appendix A.

### **The GER1500 spectroradiometer**

The Geophysical Environment Research 1500 spectroradiometer, (Figure 3.2) is a visible and near infra-red spectrometer, measuring wavelengths of 350-1050 nm on a 512 silicon photo-diode array. The wavelength range is covered in nominal bandwidths of 1.5 nm with automatic dark current correction. Integration time is user selected with

options of 5 milliseconds and upwards. The spectrometer head measures 8.3 x 15.2 x 19.7 cm and weighs just 2 kg including the batteries.

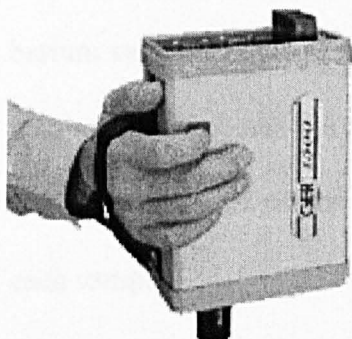


**Figure 3.2** The GER 1500 spectroradiometer.

The field of view (FOV) is  $4^\circ \times 5^\circ$  with fore-optic options giving FOV up to  $23^\circ$ . There is a built in laser sighting mechanism to allow accurate positioning when the instrument is being hand-held. The spectrometer can be operated in stand-alone mode with an internal memory of 500 spectra or via a laptop PC with direct data download giving a much higher data capacity. As a stand-alone spectrometer, the GER 1500 does not have the fibre-optic link of the ASD FR, which is easily damaged, thus making it more robust and more suitable for travel and tougher field conditions. The instrument can be either hand held or mounted on a standard photographic tripod. The user time is again controlled by battery life; in stand-alone mode this is 2 hours using a nickel-metal-hydride 6-volt battery. The instrument is supplied with two of these batteries giving 4 hours user time. Operation is by a scrolling menu to allow easy instrument set-up for choosing parameters such as integration times and scan averaging. Further details of the exact operation procedure of the GER 1500 can be found in Appendix A.

### **3.2.2 *In-situ* spectrometry Data Processing**

For each measurement, the *in-situ* raw data were collected along with a spectrum from a barium sulphate panel of known calibrated reflectance. Using the two spectra together it is possible to process the raw data into absolute reflectance. Thus all *in-situ* data within this project consist of one reference spectrum followed by a set of ten target spectra for each sample.

#### **ASD FR**

The raw data from the ASD FR spectrometer are combined with the reference panel data using an MS-DOS program supplied by NERC equipment pool for field spectroscopy (EPFS) called *refspec.exe*. The program produces the absolute reflectance file by producing a ratio of the target/reference spectral pair and then applying a correction using a calibration file containing information specific to the reference panel used. The program is driven by a single command line, details of which can be written as an MS-DOS batch file for semi-automatic processing. The output files are suffixed with *.abs* for absolute reflectance and are formatted as comma-delimited text files. These can then be imported into spreadsheet packages for further processing to mimic the airborne remote sensing instruments.

#### **GER 1500**

The data produced by the GER1500 are processed as for the ASD FR spectrometer using a similar program called *refg1500.exe*. The program is slightly different, as the individual wavelengths measured by each channel are different than for the ASD. The

only other difference being that the *refg1500.exe* program does not have the -r option for processing only every other channel otherwise the command line used is as for the ASD FR spectroradiometer.

### ATM filter functions

Figure 3.3 shows that for each ATM band the wavelengths measured are actually spread wider than the bandwidths suggest, for example, band seven is given the wavelengths 760-900 nm, however spectral contributions are received from wavelengths 607-1045 nm.

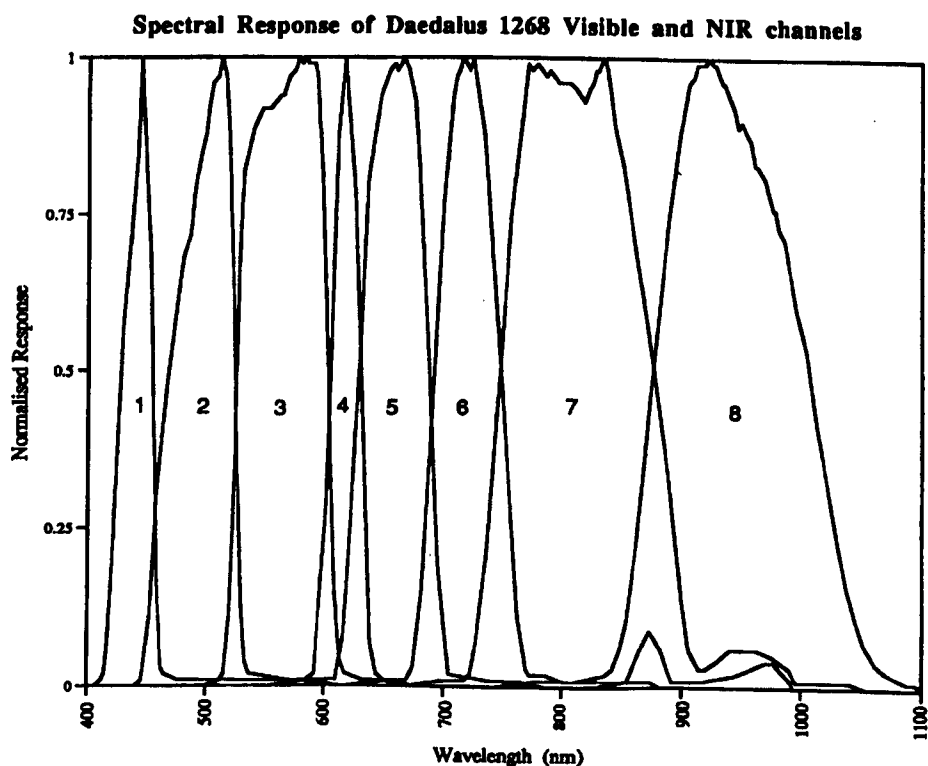


**Figure 3.3** The normalised response of the ATM sensor for channels 1-8.

This can be seen as the extent of the sloping limbs of each band response of Figure 3.3. Thus to produce a single figure for a given band from the continuous spectral data of the ASD or GER 1500 spectrometers a filter function is used. The filter functions are produced by NERC EPFS and are in the format of a comma delimited text file like the

absolute reflectance data. A diagrammatic representation of how the filter functions work is given in Figure 3.4. The multiplication of the *in-situ* data by the weighted filter function accounts for the variation in spectral contribution across the various wavelengths with the ratio of the two summations producing the single value for the whole band.

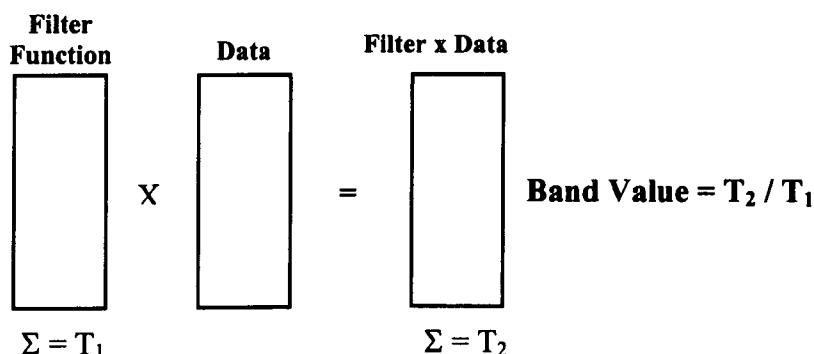


**Figure 3.4** The filter function matrix for ATM data

### CASI band selection

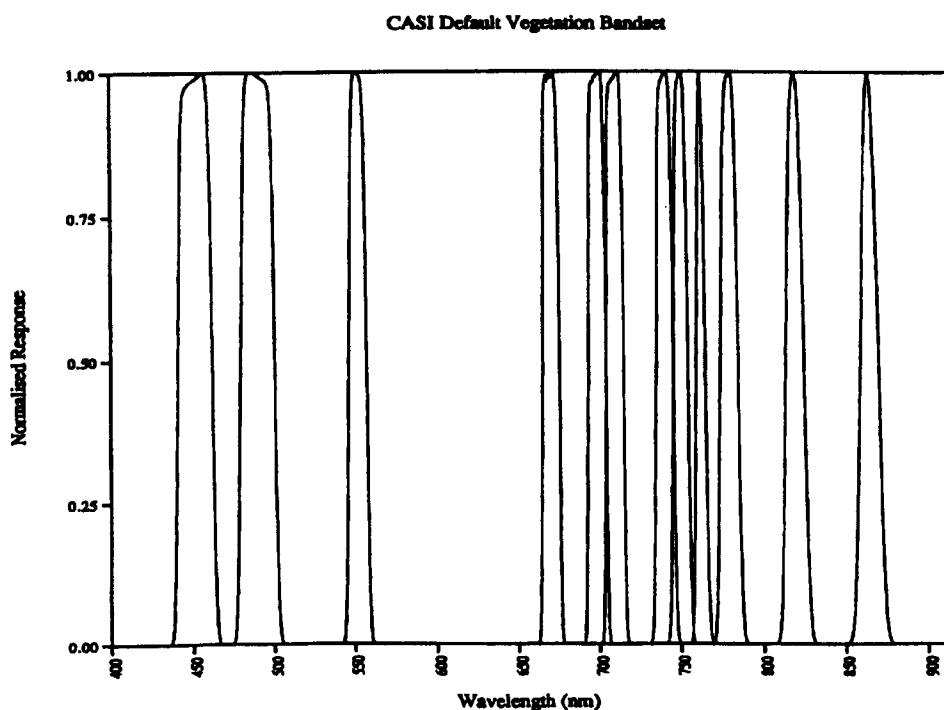


**Figure 3.5** The normalised response of the CASI sensor for the NERC default vegetation bandset.

It can be seen from Figure 3.5 that the response of the CASI is far more precise regarding the range of wavelengths selected compared to those actually measured. It should also be noted that the magnitude of response that each individual wavelength measures in comparison to its neighbouring wavelength is very similar, thus the shape resembles a rectangle far more than the normal distribution shape of the ATM. For this reason no filter functions are used just the average response across the wavelengths of the proposed waveband. The errors introduced using this method are likely to be insignificant, as the response across the narrow bands is much more uniform.

### 3.3 AIRBORNE REMOTE SENSING

#### The NERC Aircraft

The NERC aircraft, purchased in 1983, was modified by construction of floor apertures to house remote sensing instruments. The plane is a Piper Navajo Chieftain, type PA31-350, with an internal cabin size of 12.5 by 4.2 by 4.25 feet. The cabin is non-pressurised and thus the operational altitude is limited to 10000 feet (3000 meters) with an on task air speed of between 100 and 170 knots.

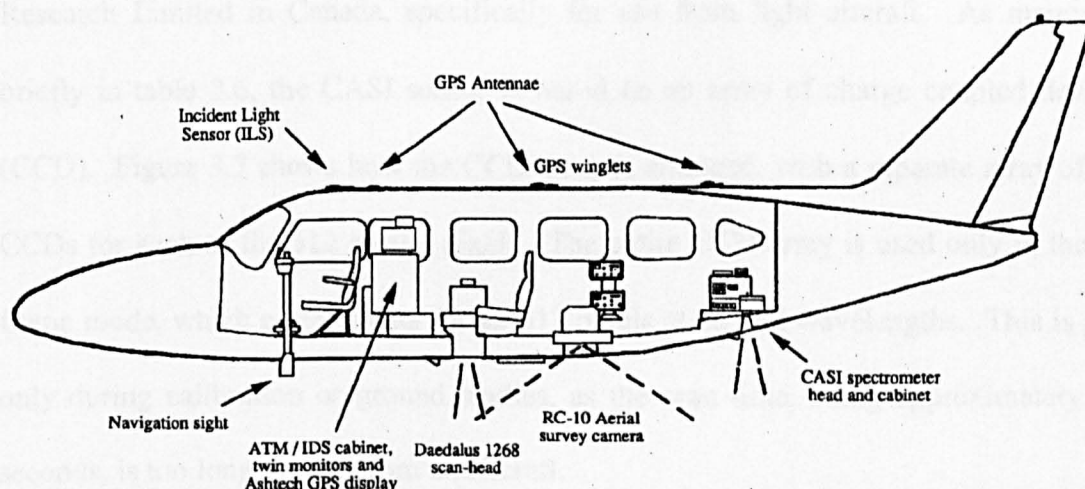


Figure 3.6 The equipment layout within the NERC aircraft, (NERC 1995).

The aircraft can carry an operational load of 2050 pounds in mass including a crew of four people and has an endurance range of 950 nautical miles, which is equivalent to approximately four hours flying time. The instruments are powered by the on board 28 volt power supply. Within the aircraft the instrumentation is arranged as shown in Figure 3.6. The CASI is towards the rear of the plane, the survey camera and ATM at the centre and the data collection controls towards the front. Other features such as GPS antennae and incident light sensors are mounted on the outside of the fuselage. The GPS antennae are used for determining the positioning and also for measuring the roll pitch and yaw of the aircraft. This information is then used in the NERC integrated data system (IDS) to roll correct and geometrically correct the data (Wilson, 1996) this is discussed in more detail in section 3.3.2.

### **3.3.1 Airborne Remote Sensing Instrumentation**

#### **Compact Airborne Spectrographic Imager (CASI)**

The CASI is an across-track scanning or “push-broom” sensor developed, by Itres Research Limited in Canada, specifically for use from light aircraft. As mentioned briefly in table 2.6, the CASI sensor is based on an array of charge coupled devices, (CCD). Figure 3.7 shows how the CCD array is arranged, with a separate array of 288 CCDs for each of the 512 spatial pixels. The entire CCD array is used only in the full frame mode, which collects data for all 512 pixels at all 288 wavelengths. This is used only during calibration or ground studies, as the scan time, being approximately two seconds, is too long for use from an aircraft.

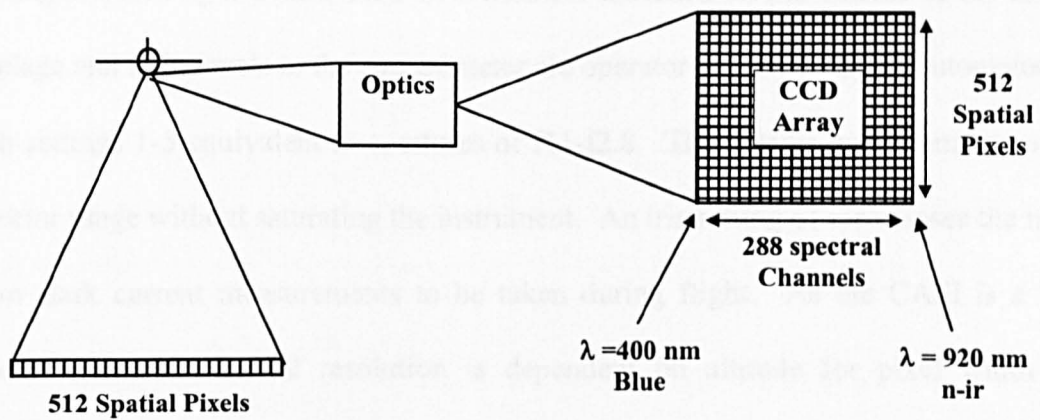


**Figure 3.7** The internal set-up of the Compact Airborne Spectrographic Imager.

For operational use the CASI has three other modes of operation, spatial, spectral and enhanced spectral. Spatial is the mode of operation that is most commonly used. This allows complete spatial coverage of the 512 pixels but wavelength coverage is limited to up to 18 bands. Despite this apparent limiting factor the CASI still has an advantage over most instruments as the 18 bands can be positioned anywhere along the 400-915 nm wavelength range, in bands as wide or as narrow as the user chooses. The only restriction is the signal to noise ratio, which may be less for narrower bands. In spectral mode, or “push-rake configuration” the CASI collects information for all 288 spectral channels but only for 39 pixels. These can be distributed throughout the 512 pixel swath at 4, 8, 12 or 16 pixel spacing, giving the image the appearance of a raked pattern. To enable the user to visualise an image collected in the spectral mode, a monochrome “scene recovery channel” spatial image is provided. The fourth mode, the enhanced spectral mode, is a compromise between spatial and spectral modes. This allows the user to obtain maximum spectral data at maximum spatial coverage (288 spectral channels for up to 101 adjacent pixels). However, the fewer spectral channels chosen, the shorter the integration time and the finer the spatial resolution can be. Down-

welling incident light is measured with a sensor mounted on the outside of the aircraft fuselage and light levels to the spectrometer are operator controlled by an automated iris with settings 1-5 equivalent to apertures of f11-f2.8. This allows maximum use of the detector range without saturating the instrument. An iris setting of zero closes the iris to allow dark current measurements to be taken during flight. As the CASI is a push broom sensor the spatial resolution is dependent on altitude for pixel width and integration time for pixel length. These are calculated using equations 3.1 and 3.2.

$$\text{Pixel Width (m)} = 1.5 \times 10^{-3} * \text{Altitude (m)} \quad [3.1]$$

$$\text{Pixel Length (m)} = \frac{(\text{Int. Time (ms)} * \text{Ground Speed (m/s)})}{1000} \quad [3.2]$$

As the pixel width and length are determined by specific parameters it is possible to calculate the approximate spatial resolution prior to flight. However, should light levels vary greatly throughout the day, a slight adjustment in integration time, speed or altitude can be made to maintain a square pixel. In extreme circumstances a pixel with a 2:1 length to width ratio may be obtained which can be resampled during processing.

### **Daedalus 1268 Airborne Thematic Mapper (ATM)**

The Daedalus 1268 Airborne Thematic Mapper (ATM) is a fixed band along track scanning or “whisk-broom” sensor whose wavebands are almost identical to those of the satellite, Landsat Thematic Mapper.

ATM Band No.	Wavelengths ( $\mu\text{m}$ )	Equivalent Landsat TM Band No.
1	0.42-0.45 (blue)	
2	0.45-0.52 (blue)	1
3	0.52-0.60 (green)	2
4	0.605-0.625 (green)	
5	0.63-0.69 (red)	3
6	0.695-0.750 (red)	
7	0.76-0.90 (n-ir)	4
8	0.91-1.05 (n-ir)	
9	1.55-1.75 (mid-ir)	5
10	2.08-2.35 (mid-ir)	7
11	8.5-13.0 (thermal-ir)	~6

**Table 3.2** The ATM Bandset

This similarity has made the ATM the most frequently used sensor for development of algorithms applied to Landsat imagery. The fixed bandset of the ATM is shown in table 3.2. Figure 3.8 shows the internal mechanism of the ATM. Light is captured and directed into the detector by a rotating scan mirror. The visible and near infra-red wavelengths, that is channels 1 to 8, are measured on a silicone diode array, which receive light split by a prism. Channels 9, 10, and 11 are each measured by individual detectors, which are housed in dewers cooled by liquid nitrogen. Channels 1 to 10 are calibrated on the ground, however the thermal channel (11) is calibrated in flight using two black bodies set above and below the expected temperature range .

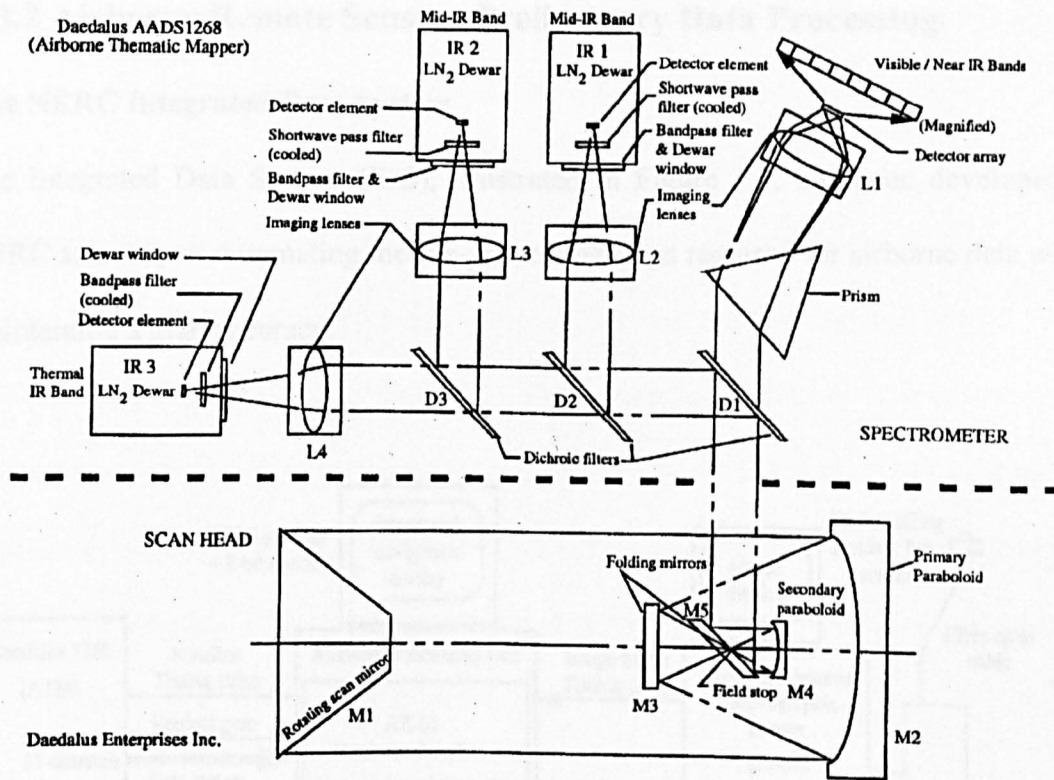


**Figure 3.8** The internal optics and detectors of the Daedalus ATM. (NERC 1995).

The ATM swath width is covered by 716 pixels, as opposed to the 512 pixels of the CASI and most other instruments, and has a much wider field of view, up to 90°. There are three scan speeds of 50, 25 or 12.5 scans per second with a usual overlap of 10% of the whiskbroom scan to avoid gaps in the image. The ground spatial resolution is dependent on altitude and with an IFOV of 2.5mrad or approximately 0.14°, this gives a resolution of 2.3m at 1000m altitude.

### 3.3.2 Airborne Remote Sensing Preliminary Data Processing

#### The NERC Integrated Data System

The Integrated Data System (IDS), illustrated in Figure 3.9, has been developed by NERC as a way of automating the pre-processing steps required for airborne data whilst maintaining a high accuracy.

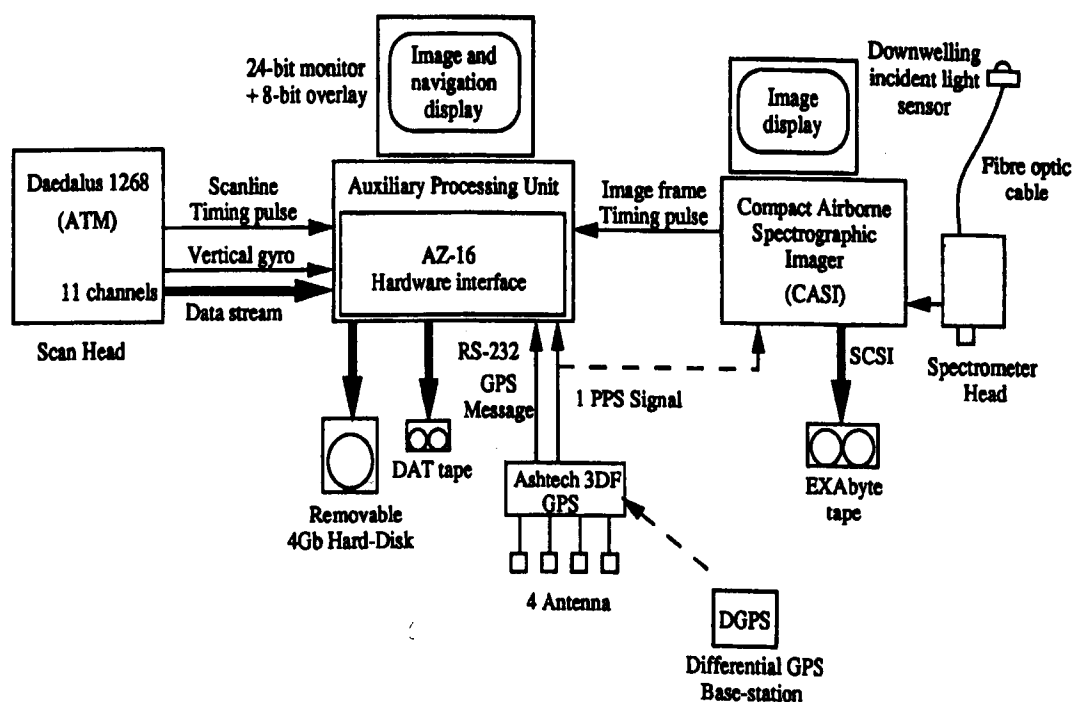


**Figure 3.9** The NERC Integrated Data system, (NERC 1995).

The system aims to use a cross formation of four GPS receivers to determine the roll, pitch and yaw of the aircraft as an alternative to the standard vertical roll gyro technique installed in most other aircraft. With a gyro system the corrections for aircraft roll and geometric correction are performed separately, whereas with the integrated data system, the GPS derived information is used to roll correct and geometrically correct the data in

one step as detailed in the following paragraph. (At the time of receiving the data for this study, this system was not yet fully developed.)

### **Processing with *exhdf* and *gcorr***

The programs to import the data into image processing systems are supplied by NERC airborne remote sensing with the data. There are two command-line driven UNIX programs, *exhdf* and *gcorr*. The first allows access to the header information and conversion between file formats and the latter geometrically corrects the data using the integrated GPS data. The commands required and all the possible options are provided with the data in the form of a word document.

## **3.4 GLOBAL POSITIONING SYSTEM**

### **3.4.1 The Principle of the Global Positioning System**

The Global Positioning System (GPS) is based on a network of 24 satellites, of which 21 are used with 3 active spares, operated by the United States Department of Defence. Each satellite orbits the Earth twice a day at an altitude of 11000 nautical miles. The satellites are distributed throughout six orbital planes therefore between five and eight satellites are visible to a receiver from any point on the Earth's surface, however a minimum of four satellites is usually required for reliable data. Each satellite broadcasts two signals, the precise positioning system (PPS) and the standard positioning system (SPS). At the time of data collection, the precise positioning system was available only to authorised users such as US and allied military and the standard positioning system is available to all civilian users. The reduction in accuracy of the SPS was achieved by intentionally degrading the signal using a system called selective availability (SA) which

used a changing time bias. This time bias is different for each satellite thus the errors at the receiver are a function of the combination of the satellites used and will vary with position. The errors due to selective availability were removed in May 2000 improving accuracy for non-military users. The satellite signals are also subject to delays caused by the distance they travel, which can introduce errors into the final position obtained. Tropospheric delays are caused by variation in air temperature and humidity and can introduce errors of around 1m, ionospheric delays can introduce errors of up to 10m but can be removed by modelling the ionosphere. On reaching Earth, the satellite signal may be subject to reflectance from nearby surfaces giving rise to errors of approximately 0.5m.

### **Differential GPS**

The most common technique for improving the accuracy of the position obtained from the global positioning system is to use differential GPS (DGPS). This requires two GPS receivers, one stationary and one mobile, to give a comparison of the changing time bias from the selective availability. This can be done as a post-processing technique or in real time by transmitting the necessary corrections from the base station back to the mobile receiver by radio signal. As the selective availability signal is constantly changing, these differential corrections must be transmitted to the mobile receiver at a faster rate than they are changed in the selective availability signal, that is at least every twenty seconds. Although using differential GPS can remove the selective availability signal the technique does not remove errors due to receiver noise or reflected signals but accuracy is considerably improved from 100m to approximately 15m. Accuracy can be improved further still by using carrier phase techniques. Rather than using the ephemeris data that are transmitted by the satellite, carrier phase GPS uses the

transmitting signal itself to improve the position obtained by utilising the Doppler shift effect. The difference in the phase of the signal reaching the base station and the mobile receiver can give military users accuracy in the order of millimetres. This higher resolution of positioning is obtained because of the short wavelength of the carrier signal, approximately 19cm. The only requirement for carrier phase techniques is that the base station and the mobile receiver must be close enough to be subject to the same ionospheric delays. This limits the distance between them to approximately 30km.

### **3.4.2 GPS Data Processing**

Information on the position of the samples taken from the boat were obtained using the Magellan Promark X CP differential GPS, with carrier phase capabilities to give sub-meter accuracy. This was then processed using the Magellan MSTAR software and converted from latitude and longitude to UK national grid co-ordinates. The GPS data were output in an ASCII format, which could be easily imported into Microsoft Excel for further processing.

In Excel the data were plotted as velocity in N-S dimension and velocity in E-W dimension verses time as shown in Figure 3.10. This enabled the sampling times to be verified against the areas of the plot where both velocities were minimal. During the sampling period, which could last approximately 30 seconds, the engine had to cut to minimise the effect of foam due to turbulence on the in-situ spectra, thus the boat was never totally stationary. To determine a position for the sample site an average position was obtained for the 30 second sampling period where the motion was at a minimum. This is shown in Figure 3.11.

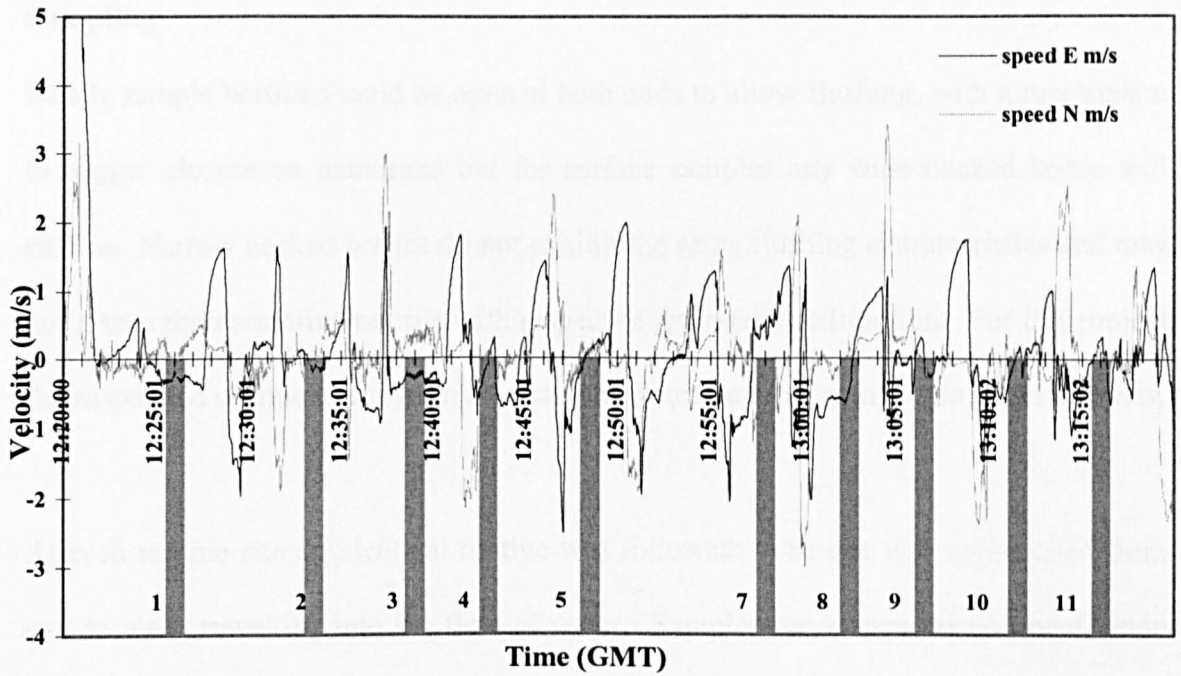


**Figure 3.10** The velocity plot taken from GPS data collected on the 6<sup>th</sup> June 1996 off Warton Bank, with the sample sites shown as shaded grey bars corresponding to areas of least motion.

**Sample Site 2, 6th June 1996.**

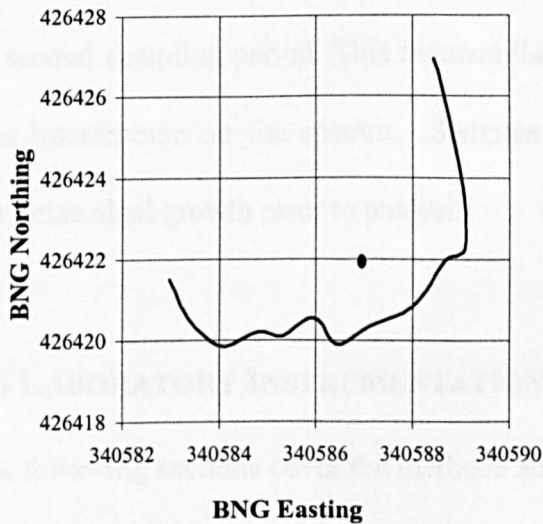


**Figure 3.11** The GPS plot over a typical 30 second sampling period, site 2, showing the movement during that period (line) and the mean position (circle).

### **3.5 FIELD METHODOLOGY**

#### **Sampling**

Ideally sample bottles should be open at both ends to allow flushing, with a mechanism to trigger closure on command but for surface samples any wide necked bottle will suffice. Narrow necked bottles do not exhibit the same flushing characteristics and may not give a representative sample with respect to grain size distribution. For this project the suspended sediment and grain size samples were sampled using wide necked bottles.

At each sample site an identical routine was followed. The site was approached from east to west, travelling into the flow of water. Samples for suspended sediment, grain size and radionuclide analysis were collected from the port side of the boat, facing south. Spectra were taken from the starboard side of the boat facing north. The spectra were taken arms length from the side of the boat, with the spectrometer head approximately 50cm above the surface of the water at nadir. Whilst the spectra were collected the boat engine was put into neutral and the boat allowed to drift for the 10 to 15 second sampling period. This reduced the wake from the boat minimising foam and thus interference on the spectra. Samples were then stored in the dark at  $<4^{\circ}\text{C}$  to minimise algal growth prior to analysis.

### **3.6 LABORATORY INSTRUMENTATION AND METHODOLOGY**

The following sections cover the methods and instruments used within the laboratory in addition to the smaller field instruments which are laboratory calibrated such as turbidity and salinity meters.

### **3.6.1 Suspended Sediment**

Prior to suspended sediment analysis it is necessary to have some knowledge of the values to be expected, as this influences both the filter paper size and type and the sample size. Most methods require a minimum of 50 mg of sediment making one-litre samples sufficient for estuaries such as the Ribble where the suspended sediment loading is shown in Environment Agency data to be around 50-200 mg l<sup>-1</sup>.

The method used for determination of suspended sediment was influenced strongly by the necessity to keep the suspended sediment analysis and the radionuclide analysis comparable. This is due to the fact that the suspended sediment data for the 6<sup>th</sup> June 1996 was taken from the radionuclide analysis. Therefore, any subsequent suspended sediment analysis must be performed using the same equipment and conditions. The choice of filter papers and drying temperature was restricted to those used for the radionuclide determination, otherwise the methodology was true to the standard methods employed by the recommended suspended sediment analyses. The basic procedure entails filtering the known volume of sample through pre-weighed filter papers and weighing the residue. This can be carried out using either vacuum or positive pressure filtration but vacuum pressure was used in this project due to the availability of equipment. Only a gentle vacuum pressure must be applied to prevent premature clogging as the sediment is pulled deeper into the pores of the filter paper.

#### **Sample Preparation**

The most commonly used pore size used to obtain suspended sediment data in marine work is 0.4µm (McCave 1979) with filter paper sizes ranging from 4.7cm – 29cm diameter. There are three basic types of filter paper on the market, cellulose esters,

track-etched membranes and glass fibre. The track-etched membranes can only take the smallest of suspended sediment loads making them unsuitable for most estuaries. The glass fibre filters do not have a defined pore size and are generally considered to be a nominal pore size of approximately 1.2 $\mu$ m. As the suspended sediments can be assumed to consist largely of the finer particle sizes, this makes the glass fibre filters unsuitable. Thus it was decided to use the cellulose ester type of filter paper. Cellulose ester filters contain some soluble material therefore it is necessary to run blanks. They are also hygroscopic, which makes their mass vary with humidity. Cellulose ester can also be rendered transparent by a few drops of cedar oil (with refractive index of 1.51) allowing a microscopic examination of the residue if this information is required. The cellulose ester filter paper is also suited to the suspended sediment loads associated with estuarine samples, in addition to being available in both the 9cm diameter for suspended sediment analysis and 29cm diameter used for the radionuclide analysis.

Once the filter paper type has been selected the filters must be numbered and pre-weighed, and then handled only using tweezers to avoid the papers absorbing oils from the hands. The samples were then filtered under a slight vacuum and washed with three 20 ml aliquots of distilled water to remove any salt in the sediment residue. The papers are then allowed to air dry under vacuum for 1 minute to remove excess moisture before being removed from the filter cup. The entire sample should be filtered, as representative sub-samples are difficult to obtain. The volume must be determined as accurately as possible; therefore the sample must be transferred to the filter via a measuring cylinder. If the suspended sediment loading is particularly high a glass fibre filter paper placed underneath the cellulose ester paper will even out the pressure

exerted by the vacuum and prevent clogging. Blanks were treated in exactly the same way as the samples.

Drying is commonly carried out at 105°C followed by cooling in a desiccator to eliminate all water but on removal from the desiccator a cellulose ester paper will start to absorb atmospheric water making accurate weighing to four decimal places difficult. In addition, driving off water at such a high temperature can remove water from the internal structure of the clay particles, which makes this unsuitable for the radionuclide analysis. For this reason the filter papers were dried for 24 hours at 40-45°C and cooled to room temperature in a well ventilated room. The variations in mass caused by humidity should be the same for the samples and blanks, therefore eliminating this source of error.

Before weighing the balance was calibrated using the supplied standard mass. The balance was allowed to achieve equilibrium before weighing the samples. The best way to do this is to perform some pre-weighing for approximately 15 minutes prior to weighing the samples. The balance used for this project was a Mettler-Toledo AB204 capable of weighing 10mg to 210g to 4 decimal places, with an error of plus or minus 1mg. Samples were weighed to four decimal places to allow accurate calculation of suspended sediment concentration.

Suspended sediment concentration is calculated by determining the mass of the sediment contained on the filter paper in milligrams after adjustment for the average percentage weight loss of the blanks. The mass, in milligrams, is then divided by the known volume in litres to give a suspended sediment concentration in  $\text{mg l}^{-1}$ .

### **3.6.2 Particle Size**

To define a single value for a particle size is far more complex than it would first appear, particularly for natural sediment suspensions. The reason for this is the irregular shape of particles where the length width and thickness may all be different. So which value should be used? All particles have some properties that can be given as a single value such as mass, volume and surface area. However, the only real particle shape that can be expressed using a single value is the sphere. For this reason particle sizing by many methods expresses size of a particle as that of the equivalent sphere. For each particle there is a choice of possible equivalent spheres, the sphere of the same mass, volume, surface area, maximum length, minimum length or sedimentation rate. All of these possibilities are correct but each refers to a different property. This highlights the need for standardisation within and possibly between studies in the measurement of particle size.

#### **Choice of technique**

The most obvious and simple technique for determining particle size is by examining the particles under a microscope. This is however to give an accurate representation of grain size distribution a large quantity of the individual grains will need to be examined. Thus the technique is not practical. It can however give a useful indication of the grain shape if this parameter is required.

For suspended sediment one of the oldest particle sizing techniques is to use the gravitational sedimentation rate. This is particularly useful for the finer sediments and

the equipment can be as simple as a measuring cylinder and a pipette. The technique is based on Stokes' Law and details of the method can be found in Dyer (1979). The potential problems with this method are that the density of the material being analysed is required. The final result is not related to the diameter but the settling rate of an equivalent sphere, which is not valid for sheet like particles such as clays as it gives a smaller value than the reality. For particle sizes greater than 50 $\mu\text{m}$  the settling tends to be turbulent making Stokes' Law invalid and thus giving erroneous results. A further problem is introduced for particles less than 2 $\mu\text{m}$  as resistance to settling by Brownian motion becomes significant thus this method has a very limited size range, (Clifton *et al.*, 1999).

The technique of electrozone sensing is more commonly known as the Coulter Counter, a technique originally developed for sizing blood cells. The principle involves the particles passing through an orifice which has a voltage applied across it. As each particle passes there is a voltage peak. The particle size is then determined by comparing the peak area with those for spheres of a known size. The particles being measured must be kept in suspension whilst flowing slowly through the orifice, which is difficult for the larger particles and with a range of particle sizes there is a risk of blocking small orifice of the detector.

### **Laser Diffraction: The chosen method**

Laser diffraction is a more recent method that is becoming more common as a particle sizing technique. The correct name is Low Angle Laser Light Scattering (LALLS) and is suitable for particles over a 0.1-2000  $\mu\text{m}$  range making it a practical option for many applications. The basic principle relies on the fact that the angle of diffraction is

inversely proportional to particle size. This instrument consists of a helium-neon laser, with a wavelength of 638.2 nm, and between sixteen and thirty-two detectors of photosensitive silicon. For the smaller particles, 1 nm to 1  $\mu\text{m}$ , a photo-multiplier tube is needed to amplify the scattered light signal. The sample is introduced into the laser beam by circulating the sediment suspension in front of the beam but other applications may use air-blowing of powders or aerosol spray depending on the substance being measured. The basic assumptions of this technique are:

1. that the particle is larger than the wavelength of the light which is scattered
2. all particle sizes scatter light at the same efficiency and
3. the particle is opaque and transmits no light.

The main advantages of laser diffraction as a particle sizing technique are that the method is absolute and does not require daily calibration, and also covers a large particle size range, which is necessary for natural suspensions. Samples need no preparation other than shaking to attain the suspension although for samples with a sediment load below 50 mg/l it may be necessary to concentrate the sample by evaporation. In some circumstances suspensions may require the addition of a dispersing agent, however none were used within this study, as it was necessary to maintain the suspensions in their natural state, including the floccs.

The samples taken for particle size analysis were two litres in volume and collected in wide necked plastic bottles. The samples were stored at for 3 days below 4°C in the dark to prevent algal growth. These were then analysed using the Malvern Mastersizer at Westlakes Scientific Consulting Ltd. The details of the operation procedure can be found in appendix A.

### **3.6.3 Gamma spectroscopy**

Gamma spectrometry is a complex subject which is covered in detail in many radiation detection publications such as Knoll (1989) but a very brief outline of the principles, based on these texts, is presented here.

The detection of a gamma ray photon relies on the photon interacting within absorbing material. During the interaction the gamma ray photon must transfer all or part of its energy to an electron within this material. Thus to be a detector of gamma rays the detector must provide the absorbing material to yield the fast electrons in addition to acting as a detector for secondary fast electrons. There are two principal types of gamma detector, the sodium iodide (NaI(Tl)) type which have a high sensitivity and poor energy resolution and the hyper-pure germanium (HPGe) or the older lithium drifted germanium (Ge(Li)) semi-conductor types which have a high energy resolution. Which detector type is chosen depends on the resolving power required. This project required high-energy resolution to detect a variety of radionuclides that could be present in the samples, thus a semi-conductor type was chosen. These detectors work on the semi-conductor energy band gap principal, where valence electrons are excited by ionisation until they have sufficient energy to cross the forbidden band where they are detected using an applied electric field. The pulse signal of the electron in the electric field is amplified and processed to produce the data. The detectors must be kept at liquid nitrogen temperature to reduce detector noise. Before use the detectors must be calibrated with a known traceable standard using the same geometry as the samples.

In the course of this project, only caesium was obtained in sufficient quantities to produce a complete dataset due to small sample size

### **Detector Calibration**

Gamma detection is sensitive to the geometry of the sample, such as size, shape and density. Therefore, the detector must be calibrated using a known standard in a sample medium identical to the environmental samples to be measured. A blank filter paper was spiked with a known quantity of gamma emitting tracers in a liquid medium supplied by the National Physical Laboratory. The paper was folded in the same pattern as the sample papers and counted until a clear spectrum was obtained, a period of approximately four hours. The mixed standard consisted of  $^{241}\text{Am}$ ,  $^{109}\text{Cd}$ ,  $^{57}\text{Co}$ ,  $^{139}\text{Ce}$ ,  $^{203}\text{Hg}$ ,  $^{113}\text{Sn}$ ,  $^{85}\text{Sr}$ ,  $^{137}\text{Cs}$ ,  $^{60}\text{Co}$  and  $^{88}\text{Y}$ . These gamma emitters cover an energy range of 59KeV to 1836KeV.

The detector used throughout this project was an Ortec 30% efficiency HPGe detector at Westlakes Scientific Consulting Ltd. The software used to resolve the data was Fitzpeaks (version 2.08). For analysis of gamma emitting radionuclides, ten litre samples were taken and filtered through pre-weighed 293mm diameter cellulose-nitrate membrane filters. The filtering assembly is shown in Figure 3.12. The sample is fed to the filter by a diaphragm pump driven by compressed air at 2 bar pressure. The filter paper is set into an acrylic block with the base grooved with concentric circles and holes for the filtrate to pass through. Cellulose nitrate filter papers of this diameter tend to be brittle and must be handled with care when weighing. After filtration the papers were dried for twenty-four hours at 45-50°C until three consecutive masses were obtained.

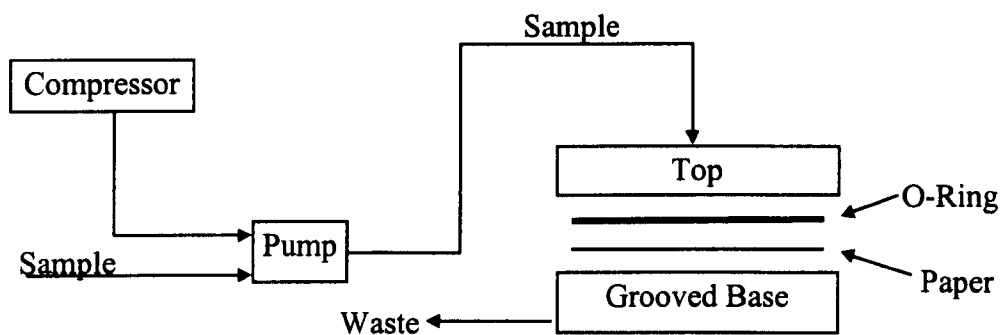


**Figure 3.12** The filter assembly used for radionuclide sample preparation.

### 3.6.4 Turbidity

Turbidity meters use light to measure the clarity of water, as the clarity is reduced by suspended sediment. The way in which the turbidity and suspended sediment concentrations are related depends on the properties of the sediment and the instrument used. A fully comprehensive study of turbidity can be found in Gippel (1989), but below is a very brief outline of the main points based on the above publication that are relevant to this project.

#### **Turbidity and suspended sediment concentration**

Turbidity is known to increase in relation to increasing suspended sediment concentration. It would be expected that the relationship between turbidity and suspended sediment concentration is linear according to the Beer-Lambert law, however results shown in Gippel (1989) indicate that this is not the case. Non-linearity effects are introduced by high SSC. The turbidity values are wavelength dependent but the rate of change of absorbance is not wavelength dependent. This wavelength dependence implies that care should be taken when comparing data from different turbidity meters,

which although related will not be directly comparable. A possible solution to this has been applied by the ISO 7027 standard which uses a monochromatic light source of 860 nm, which has the added advantage of not encouraging algal growth as it is in the near infra-red.

### Turbidity and particle size

As the particle size decreases the surface area to volume ratio of the particle increases, thus light is more effectively scattered by the smaller particles. To illustrate this, a basic experiment was performed on the measurement of turbidity for known suspended sediment concentrations of different grain sizes using dry sieved natural sediment. The results given in Figure 3.13 show that it is indeed the smaller grain size fraction that gives the higher turbidity reading for the same suspended sediment concentration.

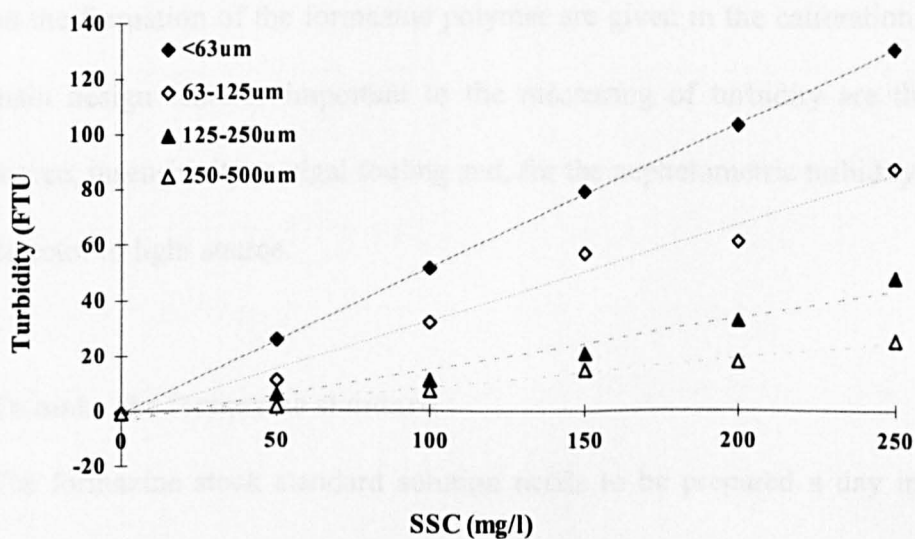


**Figure 3.13** The variation in the turbidity SSC relationship with grain size.

## **Turbidity meters**

There are two types of turbidity meter commercially available, the attenuation turbidity meter and the Nephelometric turbidity meter. The attenuation turbidity meter is also known as the beam transmissometer. This measures the loss of light intensity of the light source over a known path length. This type of turbidity meter can underestimate the turbidity as some light scattered by particles will remain in the path indicating a higher light reading than there should actually be. The Nephelometric turbidity meters measure scattered light by having the detector aligned at an angle to the original light source. This angle is generally 90° but may vary between instruments. The turbidity values given by each type of meter will be different but directly related. Turbidity is not actually measuring suspended sediment but the water clarity in comparison to an artificial formazine standard with which the instrument is calibrated. Formazine is an aqueous dispersion of an insoluble polymer of 2.5 µm mean diameter particles. Details on the formation of the formazine polymer are given in the calibration procedure. The main design features important to the measuring of turbidity are the constant light source, insensitivity to algal fouling and, for the nephelometric turbidity meters, angle of detector to light source.

### **To make the formazine standard**

The formazine stock standard solution needs to be prepared a day in advance as the polymer takes twenty-four hours to form.

1. Dissolve 10 grams of hydrazinium sulphate (hydrazine sulphate) in distilled water and dilute to 1 litre in a volumetric flask.

2. Dissolve 100 grams of hexamine (hexamethylenetetramine) in distilled water and dilute to 1 litre in a volumetric flask.
3. Mix the two solutions in a 2.5 litre glass bottle and allow to stand undisturbed for twenty four hours at 25°C. The resulting suspension will have a turbidity of 4000 FTU (formazine turbidity units).

The stock suspension should be kept in a cool dark place and is stable for up to one year. Dilutions of the stock suspension should also be stored in glass bottles in a cool dark place. Suspensions of greater than 400 FTU are stable for up to a month and at turbidities less than 400 FTU new standards should be made daily.

The dilutions of the 4000 FTU stock standard used to create the working standards are given in table 3.3.

<b>Turbidity (FTU)</b>	<b>Vol. of 4000 FTU stock (ml)</b>	<b>Dilute to Vol. (litres)</b>	<b>% Deflection Partech 7000-3RP</b>
0	0	1	0
50	12.5	1	10
100	25	1	21
200	50	1	42
400	100	1	78
500	125	1	95

**Table 3.3** The preparation of the formazine standards for turbidity calibration of the Partech 7000-3RP MKII turbidity meter used for testing experimental apparatus.

## **The Partech 7000-3RP MKII**

The Partech 7000-3RP MKII is a twin gap attenuation transmissometer with a single light source and a differing path length either side. The turbidity is measured using a ratio of the two path lengths as a compensatory technique. Compensation is provided, as both detectors receive the same light intensity, therefore when the lamp ages and light output varies, it varies equally for the two detectors. Secondly, algal growth will foul each window equally also reducing errors. These features prolong the operational life of the instrument up to fourteen times longer than a comparable single gap transmissometer. The instrument can be calibrated to three scales of sensitivity using the three ranges should large variable ranges of turbidity be expected. For this project only one was used as the instrument was used in laboratory conditions.

### **Calibration and operation**

Prior to calibration the instrument was checked to ensure that the instrument mechanically reads zero with the power off and that the windows of the light source and sensors are clean. The sensor is switched on and allowed to stabilise. The instrument is then set to zero, after which it is ready for calibration. The sensor head is then placed in the maximum standard and the span control is adjusted until the meter shows full or maximum deflection. The sensor head is then rinsed and readings for the intermediate standards obtained to give a calibration curve of percent deflection and turbidity.

The meter can be calibrated to known concentrations of suspended sediment but a calibration curve of suspended sediment will be more difficult to obtain accurately. This is because sediment is more difficult to keep in suspension without introducing a stirring mechanism. In addition to suspension difficulties it must be remembered that

sediment type and particle size will affect the readings obtained. Therefore it is necessary to calibrate the meter using the same sediment that is to be measured *in-situ*.

### 3.6.5 Salinity

The formal definition of is given in terms of a conductivity ratio,  $K_{15}$ , which is the ratio of the conductivity of the seawater sample to the conductivity of a standard potassium chloride solution at 15°C and 1 atmosphere pressure, (Open University 1989). The concentration of the standard potassium chloride solution should be 32.4356 gkg<sup>-1</sup>. This is then related to salinity using equation 3.3. The units of salinity are given in parts per thousand (‰) or grams per kilogram.

$$S = 0.008 - 0.1692K_{15}^{1/2} + 25.381K_{15} + 14.0941K_{15}^{3/2} - 7.0261K_{15}^2 + 2.7081K_{15}^{5/2} \quad [3.3]$$

Within this project, the salinity was measured using a Hanna HI 9033 conductivity meter with automatic temperature compensation. Conductivity corrected to 15°C was then substituted into equation 3.3.

#### Calibration of the Hanna HI 9033

The probe is connected to the meter with the sleeve properly inserted into the probe with the holes at the top. The instrument is then calibrated in a beaker filled to a depth of greater than 8cm with a 12880μS/cm. The probe is inserted and stirred to release any trapped air bubbles. The appropriate range is selected and the instrument is allowed five minutes for the temperature to stabilise. The calibration screw is then turned to give the correct reading at 25°C. Measurements are taken by selecting the correct range and simply reading off the meter display.

### **3.7 CHAPTER SUMMARY**

This chapter discusses the theory and techniques of the key methodologies used in this PhD. It is perhaps interesting to note that the techniques cover a range of scales of measurement of environmental phenomena - from atomic level in the detection of environmental radioactivity to the measurement of large-scale dynamic systems through remote sensing.

This thesis allies these techniques to develop and validate a methodology for the evaluation of the fate of sediments and sediment bound radionuclides throughout a flood cycle in the Ribble estuary. This work will result in the ability to identify areas actively being eroded, sediment transport processes and net budgets for the estuary.

## **CHAPTER 4: SUSPENDED SEDIMENT CHARACTERISATION.**

### **4.1 INTRODUCTION**

As discussed in chapter two the spatial variability in suspended sediment properties such as mineralogy, grain size and overall sediment colour, in addition to possible interferences from other constituents within the water column, are highly site specific. These factors have a significant influence on the reflectance characteristics of suspended sediments and hence the remote sensing of their properties. Consequently, this has resulted in the absence of a universal remote sensing suspended sediment algorithm. A given relationship can be assumed to be true only for the area in which it was derived. The approach adopted here is to characterise the relationship between reflectance and suspended sediment from first principles. The first priority is to gain some knowledge of the suspended sediment properties, such as the sediment grain size and the SSC range. The chapter also tests a key hypothesis to this research work: A systematic relationship exists between SSC and the associated radionuclide concentration adsorbed on to the sediment.

This chapter then determines the relationship between SSC and reflectance and goes on to establish the best wavelength settings, so that the CASI can be optimised for this project. This work is undertaken through a series of *in-situ* (section 4.2) and carefully designed laboratory experiments (section 4.3). Each section will present the experimental objective, method, results and discussion for each parameter, written as if each were a separate experiment.

## **4.2 THE *IN-SITU* PROPERTIES OF THE SUSPENDED SEDIMENT**

The estuarine environment is both spatially and temporally highly dynamic. The movement of radionuclides is governed by the sediment transport mechanisms, which are a direct result of the interaction of the estuarine currents, both tidal and wind driven, with the deposited sediment. Prior to any remote sensing study it is necessary to have a basic understanding of the environment to be observed remotely such as the SSC range, grain size and their spatial and temporal variations. Any sampling within an estuarine environment must be both spatially and temporally representative to enable meaningful interpretations and appropriate conclusions to be drawn. With the advent of hyperspectral remote sensing platforms such as the CASI we can eliminate the need for interpolations between spot samples and reduce errors resulting from temporal inconsistencies. These systems enable subtle spectral variations in the reflectance characteristics of suspended sediment and other water quality parameters to be monitored. Careful spectral characterisation from *in-situ* and laboratory measurements is required so that the CASI instrument bandwidths can be optimised for the required application.

### **Sampling logistics**

The estuary has a limited number of launch sites operational only for the two hours either side of high water. This two hour time limit is sufficient for the preliminary work investigating sediment properties, it is not be suitable for ground truthing the flight data. For the fieldwork needed to ground truth the flight data, the boat was launched on the previous high water at around midnight. The fast flowing currents and movements of the bed sediments made anchoring impossible. Therefore, the boat was moored to a

training wall marker-post at a position suitable for data acquisition during the flood tide the following morning.



**Plate 4.1** The boat used for fieldwork moored to the training wall, waiting for the flood tide. 20-7-97.

#### **4.2.1 The hypothesis of a relationship between suspended sediment concentration and adsorbed radionuclide concentration.**

##### **Experimental objective**

To date, most of the published data on radionuclide concentration in estuarine sediments are derived from the deposited sediment and the results vary between estuaries. It is not known if there is a relationship between SSC and the associated radionuclide concentration, or given its existence, whether this is temporally or spatially stable.

Therefore, to test the above hypothesis (see section 4.1) and establish the relationship, suspended sediment data were analysed for radionuclide concentration as detailed below.

### Methodology

On the 6<sup>th</sup> June 1996 the high water of 9.0m (Ordnance Datum Newlyn) was predicted for 1433 hours GMT (1533hrs BST). The boat, launched off Blackpool beach at 1200 noon (BST), entered the Ribble estuary with the incoming flood tide. Over the flood tide, twelve samples, each 10 litres in volume, were taken in wide necked bottles. The sample sites were located using a differential GPS as detailed in sections 3.4.1 and 3.4.2. The locations of each sample are given in table 4.1 and shown in figure 4.1.

Site No.	Easting	Northing	Site No.	Easting	Northing
1	340558	426491	7	340531	426502
2	340587	426422	8	340476	426424
3	340546	426513	9	340531	426548
4	340575	426451	10	340551	426422
5	340512	426526	11	340542	426493

**Table 4.1** The Ordnance Survey National Grid coordinates of the sample sites off Warton Bank, collected on the 6th June 1996.

The samples were stored in a refrigerated room in the dark until processing could be carried out, one month later. The samples were processed for analysis by gamma spectroscopy as detailed in section 3.5.3. To assess the temporal stability of any relationship between suspended sediment and radionuclide content, a further four 10 litre samples were taken during the acquisition of the remote sensing data, on the 20<sup>th</sup> July 1997. This was a comparable spring tide where high water was at approximately

1230 (BST) and at a height of 9.1m (ODN). These were processed using the same method as for the 6<sup>th</sup> June 1996, as detailed in section 3.5.3.

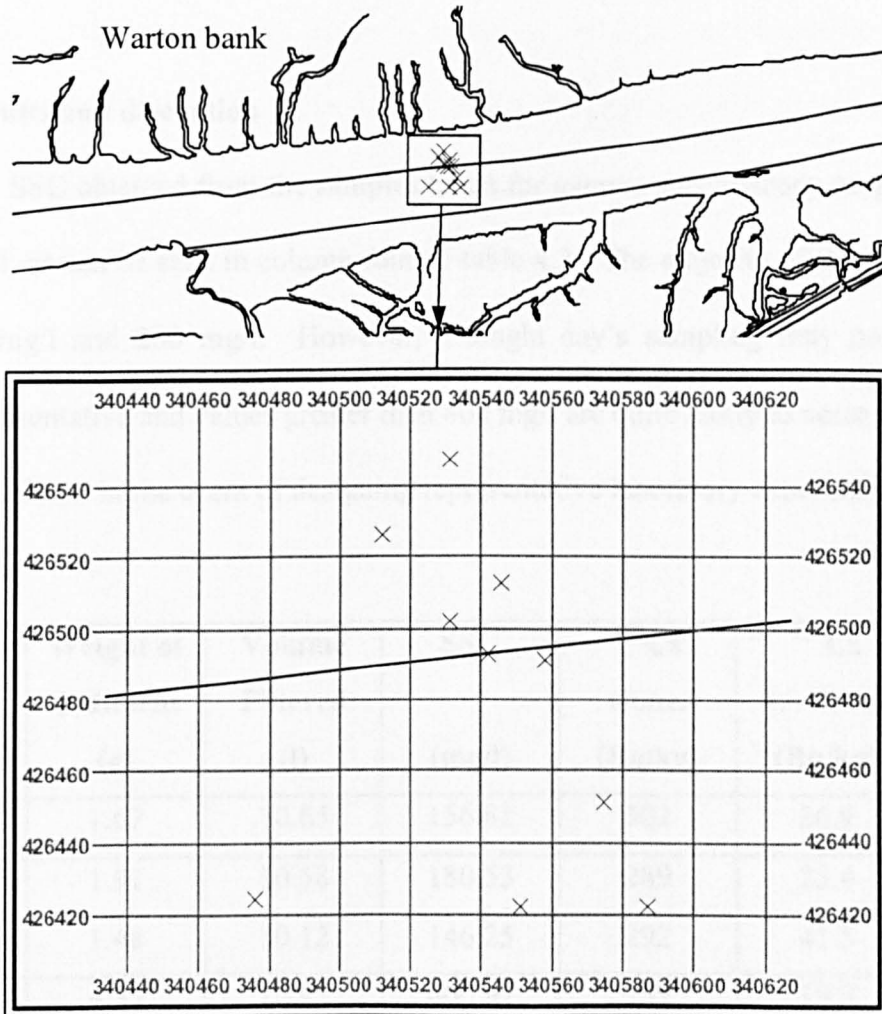


**Figure 4.1** The location of the 6<sup>th</sup> June 1996 samples sites relative to the training wall.

As suspended sediment data are expressed as mass per unit volume, the results of the gamma spectroscopy were then converted from Becquerels per kilogram (Bq/kg), (C), to Becquerels per litre (Bq/l), (L), using the sample volume and sediment weight as shown in equation [4.1].

$$L = \frac{CM}{V} \quad [4.1]$$

Where M is the mass of sediment in kilograms and V is the volume of the sample in litres.

### Results and discussion

The SSC obtained from the samples taken for gamma spectroscopy ranged from 30-400 mg/l, as can be seen in column four of table 4.2. The majority of the SSC fall between 30 mg/l and 200 mg/l. However, a single day's sampling may not be considered representative and values greater than 400 mg/l are quite likely to occur and this must be considered in the event of designing representative laboratory experiments.

Site No.	Weight of Sediment (g)	Volume Filtered (l)	SSC (mg/l)	<sup>137</sup> Cs Conc. (Bq/kg)	<sup>137</sup> Cs +/- Error (Bq/kg)	<sup>137</sup> Cs Conc. (Bq/l)
1	1.67	10.65	156.81	302	26.9	0.047
2	1.91	10.58	180.53	289	23.4	0.052
3	1.48	10.12	146.25	292	41.5	0.043
4	4.35	10.85	400.92	289	19.8	0.116
5	2.28	10.27	222.01	352	25.0	0.078
7	2.43	11.11	218.72	344	19.5	0.075
8	2.98	10.84	274.91	332	27.8	0.091
9	2.25	11.15	201.79	257	26.4	0.052
10	1.86	10.58	175.80	314	19.7	0.055
11	0.70	10.04	69.72	419	42.5	0.029
13	0.35	11.09	31.56	563	78.3	0.018

**Table 4.2** The SSC and associated <sup>137</sup>Cs activities, Warton Bank, 6<sup>th</sup> June 1996.

The radionuclide data from the gamma spectroscopy showed that only  $^{137}\text{Cs}$  was abundant enough to produce a complete data set. Other radionuclides were detected, such as  $^{214}\text{Pb}$ ,  $^{40}\text{K}$  and  $^{214}\text{Am}$  but each only in single samples. The concentration of  $^{137}\text{Cs}$  in Bq/l was plotted against the suspended sediment concentration as shown in Figure 4.2. It can be seen that there is a linear relationship between suspended sediment and radionuclide concentration. To this the 1997 data were added to show the temporal stability of the relationship. Thus, the first hypothesis has been shown to be correct.

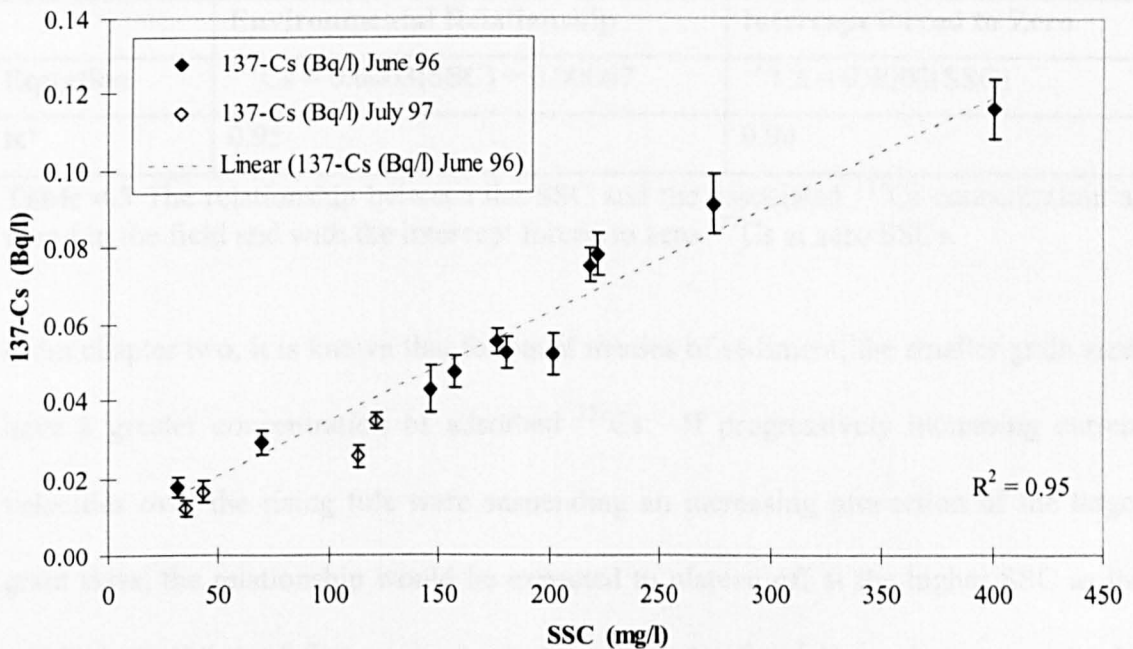


**Figure 4.2** The environmentally derived relationship between suspended sediment and the associated  $^{137}\text{Cs}$  concentration and its temporal stability.

Table 4.3 shows the relationship to have an intercept on the  $^{137}\text{Cs}$  axis of 0.00067 Bq/l, this implies that there is a surplus of 0.00067 Bq/l on the filter paper when there is zero suspended sediment. This is likely to be introduced as a result of sampling or analytical error. In these conditions it is anticipated that where there is no suspended sediment there would be no  $^{137}\text{Cs}$  activity present. To satisfy this condition the regression line

was forced through the origin. Table 4.3 shows that this forcing of the data through the origin has an almost inconsequential effect on the linearity of the relationship, as indicated by the good  $R^2$  value. If the intercept of 0.67mBq/l is not a result of analytical error then this suggests that some caesium is coming out of solution and binding to the filter paper. This is not unlikely as caesium has a higher solubility than most other radionuclides and the value of 0.67mBq/l is considered a value within the range expected (McDonald *pers comm.*).

	<b>Environmental Relationship</b>	<b>Intercept forced to Zero</b>
<b>Equation</b>	$^{137}\text{Cs} = 0.0003(\text{SSC}) + 0.00067$	$^{137}\text{Cs} = 0.0003(\text{SSC})$
<b><math>R^2</math></b>	0.95	0.94

**Table 4.3** The relationship between the SSC and the associated  $^{137}\text{Cs}$  concentration as found in the field and with the intercept forced to zero  $^{137}\text{Cs}$  at zero SSCs.

From chapter two, it is known that for equal masses of sediment, the smaller grain sizes have a greater concentration of adsorbed  $^{137}\text{Cs}$ . If progressively increasing current velocities over the rising tide were suspending an increasing proportion of the larger grain sizes, the relationship would be expected to plateau off at the higher SSC as the relative proportion of fine grain sizes, per unit mass of sediment, decreases. As the relationship is linear with no apparent change in gradient at the higher SSC it suggests that the composition of the sediment with respect to grain size must be relatively uniform irrespective of current velocity for the range of velocities measured during this sampling period.

There are a further four points on the graph in Figure 4.1 that were collected in 1997 approximately twelve months after the main data set, on a comparable spring tide of

9.1m height above Ordnance Datum Newlyn (ODN). These were collected to examine whether the relationship was temporally stable. It can be seen from Figure 4.2 that the 1997 data points are in agreement from those of the 1996 data. This indicates that the relationship is temporally stable, at least within a time-scale of two years. The four points form a single check on temporal stability, whilst not conclusive given the limited range of suspended sediment (0-120 mg/l), show that the deviation from the 1996 derived values is clearly minimal.

## **4.2.2 Grain size**

### **Experimental objective**

The grain size of the suspended sediment is one of the most important controlling factors for radionuclide concentration, sediment transport and reflectance as can be seen from chapter 2. Thus, the data presented below were collected to investigate the spatial and temporal variations that occur in grain size during a flood tide.

### **Methodology**

Samples for sediment grain size were collected on three occasions during 1996. The first set was collected on the 6<sup>th</sup> June 1996 off Warton bank over a rising tide to examine how the sediment grain size varies temporally for a small area. These were collected concurrently with the radionuclide data presented in section 2.2.1 by varying the sampling either side of the axial convergence front, which forms during the flood tide. The second and third samples sets were collected on the 3<sup>rd</sup> and 4<sup>th</sup> of August 1996 to examine the spatial variation of suspended sediment grain size. The samples were collected following a route which ran in an Easterly course from Warton Bank (1) to the confluence (2) with the River Douglas and then from Bull Nose Point (3) at Preston

Docks in a Westerly direction back towards the confluence of the Ribble and Douglas (4). This was done to ensure that the samples were collected from both fresh and saline waters giving the maximum possible variations in sediment properties. A simplified diagram of the sampling route taken is shown in Figure 4.3.

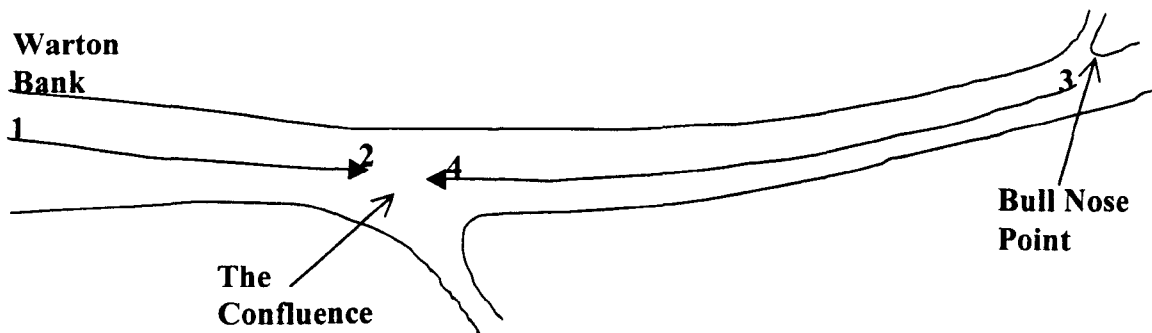


**Figure 4.3** The longitudinal sampling regime used on the 3<sup>rd</sup> and 4<sup>th</sup> August 1996.

### **Results and discussion**

The sediment grain size data for three different days are given in detail in appendix B and represented graphically in Figure 4.4. It can be seen that for all four data sets the clay and silt fractions, that less than 63 $\mu$ m, dominate the suspended sediment, however it is the clay fraction that plays an important role in the transport of radionuclides. Therefore the basic descriptive statistics for the %clay fraction of each data set are given in table 4.4.

From these it can be seen that the data collected on the 6<sup>th</sup> June 1996 has the highest variability of percent clay, yet we know that for this data set the relationship between suspended sediment and <sup>137</sup>Cs concentrations is very linear. It can then be suggested that the data sets for which the variability in percent clay is low are also likely to be linear.

Sample Date	6/6/96	3/8/96	4/8/96	20/7/97
No. of samples	11	15	12	23
Mean (%)	6.44	7.70	7.45	3.13
Minimum (%)	3.62	5.96	5.47	1.55
Maximum (%)	13.45	11.68	10.93	4.70
Standard Deviation	3.83	1.38	1.754	0.77
Standard Error	1.15	0.36	0.51	0.16
CV (%)	59.47	17.91	23.53	24.71

**Table 4.4** The basic descriptive statistics for the %clay fractions (<2 $\mu$ m) of the four grain size distribution data sets.

To statistically assess whether the four data sets are of similar composition with respect to percent clay content, the data were first tested for normality using the Anderson-Darling normality test. The results showed that the distributions of the percent clay data were normal for the data collected on the 4<sup>th</sup> August 1996 and 20<sup>th</sup> July 1997 but were not normal for the data collected on the 6<sup>th</sup> June and the 3<sup>rd</sup> August 1996. Thus, non-normality was assumed for all the data so that all four sets could be compared using a Kruskal-Wallis test, the non-parametric equivalent of the ANOVA. The output of the Kruskal-Wallis test showed that the data came from different populations. To investigate the differences between each data set a “Multiple Comparison between Treatments” test was performed using the outputs from the Kruskal-Wallis test. The results showed that it was the fourth data set, collected on the 20<sup>th</sup> July 1997 during the remote sensing flights, which appeared to come from a different population. Despite the apparent singularity of the data set from the 20<sup>th</sup> July 1997 it is interesting to note that in Figure 4.2 the four data points collected on this day still lie on the straight line of the suspended sediment-<sup>137</sup>Cs concentration relationship derived on the 6<sup>th</sup> June 1996.

Thus, it can be said that the 20<sup>th</sup> July 1997 data set being from the different sediment population has a negligible effect on the relationship between SSC and <sup>137</sup>Cs.

It is known that the suspended sediment reflectance relationship is also sensitive to grain size changes. As the composition of the sediment as a whole is dominated by the smaller grain size fractions it is assumed that the reflectance of the sediment will remain relatively proportional to the SSC. This will be investigated in sections 4.3.3 and 4.3.4. There appears to be a noisy trend of decreasing sand content and increasing silt content on Figure 4.4c, however, the clay content, the primary cause of light scatter, remains more constant. Any variation in grain size of the suspended sediment throughout the rising tide will be dependent on factors such as local sediment sources and current velocities, which cannot be predicted accurately. Variations such as this could not be corrected for in a suspended sediment-reflectance algorithm on a pixel by pixel basis. Thus, the suspended sediment grain size is assumed to be spatially and temporally constant over the rising tide.

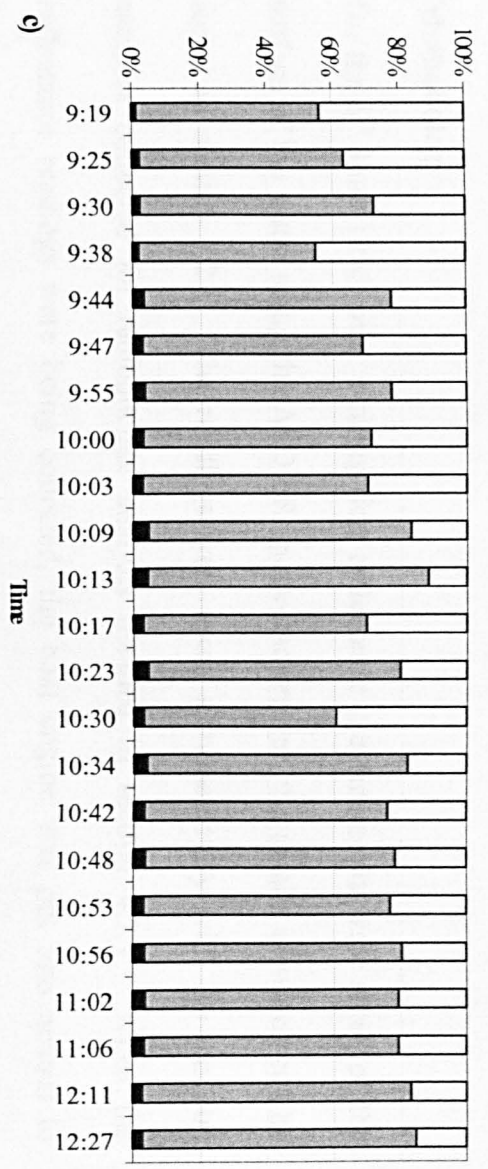
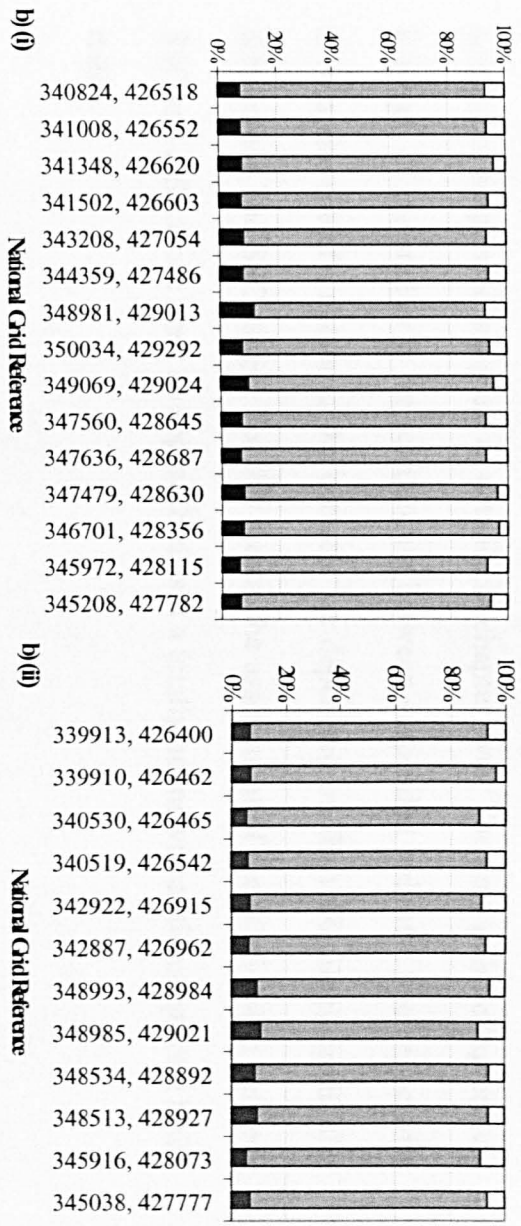
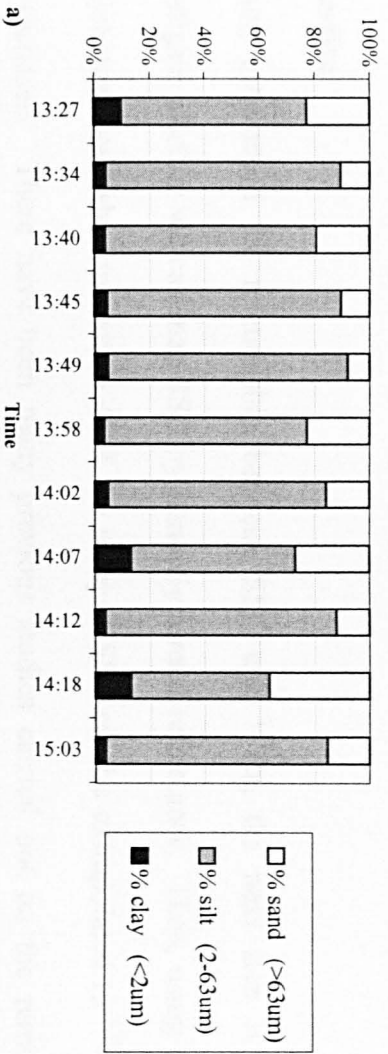


**Figure 4.4** The grain size distributions for the suspended sediment of the Ribble estuary. a) Temporal variations off Warton Bank, 6-6-96, approximate grid reference 340520, 426480. b) Spatial variations for the whole estuary, b)(i) 3-8-96 and b) (ii) 4-8-96. c) Temporal variations off Warton Bank, 20-7-97, approximate grid reference 340520, 426480.

### **4.2.3 The *in-situ* reflectance of suspended sediment**

#### **Objective**

Having established the relationship between SSC and  $^{137}\text{Cs}$ , the next step is to investigate whether we can map SSC by remotely sensed reflectance. Then, using the relationship established in section 4.2.1 the mapped SSC can be extrapolated to  $^{137}\text{Cs}$  concentration. There have been many previous studies carried out on the remote sensing of suspended sediment as detailed in chapter two. The only point of agreement between all the studies is the relationship between suspended sediment and reflectance is of a site specific nature as the controls are dependent on the mineralogy, grain size distribution and SSC range. For this reason the assessment of the relationship between SSC and reflectance must be approached as if a totally unknown relationship were being tested.

#### **Methodology**

On the 6<sup>th</sup> June 1996, over a rising tide, reflectance measurements were taken of the surface of the water using the ASD FR spectroradiometer, the details of which can be found in section 3.2.1. The readings were taken simultaneously with the ten litre samples collected for radionuclide analysis detailed in section 4.2.1. When the reflectance readings were being collected, the boat engine was put into neutral to minimise the amount of surface disturbance produced by the bow wave. The reflectance readings were taken from the rear port quarter of the boat, as far out from the boat as the ASD FR fibre-optic cable (section 3.2.1) would allow and with the spectrometer head at nadir approximately 50cm above the surface of the water. The sample locations were the same as those for the radionuclides presented in Figure 4.1 and table 4.1. The

reflectance spectra were processed as detailed in section 3.2.2 to obtain continuous spectra and then into a selection of possible CASI bandwidths.

### Results and discussion

Figure 4.5 shows three of the continuous ASD reflectance spectra for wavelengths 400nm to 1000nm. The reflectance increases from 400nm to 600nm where it either plateaus off or decreases slightly before the chlorophyll absorbance feature at around 685nm is observed. The reflectance is increased slightly around 800nm to 840nm, after which the reflectance decreases steadily. Above 950nm the spectra become very noisy, limiting the useful spectral data to below 920nm.

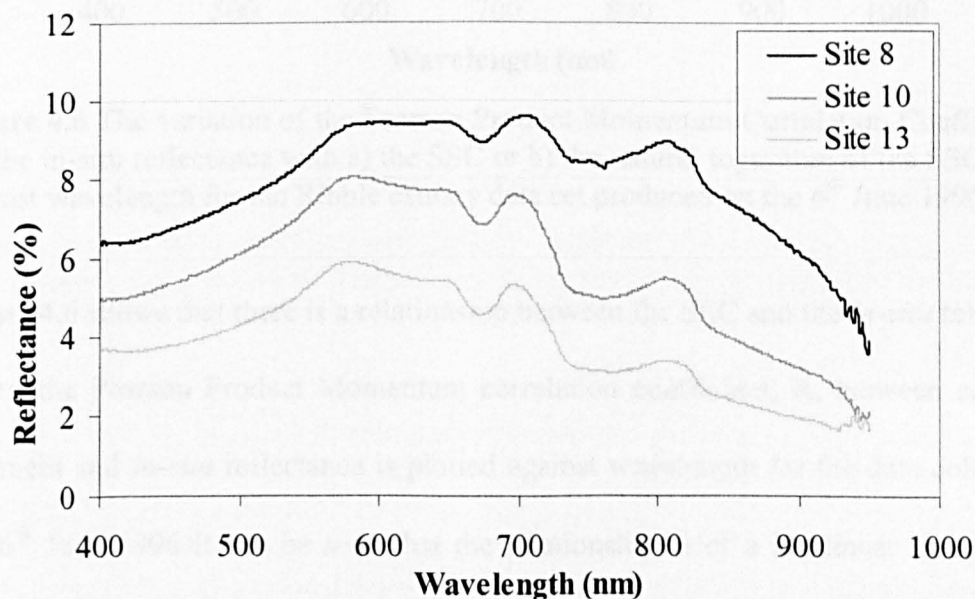


**Figure 4.5** A selection of continuous reflectance spectra of the Ribble estuary, 6<sup>th</sup> June 1996. Sites 8,10 and 13 correspond to SSC of 275 mg/l, 176 mg/l and 32 mg/l respectively

It can be seen from Figure 4.5, across the whole wavelength range, reflectance increases with SSC. Thus, theoretically, reflectance at all wavelengths may correlate well with the SSC. However, as detailed in section 2.5.2, it is known that at wavelengths below 700nm there can be interference in the suspended sediment reflectance correlation from

the dissolved constituents of the water column such as chlorophyll and Gelbstoff (Bale *et al.*, 1994, Hudson *et al.*, 1994).

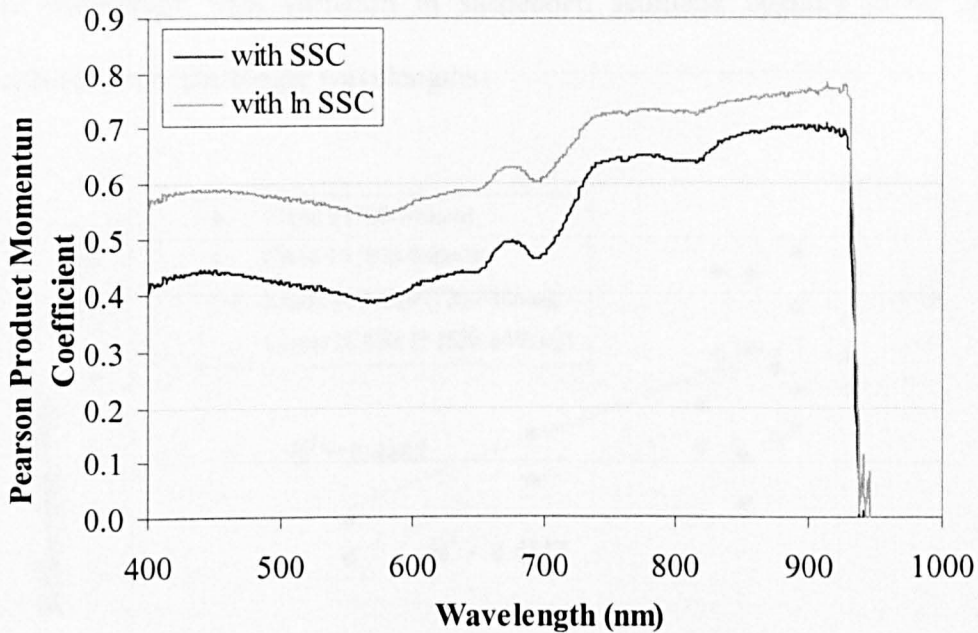


**Figure 4.6** The variation of the Pearson Product Momentum Correlation Coefficient, R, for the in-situ reflectance with a) the SSC or b) the natural logarithm of the SSC, plotted against wavelength for the Ribble estuary data set produced on the 6<sup>th</sup> June 1996.

Figure 4.6 shows that there is a relationship between the SSC and the *in-situ* reflectance. When the Pearson Product Momentum correlation coefficient, R, between suspended sediment and *in-situ* reflectance is plotted against wavelength for the data collected on the 6<sup>th</sup> June 1996 it can be seen that the relationship is of a log-linear nature as this produces the higher correlations at all wavelengths. All log-linear correlations are significant ( $p < 0.05$ ) but the correlation increases rapidly after 700nm and is at a maximum between 800nm and 900nm. The correlation being higher at the longer wavelengths is most likely due to the absence of interference due to chlorophyll and Gelbstoff as mentioned above.

Figure 4.7 shows the log-linear relationships at two different wavelengths from the region of the higher correlations. The graphs illustrate clearly that although the  $R^2$  value and the amount of scatter within the sample points may vary, the actual rate of increase of reflectance with variation in suspended sediment appears to be approximately constant over the longer wavelengths.

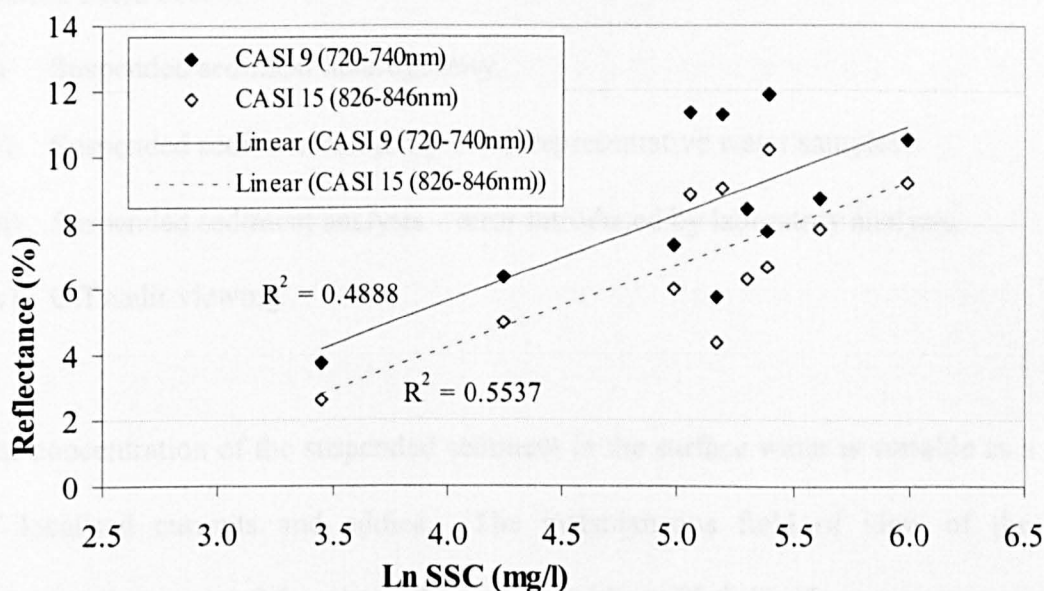


**Figure 4.7** The in-situ relationship between the natural logarithm of the SSC and *in-situ* reflectance at two possible 20nm wide CASI bands, for the Ribble estuary 6<sup>th</sup> June 1996.

The data used in Figure 4.7 had been processed into possible CASI bands using an averaging method as described in section 3.2.2 and 4.3.7. The correlation coefficient,  $R$ , of the relationship is comparable with those of other field-based studies. For example, two studies in Swansea Bay using ATM wavelengths, by Collins and Pattriachi (1984) and Rimmer *et al.* (1987), achieved correlation coefficient values,  $R^2$ , of 0.42 and 0.62 respectively using logarithmic-linear regression techniques. The second study by Rimmer *et al.* (1987) improved the correlation by including salinity in the regression equation. This method is unlikely to improve the regression results for the Ribble estuary as it is shown in section 4.3.5 that salinity has no systematic effect on the

reflectance of a given SSC. Other studies, such as Tassan (1994), comment that CASE II waters, that is those containing significant amounts of suspended sediment, are poorly correlated.

The scatter within the *in-situ* relationship could be introduced from a variety of possible sources listed below.

- (i) Suspended sediment heterogeneity.
- (ii) Suspended sediment sampling – non-representative water samples.
- (iii) Suspended sediment analysis – error introduced by laboratory analysis.
- (iv) Off nadir viewing.

The concentration of the suspended sediment in the surface water is variable as a result of localised currents and eddies. The instantaneous field of view of the ASD spectroradiometer at 0.5m above the surface with an 8° field of view is approximately 38.4 cm<sup>2</sup>. Within that area, the SSC may not vary greatly; the variation is likely to be greater between subsequent spectra. It can be assumed that this variability in SSC between subsequent spectra will be randomly distributed around an average value and that overall the scatter introduced from this source will be negligible as all data were taken from an average of ten replicate spectra. The sampling and analysis of suspended sediment is another possible source of scatter. The sampling and analysis methods used are recorded in chapter three, section 3.5.1. For the ground truthing data, collected simultaneously with the remote sensing data, sample replicates will be used to assess this possible source of error.

It is likely that the main source of scatter within the SSC reflectance relationship is a result of off nadir viewing caused by the movement of the water surface due to ripples. It is known that the strength of the relationship is reduced by off nadir viewing (Ferrier, 1995) and that although the spectrometer head is at nadir the surface of the water is never exactly horizontal. When the area viewed by the spectrometer is as small as 38.4 cm<sup>2</sup> this movement of the water will have a considerable effect on changing the apparent viewing angle. This will introduce a large amount of scatter into the *in-situ* reflectance data and is most likely the main cause of the scatter evident in the data presented in Figure 4.7. However, when the relationship between SSC and reflectance is considered on a scale of a 2.5m by 2.5m pixel, this effect will be reduced, as the effect of a ripple measured from a height of 1500m over such a large scale will be minimal.

#### **4.2.4 Summary and conclusions**

The preliminary *in-situ* work on the Ribble estuary confirmed the first hypothesis, that there was a relationship between the SSC and the associated radionuclide concentration. Extra data points taken approximately twelve months after the initial data showed the temporal stability of the relationship. This suggests that the SSC, derived from remotely sensed data, can act as a surrogate of the <sup>137</sup>Cs concentration. The grain size data showed that the suspended sediment of the estuary was dominated by the <63µm fraction and that the spatial and temporal variations are minimal. The relationship between *in-situ* reflectance and SSC is of a log-linear nature but is subject to some scatter.

The relationship between *in-situ* reflectance and SSC is not as well defined as initially hoped, therefore further laboratory work is needed to achieve a greater confidence in the

relationship. It is necessary to understand the dependence of the SSC reflectance relationship on the possible natural variables such as grain size and salinity.

### **4.3 A LABORATORY ANALYSIS OF THE CONTROLS ON THE SUSPENDED SEDIMENT REFLECTANCE RELATIONSHIP**

#### **Introduction**

As a result of the scatter in the *in-situ* SSC reflectance relationship, shown in Figure 4.7, laboratory work was performed to determine the exact nature of the relationship and the influence of grain size in a controlled environment. Firstly, the equipment was designed and the behaviour of sediments in the apparatus tested. Secondly, spectral experiments were used to examine each of the possible variables for which previous studies do not exist, such as clay content, contribution of the larger grain sizes and salinity.

#### **4.3.1 Design and testing of the experimental apparatus**

##### **Objective**

A controlled environment must be created that is representative of the natural environment in which the *in-situ* measurements are being taken. The suspended sediment in the tank must be evenly distributed to accurately represent SSC produced by adding a known amount of sediment. Thus, the spatial variability across the surface and with depth is examined to see how the sediment is distributed throughout the water after stirring. The settling rate of the sediment after stirring stops is determined to assess the time limit in which representative spectra can be taken.

## Methodology

The laboratory apparatus consisted of a black plastic cistern-expansion tank and a paddle for manual stirring. The tank was sanded to give a non-reflective matt finish inside and the paddle was coated with matt black paint so that it could be pulled out of the field of view of the spectrometer but left in the tank during the experiments. The basic laboratory apparatus is shown in Figure 4.8.

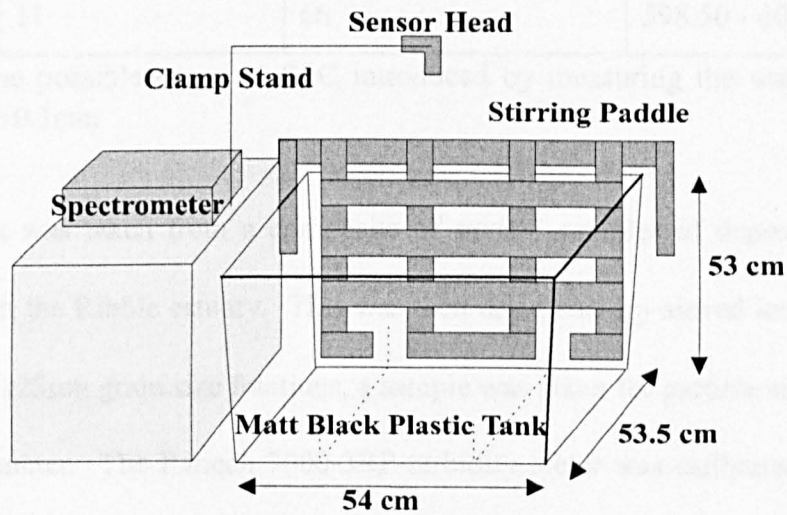


**Figure 4.8** The arrangement of the laboratory apparatus

The tank was carefully filled with exactly 110 litres of tap-water and the depth at the centre of the tank was noted as 40cm, a depth considered adequate for high SSC in a study by Mantovani and Cabral (1992). Therefore, in future the tank could be filled to a known depth rather than measuring out water by the litre. The error introduced by measuring the depth to  $\pm 0.1\text{cm}$  was calculated at 0.5% and the possible range for each proposed SSC is detailed in table 4.5.

SSC. (mg/l)	Mass of Sediment Added (g)	Cumulative Mass of Sediment Added (g)	SSC range at $\pm 1$ mm depth (mg/l)
0	0	0	0
50	5.5	5.5	49.88 - 50.13
100	5.5	11	99.75 - 100.25
200	11	22	199.50 - 200.50
300	11	33	299.25 - 300.75
400	11	44	399.00 - 401.00
500	11	55	498.75 - 501.25
600	11	66	598.50 - 601.50

**Table 4.5** The possible errors in SSC introduced by measuring the water volume to 40cm depth  $\pm 0.1$ cm.

The sediment was taken from a composite of several samples of deposited estuarine sediment from the Ribble estuary. This was then dried and dry sieved into  $<63\mu\text{m}$ , 63-125 $\mu\text{m}$  and  $>125\mu\text{m}$  grain size fractions, a sample was taken for particle size analysis by laser-granulometer. The Partech 7000-3RP-turbidity meter was calibrated to 500 FTU as detailed in section 3.5.4.

The maximum SSC found during the June 1996 fieldwork was 400 mg/l and it was estimated that the SSC was unlikely to exceed 600 mg/l during ground truthing of the flight data. Thus, 66g of  $<63\mu\text{m}$  sediment was added to the tank to give a concentration of 600 mg/l. It was found that the best way to add the sediment to the tank was in the form of slurry rather than as a dry powder, which tended to float and form lumps.

The surface was visually divided up into twelve points using a 3x4 grid. The tank was stirred until a constant turbidity was reached and this value noted as approximately 40% deflection on the turbidity meter. Immediately after stirring ceased the turbidity meter

head was placed at point one, at 5cm depth, and readings taken after 0, 5, 10, 15, 20, 30, 40, 50, 60, 80 and 100 seconds. This was repeated five times and the turbidity meter calibration checked after each set of five readings. This was then repeated for points two to twelve. Five sets of readings were also taken for a single point at the centre of the tank at depths of 15cm and 35cm.

## **Results and discussion**

The results, in percent deflection, were first converted to formazin turbidity units (FTU) using the calibration curve,  $FTU = 5.3875 * (\% \text{ deflection})$  with an  $R^2$  of 0.99. The five replicates were then combined to give an average data set.

### ***Spatial Variability***

The spatial variability was examined using the coefficient of variation of the twelve averaged surface points measured at 5cm depth, the results of which are shown in table 4.6. It can be seen that the variability across the surface is between 4.0 and 5.1 percent, increasing with time after stirring ceases. This was considered acceptable and within the expected experimental error.

<b>Time (s)</b>	<b>Mean of 12 Points (FTU)</b>	<b>StDev of 12 Points (FTU)</b>	<b>CV (%)</b>
<b>0</b>	232.38	9.65	4.15
<b>5</b>	231.35	9.62	4.16
<b>10</b>	229.87	9.97	4.34
<b>15</b>	226.99	9.62	4.24
<b>20</b>	226.36	9.11	4.02
<b>30</b>	221.20	10.59	4.79
<b>40</b>	217.74	9.92	4.55
<b>50</b>	213.66	9.94	4.65
<b>60</b>	209.98	8.93	4.25
<b>80</b>	203.78	10.26	5.04
<b>100</b>	197.59	10.10	5.11

**Table 4.6** The surface variability in turbidity of the experimental apparatus.

### ***Depth Variability***

The same analysis techniques used for surface variability were used to assess the variability with depth, the results are shown in table 4.7. It can be seen that between the three depth measurements the variability is in the range 1.15-4.67 % and this increases with time as the sediment starts to settle. If spectra are taken within a specified time after stirring stops, for example twenty seconds, the variability in SSC with depth can be said to be less than 2%.

Average values of the five replicate data sets (FTU)						
Time	5cm depth	15cm depth	35cm depth	Mean	StDev	CV (%)
0	232.4	227.4	234.9	231.5	3.84	1.66
5	231.3	228.4	233.8	231.2	2.70	1.17
10	229.9	226.3	232.2	229.4	2.99	1.30
15	227.0	226.3	231.1	228.1	2.62	1.15
20	226.4	223.0	230.0	226.5	3.50	1.55
30	221.2	218.2	225.7	221.7	3.80	1.71
40	217.7	215.0	221.4	218.0	3.24	1.49
50	213.7	210.7	222.0	215.4	5.86	2.72
60	210.0	207.4	216.6	211.3	4.73	2.24
80	203.8	207.4	215.5	208.9	6.00	2.87
100	197.6	210.7	216.6	208.3	9.72	4.67

**Table 4.7** The variability of the turbidity with depth.

#### *Settlement with Time*

Time	% change 5cm depth	% change 15cm depth	% change 35cm depth
0	0.00	0.00	0.00
5	-0.44	0.47	-0.46
10	-1.08	-0.47	-1.15
15	-2.32	-0.47	-1.61
20	-2.59	-1.90	-2.06
30	-4.81	-4.03	-3.90
40	-6.30	-5.45	-5.73
50	-8.06	-7.35	-5.50
60	-9.64	-8.77	-7.80
80	-12.31	-8.77	-8.26
100	-14.97	-7.35	-7.80

**Table 4.8** The settlement of the suspended sediment with time at depths of 5cm, 15cm and 35cm expressed as a percentage change of the t=0 measurement in FTU.

From the above results it can be seen that the sediment does settle as the turbidity decreases with time at all depths. The rate at which the sediment settles determines a time limit within which representative spectra can be taken.

From table 4.8 it can be seen that the percent decrease in turbidity is less for the measurements taken at 15cm and 35cm depth. This is due to there being a secondary source of sediment as it settles from above, in addition to the sediment sink due to settling. The surface measurements at 5cm depth only represent a sediment sink, thus the percentage decrease with time appears greater. To take representative spectral measurements the spectra must be collected before the SSC decreases due to settling. If we set a limit of less than 2% change in turbidity as an acceptable error, which is not excessive considering the surface and depth variability discussed above, it can be seen that all replicate spectra must be collected within 10 seconds of the stirring ceasing. It is well within the capabilities of the ASD spectroradiometer to collect ten spectra during ten seconds, however, the GER1500 spectroradiometer will require the spectra to be taken as two sets of five spectra with stirring in between.

### **4.3.2 The suspended sediment reflectance relationship**

#### **Objective**

The first objective with regard to assessing the laboratory relationship between SSC and reflectance is to examine the form of the relationship and the SSC range over which it is sensitive.

## **Methodology**

The sediment was prepared from a composite of samples of deposited estuarine sediment from the Ribble estuary. This was then dried, dry sieved and the  $<63\mu\text{m}$  fraction was used. The smaller grain size fraction was used for two reasons, firstly the suspended sediment of the Ribble estuary is predominantly  $<63\mu\text{m}$  and secondly the smaller grain sizes are easier to maintain in suspension. A sub-sample of this composite sediment was taken for particle size analysis by laser-granulometer.

The experimental tank was placed on a trolley and filled with 110 litres of water, to a depth of  $40\text{cm} \pm 0.1\text{cm}$ . The spectroradiometer was placed level with the rim of the tank and the spectrometer head positioned centrally over the tank at nadir, 40cm above the surface of the water. Sediment was weighed out in quantities as detailed in column two of table 4.5, to give cumulative SSC of 0, 50, 100, 200, 300, 400, 500 and 600 mg/l. The entire apparatus was then wheeled outside and away from the buildings to utilise the natural light. The ASD spectroradiometer is sensitive to the 50Hz cycles of mains operated lighting, effectively ruling out the use of an indoor artificial light source. The conditions were bright but overcast giving diffuse lighting. Prior to adding any suspended sediment, a reference panel spectrum was taken, the tank was then briefly stirred and ten spectra collected for 0 mg/l.

The first pre-weighed sediment sample was mixed to slurry with water from the tank. The slurry was then added to the tank and stirred vigorously for one minute to ensure that all the sediment was in suspension. A reference panel spectrum was taken and the tank stirred for a further 30 seconds. Immediately after stirring the ten spectra were collected for the 50 mg/l suspended sediment concentration. This process was then

repeated for each pre-weighed sediment sample up to the 600mg/l concentration. The raw spectra were then processed, as detailed in section 3.2.2, to continuous absolute reflectance spectra.

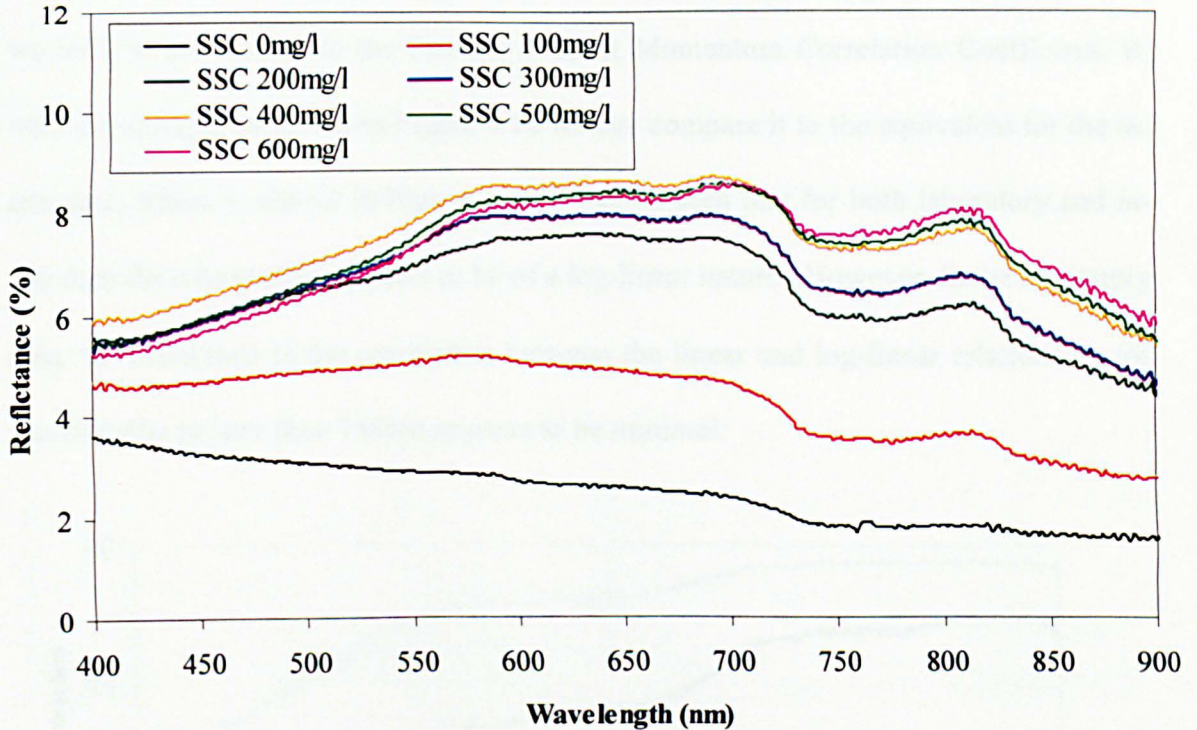
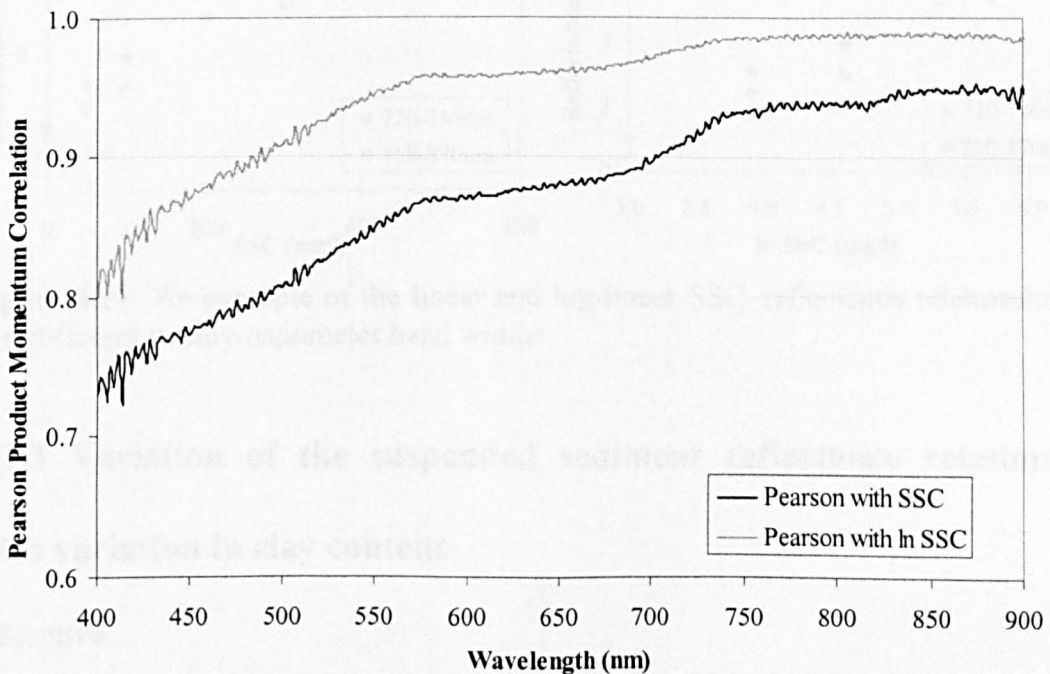


**Figure 4.9** The laboratory derived continuous reflectance spectra of a composite Ribble sediment, (91% <math> < 63\mu\text{m}</math>), using natural diffuse light.

## Results and discussion

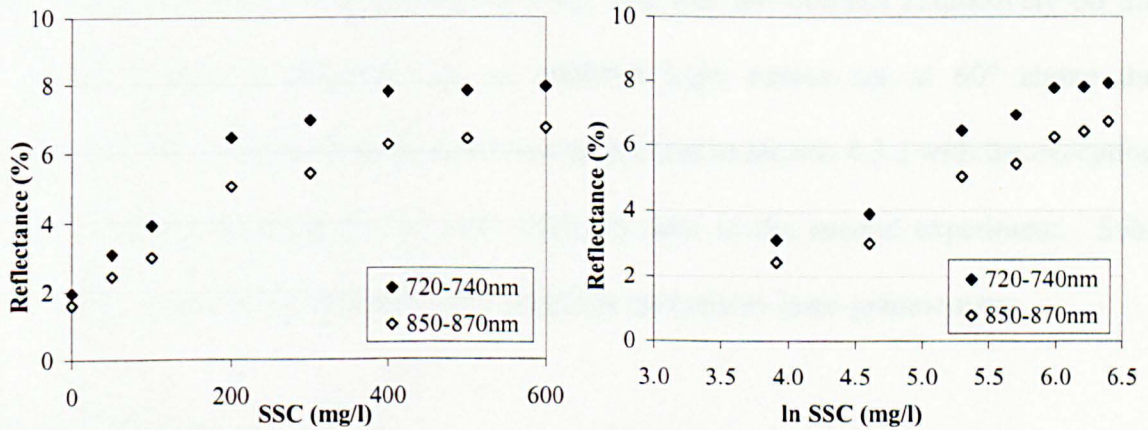
The laser-granulometer results for the composite sediment show the clay, silt and sand composition of 11.99%, 79.05% and 8.96% respectively, which is only slightly finer than can be expected in Ribble estuary suspended sediment. The spectral shape, shown in Figure 4.9, shows that the overall shape is the same as for the *in-situ* spectra but without the chlorophyll absorbance feature at approximately 685nm. This is to be expected, as phytoplankton would not survive the sediment drying, grinding and sieving processes.

Figure 4.9 shows that the percent reflectance increases with SSC for wavelengths greater than 700 nm. At wavelengths below 700nm the higher SSC are difficult to define, this is in agreement with Novo *et al.* (1991), who shows that the shorter wavelengths become insensitive to increases in SSC before the longer wavelengths. If we look at the change in the Pearson Product Momentum Correlation Coefficient, R, with wavelength as shown in Figure 4.10 we can compare it to the equivalent for the *in-situ* data, which is shown in Figure 4.6. It can be seen that for both laboratory and *in-situ* data the relationship appears to be of a log-linear nature. However, in the laboratory data, the difference in the correlation between the linear and log-linear relationship for wavelengths greater than 750nm appears to be minimal.



**Figure 4.10** The Pearson Product Momentum Correlation Coefficient, R, for the laboratory derived continuous spectra of a composite Ribble sediment, (91% <math>63\mu\text{m}</math>), using natural diffuse light.

The data were then averaged into possible CASI bands, of approximately 20nm width, to look at the rate of change of reflectance with SSC. An example of the shape of the relationship can be seen in Figure 4.11. It can be seen that the SSC reflectance relationship is initially linear but the rate of change starts to decrease around 250 mg/l, thus for a low SSC range it would be valid to use a linear relationship. After transformation of the suspended sediment data using natural logarithms the relationship is linear over the whole 0-600mg/l range, thus for higher SSC the log-linear relationship must be used.



**Figure 4.11** An example of the linear and log-linear SSC–reflectance relationship for two different twenty-nanometer band widths.

### 4.3.3 Variation of the suspended sediment reflectance relationship with variation in clay content

#### Objective

From chapter two it can be seen that the grain size has an effect on the suspended sediment reflectance relationship. It is known that the smaller grain sizes give a higher reflectance for a given SSC. The finer particles have a larger surface area to mass ratio and the clay particles have sheet like structures, which in dispersed suspensions align themselves with the water flow, largest surface uppermost. If variation in composition

were likely to have an overall effect on SSC reflectance relationship, it would be due to a variation within the clay fraction. Therefore, the effect of variation in the clay content of the suspended sediment on the relationship with reflectance needs to be investigated.

### Methodology

Three naturally occurring sediment samples were compared using the ASD spectroradiometer in natural diffuse light. In an attempt to increase the contrast in percentage clay content between samples, a second experiment was performed using a bulk sediment which was ground for zero, five and ten minutes respectively on the GER1500 spectroradiometer and an artificial light source set at 60° above the horizontal. The sediment preparation was as detailed in section 4.3.2 with the exception of the second grinding for the bulk sediment used in the second experiment. Sub-samples of each of the sediment were taken for analysis by laser-granulometry.

### Results and discussion

Sediment	% <2µm (Clay)	% 2-63µm (Silt)	% >63µm (Sand)
Composite	12.0	79.1	9.0
Warton Bank	15.5	75.1	9.3
Bulk	13.6	78.4	8.0
Bulk (ground 5 min.)	24.6	74.9	0.6
Bulk (ground 10 min.)	27.4	70.4	2.2

**Table 4.9** The grain size distribution of the Ribble sediments used to assess variation in the SSC-reflectance relationship with varying clay content.

Table 4.9 shows the grain size results of the laser-granulometry. It can be seen that the variation in clay content of the naturally occurring sediment is relatively small, the range being only 3.5%. For this reason the bulk sediment sample was mechanically ground to

increase the finer grain size fraction. The grinding process increased the  $<2\mu\text{m}$  content up to 24.6% and 27.4% after grinding for five and ten minutes respectively.

The experiments on the naturally occurring and ground sediments were performed at different times; thus the experimental set-up was slightly different. The natural sediment was examined under natural light using the ASD FR and the ground sediment examined under artificial light using the GER1500. As both the laboratory and field spectra were collected as reflectance, and thus standardised to a panel of known reflectance, the results will be comparable. However, any differences likely to be a result from the use of two different spectrometers and different lighting conditions are considered more fully in section 4.3.6. For the purpose of examining the variation in reflectance with changes in content of the  $<2\mu\text{m}$  fraction, the naturally occurring and ground sediments will be treated separately to eliminate any possible effect due to the change in spectrometer and illumination.

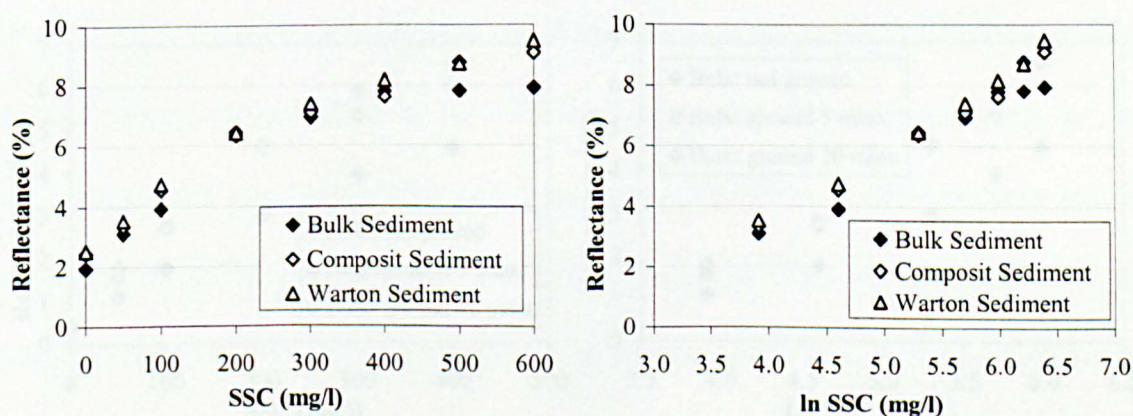


**Figure 4.12** The variation in the SSC reflectance relationship (720-740nm) with  $<2\mu\text{m}$  content for naturally occurring sediments using natural diffuse light.

Figure 4.12 shows that the suspended sediment reflectance relationship is not affected by a variation in clay content for low SSC. As the SSC increases the relationships start to diverge. Looking at the linear-linear relationship shown in the left hand graph, it can

be seen that it is the sediment with the lowest  $<2\mu\text{m}$  content (bulk) whose reflectance starts to become insensitive to the increasing SSC first. As expected, it is the sediment with the highest  $<2\mu\text{m}$  content that gives the highest reflectance and the best sensitivity in the reflectance SSC relationship.

As stated previously, the range of the variation in  $<2\mu\text{m}$  content of the naturally occurring sediments is very small so the range of  $<2\mu\text{m}$  contents was artificially increased using mechanical grinding. The naturally occurring “bulk” sediment was measured again as a different spectrometer was used and the measurements were then repeated using the ground sediments. Comparing Figures 4.12 and 4.13 it can be seen that the absolute reflectance measurements are not identical, 400 mg/l of the raw bulk sediment gives reflectances of 7.8% and 4.5% for the ASD and GER1500 spectrometers respectively. The possible reasons for this are discussed in section 4.3.6.

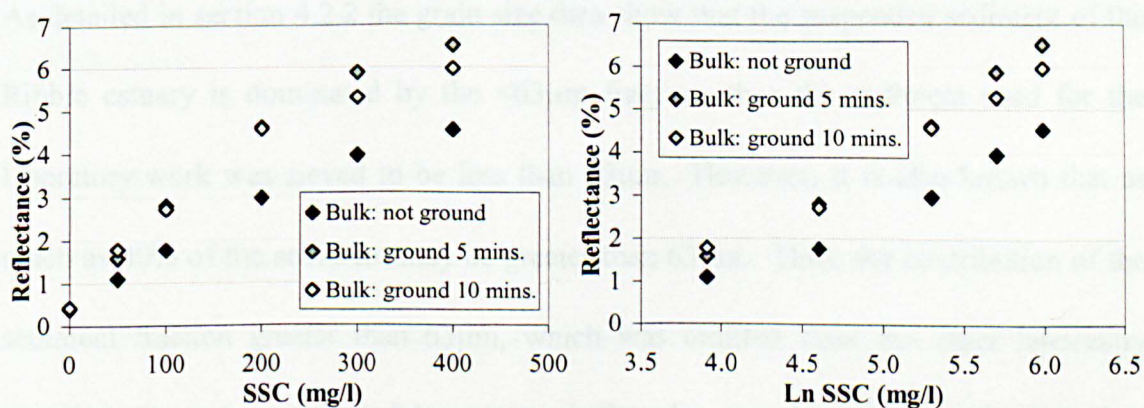


**Figure 4.13** The variation in the SSC reflectance relationship (720-740nm) with  $<2\mu\text{m}$  content for ground sediment using an artificial light at  $60^\circ$  above the horizontal.

Figure 4.13 shows that, as expected, the mechanically ground sediments with the higher  $<2\mu\text{m}$  content give a much higher reflectance than the naturally occurring sediment.

However, this is not a systematic increase in reflectance with increase in  $<2\mu\text{m}$  content as would be expected. The SSC reflectance relationships of the two mechanically ground sediments start to diverge at concentrations greater than 200 mg/l, however, the sediment with the higher  $<2\mu\text{m}$  content gives the slightly lower reflectance, contrary to expectation. It suggests that this divergence of the suspended sediment reflectance relationships may not be a systematic feature related to the percentage of the sediment less than  $2\mu\text{m}$  but more an indication of the limitations of the relationship. It may be that at higher SSC the relationship with reflectance is less reliable and more susceptible to analytical errors. This is something that must be considered should the SSC sampled during ground truthing of the remote sensing data collection exceed 250 mg/l.

#### **4.3.4 The suspended sediment reflectance relationship of the 63-125 $\mu\text{m}$ size fraction**

##### **Objective**

As detailed in section 4.2.2 the grain size data show that the suspended sediment of the Ribble estuary is dominated by the  $<63\mu\text{m}$  fraction, thus the sediment used for the laboratory work was sieved to be less than  $63\mu\text{m}$ . However, it is also known that as much as 40% of the sediment may be greater than  $63\mu\text{m}$ . Thus, the contribution of the sediment fraction greater than  $63\mu\text{m}$ , which was omitted from the other laboratory experiments, was investigated to assess whether the experiments using the less than  $63\mu\text{m}$  grain size fraction were truly representative of the reflectance from the *in-situ* estuarine sediments.

## Methodology

The composite sediment sample was processed and sieved as for the previous laboratory experiments, with the less than 63 $\mu$ m and the 63-125 $\mu$ m grain size fractions retained for use in this experiment. The experiment was performed using the ASD FR spectrometer using the experimental set-up as detailed in section 4.3.1 and semi-diffuse natural light. Sediment was added to the tank in the form of slurry in increments giving SSC of 50, 100, 200, 300, 400, 500 and 600 mg/l. Ten replicate spectra were collected of each SSC for the two grain size fractions.

## Results and discussion

Date	No. of samples	$\Sigma$ (% >63 $\mu$ m)	Average % >63 $\mu$ m
6/6/96	11	193.98	17.64
3/8/96	15	89.92	5.99
4/8/96	12	85.36	7.11
20/7/97	23	585.35	25.45
<b>Combined data</b>	61	954.61	15.65

**Table 4.10** The percentage of the sediment composition greater than 63 $\mu$ m expressed as the daily mean.

The average percentage of sediment that is greater than 63 $\mu$ m is detailed in table 4.10, with the average percentage of sediment which is greater than 63 $\mu$ m for the four data sets combined. It can be seen that the average percent of the suspended sediment that is greater than 63 $\mu$ m is approximately fifteen percent.

Figure 4.14a shows that the reflectance of the 63-125 $\mu$ m grain size fraction is markedly less than for the <63 $\mu$ m grain size fraction. The range of reflectance values between the 0mg/l and 600mg/l spectra are approximately 2% and 6% reflectance at 700nm for the

63-125 $\mu\text{m}$  and <63 $\mu\text{m}$  fraction respectively. Figure 4.14b is derived by normalising the baselines of Figure 4.14a, achieved by subtracting the 0mg/l spectra from the 600mg/l spectra for each grain size fraction. These are displayed as the upper and lower lines on Figure 4.14b

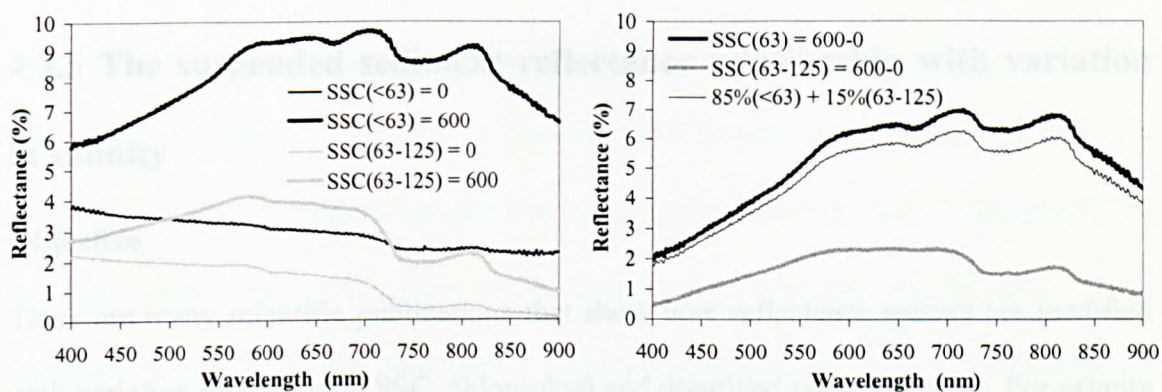


**Figure 4.14** a) The 0 mg/l and 600 mg/l spectra for the grain size fractions <63 $\mu\text{m}$  and 63-125 $\mu\text{m}$ . b) The normalised 600 mg/l spectra (600mg/l–0mg/l) for the grain size fractions <63 $\mu\text{m}$  and 63-125 $\mu\text{m}$  and the spectra which represents the in-situ suspended sediment consisting 85% of the <63 $\mu\text{m}$  plus 15% of the 63-125 $\mu\text{m}$ .

The central line displayed on Figure 4.14b is the derived spectrum representing the expected *in-situ* suspended sediment of the Ribble estuary. This is calculated as 85% of the reflectance from the <63 $\mu\text{m}$  fraction and 15% of the reflectance from the 63-125 $\mu\text{m}$  fraction. It can be seen that the spectral shape remains unchanged and the spectral reflectance values are only slightly less than for just the <63 $\mu\text{m}$  grain size fraction. If expressed as a percentage of the <63 $\mu\text{m}$  spectra, the reduction in reflectance due to the addition of 15% 63-125 $\mu\text{m}$  sediment ranges from 9.0% to 12.3%, for wavelengths 536nm and 892nm respectively.

This leads to the conclusion that, despite the larger grain sizes being omitted from the laboratory experiments for purely practical reasons, as the smaller grains are easier to keep in suspension for longer, the results of these experiments are still representative of

the suspended sediments of the Ribble estuary. The 9-12% error introduced in the absolute reflectance values as a result of the omission of the larger grain size fraction will not be introduced into the calibration of the imagery, as the calibration will be achieved using ground truth data and not laboratory derived values.

#### **4.3.5 The suspended sediment reflectance relationship with variation in salinity**

##### **Objective**

There are many scientific publications that show how reflectance spectra are modified with variation in grain size, SSC, chlorophyll and dissolved organic matter. For salinity there are numerous references to a study by Khorram (1982) in which the salinity of the San Francisco Bay delta is mapped. However, there are no laboratory-derived illustrations of how reflectance varies with a change in salinity. The objective of the following experiment is to show how a variation in the density of the water due to salinity affects reflectance.

##### **Methodology**

The bulk sediment sample obtained from the Ribble Estuary was processed as for section 4.3.1 and the <63 $\mu$ m grain size fraction used. The GER1500 spectrometer and the 1000W-video lamp were used. The artificial light source was orientated at 60° above the horizontal plane. For these experiments the SSC was kept constant at 0, 100, 200, 400 and 600mg/l and for each sediment concentration the salinity was varied through the 0‰ to 30‰ range in approximately 5‰ increments. The increments of salt

were added to the tank and stirred vigorously until completely dissolved before spectral measurements commenced.

The required salinity was achieved using sodium chloride (NaCl). Seawater contains many individual constituents and is difficult to replicate accurately. Artificial seawater can be purchased but would be expensive when used in such large quantities. The salinity of seawater is most likely to have an effect on the reflectance spectrum due to the changing density; this can be achieved using sodium chloride alone. The quantity of salt that would need to be added to the tank to give a salinity of 5‰ was crudely calculated using the known relationship of salinity being 1.807 times the chlorinity, or concentration of the halide ions, (Open University 1989). Thus five parts per thousand salinity requires 2.77 parts per thousand of chloride ions. Using the atomic masses of the chloride ion and sodium chloride as 35.5 and 58.5 respectively, 2.77 parts per thousand chlorinity (five parts per thousand salinity) requires 4.5608 grams of sodium chloride. This was then multiplied by the volume of the tank, 110 litres, to give a figure of 501.69g of sodium chloride per 5‰ increment of salinity. The actual salinity was measured for each increment in each experiment using the method detailed in section 3.5.5.

## **Results and discussion**

The results of the salinity measurements displayed in table 4.11 show that the NaCl increments produced salinity increments of slightly less than 5‰, however the approximate 5‰ increments in salinity were acceptable.

SSC mg/l	Mass of NaCl added (g)						
	0.00	501.69	1003.38	1505.07	2006.76	2508.45	3010.14
0	0.032	4.622	9.422	14.250	18.952	23.395	28.748
100	0.037	4.653	9.220	14.001	18.999	24.230	28.866
200	0.041	4.835	9.486	14.581	18.594	24.208	29.305
400	0.042	4.752	9.483	14.486	19.180	24.149	29.282
600	0.043	4.625	9.334	14.373	19.426	24.443	29.126
Mean	0.039	4.697	9.389	14.338	19.030	24.085	29.065
Std Dev	0.004	0.093	0.113	0.225	0.307	0.402	0.249

**Table 4.11** The measured salinity values in parts per thousand (‰) for each increment of NaCl added to each SSC experiment and the mean salinity across all the SSC.

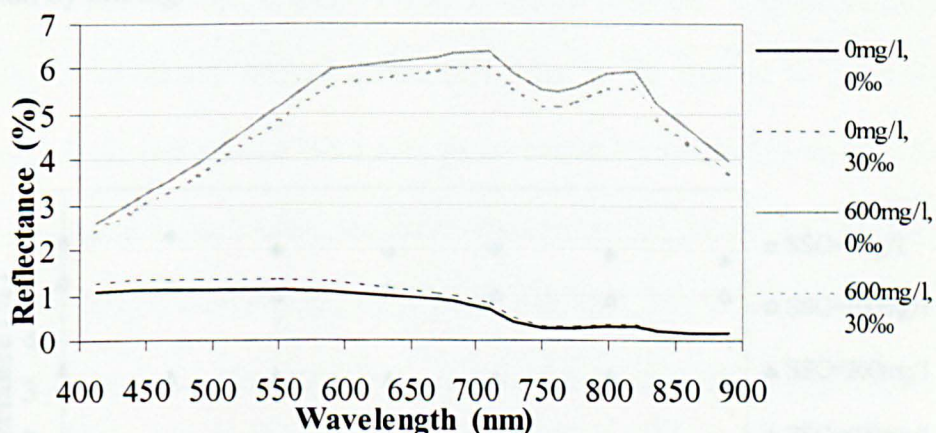


**Figure 4.15** The effect of salinity and SSC variation with wavelength.

Figure 4.15 displays the reflectance spectra for the maximum salinity range of 0‰ to 30‰ at 0 mg/l and 600 mg/l SSC. It can be seen that for 0 mg/l and 600 mg/l the difference in spectral reflectance across the salinity range is minimal. It is also evident that there appears to be no systematic relationship between salinity and reflectance, for 0 mg/l the increase in salinity gives an increase in reflectance whereas at 600 mg/l the increase in salinity produces a decrease in reflectance.

Concentrating on a single CASI waveband as shown in Figure 4.16 can see this lack of a systematic relationship more clearly. In this graph, each horizontally parallel data series represents a single SSC and the x-axis represents the salinity range. It is clear that there is no systematic relationship between reflectance and salinity at any SSC. Any variation in reflectance for a given SSC appears to be totally random. This raises important questions about the study by Khorram (1982) that claimed to map salinity in the San Francisco Bay area. The most likely explanation is that the study was not directly mapping salinity but some parameter that correlates with salinity, such as the dissolved organic matter content of the water, which is inversely correlated to salinity as a result of dilution by mixing.

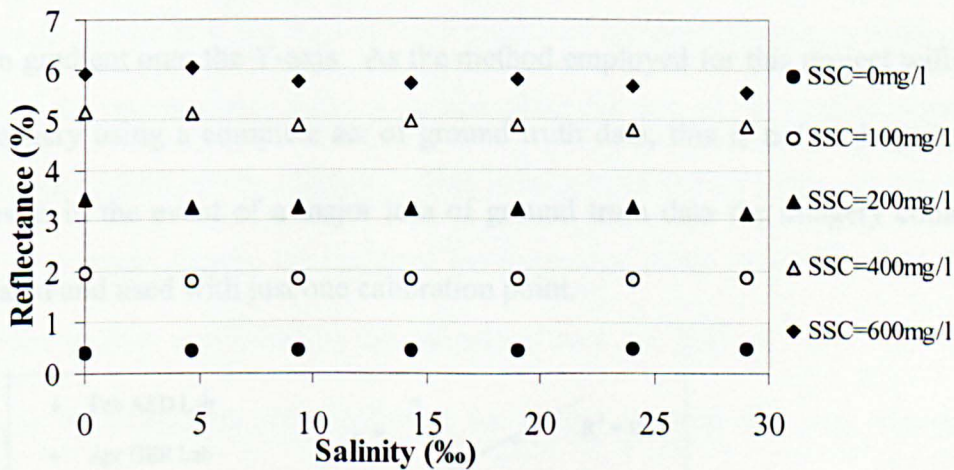


**Figure 4.16** The variation of laboratory reflectance with salinity for the various SSC.

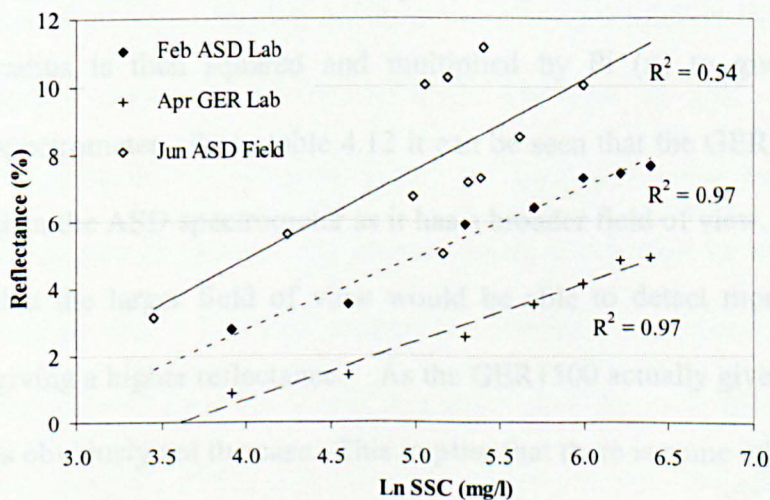
### 4.3.6 Comparison of spectrometers and illumination conditions

Figure 4.17 shows that there is a considerable difference in the results of the SSC reflectance relationship from the two spectrometers under differing conditions.

The main features to note in the above diagram are:

- The increased scatter around the regression line in the field environment
- The similarity of the gradients of the three lines.
- The reflectance detected by the ASD is greater than the GER1500

The possible reasons for the increased scatter in the field conditions have been discussed in section 4.2.3. It is very interesting to note how the gradient of each of the lines in Figure 4.17 is approximately the same. This suggests that irrespective of the spectrometer used and the conditions in which the spectra are collected, the rate of change of reflectance with change in SSC is always constant. The implications of this are that if a laboratory derived calibration were to be applied to remotely sensed imagery, at least one ground truth data point would be needed to anchor the line of known gradient onto the Y-axis. As the method employed for this project will calibrate the imagery using a complete set of ground truth data, this is not an important issue. However, in the event of a major loss of ground truth data the imagery could still be calibrated and used with just one calibration point.



**Figure 4.17** The relationship between reflectance and the natural logarithm of SSC at 766-768nm for the two different spectrometers used in the laboratory and field environments.

The main difference between the spectrometers is that the ASD gives a consistently higher reflectance than the GER1500. The possible reasons for this could be difference in field of view (FOV) or illumination.

	ASD (Field)	ASD (Lab.)	GER1500 (Lab.)
<b>FOV, <math>\theta</math></b>	8°	8°	15°
<b><math>\theta \div 2</math></b>	4°	4°	7.5°
<b>Height (cm)</b>	~50	40	40
<b>Radius (cm)</b>	3.49	2.80	5.27
<b>IFOV Area (cm<sup>2</sup>)</b>	38.4	24.6	87.1

**Table 4.12** The difference in the areas viewed by the spectrometers under the different conditions.

Table 4.12 shows how the field of view (FOV) of the spectrometer in degrees and the height of the spectrometer above a surface affect the area of the surface viewed or the instantaneous field of view (IFOV). This is calculated in two steps, assuming that the IFOV is circular. Firstly, the radius of the theoretical circle is calculated as the height above the surface multiplied by the tangent of half the field of view. The calculated radius is then squared and multiplied by Pi ( $\pi$ ) to give the area viewed by the spectrometer. From table 4.12 it can be seen that the GER1500 views a far larger area than the ASD spectrometer as it has a broader field of view. Thus, it would be expected that the larger field of view would be able to detect more back-scattered light, thus giving a higher reflectance. As the GER1500 actually gives the lowest reflectance, this is obviously not the case. This implies that there is some other factor responsible for the differing reflectance values. The only other variable in the experimental set-up is the illumination. The ASD spectrometer is sensitive to the 50Hz cycles of any mains

operated light source; thus natural light was used. For the fieldwork the skies were clear and for the ASD laboratory experiments the sky was bright but overcast. For the GER1500 laboratory experiments, a 1000W lamp was used in a room with a non-reflective covering on the walls. The result is three different illumination conditions where the brightness of the incident light appears to be related to the magnitude of the reflectance values of the SSC reflectance relationship. As the final image data will be calibrated using ground truth SSC data, the effect of the incident radiance will not be a factor but this needs to be considered if applying a laboratory derived calibration to remote sensing imagery.

#### **4.3.7 Choice of CASI Bandset**

After the initial investigations into the SSC reflectance relationship, it is known that the wavelengths of greatest importance to the study are those between 700nm and 900nm, as these wavelengths are most sensitive to the changes in reflectance with SSC. One of the major advantages of remote sensing of radionuclides using the CASI as opposed to an airborne gamma spectrometer is that the CASI is not specific to one parameter. Speed of data collection and improved spatial resolution are two more advantages. The optical data collected by the CASI can also be used for quantifying chlorophyll pigments, dissolved organic matter and for visual studies such as habitat survey. Hence the choice of data set can include bands which may be useful for studies outside the current one. For this reason the bandset was chosen by initially selecting the wavelengths used for quantifying chlorophyll by solar stimulated fluorescence (Gower and Borstad, 1990) and dissolved organic matter (Wilson, 1995). The wavelengths which are used by NERC (Wilson, 1995) to detect atmospheric constituents, were also selected. This was done to avoid any atmospheric effects overlapping onto the sediment

sensitive wavelengths. The remaining wavelengths were filled with 20nm wide bands, particularly focusing on the 700nm to 900nm range, to give a total of 17 bands. Details of the chosen CASI bands are summarized below in table 4.13. Whilst it may seem excessive to collect data which are unlikely to be used in this study it must be remembered that data collection by airborne remote sensing is relatively expensive and potential uses for the data must be maximised at the collection stage.

<b>Band No.</b>	<b>Wavelengths nm</b>	<b>CASI CCD Row</b>	<b>Centre Wavelength nm</b>	<b>Parameter</b>
1	402.81 - 422.15	286-275	412	DOM
2	432.72 - 453.87	269-257	443	DOM
3	480.37 - 499.84	242-231	490	DOM
4	540.63 - 560.19	208-197	550	
5	579.78 - 599.39	186-175	590	
6	660.19 - 679.92	141-130	670	Chlorophyll (Fluor.)
7	681.72 - 685.31	129-127	682.5	Chlorophyll (Fluor.)
8	705.07 - 715.86	116-110	710	Chlorophyll (Fluor.)
9	719.46 - 739.26	108-97	729	Suspended Sediment
10	741.06 - 759.10	96-86	750	Suspended Sediment
11	760.90 - 764.51	85-83	762	Oxygen Absorption
12	766.31 - 786.18	82-71	776	Suspended Sediment
13	787.99 - 807.88	70-59	798	Suspended Sediment
14	815.13 - 824.18	55-50	820	Water Absorption
15	825.99 - 845.94	49-38	836	Suspended Sediment
16	849.56 - 869.54	36-25	859	Suspended Sediment
17	880.44 - 900.45	19-8	890	Suspended Sediment

**Table 4.13** The CASI bandset chosen for the collection of the 1997 flights on the Ribble Estuary. DOM = dissolved organic matter.

### 4.3.8 Summary and conclusions

The laboratory experiments were designed to define the possible environmental controls on the SSC reflectance relationship. The environmental variables likely to be encountered in the Ribble estuary were identified as (i) variation in SSC, (ii) the salinity gradient and (iii) variation in grain size characteristics. In addition to the actual environmental variables, some possible sources of error as a result of the experimental set-up were also examined. These were the effect of only using the  $<63\mu\text{m}$  grain size fraction and use of different spectrometers. The information gained from the laboratory experiments is summarised below:

1. The SSC reflectance relationship is linear for SSC range of approximately 0-250 mg/l or less.
2. The SSC reflectance relationship is log-linear for SSC ranges greater than approximately 0-300 mg/l.
3. If there is substantial variation in the  $<2\mu\text{m}$  content of the suspended sediment this is only likely to have an effect on the SSC reflectance relationship at the higher SSC, for example  $\text{SSC} > 500 \text{ mg/l}$ . Thus the error contribution as a result of this is likely to be less than the suspended sediment sampling and analytical errors, which are discussed in chapter 5.
4. Using only the smallest grain size fraction in the experimental set-up does not have a significant effect on the SSC reflectance relationship.
5. There is no systematic relationship between salinity and reflectance, thus the whole estuary can be mapped using a single algorithm.

6. Using different spectrometers in different conditions does give different SSC reflectance relationships but this appears to be a result of the illumination conditions.

#### **4.4 CHAPTER SUMMARY**

This chapter has attempted to prove the initial hypothesis and demonstrated a reliable relationship between SSC and  $^{137}\text{Cs}$  concentration. It has also been able to address other issues relating to the properties of the water column and the possible effect on reflectance. It is now known that the relationship between SSC and the associated radionuclide concentration allows the measurement of SSC to act as a surrogate for the associated  $^{137}\text{Cs}$  concentration. The SSC can be measured using remotely sensed reflectance by a single algorithm without interference from changes in salinity, sediment composition and chlorophyll over the entire estuary. The next logical progression is to examine the acquisition of the remotely sensed imagery and the ground truth calibration data. Once the imagery has been collected, it is necessary to assess which pre-processing steps are needed without introducing further errors into the data and to calibrate the imagery to SSC and  $^{137}\text{Cs}$  concentration. This will be covered in the following chapter.

# **CHAPTER 5: ACQUISITION AND PROCESSING OF REMOTE SENSING DATA**

## **5.1 INTRODUCTION**

This chapter presents the methodology and results of the pre-processing and calibration of the time series of imagery acquired of the Ribble estuary, specifically for this investigation, on the 20<sup>th</sup> July 1997. Ground survey data results are presented and integrated with the imagery to produce a series of images of SSC, which are presented in chapters six and seven. Also included in this chapter are the steps undertaken to normalise the image data to account for variations in sun angle during the acquisition of the image data. This is perhaps one of the most important of the processing steps to minimise errors in image to image comparisons. The images produced represent one of the first published time series of images over a flood tide and the data produced from this chapter are crucial to the interpretation of sediment and radionuclide entrainment, transport and net budgets in the Ribble estuary.

## **5.2 DATA ACQUISITION**

For the production of quantitative information, it is fundamental that data acquisition through remote sensing is undertaken with a carefully planned ground truthing campaign. The spatial resolution and swath width of the imagery acquired is a function of speed and altitude and must be selected to cover the area required at a resolution suitable for identifying and quantifying features of interest. The alignment of the sensor with the sun, flight direction and the time of flight is also of paramount importance and will be discussed with specific reference to the Ribble estuary in section 5.2.1.

## 5.2.1 Choice of Flightline

Theoretically the ideal flightline would lie in a North-South orientation (Wilson 1995). The plane flies with the nose slightly raised and the sensor scanning forward of the aircraft, consequently the line should be flown heading North. As the day progresses, the angle of the sun above the horizon changes, this change is at a minimum when the sun is at its highest, between 11:00am and 2:00pm. Data collected between these times are ideal, as the data are almost directly comparable requiring no correction for the change in angle of the sun above the horizon.

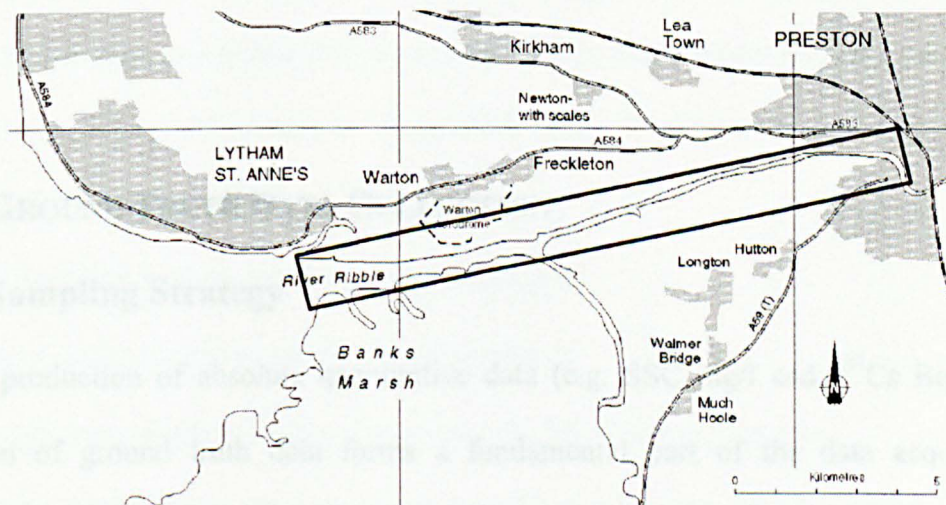


**Figure 5.1** The area of the proposed CASI flightline

Figure 5.1 shows that the Ribble is an ideal shape for airborne remote sensing campaigns, the flight altitude being a function of compromise between covering as much of the estuary within a single flight line with the highest resolution. At a 2.5m x 2.5m, spatial resolution the swath width of the CASI image would be 1.28km, which can cover the entire estuary from Penwortham in the east to Lytham St Anne's in the west excluding the extreme outer estuary. However, the east-west orientation does not enable the effective application of a north-south flight line. The single east-west flight line will result in the image being illuminated unevenly, being brighter on the South

side of the image (Wilson 1995). Ideally, the line would be flown repeatedly during a spring flood tide, where the high tide occurred at approximately 2:00pm. This would result in the majority of the flights being obtained during the period in which the angle of the sun above the horizon varies least. However, to achieve this coincidental with cloud free skies in the UK climate would be impractical within the time constraints of this investigation. Thus compromises had to be made and whilst the data were obtained on a cloud free day (20<sup>th</sup> July 1997) on a spring tide, the high water occurred earlier than planned, at 1107 GMT. This will cause a progressive brightening of the sequential images with time as the sun rises. These effects resulting from east to west flights and the changing solar elevation angle, will be investigated and corrected for in section 5.3.3.

## **5.3 GROUND TRUTH DATA COLLECTION**

### **5.3.1 Sampling Strategy**

For the production of absolute quantitative data (e.g. SSC mg/l and <sup>137</sup>Cs Bq/l) the collection of ground truth data forms a fundamental part of the data acquisition procedure. The data collected during the June 1996 fieldwork have shown that the relationship between SSC and caesium concentration is linear. Chapter four has demonstrated that there is no significant difference between the suspended sediment characteristics of samples collected off Warton bank and samples collected along the length of the estuary (section 4.2.2). Thus, these preliminary results coupled with limited resources (i.e. a single boat) and the potential of time lost travelling between widely spaced sample sites, resulted in the optimum sampling strategy being to remain off Warton Bank. Sequential data were collected at five-minute intervals, on either side of the axial convergence front throughout the image acquisition period of the flood tide.

Data collected during this ground truthing exercise, presented in section 4.2.1, have shown that this  $^{137}\text{Cs}$ -SSC relationship is temporally stable. Thus the relationship derived in June 1996 can be used to calibrate the images to  $^{137}\text{Cs}$  concentration. It is known that the relationship between SSC and reflectance is more susceptible to scatter and the reflectance is more dependent on the illumination and conditions at the time of data collection. For this reason the images must be calibrated with data collected simultaneously to give a valid SSC radiance relationship.

Having launched the boat on the previous high water, sampling on the incoming tide commenced as soon as the water depth allowed, just a few minutes after the passing of the tidal bore, and coincided with the acquisition of the first flight line. At each sample site the following were taken:

- 3 replicate 1 litre water samples for SSC analysis
- 1 litre of water for grain size distribution analysis
- Ten replicate reflectance spectra measured by ASD FR spectrometer
- pH and salinity (measured on return to shore from grain size sample bottles)
- Position by Differential GPS

In addition to the above, at four random locations a ten litre sample was taken for  $^{137}\text{Cs}$  analysis to investigate the temporal stability of the SSC  $^{137}\text{Cs}$  relationship. The results from these samples are presented in section 4.2.1. Given the observed variability in the SSC estimates (section 4.2.3) three replicate samples were used for the suspended sediment analysis in an attempt to quantify the potential variability for each of the twenty three sampling points.

### **5.3.2 Processing of the Ground Truth Data**

The DGPS data collected were processed using the techniques discussed in section 3.4.1 to locate each sampling point. Water samples were processed in order of priority due to degradation. To inhibit algal growth, the ten litre samples for radionuclide analysis and the one litre grain size samples were stored in the refrigerator. The suspended sediment samples were stored at room temperature, in the dark for three days before being filtered and analysed using the method detailed in section 3.5.1. The grain size samples were then analysed, after vigorous shaking to resuspended the sediment in the sample, using the Malvern Mastersizer as detailed in section 3.5.2. The ten litre radionuclide samples were then analysed using gamma spectroscopy, as described in section 3.5.3.

The ASD spectra were converted to absolute reflectance before the replicate spectra were averaged to give a single representative spectrum for each site. These spectra were then averaged over the appropriate wavelengths to represent the CASI bandset. The details of these techniques can be found in section 3.2.2.

### **5.3.3 Ground Truth Results**

The data collected off Warton Bank, shown in table 5.1, were collected within a 326m by 209m area, which is bounded by a box with upper left and lower right co-ordinates of 340354E, 426591N and 340680E, 426382N. This area covers the main channel and the mudflats outside the training wall, which were sampled once the water depth allowed access.

Site I.D.	Pos. Wrt. front	Time (GMT)	GPS Position (E, N)	Salinity (‰)	pH	<i>In-situ</i> Reflectance CASI 9 (720-740nm)		
						Mean	Std Dev.	CV (%)
1	C	0819	--No GPS--	7.5	8.90	3.76	0.26	6.9
2	C	0825	--No GPS--	12.0	8.67	4.15	0.16	3.9
3	N	0830	340613, 426525	10.3	8.72	3.59	0.17	4.7
4	N	0838	340655, 426485	15.5	8.40	3.12	0.20	6.4
5	S	0844	340638, 426448	18.7	8.25	3.48	0.10	2.9
6	N	0847	340618, 426527	18.6	8.21	3.35	0.16	4.8
7	S	0855	340658, 426429	21.0	8.08	3.72	0.11	3.0
8	N	0900	340630, 426500	18.6	8.23	3.05	0.11	3.6
9	N	0903	340616, 426538	18.7	8.19	3.25	0.13	4.0
10	S	0909	340354, 426409	22.3	8.23	4.23	0.24	5.7
11	C	0913	340680, 426477	23.3	8.18	3.03	0.12	4.0
12	N	0917	340629, 426536	24.1	8.16	4.10	0.25	6.1
13	S	0923	340590, 426401	25.4	8.23	3.90	0.30	7.7
14	N	0930	340623, 426544	24.8	8.25	2.76	0.07	2.5
15	S	0934	340611, 426386	24.6	8.21	3.86	0.20	5.2
16	N	0942	340593, 426533	29.5	8.19	2.75	0.05	1.8
17	S	0948	340627, 426422	29.5	8.25	3.06	0.14	4.6
18	N	0953	340599, 426542	29.6	8.26	2.11	0.07	3.3
19	N	0956	340609, 426591	28.3	8.14	2.46	0.10	4.1
20	S	1002	340587, 426382	30.0	8.26	2.10	0.44	21.0
21	N	1006	340545, 426560	27.8	8.24	1.96	0.23	11.7
22	N	1111	340576, 426535	30.1	8.20	-	-	-
23	N	1127	340601, 426507	30.9	8.18	-	-	-

**Table 5.1** The ground truth results for electronically measured parameters. Column two relates to the position within the channel, centre (C), North (N) or South (S).

Throughout the sampling session it can be seen that the salinity generally increased with time as the salinity results show a salinity gradient of 7.5‰ to 30.9‰. This is a typical range for a macrotidal UK estuary.

The ground truth data have been separated into parameters measured electronically, shown above in table 5.1 and parameters derived from laboratory analysis, given below in table 5.2.

The salinity data show an interesting feature just after the start of the flood tide. At 0855 to 0910, the samples taken from the South side of the channel show a markedly higher salinity than for the north side of the channel. This suggests that the incoming tide may hug the South side of the channel. If this is the case we can expect a higher SSC on the south side of the channel to be evident on the imagery. However, after the initial tidal surge, the difference in salinity on either side of the axial convergence front appears to be negligible. The pH measurements vary randomly around 8.29 and show no trend in the variation of pH with time. The pH of deep-sea water is usually around 8.5, therefore the measured value is as expected. An obvious trend would only be expected if there was a large difference in the pH of the fresh and saline waters, thus the pH could be used to illustrate the extent of mixing but this is not the case for the Ribble estuary.

Site I.D	Time (GMT)	Clay (%)	Silt (%)	Sand (%)	SSC		
					Mean (mg/l)	Std. Dev.	CV (%)
1	0819	1.55	54.87	43.58	96.5	9.3	9.6
2	0825	2.15	61.62	36.22	141.4	64.0	45.3
3	0830	2.25	70.26	27.49	69.0	10.0	14.5
4	0838	1.94	53.11	44.95	65.2	7.8	12.0
5	0844	3.11	74.47	22.42	95.3	7.8	8.2
6	0847	2.68	66.18	31.14	84.5	16.6	19.7
7	0855	3.38	74.01	22.60	112.9	16.6	14.7
8	0900	2.72	68.67	28.62	76.4	5.1	6.7
9	0903	2.71	67.51	29.78	91.3	34.6	37.9
10	0909	4.70	78.25	17.04	205.1	23.7	11.6
11	0913	4.38	84.00	11.62	98.6	11.5	11.7
12	0917	2.90	66.91	30.20	119.9	36.0	30.0
13	0923	4.31	75.57	20.12	148.0	14.0	9.5
14	0930	3.00	57.78	39.22	91.9	12.8	13.9
15	0934	3.89	78.09	18.02	121.9	5.3	4.4
16	0942	3.09	72.95	23.96	63.5	34.1	53.7
17	0948	3.51	74.79	21.70	81.2	21.2	26.1
18	0953	3.16	73.60	23.23	53.4	11.5	21.5
19	0956	3.59	76.81	19.61	54.3	10.1	18.6
20	1002	3.69	75.57	20.74	73.2	13.3	18.2
21	1006	3.45	75.75	20.79	18.5	27.5	148.7
22	1111	2.98	80.03	16.99	36.1	6.6	18.3
23	1127	2.91	81.78	15.31	18.1	26.7	147.5

**Table 5.2** The ground truth results for laboratory analysed sediment parameters.

The *in-situ* reflectance measurements are given as the average of the ten replicates with the standard deviation. So that the variation in one set of spectra can be compared with another set of spectra with a different mean, the coefficient of variation was calculated.

This shows that the variation within a set of ten replicate spectra can range from 1.8% to 21% with an average of 5.6%. However, it can be seen that the majority of the coefficients of variation are around three or four percent. This is relatively small and can be considered an acceptable error for an environmental measurement. Unfortunately the last two sample sites have no *in-situ* reflectance measurement due to a power supply failure.

The grain size distribution of the suspended sediment is discussed in section 4.2.2 in relation to the other data sets; however, table 5.2 shows that for the ground truth data set, the percentage clay fraction remains consistently low at less than five percent. Although variable, there appears to be an underlying increase in silt content from about 60% at the start to about 80% at the end of the sampling period. Similarly, sand concentration decreases from approximately 35% to 15%. This may have some consequence on the accuracy of the calibration, resulting in under estimation of SSC at the start of the tide and over estimation towards the end of the tide. However, the magnitude of the error is likely to be relatively small in relation to the sampling and analytical errors resulting from the measurement of *in-situ* SSC.

The SSC range from 18.1 mg/l to 205.1 mg/l. These values lie within the linear portion of the laboratory-derived relationship, suggesting that a linear relationship, as opposed to a log-linear relationship, may be used to calibrate the images. The majority of the SSC values lie between 40 and 120 mg/l, with only two values below 30 mg/l and one value exceeding 150 mg/l. The replicate SSC samples show a large variation, and therefore a large standard deviation. This implies that either the suspended sediment was patchy on a small local scale or that the laboratory analysis results contained errors.

## **5.4 IMAGE PRE-PROCESSING**

The NERC imagery was delivered in October 1998 and was provided in a hierarchical data format (.hdf). The data had been radiometrically corrected prior to delivery to the NERC level 1b (Wilson 1995). In addition to the data, NERC supplied software for format conversion (EXHDF) and automated geocorrection (GCORR). The NERC software is command line driven; these commands are discussed in greater detail in section 3.3.2. Before calibration, using the ground truth data collected simultaneously with the imagery, the data must be subjected to various pre-processing stages to correct for the movement of the aircraft, geographical location, atmospheric effects and illumination variation. These processes are discussed in the following sections.

### **5.4.1 NERC Geometric Correction**

The NERC GCORR software was used to correct the imagery for the roll, pitch and yaw of the aircraft. The program also simultaneously corrects the image to geographical co-ordinates. An example of the output of this program is displayed as a red, green and blue colour composite in Figure 5.2. The upper image is an example of the raw data and the bottom image shows an example of the NERC GCORR corrected data. The difference in brightness of the two images is due to the automatic stretch applied by ERDAS being affected by the black void resulting from the re-orientation of the image during geometric correction. The stretch of river illustrated is very straight due the canalisation carried out during the early 1900s. The area bounded by box 1 shows a typical distortion resulting from the roll of the aircraft. Distortions due to pitch and yaw are less obvious to the naked eye but are equally important. In the lower image some small distortions due to aircraft roll are still visible, as in boxes 2 and 3. The most

likely cause of the roll distortions not being completely removed is that the auxiliary GPS data were not downloaded frequently enough. When a digitised 1:10,000 Ordnance Survey map was overlaid onto the image or successive images were overlaid onto each other, considerable errors were visible in the geographic co-ordinates of the imagery, with errors around Preston docks being up to 200m. Data that appear spatially correct but contain some errors could be used for many purposes, but for this study it was necessary to locate the ground truth sample sites accurately and to have the images geo-corrected accurately enough to animate the SSC images. To achieve this, some additional geo-rectification was necessary.



**Figure 5.2** The Ribble estuary, 20<sup>th</sup> July 1997. CASI data displayed as a true colour composite. a) The raw CASI data and b) the CASI data corrected using the NERC GCORR software.

## 5.4.2 Manual Geometric Correction

Manual geocorrection was performed in the ERDAS image processing software package on the NERC GCORR data. The technique involves selecting a ground control point (GCP) on the uncorrected image and linking it to a point on a corrected image or a map co-ordinate. This is repeated until a grid covering the whole image is built up. The uncorrected image is then transformed to fit the reference co-ordinates using a transform order and method that is user selected. All the images were corrected using a third order polynomial transform resampled using the nearest neighbour method. The larger the order of the transform, the more intricate the transformation. However, this can lead to the image being warped into impossible shapes particularly at the edges of the image where the ground control points tend to be fewer, thus the order of transformation was kept down to three.

Image	Mid Flight Time (GMT)	No. of GCPs	Control Point Errors (m)		
			X Direction	Y Direction	Total (RMS)
c20102	08:12:32	76	1.61	1.92	2.51
c20103	08:30:05	59	1.63	1.71	2.37
c20104	08:45:28	59	1.73	1.78	2.49
c20105	09:02:17	54	2.05	2.54	3.27
c20106	09:20:39	59	2.09	2.12	2.98
c20107	09:37:26	47	1.57	2.34	2.82
c20108	09:55:45	73	1.72	2.18	2.78
c20110	11:11:23	58	1.46	2.19	2.64
c20111	11:25:43	61	1.68	1.88	2.52

**Table 5.3** The details of the manual geometric correction errors.

The nearest neighbour re-sampling was chosen to maintain data integrity. This technique takes the value of the nearest pixel, thus keeping the original data values, whereas the other techniques take an average or weighted average of the surrounding pixels of the uncorrected image to give a value for the corrected image. This averaging can make the corrected image appear visually smoother, but the data are not true to the original image. As these data are to be used quantitatively it was deemed necessary to conserve the original data values.

Table 5.3 shows the ground control point information for the nine flight lines of the Ribble Estuary. Given the original pixel size of 2.5m x 2.5m, the errors of the transformation are approximately one pixel. This means that the pixels of the geo-corrected image are approximately within one pixel of the correct co-ordinate. In reality, within an image some pixels will be very accurate, whilst others will carry a larger error. The pixels with the larger errors are more likely to occur towards the edges of the image or in areas where few ground control points could be found or around the localities where the NERC GCORR program had not completely removed the roll effects. When overlaid, the manually corrected images fitted the digitised map well and were lined up with each other correctly, with the exception of image c20105, which still contained considerable distortions due to plane roll effects which were not removed by the NERC GCORR program. Unfortunately, this error due to aircraft roll cannot be corrected for manually and must remain in the imagery.

### **5.4.3 Atmospheric Corrections**

As discussed in chapter two there are various methods of correcting for the amount of light reflected back to the sensor from particles in the atmosphere between the sensor

and the target. These techniques range from complex radiative transfer models and the simplified versions of these models, (Rahman and Dedieu 1994), to simple haze corrections, which correct the darkest pixel to zero (Chavez 1988). The simple haze corrections require no additional data and are the most suitable choice for a study such as this. However, the main assumption with the darkest pixel haze correction is that the atmosphere is uniform across the image. In this study the imagery is to be calibrated using ground truth data, therefore if the atmosphere is assumed to be uniform across and between images then haze correction will not be crucial and the atmospheric component will be a constant. There are other atmospheric factors that are likely to have a much greater effect on the imagery. These are the increase in path length towards the edge of an image and the effect of the variation in illumination between images as the sun rises above the horizon. These two factors are investigated in the following paragraphs.

### **Path Length Correction**

During data collection the image is collected as successive lines of 512 pixels. As these are being collected simultaneously from a single point the light being reflected from the edges of the image must travel through a greater length of atmosphere than the light reflected from the centre. This is called the path length effect and is often visible as a blue haze along the edges of the image. Using simple right-angle triangle trigonometry it can be calculated that for a lens with a  $42^\circ$  FOV, as used on the CASI, flown at an altitude of 1500m the path length at the edge is 1605m. This gives an excess of 105m of atmosphere for the outer pixels. The magnitude of the effect on the imagery was investigated on non geo-corrected CASI imagery of the Ribble estuary collected during 1995.

To investigate how the radiance varies with pixel number, it is necessary to find a uniform surface across the width of the image. As this is not possible the image was treated as two separate halves and fields that covered approximately half the image were used to assess variance in radiance with pixel number. Treating the image as two separate halves has the added advantage of accounting for the image being brighter on one side of the image than the other due to uneven illumination.

Figure 5.3: Diagrammatic representation of the equation generation method for path length correction.

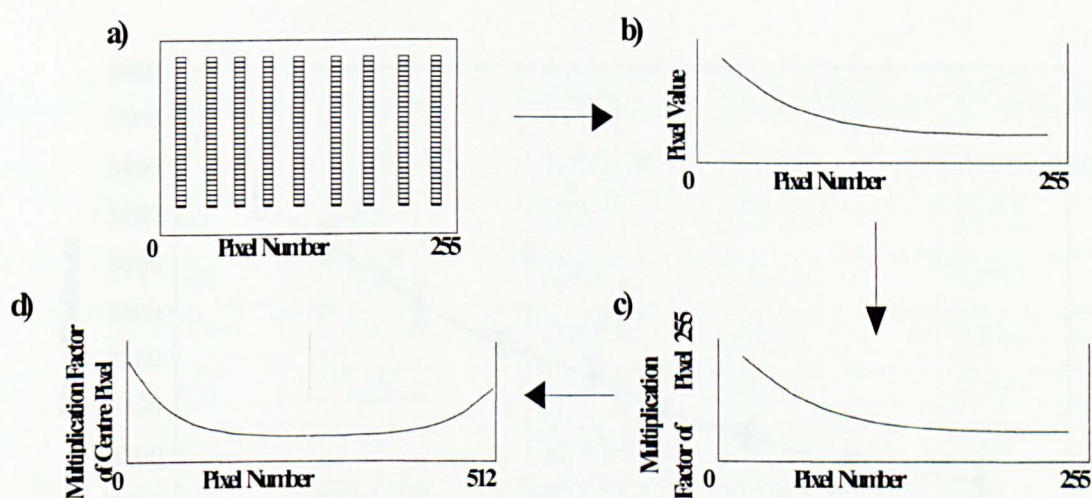


**Figure 5.3** A diagrammatic representation of the equation generation method for path length correction. a) Pixel sampling, b) the variation of radiance with pixel number, c) the calculation of the variation of radiance as a multiplication factor of the centre pixel and d) the combining of the two halves of the image to give a single equation. The raw data is then divided by the final best-fit equation.

Figure 5.3 shows the basic steps of the investigation into the effects of increased path length at the edges of the image. Firstly, the average of ten pixels were sampled from a given position on the image, this was repeated at approximately twenty pixel intervals for pixels 0 to 255 or 512 to 256. When the average pixel value is plotted against the pixel number it can be seen that the average pixel value decreases towards the centre of the image for a uniform surface (Figure 5.4). This can then be either extrapolated to

pixel 255, or if the best fit line starts to increase before reaching pixel 255, the line can be forced using a suitable value. This is then repeated for all bands. The effect observed in Figure 5.4 is a good example, but with increasing wavelength, the  $R^2$  of the best-fit line generally decreases and the error bars increase. Thus in an attempt to quantify this variation with wavelength, the significance was calculated by dividing the range of radiance values by the maximum radiance and multiplying by 100%. These values are presented in table 5.4.

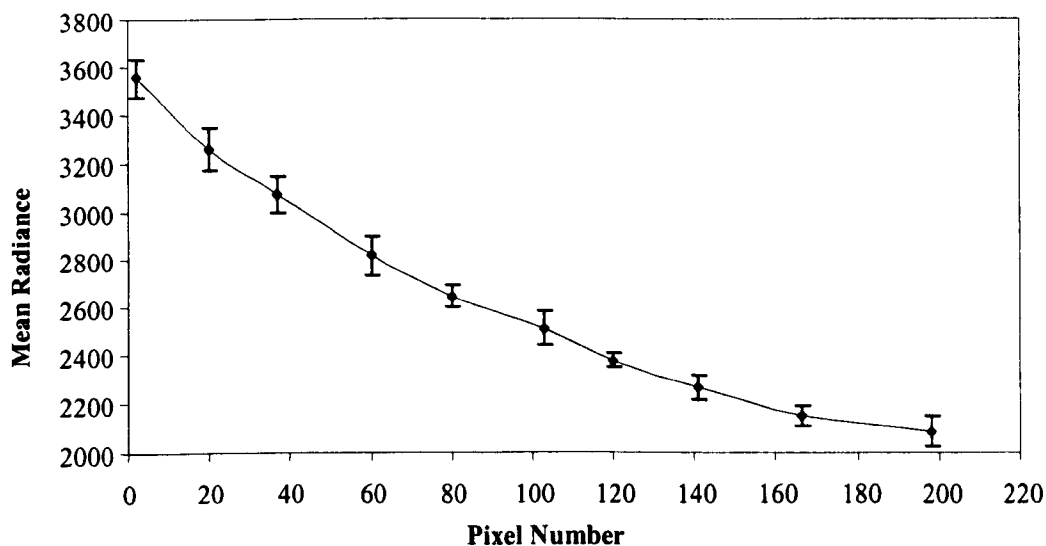


**Figure 5.4** An example of the mean radiance plotted against the pixel value as illustrated diagrammatically in Figure 5.3b. The data represents the southern side of the estuary from a field on Longton Marsh for CASI band 1, 402-422nm, image c213011b.img.

The significance of the decrease in radiance across the image (column 5, table 5.4) is obtained by dividing the range of values by the maximum radiance and multiplying by 100%. The value obtained will be small if the variation in radiance across the image is due solely to random noise but will be larger if there is a definite systematic change in radiance with pixel number. From table 5.4 it can be seen that this significance is greatest for the first two wavebands, after which it decreases.

For the longer wavelengths, the significance does increase but so does the scatter around the best-fit line, that is  $R^2$  decreases. This suggests an increase in the random noise effect. It is possible to conclude that it is only the blue wavelengths that need correcting for the increase in path length as they show a high significance in the change in radiance with pixel number and a high  $R^2$ . This is to be expected as it is the blue wavelengths that are affected by Mie scattering (Jerlov, 1986). These are the wavelengths used for remote Gelbstoff analysis.

<b>Band No.</b>	<b>Wavelengths (nm)</b>	<b>Maximum Radiance</b>	<b>Minimum Radiance</b>	<b>Significance (%)</b>	<b><math>R^2</math> of best-fit equation</b>
1	402-422	3553.8	2087.7	41.25	<b>0.998</b>
2	433-454	3620.4	2744.1	24.20	<b>0.995</b>
3	480-500	3281.2	2981.0	9.15	<b>0.978</b>
4	502-519	3129.6	2989.8	4.47	0.909
5	546-566	3871.3	3803.7	1.75	0.10
6	610-630	2661.8	2455.3	7.76	0.67
7	660-680	2143.6	1896.2	11.54	0.65
8	682-685	2067.0	1802.6	12.79	0.66
9	705-716	4229.8	3795.9	10.26	0.94
10	745-759	12917.1	10330.0	20.03	0.58
11	761-765	6463.0	5412.5	16.25	0.18
12	766-784	12981.6	10668.5	17.82	0.87
13	815-824	9333.0	7515.9	19.47	0.44
14	846-884	12080.1	9324.8	22.81	<b>0.97</b>

**Table 5.4** The significance of the relationship of radiance with pixel number for a uniform surface of the southern side of image c213011b.img and the variation at different wavelengths.

From table 5.4 it can also be said that band 14 requires path length correction. This is because the data were flown using the NERC default SeaWiFS bandset and band 14 is known to be sensitive to atmospheric aerosols (Wilson 1995).

No path length correction is required to produce SSC images, as the wavelengths used are not affected by the systematic increased scatter towards the edges of the image. However, the proposed path length correction method for the blue wavelengths is briefly outlined below. As surfaces vary over an image the increase in radiance with path length cannot be expressed as radiance as each surface will have a different radiance. However, the increase in radiance with path length can be expressed as a factor of the central pixel if the central pixel is made equal to one. To do this, the best-fit line must be derived from data forced or extrapolated to the central pixel. The multiplication factor is then calculated by dividing the value at a given pixel position by the value of the central pixel. This is then plotted against pixel number as shown in Figure 5.3c. The multiplication factors from the two halves of the image are then combined to give a single best-fit quadratic equation as illustrated in Figure 5.3d. If the illumination of the image is directly from the South and the image was flown south to North this plot will be symmetrical, however in most cases it will be asymmetrical. Once the single quadratic equation has been derived the image can be corrected in any standard image-processing package.

An example of the result of this correction technique is shown in Figure 5.5. In this example the image has bands one, two and three (blue, blue and green) displayed as a red green and blue image, thus the colours may appear unnatural. This exaggerates the haze effect making it more visible. It can be seen that the raw image shows

considerable blue haze on the left side of the image and an overall variation of brightness across the image. The corrected image shows no blue haze on the left of the image and a much more consistent brightness across the image. Visually, it is apparent that the correction technique works very well.

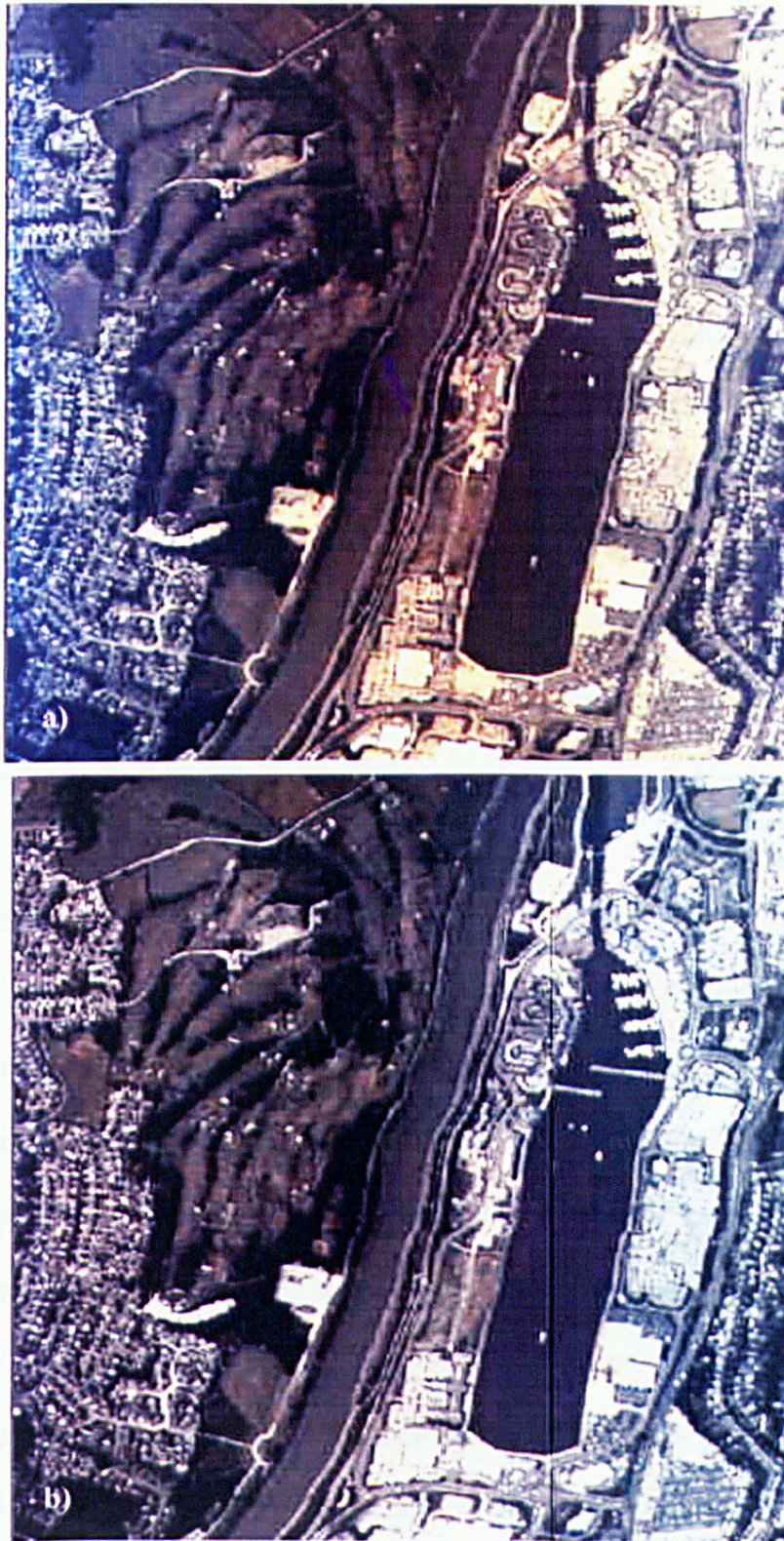


**Figure 5.5** An example of a path length correction of bands 1,2 and 3 (blue, blue and green) of image c213011b.img, the Ribble estuary, 1st August 1995. a) The raw data, b) the corrected data.

## **Sun Angle Correction**

The data were collected over a period of approximately four hours. During this time the sun was continually rising, substantially altering the illumination conditions between images. From section 4.3.6 it is known that this change in illumination will have an effect on the relationship between the SSC and the reflectance. Satellite imagery taken with different solar elevation is often normalised using a simple cosine correction technique. However, that technique requires knowledge of the exact solar elevation angle above the horizon and yields no information on the way in which this variation in sun angle affects the imagery. Therefore, this study will investigate the changes between the images and suggest an empirical method of correction, which requires no information on the exact solar elevation angle.

Firstly, four different surface types were selected for investigation. These were Preston dock, a tarmac road surface, a field and a sewage works filter-bed. These represent most of the surface types throughout the images and were selected for easy identification and location on each image. The location details of the four surfaces are given below in table 5.5. By using a range of surface types it can be established whether any change in radiance between images is a function of the surface type or change in solar elevation. If all surfaces vary in the same manner over time the variation must be due to the change in solar elevation angle. At each location the same 3 by 3 grid of pixels was sampled to give an average value and an indication of the variation within the sample grid at one standard deviation. These values were then plotted against time and are displayed in Figure 5.6. It can be seen that generally the 3 by 3 grid of pixels show little

variation in radiance with the exception of three points where the error bars at one standard deviation are evident.

<b>Surface</b>	<b>Easting (BNG)</b>	<b>Northing (BNG)</b>
<b>Docks</b>	351700	429600
<b>Filter-bed</b>	345545	428115
<b>Field</b>	343025	427250
<b>Tarmac</b>	336760	426960

**Table 5.5** The approximate locations of the four surface types used for derivation of the sun angle correction.

Each surface type shows some increase in radiance with time, however, the higher the initial radiance value the larger the rate of increase appears to be. There are three points that appear to be in disagreement with the general trends and decrease towards the final image: the final point in the filter-bed series and the last two points in the dock series. On these three points, the error bars are small enough to indicate that the average radiance value is representative of the real radiance. The reflectance of the filter bed at the sewage works would decrease suddenly if the filter bed were switched on, as the water running over the pebbles would attenuate the reflectance of the pebbles. As this is an operational sewage works this possibility cannot be ruled out, thus this point was removed from further analysis of the data. At the time of data collection the inner dock was subject to a bloom of blue-green algae, this is a natural phenomenon that occurs in standing water under warm sunny conditions, usually around July or August. One of the features of phytoplankton is that it is subject to distinct diurnal cycles and as the sun rises so the algae rise to the surface of the water column. The algae may substantially affect the reflectance of the water in the dock basin. Although the wavelengths used in Figure 5.6 are greater than 700nm and therefore considered to be outside the range

affected by chlorophyll, the algae are present in such large quantities it is possible that there will be some general particulate scattering effects. The dock data appear linear for the first two hours and it is only the last two images that appear to be subject to this effect. Thus these two data points have been omitted from the data in Figure 5.7.

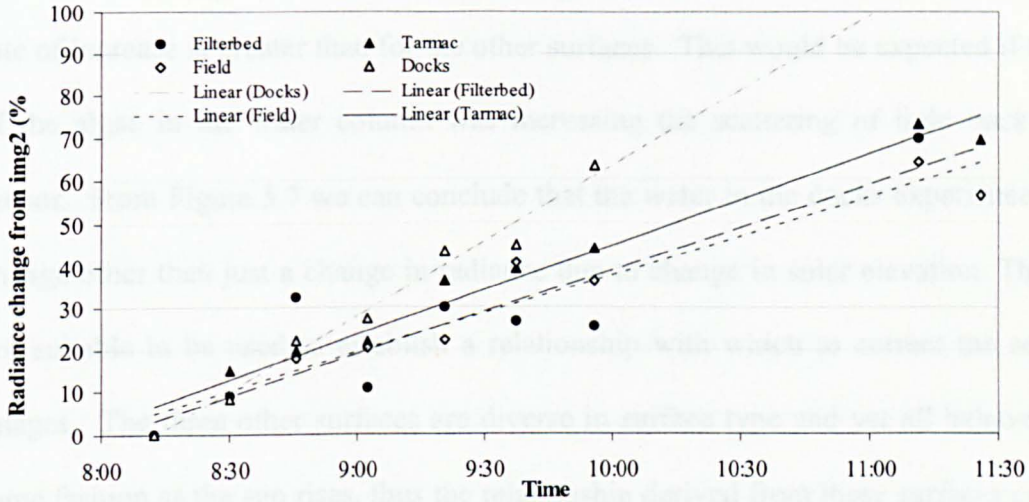


**Figure 5.6** The variation in radiance of a 3x3 grid of pixels with time for four different surface types. CASI band 9, 720-740nm. Error bars represent  $\pm$  one standard deviation.

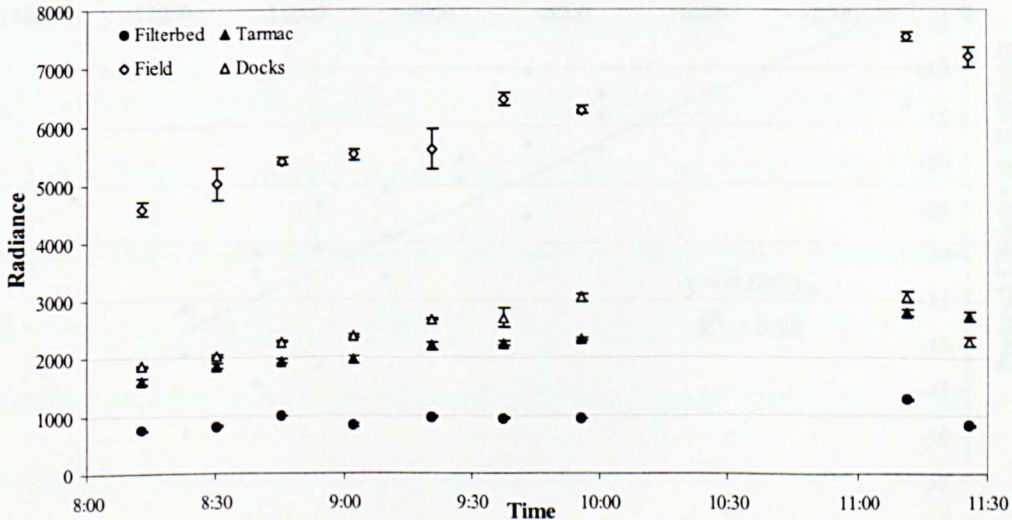


**Figure 5.7** The percentage change in radiance, relative to the first image, plotted against time for four different surface types. CASI band 9, 720-740nm.  $R^2$  values for the docks, tarmac, filter-bed and field are 0.98, 0.97, 0.79 and 0.94 respectively.

By expressing the change in radiance relative to the first image, a percentage correction factor can easily be calculated for each surface type. This percentage correction factor is plotted against time in Figure 5.7 and shows that once the change in radiance across the series of images has been converted to a percentage, the rate of change of radiance is almost constant for all surfaces. The exception to this is the docks. For this surface, the rate of increase is greater than for the other surfaces. This would be expected if the rise of the algae in the water column was increasing the scattering of light back to the sensor. From Figure 5.7 we can conclude that the water in the docks experiences some change other than just a change in radiance due to change in solar elevation. Thus it is not suitable to be used to establish a relationship with which to correct the series of images. The three other surfaces are diverse in surface type and yet all behave in the same fashion as the sun rises, thus the relationship derived from these surfaces could be used to correct the image series

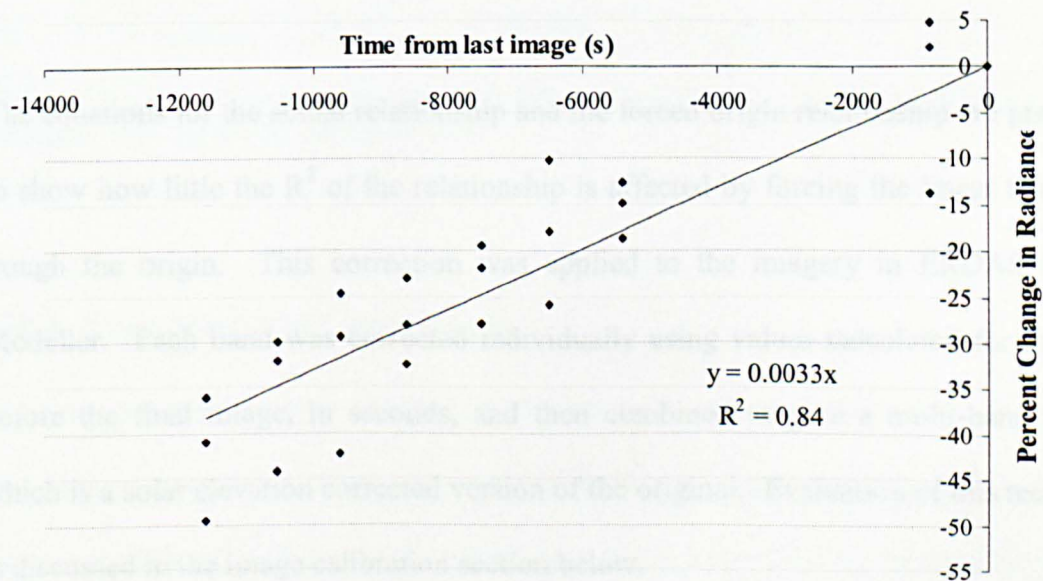


**Figure 5.8** The percentage change in radiance, relative to the last image, plotted against time for the combined data from three different surface types, with the origin forced to zero. CASI band 9, 720-740nm.

The images can be normalised to either the first image by reducing the radiance of the subsequent images or to the last image by increasing the radiance of the previous images. A study by Novo *et al.* (1989) has shown that the SSC reflectance relationship is strongest for a high solar elevation, when the radiance is at a maximum. This suggests that the data should be normalised to the final image, when the sun is higher in the sky. For the three surface types, the change in radiance of each surface was calculated as a percentage of the final image, and these data were then combined to give a single data set. This was then plotted against time to give a linear relationship as shown in Figure 5.8. It can be seen that by correcting the images to the final image the percent change in radiance becomes negative, but the relationship is still linear. As the data have been normalised to the final image, the linear trend line was forced through the origin to eliminate the necessity for any minor correction to the final image. This linear relationship was calculated for each band and the equations used are tabulated below in table 5.6.

The equations for the actual relationship and the forced origin relationship are presented to show how little the  $R^2$  of the relationship is affected by forcing the linear trend line through the origin. This correction was applied to the imagery in ERDAS Spatial Modeller. Each band was corrected individually using values calculated for the time before the final image, in seconds, and then combined to give a multi-band image, which is a solar elevation corrected version of the original. Evaluation of this technique is discussed in the image calibration section below.

CASI Band	Equation of Linear Trend	R <sup>2</sup>	Equation of Linear Trend Forced to origin	R <sup>2</sup>
1	$Y = 0.0031x + 1.4053$	0.866	$Y = 0.0029x$	0.863
2	$Y = 0.0032x + 2.3007$	0.852	$Y = 0.0029x$	0.844
3	$Y = 0.0033x + 1.5889$	0.863	$Y = 0.0031x$	0.860
4	$Y = 0.0034x + 1.9185$	0.837	$Y = 0.0032x$	0.833
5	$Y = 0.0035x + 2.3208$	0.799	$Y = 0.0032x$	0.793
6	$Y = 0.0033x + 3.7167$	0.678	$Y = 0.0029x$	0.664
7	$Y = 0.0032x + 4.6758$	0.538	$Y = 0.0027x$	0.519
8	$Y = 0.0034x + 1.9246$	0.788	$Y = 0.0031x$	0.784
9	$Y = 0.0035x + 1.8342$	0.846	$Y = 0.0033x$	0.842
10	$Y = 0.0034x + 0.7858$	0.872	$Y = 0.0033x$	0.871
11	$Y = 0.0037x + 1.5778$	0.865	$Y = 0.0036x$	0.862
12	$Y = 0.0034x + 1.0236$	0.876	$Y = 0.0033x$	0.875
13	$Y = 0.0034x + 1.5199$	0.865	$Y = 0.0033x$	0.862
14	$Y = 0.0035x + 1.5178$	0.861	$Y = 0.0034x$	0.859
15	$Y = 0.0034x + 1.2792$	0.860	$Y = 0.0033x$	0.858
16	$Y = 0.0033x + 0.6632$	0.861	$Y = 0.0033x$	0.861
17	$Y = 0.0034x + 1.0133$	0.854	$Y = 0.0033x$	0.853

**Table 5.6** The empirical solar elevation correction equations as derived from the image data and with the origin forced to zero.

#### 5.4.4 Summary and Conclusions

The image pre-processing detailed in the above paragraphs are some of the most important stages of this study. The purpose of these pre-processing steps is to correct for any variation in radiance that results from sources other than the light reflected from the suspended sediment, such as the atmosphere. This must be achieved without introducing errors, which may bias the results obtained from the data.

The NERC automated geo-correction system was found to be inadequate for the purposes of this project as the images did not lie directly on one another when overlaid using the NERC GCORR generated co-ordinates. These errors appear to be introduced by the inability of the NERC GCORR program to remove the most severe distortions caused by the roll of the aircraft as the image most seriously effected by these sharper roll distortions showed the greatest variation from the overlaid 1:10,000 digitised map. For this reason each image was then stretched to fit the map more accurately using a manual geometric correction technique. This resulted in a much more accurate fit of the images to the digitised map with errors of approximately one pixel or 2.7m.

The investigation into atmospheric effects on the imagery showed that, as this study utilises the longer wavelengths, the data did not need to be corrected for the longer path length towards the edge of the image. The technique suggested to correct for this increased path length appears to visually improve the images but is only required for the shorter wavelengths, for example less than 500nm. The increase in the angle of solar elevation was found to have a much greater effect on the series of images than path length, the effect increasing the radiance. This increase in radiance was found to vary systematically with time and could therefore be corrected for.

## **5.5 IMAGE CALIBRATION**

To investigate whether the calibration of the imagery is improved by the solar elevation correction technique it is necessary to assess the relationship between SSC and image radiance before and after solar elevation correction. To do this, radiance values were obtained for the 3x3 grid of pixels that were sampled for SSC. In recording the pixels values care was taken to ensure that the mixed pixels, where radiance was increased due

to the white hull of the boat, were avoided thus giving a more accurate value for the SSC. From these values, a mean and standard deviation were obtained. The relationship between the SSC and the raw or corrected radiance were plotted and the best fit linear trend line determined. These are shown in Figures 5.9a and 5.9b.

From Figure 5.9 it can be seen that the solar elevation correction technique significantly improves the linear relationship between SSC and radiance. This confirms that if imagery is to be calibrated for SSC it must first be corrected for any variation in solar elevation angle during the data collection period. It is also apparent from the size of the error bars that the largest error is in the sampling and analysis of the SSC and not the variation in pixel values obtained from the image data. The relationship derived from Figure 5.9b is the relationship that has been used to calibrate the image data to SSC.

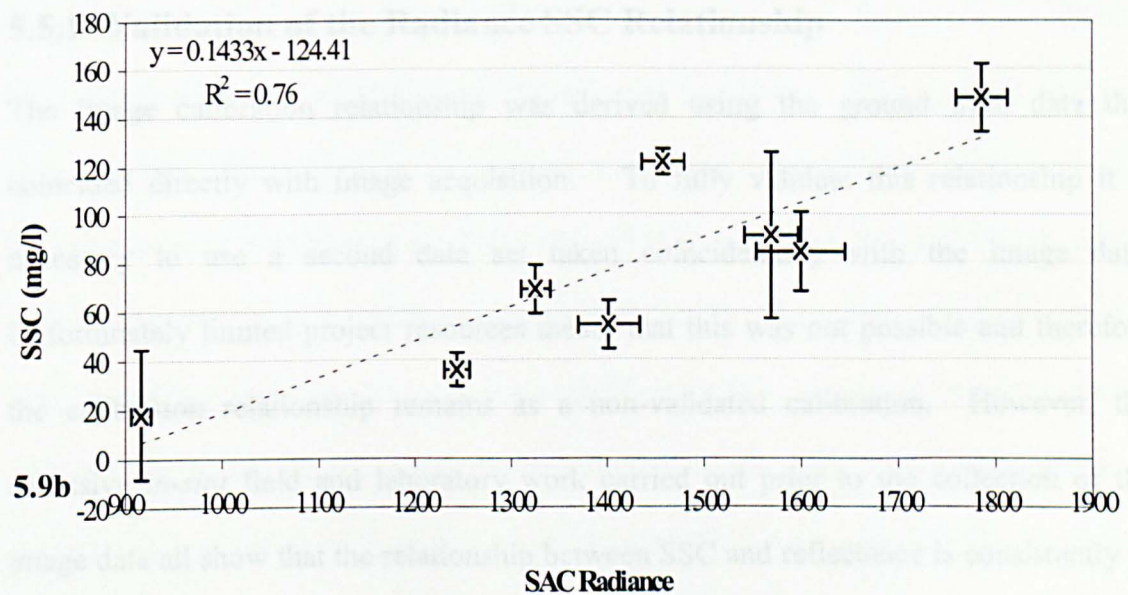
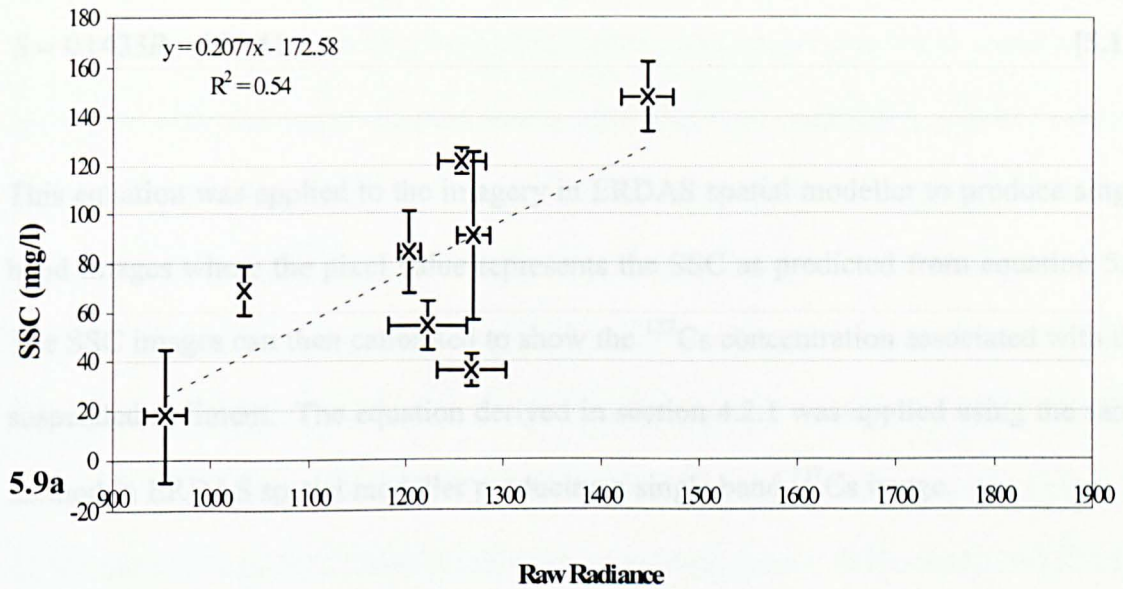


**Figure 5.9** The SSC radiance relationship for CASI band 9 at 720-740nm derived from image data 5.9a) before and 5.9b) after empirical sun angle correction. Error bars represent  $\pm 1$  standard deviation.

Having corrected the images for the various external effects on the sensor such as the motion of the aircraft, position and variation in solar elevation, the images are then calibrated to represent the SSC. The relationship used to do this is illustrated in Figure 5.9b and is given in equation 5.1 below, where S is the SSC and R is the image radiance, corrected for change in solar elevation angle.

$$S = 0.1433R - 124.41 \quad [5.1]$$

This equation was applied to the imagery in ERDAS spatial modeller to produce single band images where the pixel value represents the SSC as predicted from equation 5.1. The SSC images can then be calibrated to show the  $^{137}\text{Cs}$  concentration associated with the suspended sediment. The equation derived in section 4.2.1 was applied using the same method in ERDAS spatial modeller producing a single band  $^{137}\text{Cs}$  image.

### **5.5.1 Validation of the Radiance SSC Relationship**

The image calibration relationship was derived using the ground truth data that coincided directly with image acquisition. To fully validate this relationship it is necessary to use a second data set taken coincidentally with the image data. Unfortunately limited project resources meant that this was not possible and therefore the calibration relationship remains as a non-validated calibration. However, the extensive *in-situ* field and laboratory work carried out prior to the collection of the image data all show that the relationship between SSC and reflectance is consistently of a linear nature. The relationship derived to calibrate the images to SSC is also linear in nature with an  $R^2$  of 0.76. This high  $R^2$  value shows that the calibration relationship is very strong for an environmentally derived relationship and thus likely to be representative of the SSC.

## **5.6 CHAPTER SUMMARY**

This chapter has presented the methodology developed to process and calibrate the time series of airborne imagery for a flood tide sequence. The data were collected using east-

west flight lines despite a theoretical preference for North-South orientated lines. Simultaneous ground truth data were collected with the imagery and were found to be in agreement with previously sampled *in-situ* data. Replicate suspended sediment samples showed that there are significant errors produced in the standard sampling and analysis procedures used and these are generally far greater than those for the spectral analysis. The SSC was in the range 0-200 mg/l, a concentration range known to have a linear correlation to reflectance. The pre-processing showed that the NERC GCORR geometric rectification software did not remove all the image distortions due to the roll of the aircraft, especially those resulting from high frequency movements, and this led to geographic co-ordinate errors. Thus the imagery had to undergo an additional geocorrection using manual ground control point techniques. This resulted in a root mean square positional error of approximately one pixel for the CASI imagery. Investigations into atmospheric effects showed that correction for path length effects was not necessary at wavelengths used to measure SSC. The variation in radiance with time caused by the rising of the sun was a significant effect. As this increase in radiance with increased solar elevation was a systematic effect, it could be empirically corrected for without knowledge of the exact angle of solar elevation. Applying this correction for the change in solar elevation angle significantly improved the SSC calibration of the images. ( $R^2 = 0.54$  to  $R^2 = 0.76$ ).

## **CHAPTER 6: AIRBORNE REMOTE SENSING OF SEDIMENT**

### **TRANSPORT OVER A FLOOD TIDE IN THE RIBBLE ESTUARY**

#### **6.1 INTRODUCTION**

This chapter presents the SSC results derived from a series of nine images taken over a rising spring tide characterising SSC, enabling the remobilisation and transport to be studied at high spatial resolution, probably for the first time. The data have been divided into four geographical areas: The outer estuary at Warton Bank, the confluence of the rivers Ribble and Douglas, the narrow canalised stretch of the Springfields discharge area of Savick Brook and the upper estuary from Preston Dock to Penwortham. The precise details of the four areas are given in table 6.1. The chapter has been divided into these four geographical areas providing detailed image descriptions and interpretations. The key findings are summarised at the end of each section

<b>Area Name</b>	<b>Upper Left (OS BNG)</b>	<b>Lower Right (OS BNG)</b>	<b>Size (km)</b>
<b>Warton Bank</b>	337100E, 427700N	341600E, 425850N	4.5 x 1.85
<b>The Confluence</b>	341300E, 428000N	344850E, 426100N	3.55 x 1.9
<b>Savick Brook</b>	345000E, 429500N	349500E, 427400N	4.5 x 2.1
<b>The Docks</b>	349500E, 429650N	352500E, 428800N	3.0 x 0.85

**Table 6.1** The location details of the four geographical areas of chapter six.

#### **6.2 AREA 1: THE OUTER ESTUARY: WARTON BANK**

##### **6.2.1 Introduction**

Area 1 contains the reach of the estuary that is least constrained by the training walls and thus the behaviour is likely to be similar to that of a non-engineered estuary. This

area contains large intertidal areas, which have been shown to be accreting BNFL Sellafield derived radionuclides (Rainey, 1999).

### **6.2.2 08:11 GMT, Figure 6.1a**

Figure 6.1.a of the CASI and associated ATM thermal band shows that the water is confined within the training walls and SSC range is approximately 0-180 mg/l, with little thermal structure. The tidal bore is just visible on the north bank at 341640E, labelled as **A**. The higher SSC is in the turbulent water that follows the tidal bore. A tongue of low SSC, less than 20 mg/l, enters the estuary at Lytham, with higher sediment concentrations at the edges. The SSC then increases steadily within the estuary exhibiting a V-shaped intrusion pattern. This pattern is disturbed at about 340000E where more sediment appears to be suspended from the south bank of the estuary. This sediment source appears to be producing a maximum SSC of 180 mg/l at around 341200E.

Along the centre of the outer estuary, higher suspended sediment values reflect foam and debris from the convergence of two water masses, indicative of the formation of an axial convergence front (Nunes and Simpson, 1985) (also seen in Figure 7.1). This feature stretches from the outer estuary extremes of the imagery as far as 338750E. In the outer estuary at **B**, SSC greater than 220 mg/l is evident, although aerial photographic evidence indicates that these values may be the result of foam and debris washing off a sandbank. There appears to be no thermal heating of the water.

The thermal data from the ATM shows an increase in temperature towards the upper estuary side of Warton Bank. There is also a high temperature feature along the edge of

the sandbank at 341700E, (C), which may be due to a combination of warm sediment on the sand bank producing a slight heating effect on the water, or the pushing back of warmer fresh water by the bore.

### **6.2.3 08:30 GMT, Figure 6.1b**

Figure 6.1.b shows an overall increase in SSC, approximately 30-190 mg/l. The image is affected by aircraft roll resulting in a bright feature (D). This is a function of the sensor is tilting towards the sun, altering the viewing geometry and resulting in false SSC for the calibration used in the project. Thus the values are erroneously high by as much as 100%. However, SSC patterns can be traced through the feature.

Taking this source of error into account, it can be seen that the concentrations of suspended sediment are generally lower around the Lytham area and increase towards Warton aerodrome. The water is now inundating the intertidal areas on the northern bank and on the southern bank as far as 338500E. There are higher SSC values at the edges of the water where erosion is taking place, especially around 337500-337800E on the north bank and 341600E on the south bank. The sandbank at 337830E, on the north bank, is protecting the creek outflow, at 338060E, from the flow of the incoming tide. A build-up of low SSC water, (E) can be seen inside the higher SSC resulting from the erosion of the sandbank, also evident as elevated temperatures in the thermal image.

There is an axial convergence front running the whole length of this image, although this appears as two parallel foam lines in the outer estuary (339000E-339500E). This indicates a more complex inflow of water than the expected V-shape intrusion of seawater.

#### **6.2.4 08:45 GMT, Figure 6.1c**

The SSC range for this image has increased to approximately 20-210 mg/l. The lowest SSC is in a V-shaped intrusion at the mouth of the estuary, off Lytham; the concentrations generally increase towards Warton aerodrome. Generally, there is also evidence of erosion of the mud banks on either side of the estuary. The influence of aircraft roll is also seen, though the impact is less than in the previous image. The errors introduced are estimated to be  $\pm 20$  mg/l, approximately 20% on the mean SSC estimate of 100 mg/l.

The water has inundated the southern intertidal area highlighting two island sandbanks. The narrow channels on the south side of these islands show increased SSC; most likely due to increased current velocity in the constricted channel. The northern bank (337750E and 341240E-341980E) still shows elevated SSC levels, suggesting that these are areas of erosion. The two foam lines in the outer estuary converge at (F), becoming a single very well defined axial convergence front running the length of this image.

#### **6.2.5 09:02 GMT, Figure 6.1d**

The SSC has increased to approximately 20-250 mg/l. There is an indication of aircraft roll around 341445E, which coincides with a spatial distortion and an associated decrease in SSC.

Water with low SSC is entering the estuary, approximated by a V-shaped intrusion. The SSC generally increases towards Warton aerodrome. Along the north bank of the estuary an interesting sediment pattern is developing where tongues of sediment

suspended from the banks are pulled in towards the centre of the estuary, illustrating the direction and relative magnitude of the currents created by the axial convergence. This is confirmed by the coincidental thermal image showing plumes of warmer eroded sediment (e.g. **G**). The axial convergence front is well established at the southern side of the estuary. The intrusion of lower SSC water is being confined to the North of this front and thus mixing is being inhibited by the axial convergence front. The highest SSC is now located along the southern bank of the estuary, trapped behind the axial convergence front (340175E and 341500E). The thermal image from the ATM shows that the cooler seawater penetrates well into the estuary to 339500E.

#### **6.2.6 09:20 GMT, Figure 6.1e**

There is no apparent change in range of SSC, at 10-220 mg/l. The dark area at 338300E may be due to aircraft roll as the feature has roughly parallel sides. The other alternate dark and light patches are lens shaped and are therefore unlikely to be due to aircraft roll and may be a feature of the flood tide. The lowest SSC remain in the mouth of the estuary.

The highest SSC appear along the edges of the water, suggesting erosion by turbulent wave action as this occurs along the length of the image. The only area where very little sediment appears to be resuspended at the edges is (**H**), which coincides with large mats of algal material.

The axial convergence front is still visible but not as linear. Large sinusoidal patterns are beginning to appear in the foam lines and these coincide with the lenses of low SSC water trapped to the North of the front. These lens shaped low SSC features are perhaps

the result of some lateral instability in the axial convergence front, the beginning of its eventual break up. The thermal image again reveals little structure in the outer estuary, but some warmer water is being pulled in to the centre of the channel from the North bank, indicating some erosion (338000E and 341500E).

### **6.2.7 09:37 GMT, Figure 6.1f**

The SSC has now declined to between 10-190 mg/l, and intertidal inundation is almost complete. There is little evidence of errors caused by the roll of the aircraft in this image, probably a result of the increasing solar elevation angle.

The SSC steadily increase from less than 20 mg/l at Lytham to about 160 mg/l off Warton aerodrome. The highest SSC values are confined to the edges of the water, suggesting resuspension of the sediments by the encroaching tide. This occurs in all areas except the western half of the south bank. The mat of algae on the north bank at **I**, (338200E to 338550E) still appears to be inhibiting the resuspension of sediment, as the band of higher suspended sediment at the edge of the water is much narrower. The warmer features in the south-west corner of the thermal image are due to the suspension of warm sand washed off the extensive sandbanks in that area.

The foam of the axial convergence front is still very evident, as are the sinusoidal patterns and mixing is still being inhibited, e.g. lower SSC water is trapped to the north (340100E and 341100E). The sediment suspended off the northern bank is pulled towards the centre of the estuary by the convergence current (**K**). (The short distinct white feature at **J**, (340720E, 426450N) is the wake left by a water skier.)

### **6.2.8 09:55 GMT, Figure 6.1g**

The SSC range for this image is also between 10-190 mg/l. Water of low SSC now penetrates further into the estuary, with values of approaching 0 mg/l and is again trapped to the north of the axial convergence front. Lenses of low SSC can again be seen (e.g. **L**), north of the front within the curve of a sinusoidal feature in the foam line, as also seen in Figure 6.1e. Despite apparent breaking up of the foam lines, the front still inhibits the mixing of the low and higher SSC. Sediment is still being picked up from the edges of the water on the intertidal areas. There is no evidence of the strong convergent currents pulling these suspended sediments into the centre of the channel.

The thermal image shows warm water being introduced into the estuary along the north shore at Lytham and the western end of Warton Bank. There is no evidence of sediment suspension at this location in the coincidental CASI image, indicating the possible input of warmer water from a creek or heating of the water as it passes over warmer mud banks that are not eroding. This can also be seen on the western banks of the south shore.

### **6.2.9 11:11 GMT, Figure 6.1h**

The SSC range has now decreased to approximately 0-160 mg/l. There is a large intrusion of water with very low SSC (<40 mg/l) penetrating along the centre of the estuary as far as 340300E. The sediment being resuspended at the edges of the water is now much lower than in the previous images. This is possibly due to the much-reduced turbulent currents as the water is approaching the slack period around high water. The area of highest SSC is confined to a small area of the southern bank (**M**). The foam lines are more fragmented. There are just two defined sections, one in the outer estuary

and one developing around 339700E on the south bank and running towards the centre of the main channel to form the axial convergence front for the upstream section of the river.

The thermal image shows considerable structural detail and an overall rise in temperature. This may partly be due to the slowing of the currents creating less turbulence, which reduces mixing and allows the surface of the water to be warmed by the sun. In addition, the underlying sediment is heating areas of shallow water. It can be seen that the direction of flow is still inward and that time of slack water has not yet been reached. The two parallel fronts at the creek entrance on the south bank at N (339800E) are strong enough to inhibit mixing of the water bodies as the warmer water to the north of the main front is not mixing with that to the south. The second front is preventing warmer water from the creek flowing back into the river.

#### **6.2.10 11:25 GMT, Figure 6.1i**

A further decrease in SSC is observed and the range is approximately 0-100 mg/l. Water with very low SSC penetrates into the estuary as far as 340500E. The highest SSC are associated with the backwash from the creeks in the southeastern part of the image, suggesting the water is being prevented from mixing with the main estuary channel. Foam lines at O (339800E) and P (340450E) confirm that the convergence has moved to the far south of the main channel. The thermal imagery shows that warmer water is still being swept upstream and to the south of the channel.

### **6.2.11 Warton Bank Summary**

1. The overall SSC of this image series show that there is an initial increase in SSC in the images after the passing of the tidal bore (08:45GMT and 09:02GMT). After 09:02GMT, the SSC starts to decrease as the water being swept into the estuary is of a low SSC.
2. The SSC start to decrease in Figure 6.1h (11:11) and again in Figure 6.1i (11:25), confirming that the sediments start to settle as soon as the maximum current velocity decreases.
3. The recurring sediment patterns for this outer estuary imagery consistently shows a lower SSC in the outer estuary, to the west of the image. This is due to lower suspended sediment seawater being swept into the estuary giving the V-shaped intrusion patterns that are repeatedly seen.
4. There are consistent areas of higher SSC indicating areas of erosion, these are:
  - (a) the north shore, west end of Warton Bank at approximately 337600E, 426600N
  - (b) the north shore, east end of Warton Bank at approximately 340500E, 426650N
  - (c) the south shore, opposite (b), at approximately 340250E, 426400N
  - (d) the north shore below Warton aerodrome at approximately 341250E, 426600N
  - (e) the south shore, opposite (d), at approximately 341250E, 426300N.
5. When the sediment is eroded from the intertidal zone convergent currents carry the high SSC into the centre of the main river channel. This is particularly evident in the later thermal images and is confirmed by the development of foam lines almost immediately after the passing of the tidal bore.
6. The foam lines start to break up into sinusoidal patterns later in the flood (Figure 6.1f). Despite this break up there is still enough strength in the convergence to pull

sediment in to the centre of the river and also to prevent mixing of the waters to the north and south of this front.

7. The axial convergence migrates to the south of the main channel as current flow decreases, inhibiting drainage of the southern salt marsh creeks until the full ebb tide.

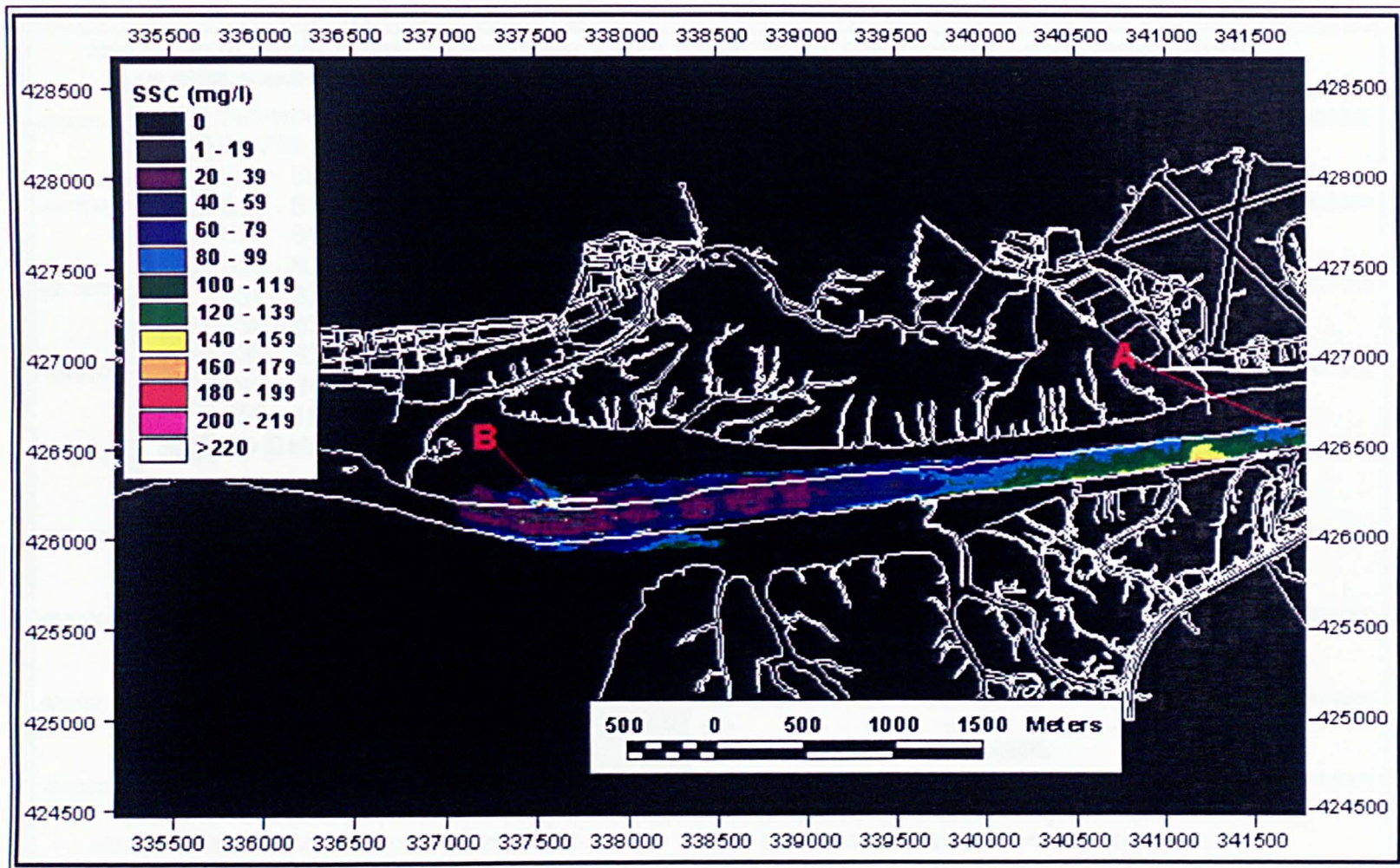


Figure 6.1a(i) CASI image calibrated to suspended sediment concentration, (mg/l), of Lytham to Warton Aerodrome, 08:11, 20-7-97

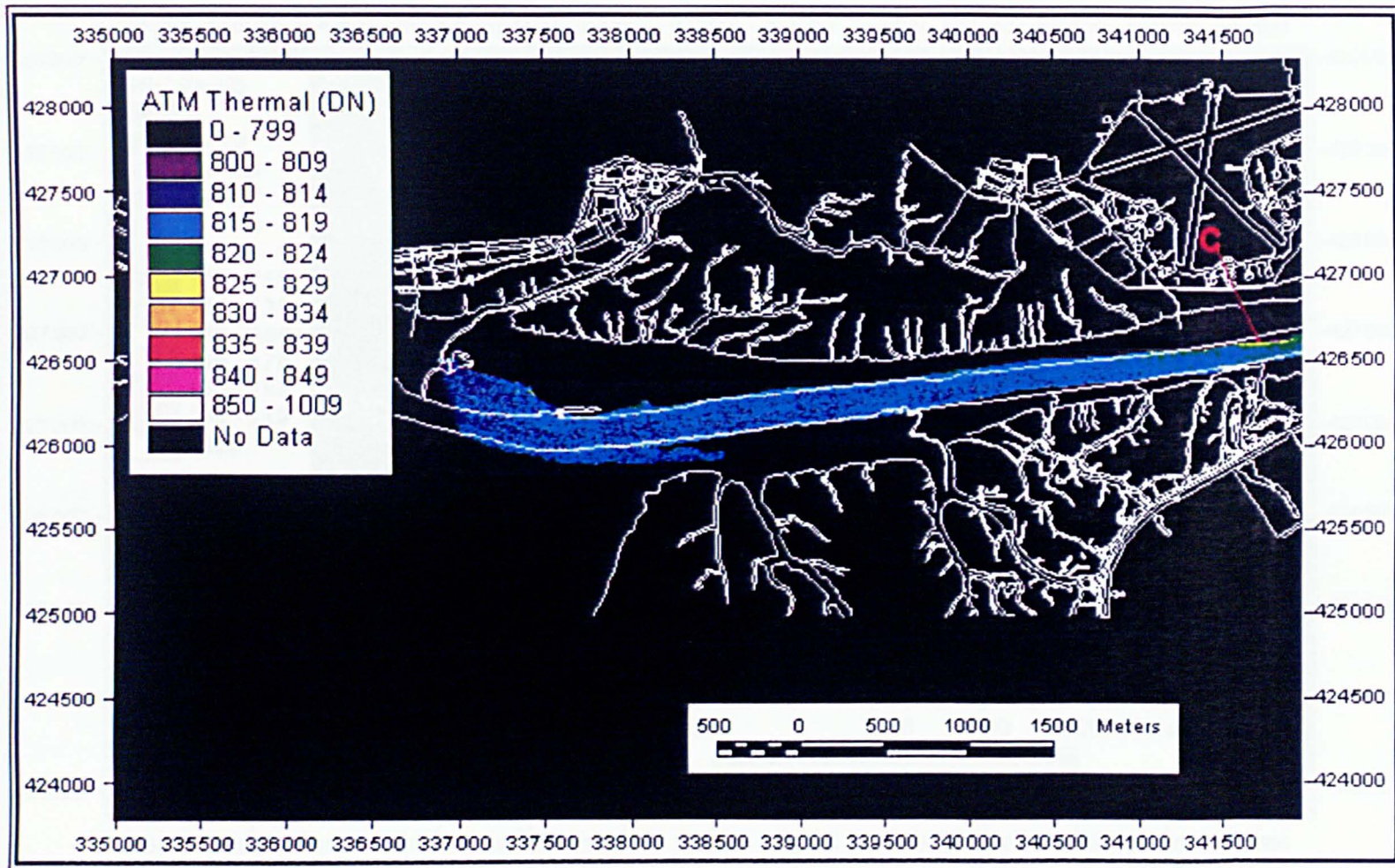


Figure 6.1a(ii) ATM thermal data of Lytham to Warton Aerodrome, 08:11, 20-7-97.

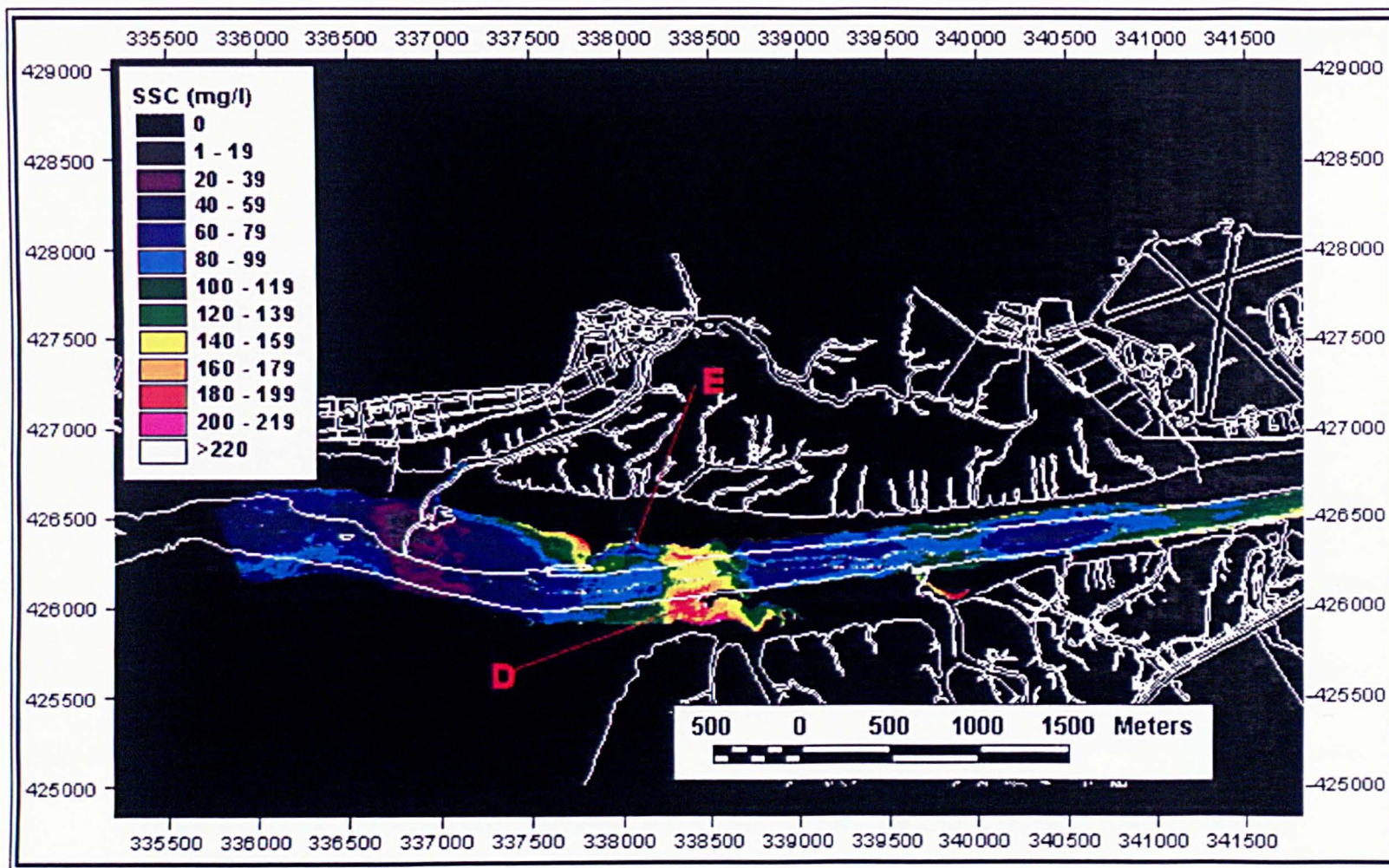


Figure 6.1b(i) CASI image calibrated to suspended sediment concentration, (mg/l), of Lytham to Warton Aerodrome, 08:30, 20-7-97.

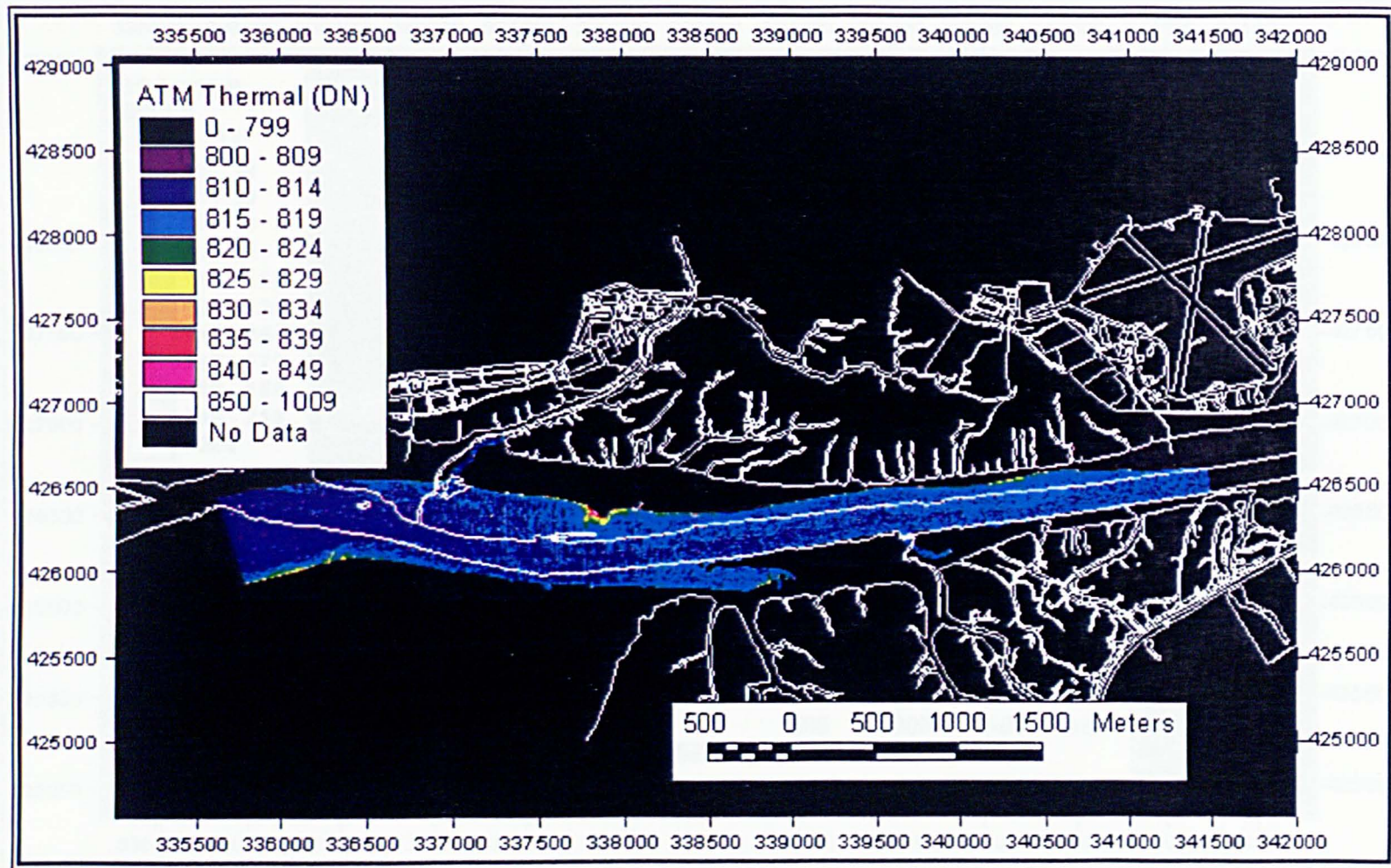


Figure 6.1b(ii) ATM thermal data of Lytham to Warton Aerodrome, 08:30, 20-7-97.

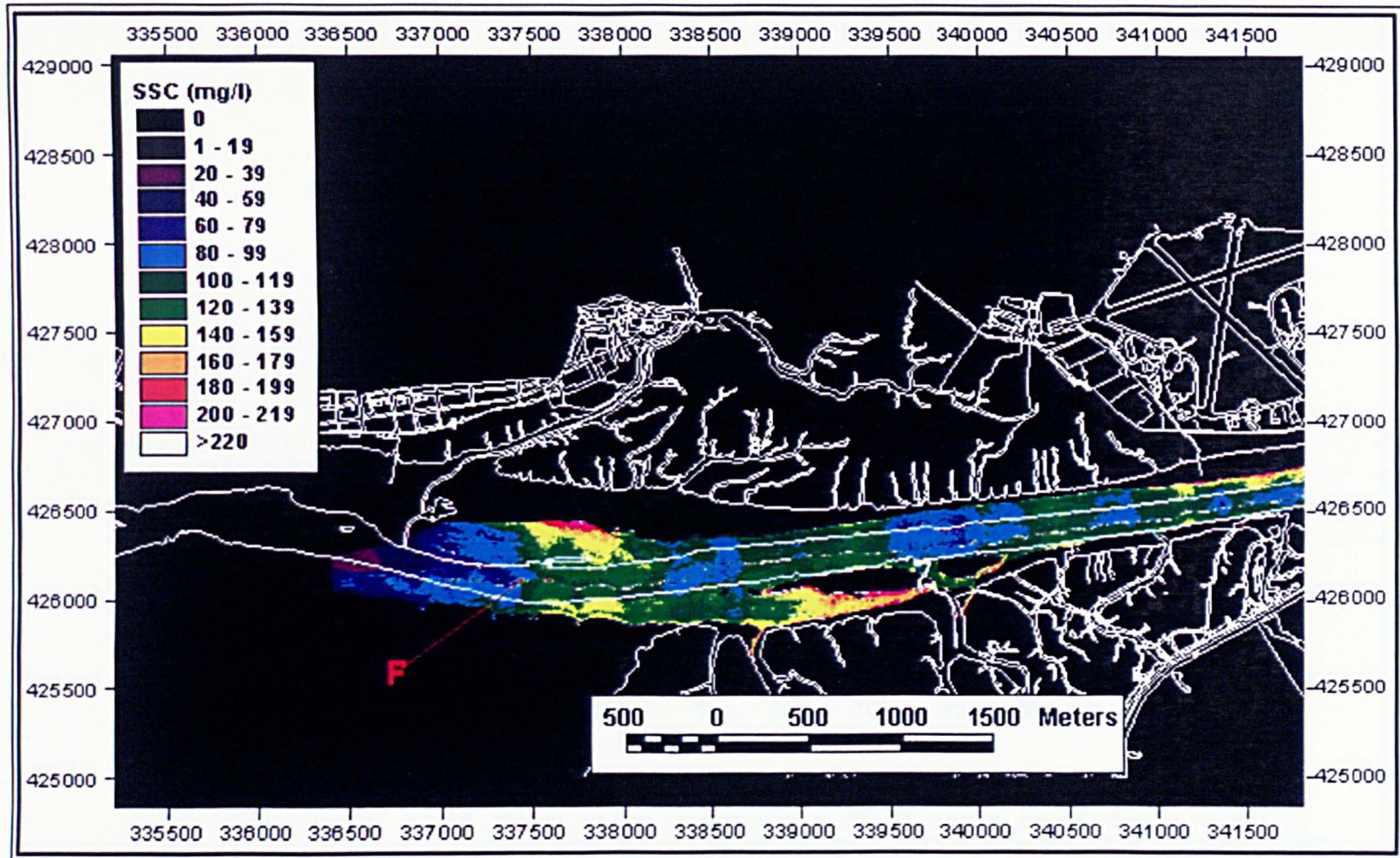


Figure 6.1c(i) CASI image calibrated to suspended sediment concentration, (mg/l), of Lytham to Warton Aerodrome, 08:44, 20-7-97.

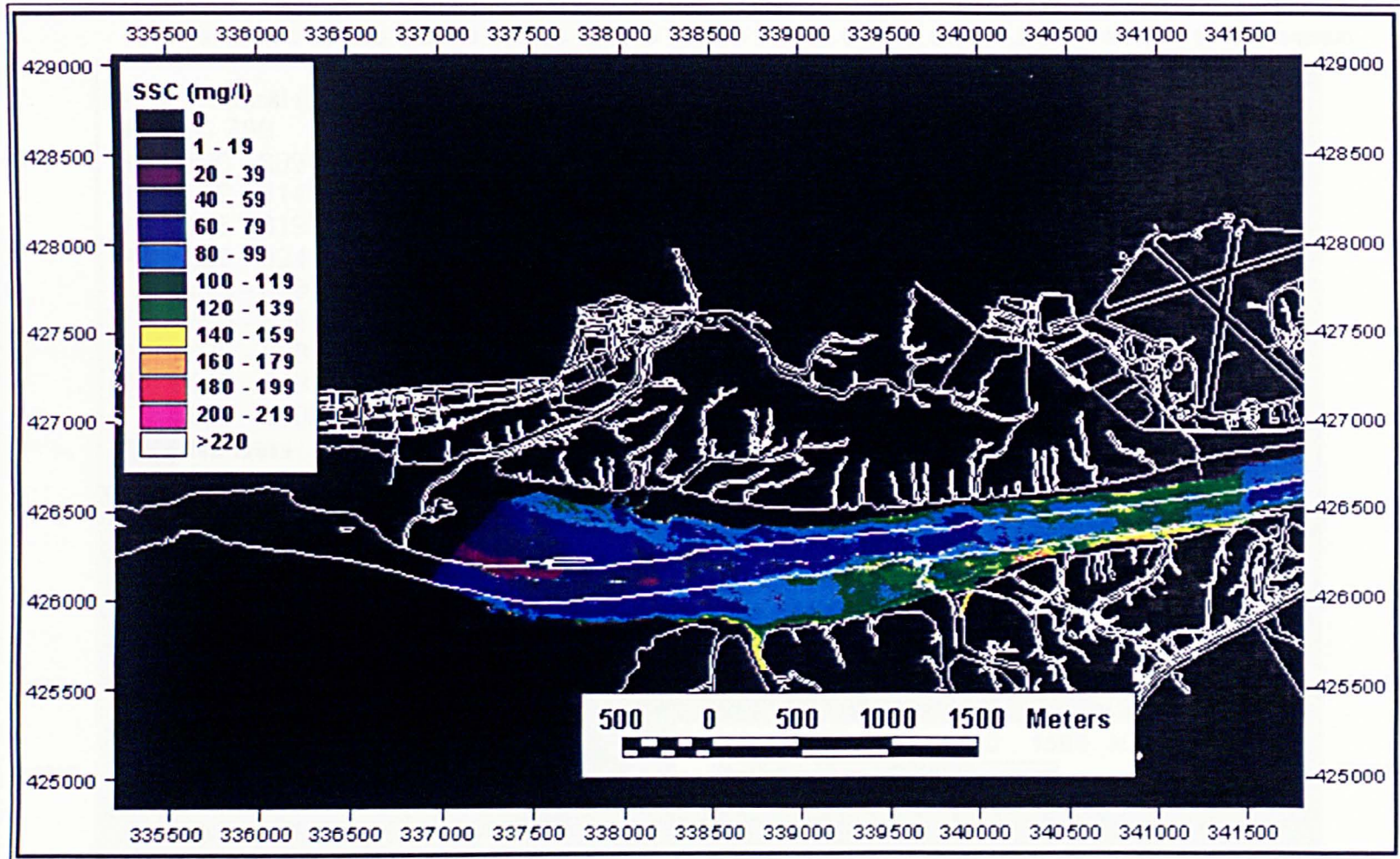


Figure 6.1d(i) CASI image calibrated to suspended sediment concentration, (mg/l), of Lytham to Warton Aerodrome, 09:02, 20-7-97.

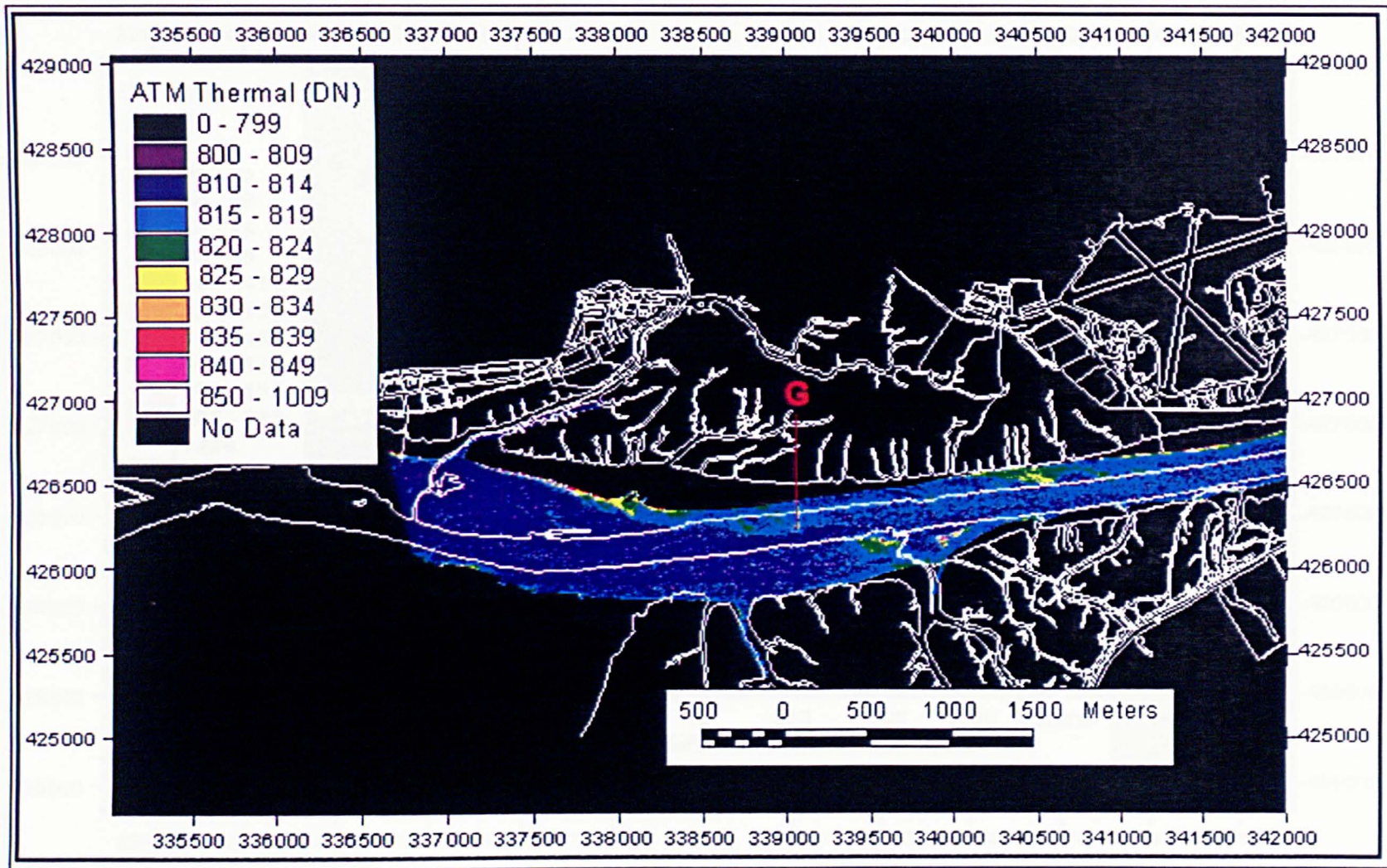


Figure 6.1d(ii) ATM thermal data of Lytham to Warton Aerodrome, 09:02, 20-7-97.

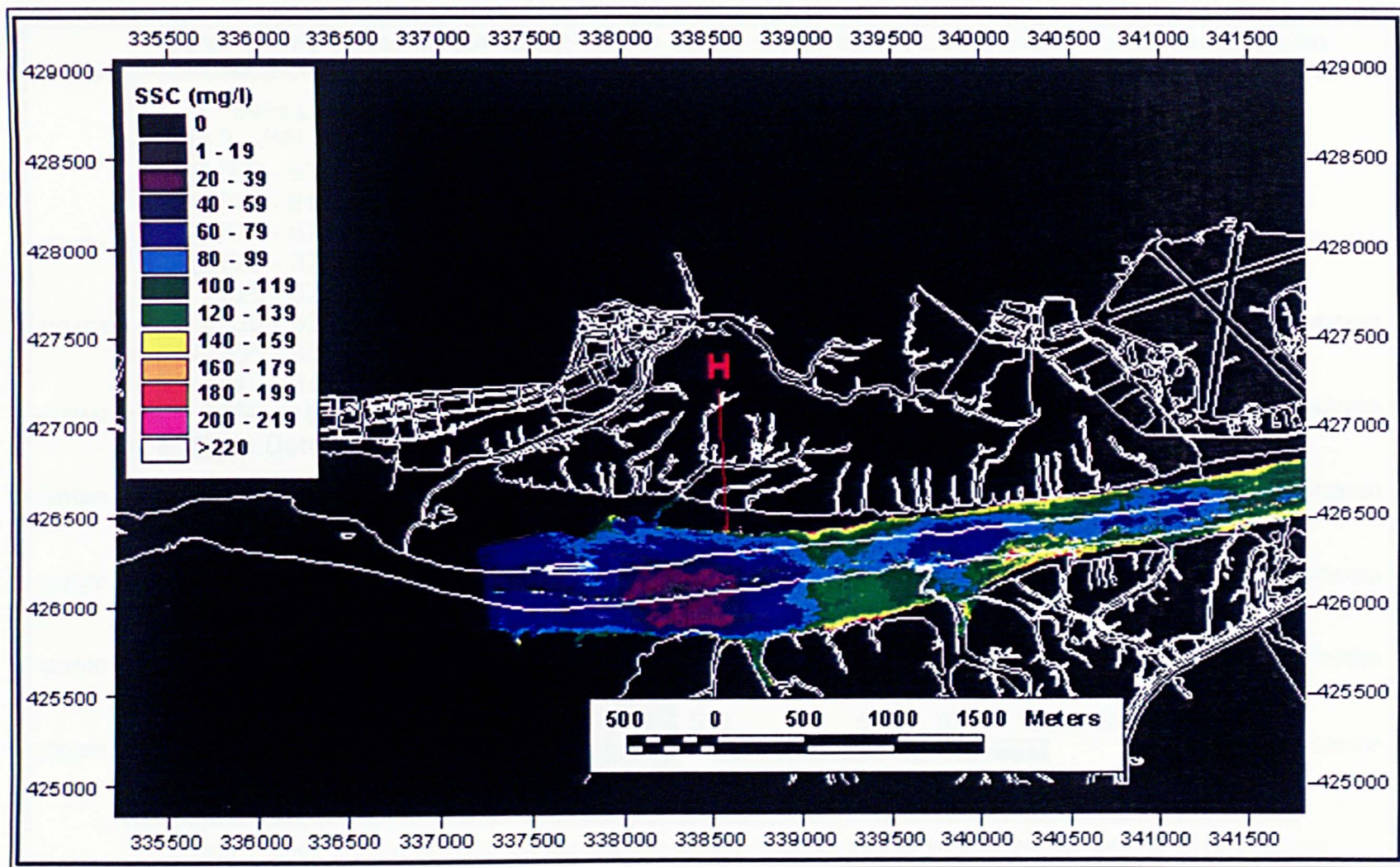


Figure 6.1e(i) CASI image calibrated to suspended sediment concentration, (mg/l), of Lytham to Warton Aerodrome, 09:20, 20-7-97.

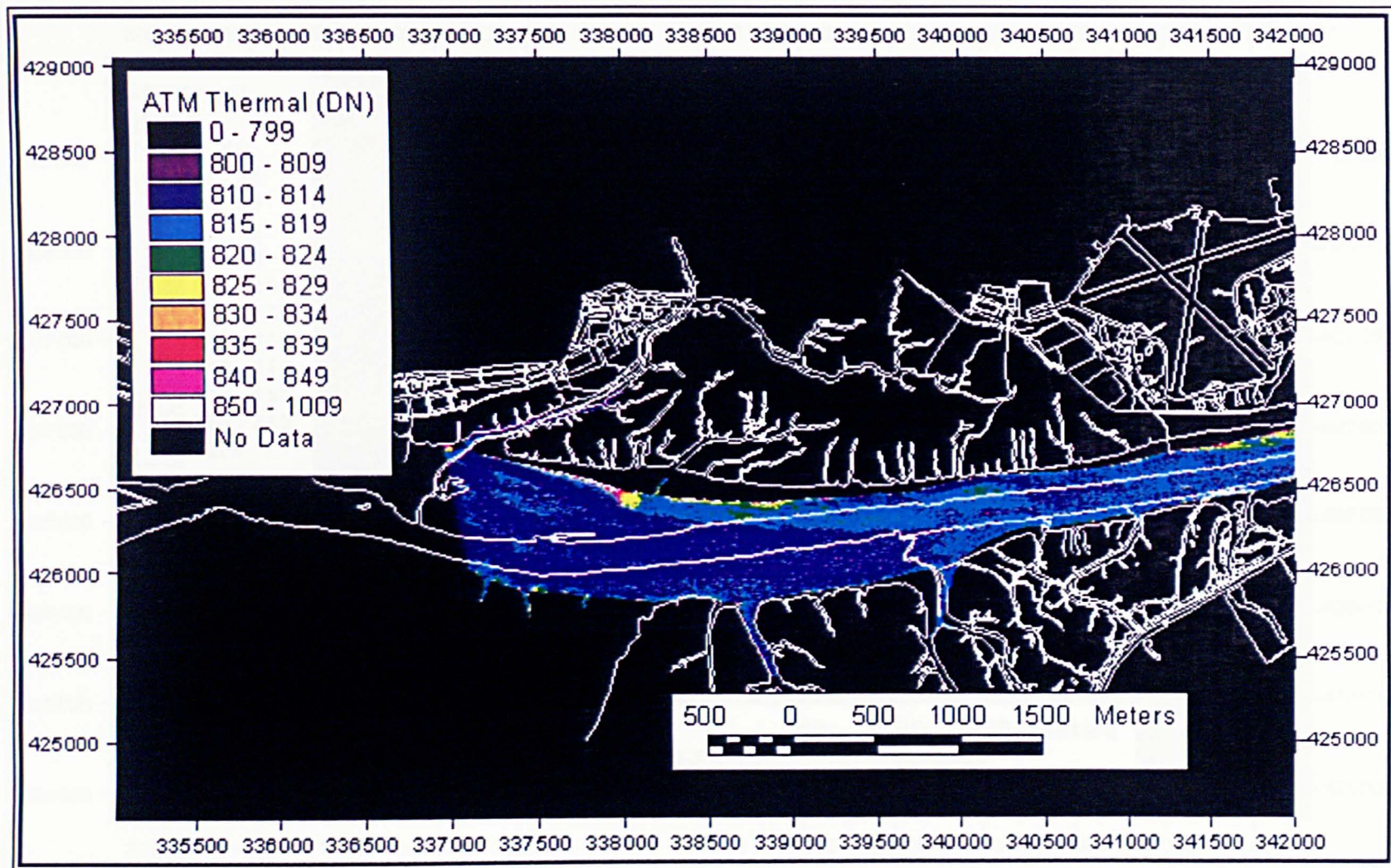


Figure 6.1e(ii) ATM thermal data of Lytham to Warton Aerodrome, 09:20, 20-7-97.

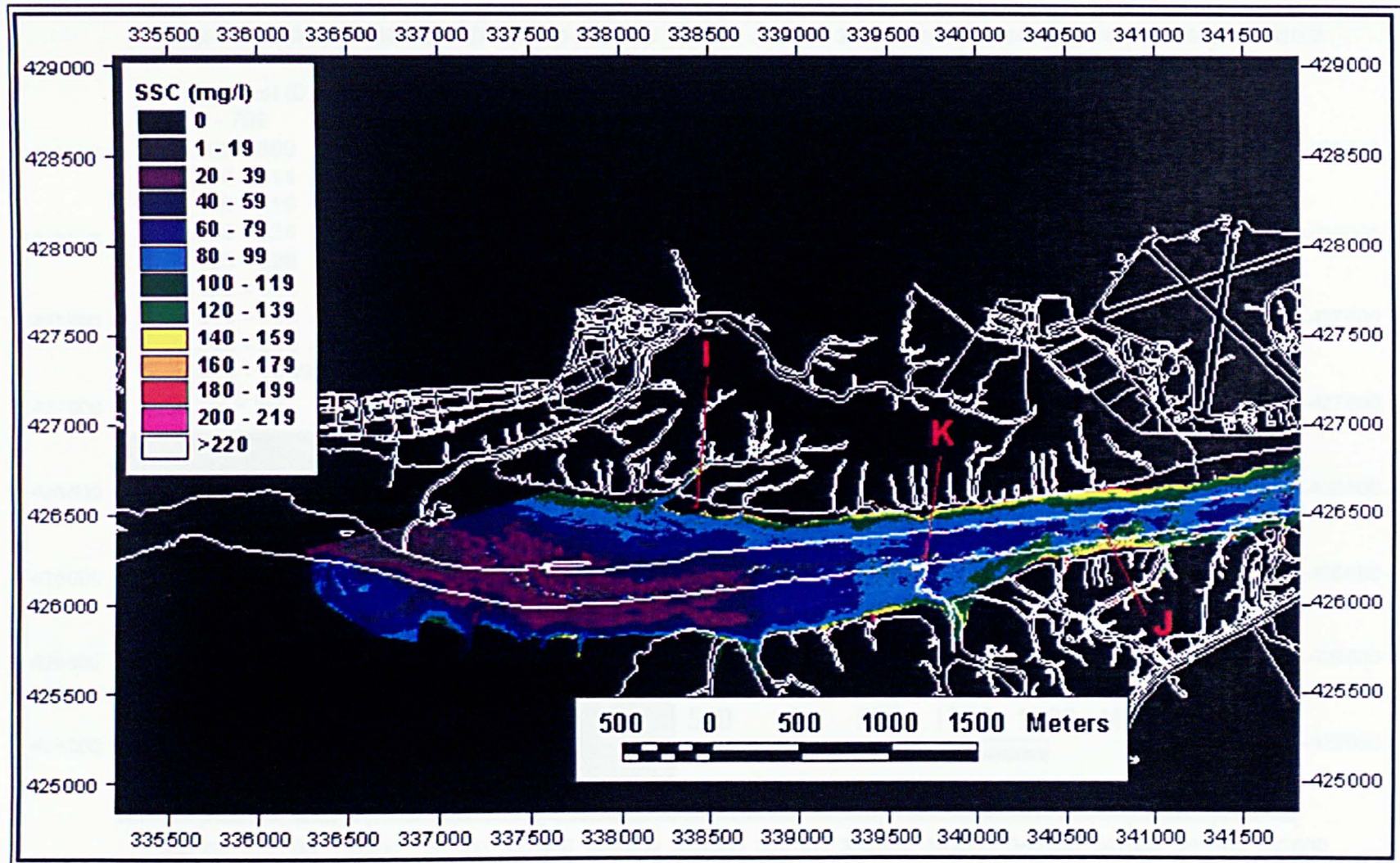


Figure 6.1f(i) CASI image calibrated to suspended sediment concentration, (mg/l), of Lytham to Warton Aerodrome, 09:37, 20-7-97.

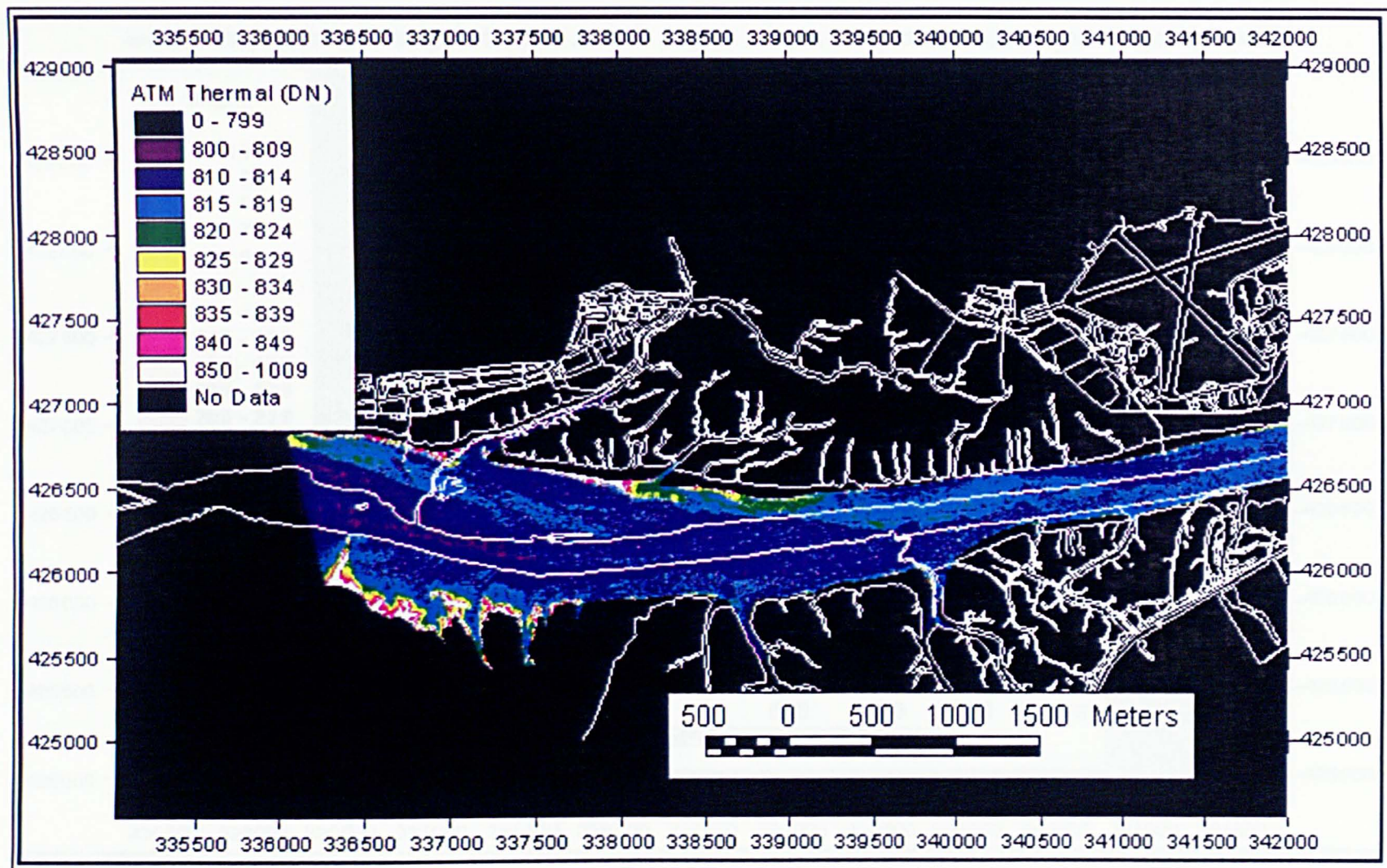


Figure 6.1f(ii) ATM thermal data of Lytham to Warton Aerodrome, 09:37, 20-7-97.

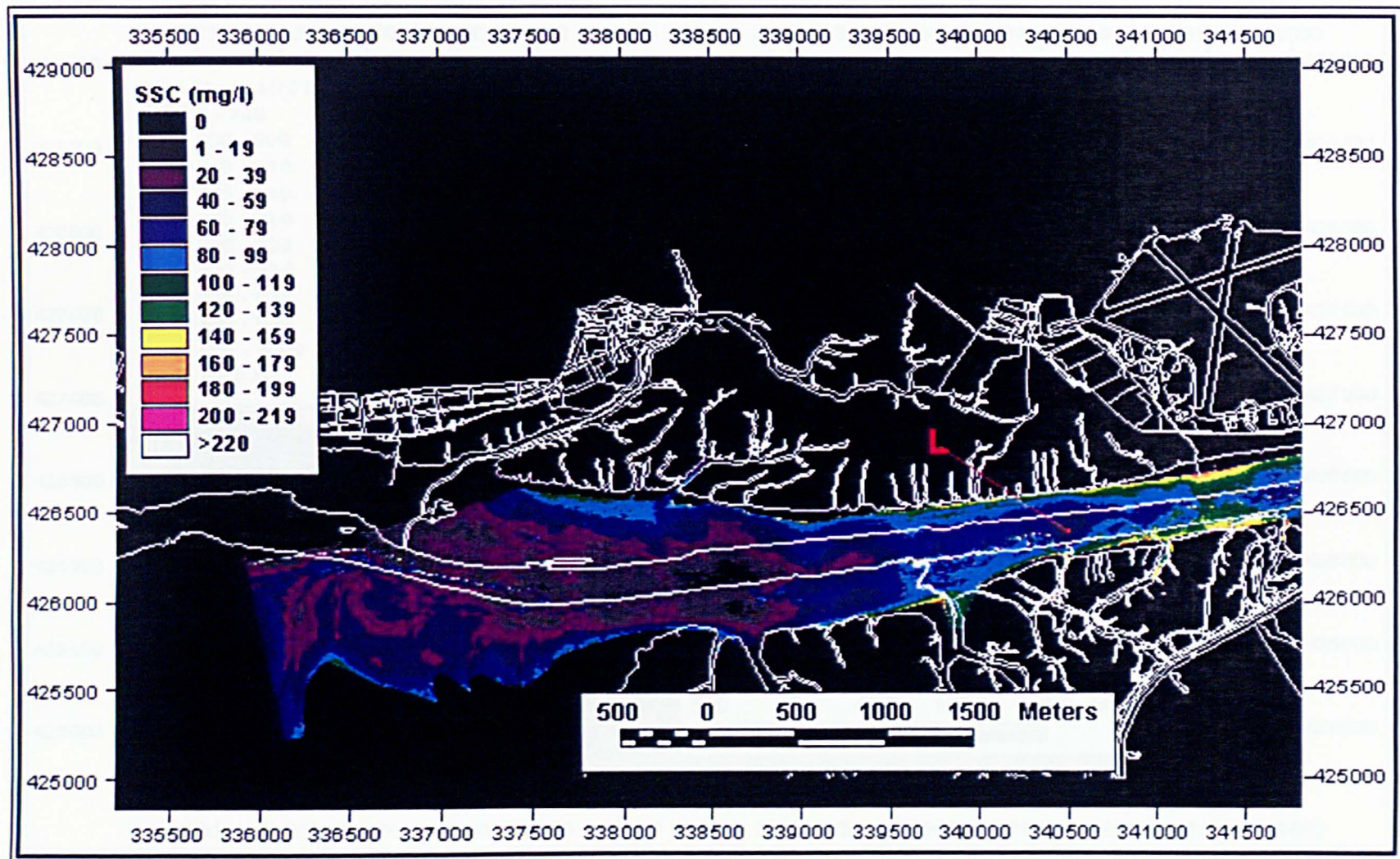


Figure 6.1g(i) CASI image calibrated to suspended sediment concentration, (mg/l), of Lytham to Warton Aerodrome, 09:55, 20-7-97.

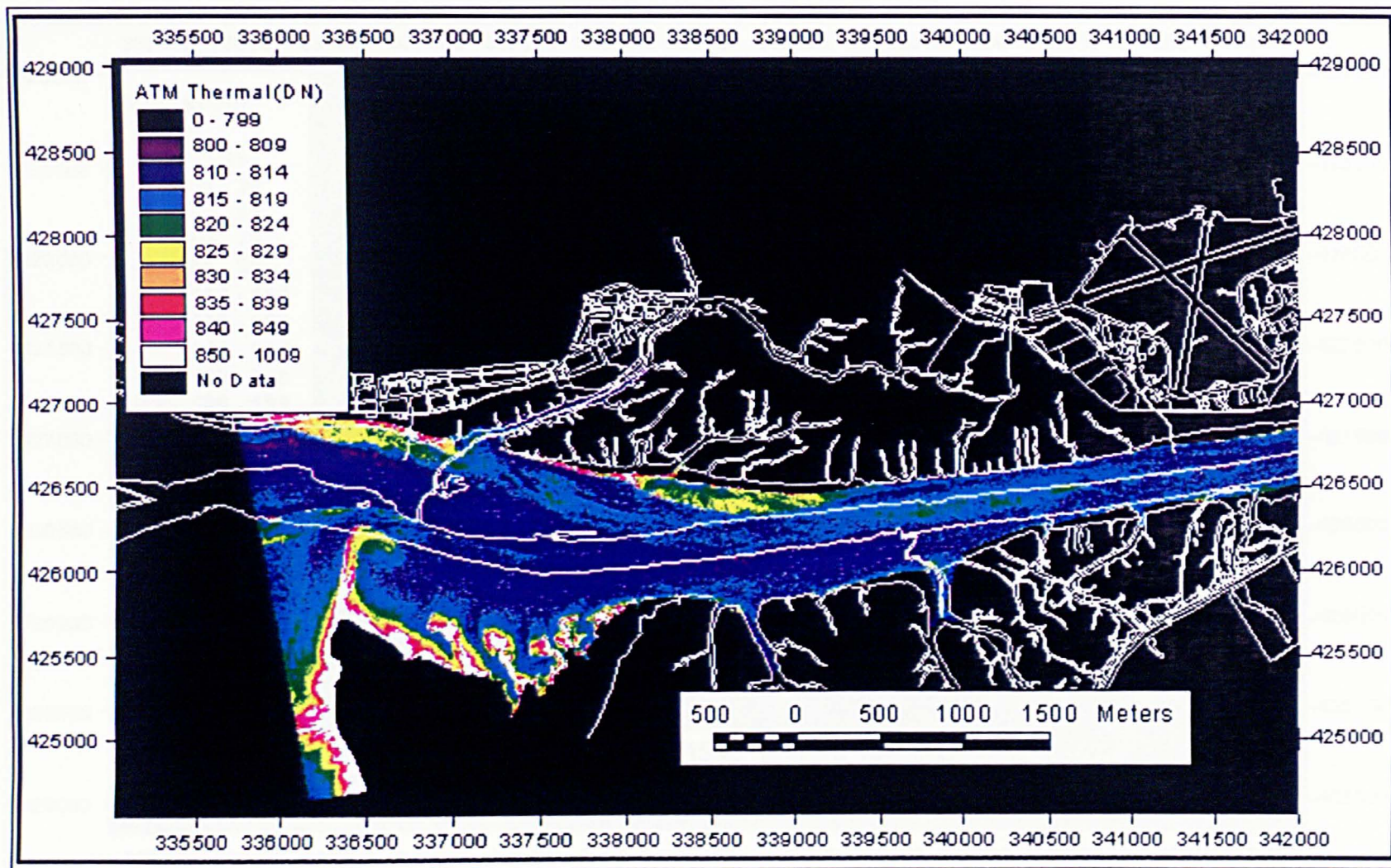


Figure 6.1g(ii) ATM thermal data of Lytham to Warton Aerodrome, 09:55, 20-7-97.

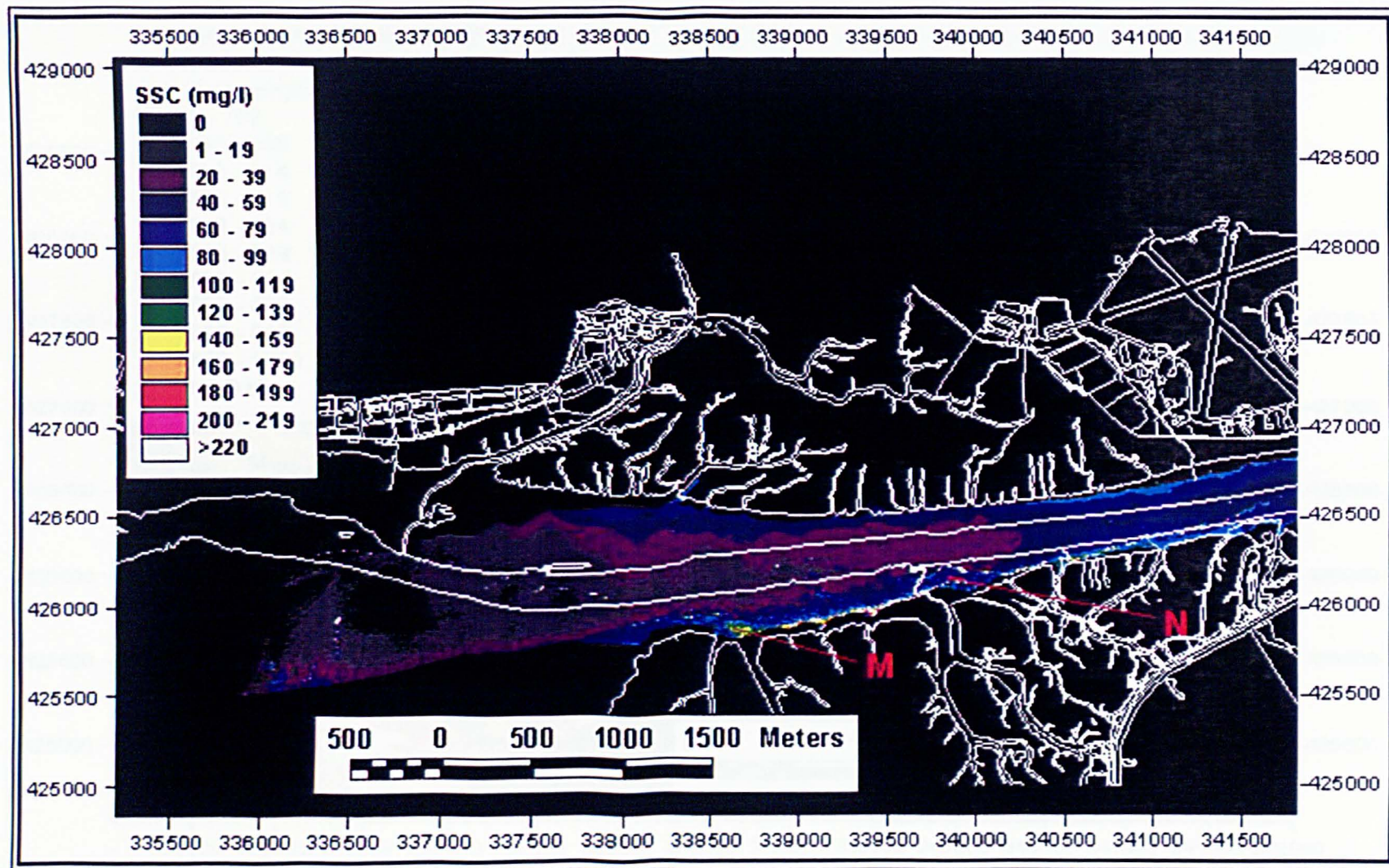


Figure 6.1h(i) CASI image calibrated to suspended sediment concentration, (mg/l), of Lytham to Warton Aerodrome, 11:11, 20-7-97.

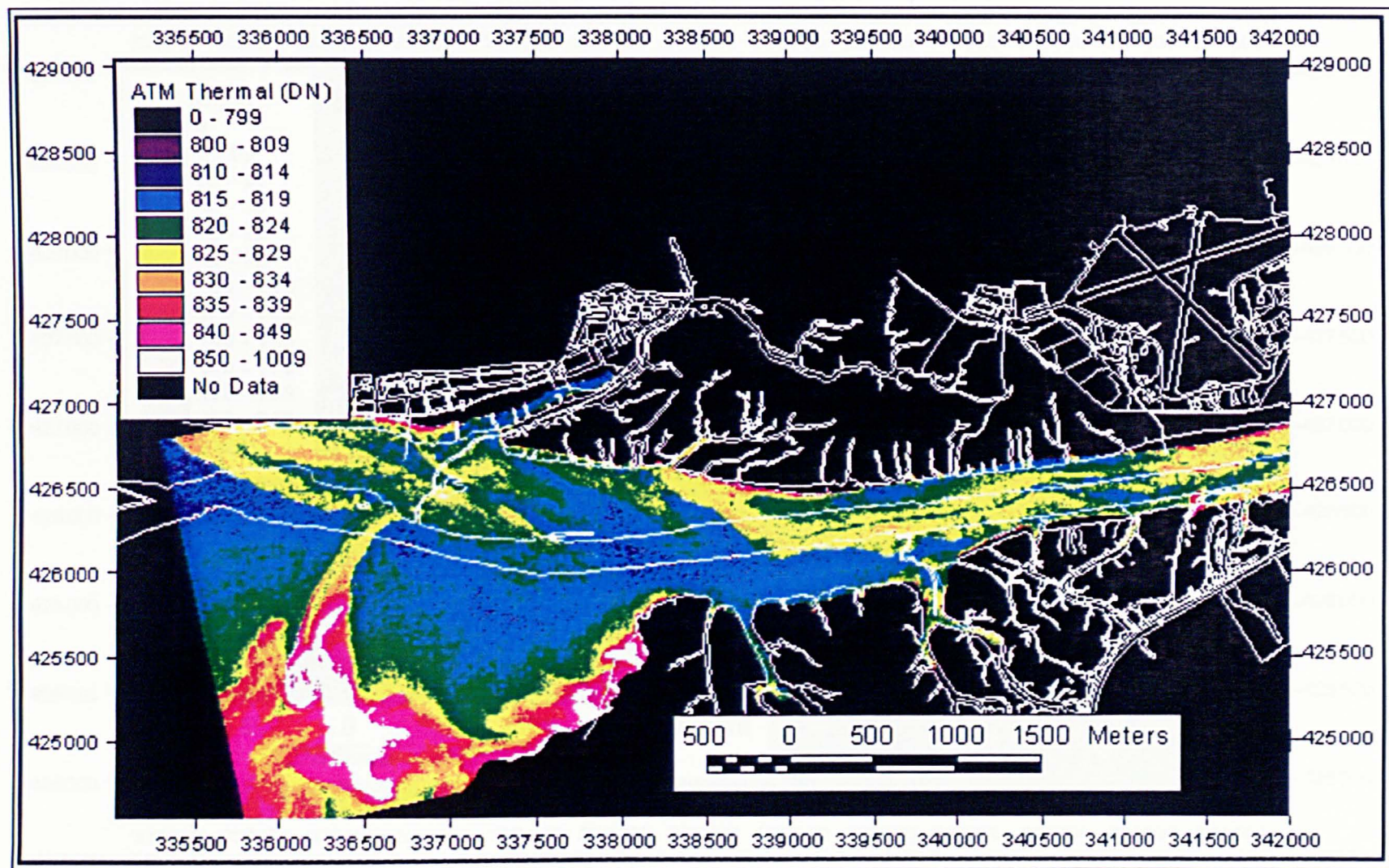


Figure 6.1h(ii) ATM thermal data of Lytham to Warton Aerodrome, 11:11, 20-7-97.

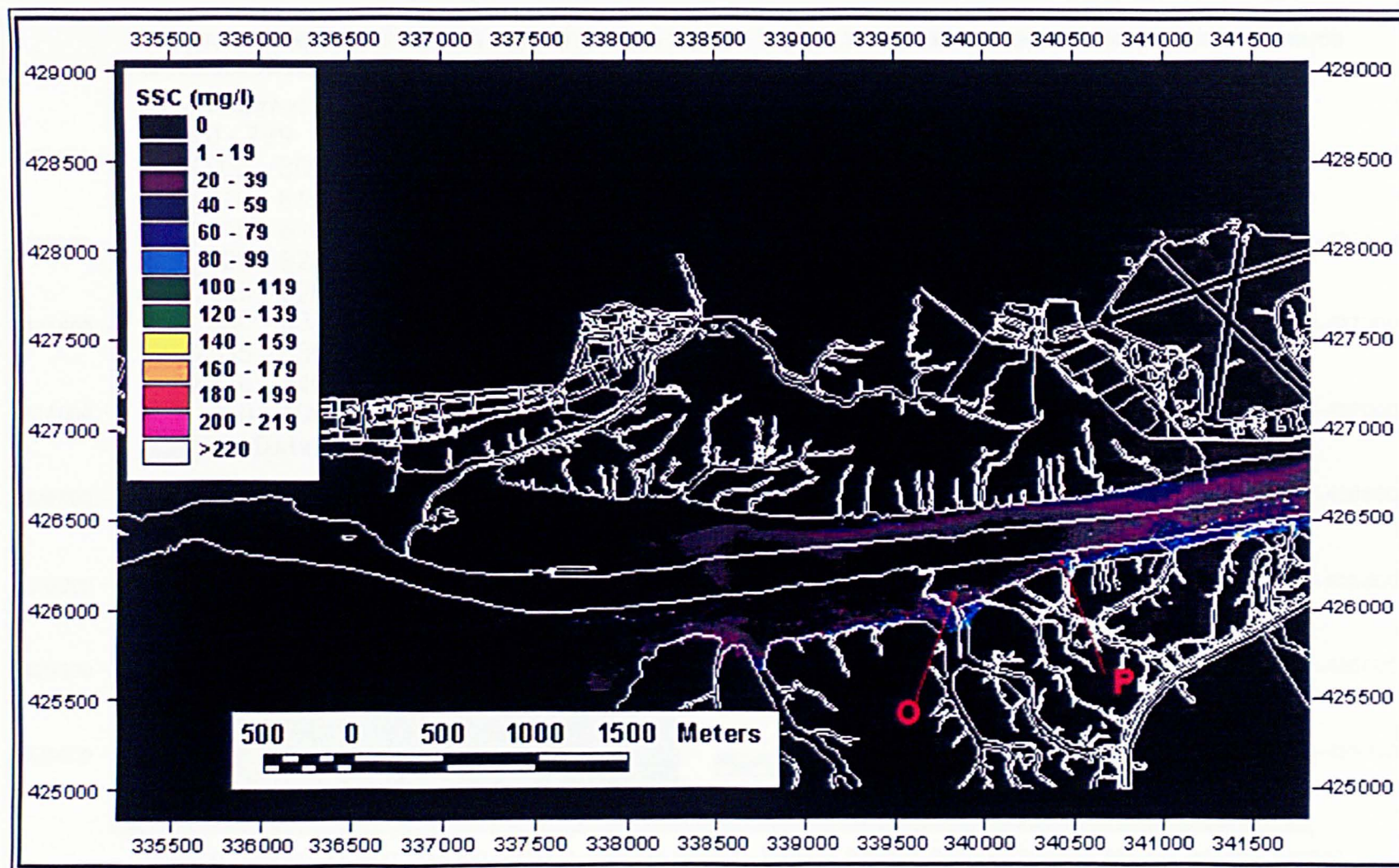


Figure 6.1i(i) CASI image calibrated to suspended sediment concentration, (mg/l), of Lytham to Warton Aerodrome, 11:25, 20-7-97.

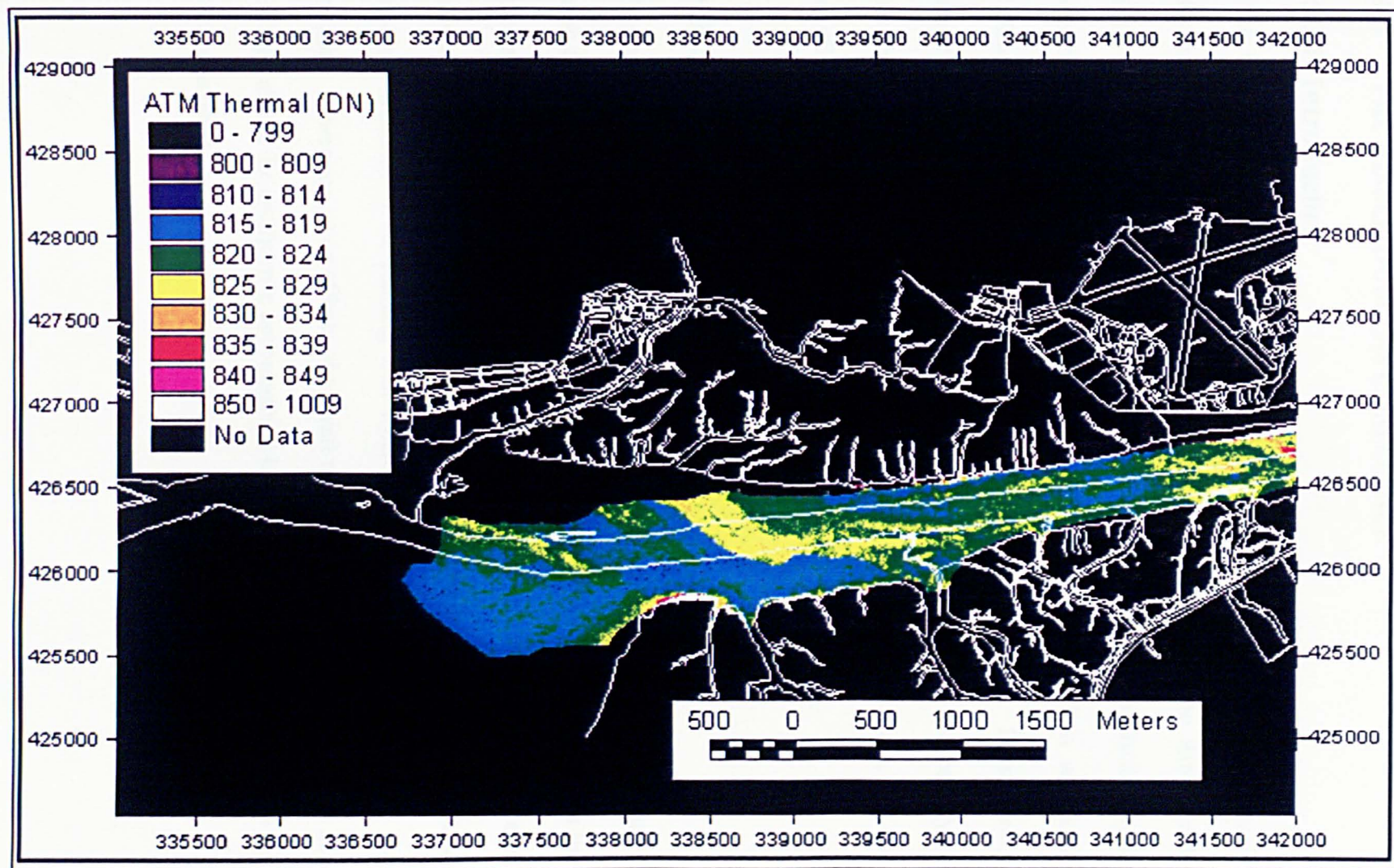


Figure 6.1i(ii) ATM thermal data of Lytham to Warton Aerodrome, 11:25, 20-7-97.

## **6.3 THE RIBBLE/DOUGLAS CONFLUENCE**

### **6.3.1 Introduction**

This is the most complex area of the whole estuary, as it is the where the river Douglas flows into the river Ribble. An investigation of this part of the Ribble estuary is particularly important, as the influence of the confluence has previously been ignored in models of sediment transport (Burton *et al.*, 1995). This section will assess the influence of the confluence on the sediment transport dynamics. In addition, major sandbanks are found within the walls that constrain this part of the estuary. These sandbanks, a function of the rapid accretion rate and confluence position, will also have an effect on the flow patterns.

### **6.3.2 08:11 GMT, Figure 6.2a**

The range of SSC in this image is approximately 60-220 mg/l and is significantly higher than the corresponding range seen in the outer estuary. The sandbanks within the main channel, as detailed in table 6.2, will play an important role in the flood tide features of this section. During ebb tides, sediment has been washed out from the intertidal areas through breaches in the training wall where it accumulates as sandbanks in the main channel. There are some effects of aircraft roll, evident as the alternate highs and lows of SSC above the confluence accompanied by a small spatial distortion of the image at the same point.

	<b>Western Limit</b>	<b>Eastern Limit</b>	<b>North or South</b>	<b>Approximate Shape</b>
<b>A</b>	341641E, 426650N	341933E, 426711N	North	Semi-circle skewed East
<b>B</b>	341970E, 426559N	342067E, 426595N	South	Semi-circle
<b>C</b>	342371E, 426808N	342585E, 426869N	North	Semicircle skewed West
<b>D</b>	342700E, 426765N	343004E, 426790N	South	Triangle: Pt 342852E,426863N
<b>E</b>	342931E, 426893N	343223E, 426905N	Central	Central wall into R. Douglas
<b>F</b>	343004E, 426972N	343607E, 427143N	North	Semi-circle
<b>G</b>	343649E, 427063N	343820E, 427136N	South	Semi-circle skewed East
<b>H</b>	343893E, 427283N	344130E, 427362N	North	Semi-circle skewed East

**Table 6.2** The positions of the sandbanks in the River Ribble-Douglas confluence area.

All areas east of the tidal bore, I, (341640E, 426645N), are not yet subject to the momentum of the flood tide. The SSC is highest where the River Douglas joins the Ribble estuary, (342890E, 426875N), probably a localised effect of the sandbank at D. The thermal image shows no thermal structure, confirming that this section of the estuary has yet to be subject to an intrusion of seawater.

### **6.3.3 08:30 GMT, Figure 6.2b**

The SSC ranges from 100-200 mg/l. There is some evidence of aircraft roll effects, indicated by the SSC decrease of 20mg/l at J, (342330E). The tidal bore is located at K, (343966E, 427275N). There is an overall increase in the SSC behind the bore in comparison to the previous image, a result of increased turbulence.

The highest SSC is where the tide washes over sandbank D (Table 6.2). Upstream of the bore, the estuary still shows higher SSC in the centre of the main channel. Once the

bore has passed here this is no longer apparent. There is also high SSC to the west of the island sandbank, **L**, (343400E). Foam lines indicating water body boundaries or convergent currents are not evident here.

#### **6.3.4 08:45 GMT, Figure 6.2c**

The range of SSC for this image is 60 mg/l to 220 mg/l. There is evidence of aircraft roll at **N**, showing an increase of 20 mg/l over a large area with a corresponding spatial distortion resulting from problems with the NERC geo-correction software.

A lens of lower SSC lies in the main channel, **M**. This is trapped within the training walls. Water has begun to inundate the northern intertidal areas. There is a line of increased SSC above the training wall, hence the wall must be creating turbulent flow, which increases SSC. Over the mud flats the SSC increases by 20-40 mg/l, increasing towards the edge of the water. SSC is also increased around and upstream of the sandbank at 342400E indicating erosion of the bank and a net upstream movement of sediment. At the confluence (343100E, 426900N) there is lower SSC in the main channel. Sediment suspended from the sandbank on the southern training wall (6.2a **E**) is being swept into the river Douglas. Above the confluence the water is well mixed with SSC of 120-160 mg/l. Foam lines of the axial convergence front have formed in the centre of the main channel to the west of the confluence and stretches as far as the entrance to Freckleton Brook, **O** (343600E, 427100N).

#### **6.3.5 09:02 GMT, Figure 6.2d**

The range of SSC for this image is approximately 40-180 mg/l. There are spatial distortions over the length of the image due to the inability of the NERC GCORR

software to correct for aircraft roll. The three areas where SSC is affected by these roll distortions are **P**, (341480E to 341950E) reducing SSC by 20 mg/l, **Q**, (342950E to 343220E), reducing SSC by up to 40 mg/l and **R**, (344600E to 344830E), increasing SSC by 20 mg/l. The SSC is generally lower in the centre of the channel increasing towards the edge of the water.

A well-defined foam line along the length of the image indicates the presence of a strong axial convergence front that shows no disruption at the confluence, implying that the sandbanks within the main channel have little effect on the convergence. There are higher SSC values above the north training wall to the west of the confluence that is not seen east of the confluence. The coincidental thermal imagery shows that there is evidence of a warm input at **S**, (342350E, 426990N). As there is no flow from the creeks on the south shore it is likely that the warmer feature is a result of sediment erosion. There is also a warming of the water where inundation has occurred over the sandbank in the central V-shape of the training walls at the confluence, possibly due to heat transfer from the warmer sediments.

### **6.3.6 09:20 GMT, Figure 6.2e**

The SSC range for this image is approximately 60-220 mg/l, an overall increase from the previous image. The SSC image shows some spatial distortions, particularly at **T**, (342400E to 343050E), where the SSC is reduced by as much as 40 mg/l or 40%. A distortion of similar magnitude is seen at **U**, (344500E to 344600E).

The lowest SSC values are seen in the centre of the main channel. The concentrations increase over the intertidal areas reaching a maximum at the water's edge. The line of

higher SSC values directly above the training wall is still visible for the western side of the image (342000E to 342800E) but not seen east of the Ribble-Douglas confluence. The highest SSC values are found at V, (343700E, 426950N), where sediment is eroding off Longton Marsh as confirmed by the thermal image. Further evidence of erosion is seen on both the CASI and ATM thermal images for both sides of the channel east of the confluence and the thermal image also suggests that sediment appears to be eroding from Warton Bank.

The foam line patterns are now more complex around the confluence area. A well-defined foam line hugs the southern side of the main Ribble channel, extending as far as the confluence, entering the channel of the river Douglas and diminishing quickly. Another foam line begins at 342820E, 426930N running parallel to the other foam line up to the confluence and on into the Ribble channel. After the confluence the foam line starts to show large sinusoidal patterns, suggesting more turbulent flow, possibly as a result of the sandbanks detailed in table 6.1. After the sandbanks, the foam line becomes more linear and evidence of suspended sediment being pulled into the centre of the channel can be seen. The thermal data show that the convergence front inhibits warmer water from Warton Bank from mixing with water in the southern part of the channel up as far as Freckleton Brook, (343650E, 427150N).

### **6.3.7 09:37 GMT, Figure 6.2f**

The range of SSC for this image is 40-200 mg/l. There is only one area that is affected by aircraft roll, where the SSC is increased by approximately 30-40% at W, (341900E to 342500E).

The lower SSC values are found in the main channel, particularly off Freckleton Brook. Laterally, the concentrations generally increase towards the shore and longitudinally, the SSC tends to increase towards the east. The area of highest SSC is off Longton Marsh on the south bank of the river at X, (344000E), evident in both CASI and ATM thermal imagery. There is also evidence of further sediment erosion along the north bank of the river at Y, (344130E).

Well-defined foam lines are visible along the entire image. To the west of the confluence the foam lines show large sinusoidal patterns with the crests approximately 400m apart, suggesting that there is convergent flow but that this must be subject to some form of shear stress. The strong foam line starts to break up on approach to the confluence, where the foam is washed over the point of the training wall and onto Longton Marsh rather than into river Douglas. Aerial photographic evidence shows that there is a foam line running down the centre of the river Douglas, but it does not form until 343840E, 426540N. In the Ribble the foam line is not re-established until approximately 1500m past the confluence (344500E, 427390N). After the confluence the foam line is more linear and dense than before, suggesting stronger convergent flow.

### **6.3.8 09:55 GMT, Figure 6.2g**

The SSC range for this image is approximately 40-200 mg/l. The lower SSC values are found in the centre of the main channel, these increase rapidly outside the constraints of the training wall. There is also a general trend of the SSC increasing towards the east. The area of highest SSC is the same as the previous image. Aerial photographic evidence suggests that the water is now up to the edge of the saltmarsh at the western extreme of Longton Marsh, where vegetation is probably resisting erosion. Therefore,

the main area of erosion is occurring a short distance to the east of the previous image. There is also significant erosion occurring along the northern bank in this same area.

Foam lines are still visible in this image but are becoming more fragmented. The foam line disappears completely around the confluence and there is no line visible around Freckleton Brook. East of the confluence the foam line starts to develop in the area where the SSCs are highest, but does not remain intact for more than 600m. It runs parallel to the riverbanks but is located above the southern training wall rather than the centre of the channel.

### **6.3.9 11:11 GMT, Figure 6.2h**

The SSC range for this image is 20-120 mg/l, an overall decrease in SSC since the previous image and also an overall increase in temperature. The time difference between the two images is the largest for the series of images due to the refuelling of the aircraft.

The lowest SSC values are found within the main channel, increasing slightly towards the east. On the intertidal areas outside the training walls the SSC does not increase as rapidly towards the shore as previously. This may be due to decreased current velocity. In this location the sediments consist of medium-coarse sand (Rainey, 1999). If there has been a significant decrease in the current velocity this sediment would not be so easily suspended. This decrease in current velocity is supported by the thermal imagery, which shows the outflow from Freckleton Brook beginning to ebb.

The foam lines indicating the presence of the axial convergence front are still visible along the length of this image. At the western end of the image the foam line is relatively linear, however, on approaching the confluence the line starts to distort into the large sinusoidal patterns seen in previous images. Nearer the confluence this breaks up into a series of individual elongated S-shapes. As the confluence is approached the distance between the crests of the sinusoidal line decrease, being 310m, 300m, 245m and 235m respectively. East of the confluence the amplitude of these sinusoidal patterns gradually decreases and again approximate a linear feature, suggesting that this sinusoidal pattern is created by the presence of the confluence. This could be a result of either the split into two river channels or the presence of the submerged sandbanks.

#### **6.3.10 11:25 GMT, Figure 6.2i**

The SSC range for this image is 0-100 mg/l, a further overall decrease. The lowest SSC values are in the main channel and around the area of the confluence. The water overlying the intertidal areas outside the training wall shows a slightly higher SSC of 20-40 mg/l but there is no increased concentration along the very edges of the image suggesting that erosion has ceased. The only area of high SSC west of the confluence is where a complex creek enters the estuary, implying that sediment is now being introduced into the estuary not by erosion but by the draining of the saltmarsh creeks. The ebbing of creek outflow on the thermal image supports this. However, at Longton Marsh just 500m east, warmer water/sediment is being pulled from the shoreline towards the centre of the main channel but with a distinct easterly flow pattern suggesting there is still some convergent flow. The large areas of white along the edges of the thermal image, representing the warmest areas, are likely to be areas where

shallow water is warmed by the underlying mud banks as there is no corresponding high SSC in the CASI image.

The foam lines are less visible on this image but they are very similar to that of the previous image. The large elongated S-shapes can be seen to the west of the confluence where the foam dissipates and becomes very fragmentary. The linear convergence is not reformed until approximately 1300m east of the confluence at **Z**, (344400E, 427380N).

### **6.3.11 Confluence summary**

1. The confluence area shows a continuation in the general pattern of higher SSC towards the upstream of the image, also observed in the outer estuary.
2. The overall SSC rises through Figures 6.2a to 6.2c (08:11 to 08:44 GMT) after which the concentrations remain approximately constant until settling of the suspended sediment occurs in Figures 6.2h (11:11 GMT) and 6.2i (11:25 GMT).
3. There are significant quantities of sediment being resuspended as the tide floods the sandbanks contained within the training walls of the main river channel that are visible in the first low water image.
4. As the tide starts to wash over the sandbank in the point of the confluence there is a large increase in SSC as sediment is eroded (Figures 6.2c to 6.2f, 08:44 to 09:55 GMT). As this supply of sediment is eroded off the initial point of the sandbank the SSC shows evidence of the erosion zone progressing along Longton Marsh in an easterly direction.

5. Another area of erosion introducing sediment into the estuary is that of the creek at the eastern end of Warton aerodrome, this is particularly evident in Figure 6.2f (09:55 GMT).
6. The foam lines marking the axial convergence front appear to be subject to greater lateral stresses here than other sections of the river, as sinusoidal patterns that develop later in the flood tide, are larger for this area.
7. The thermal data of Figures 6.2h and 6.2i show that the water flowing into the Ribble from Freckleton Brook has started to ebb, therefore the current velocity of the flood tide must be greatly reduced by 11:00am.

This image series has shown the confluence area to be more complex than the Warton Bank section as the basic estuarine V-shape intrusions are not evident. The confluence itself produces a turbulence that results in the main area of resuspension of sediment being from Longton Marsh. The formation of the axial convergence front is not affected, however the instabilities giving sinusoidal patterns during the collapse of the front are greater in this area.

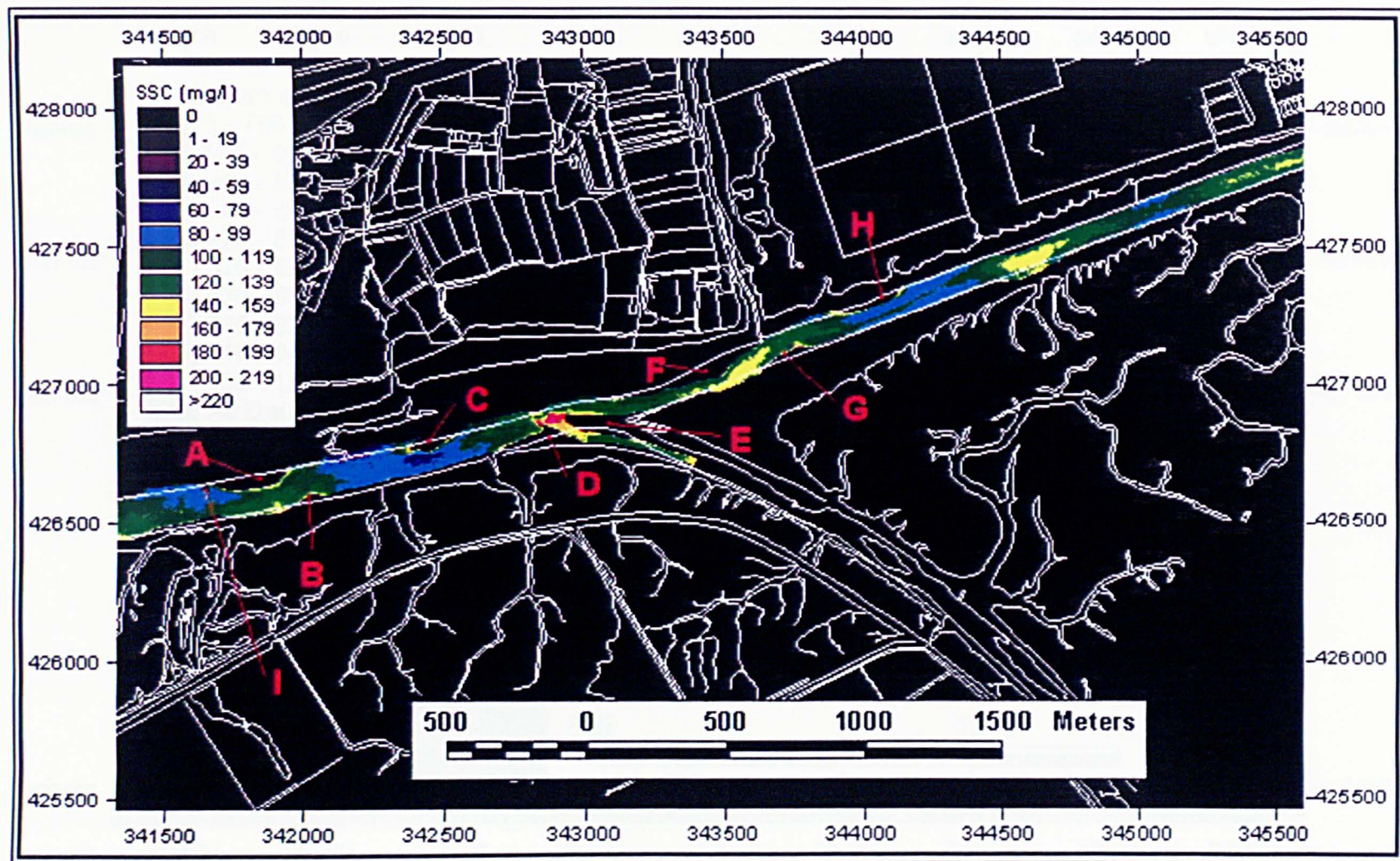


Figure 6.2a(i) CASI image calibrated to suspended sediment concentration, (mg/l), of the confluence area, 08:11, 20-7-97.

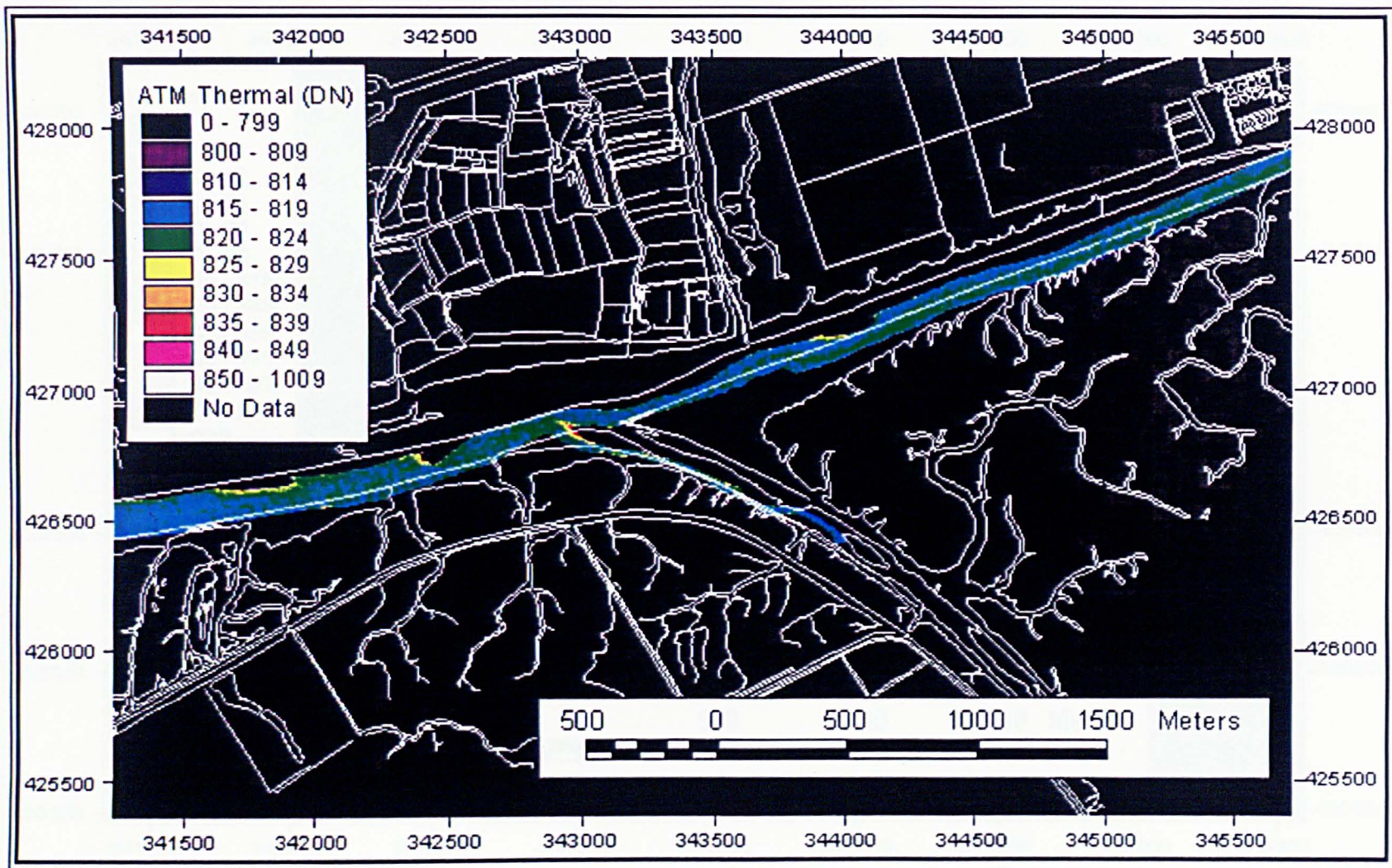
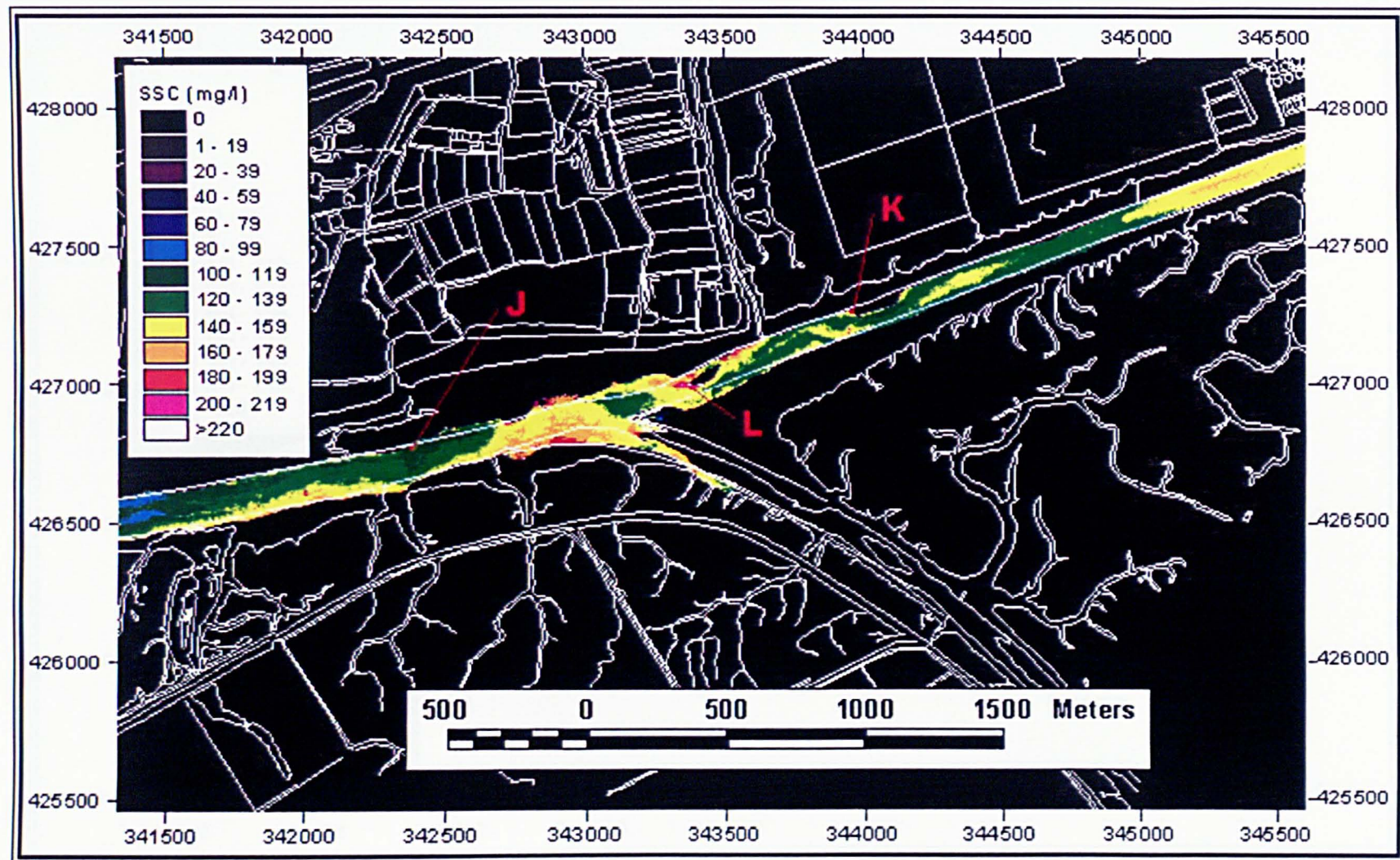


Figure 6.2a(ii) ATM thermal data of the confluence area, 08:11, 20-7-97.



**Figure 6.2b(i)** CASI image calibrated to suspended sediment concentration, (mg/l), of the confluence area, 08:30, 20-7-97.

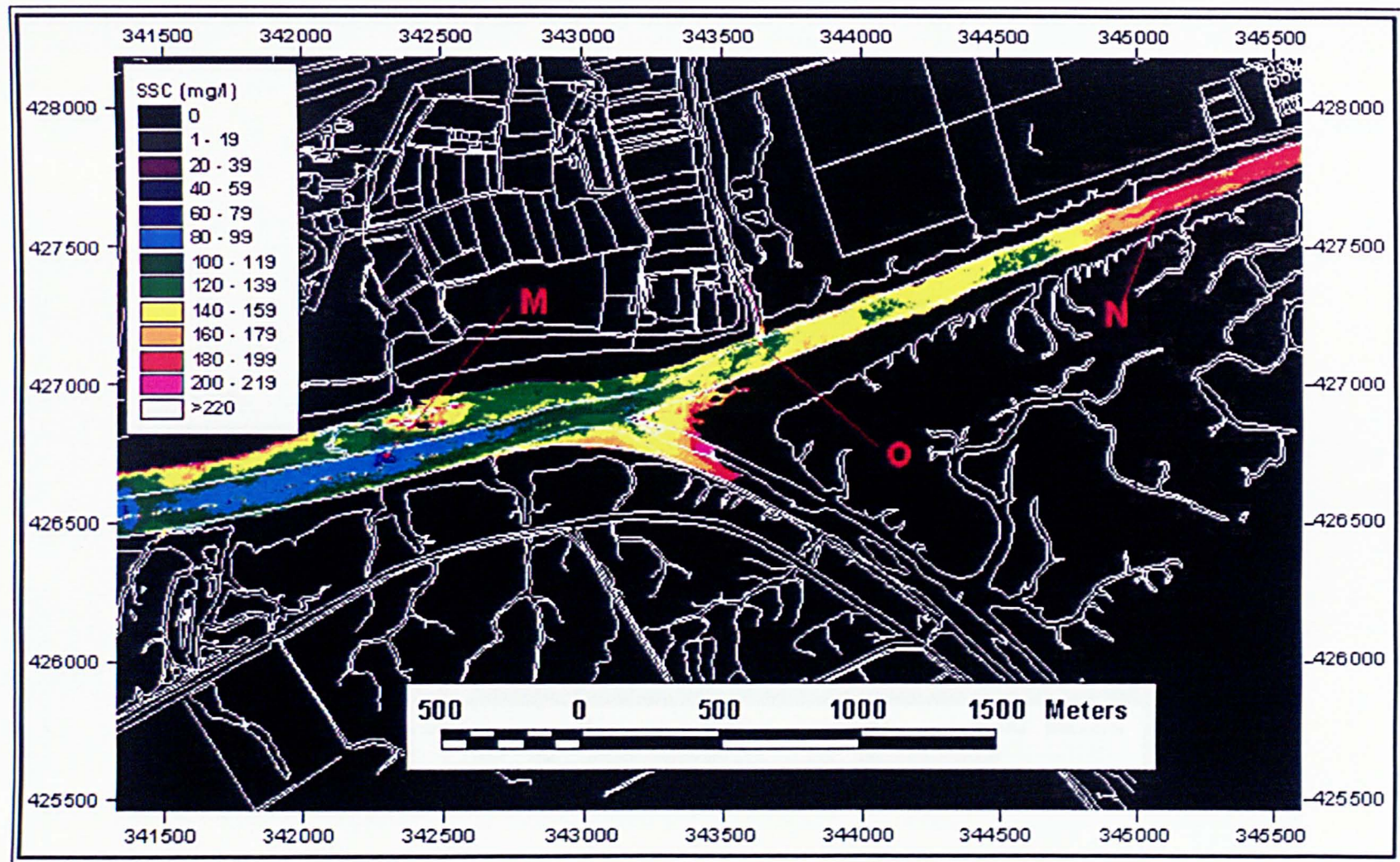


Figure 6.2c(i) CASI image calibrated to suspended sediment concentration, (mg/l), of the confluence area, 08:44, 20-7-97.

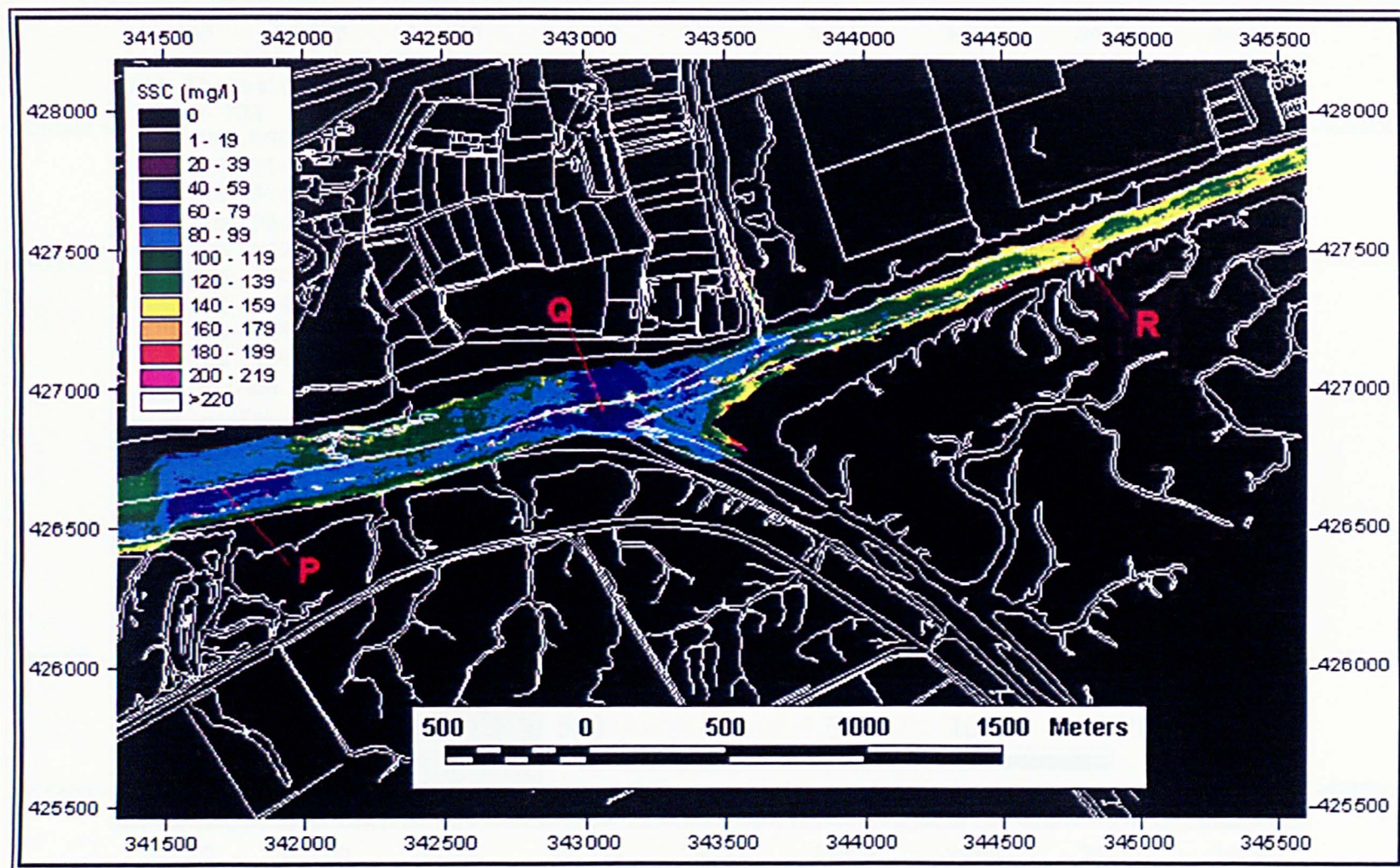


Figure 6.2d(i) CASI image calibrated to suspended sediment concentration, (mg/l), of the confluence area, 09:02, 20-7-97.

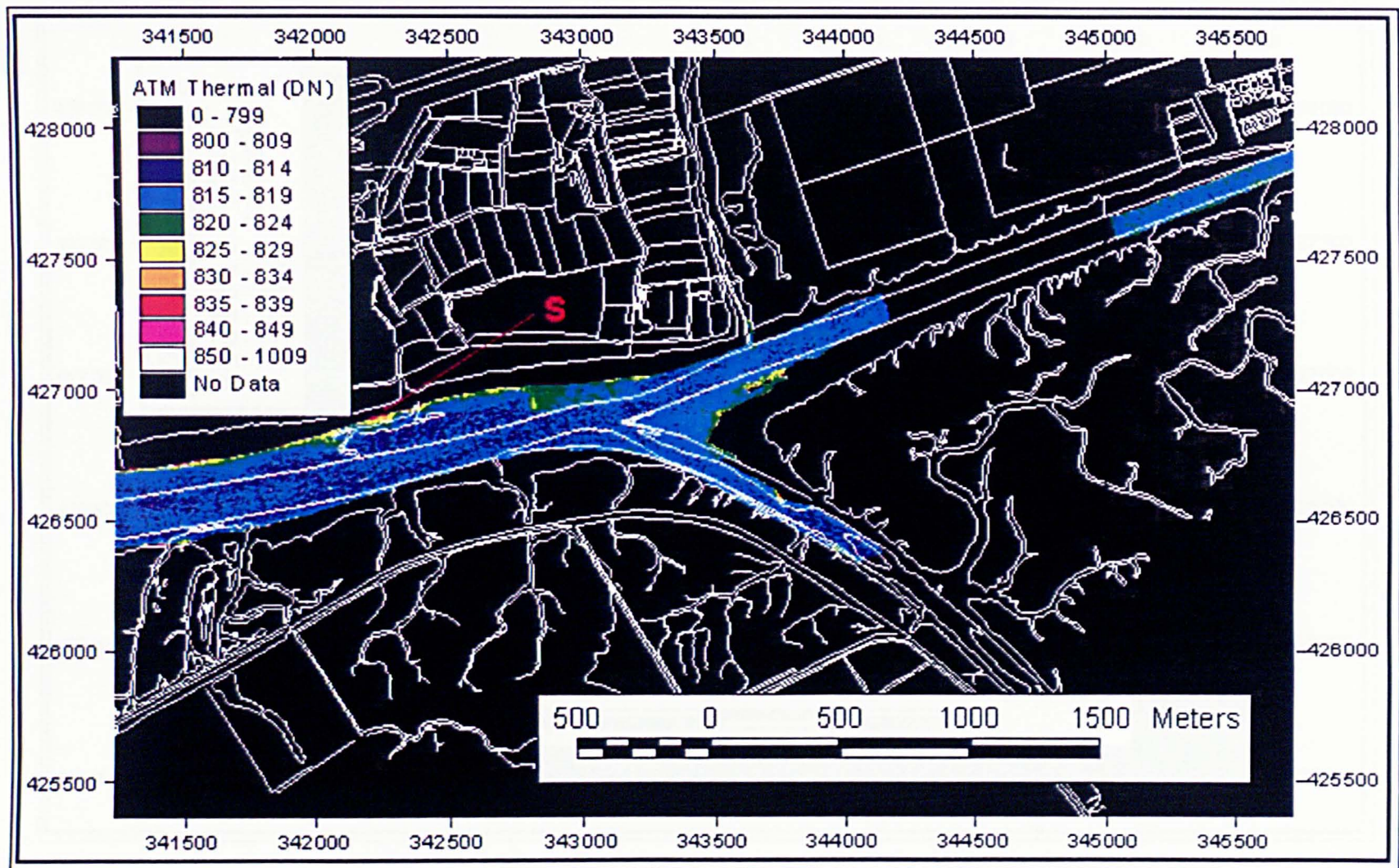


Figure 6.2d(ii) ATM thermal data of the confluence area, 09:02, 20-7-97.

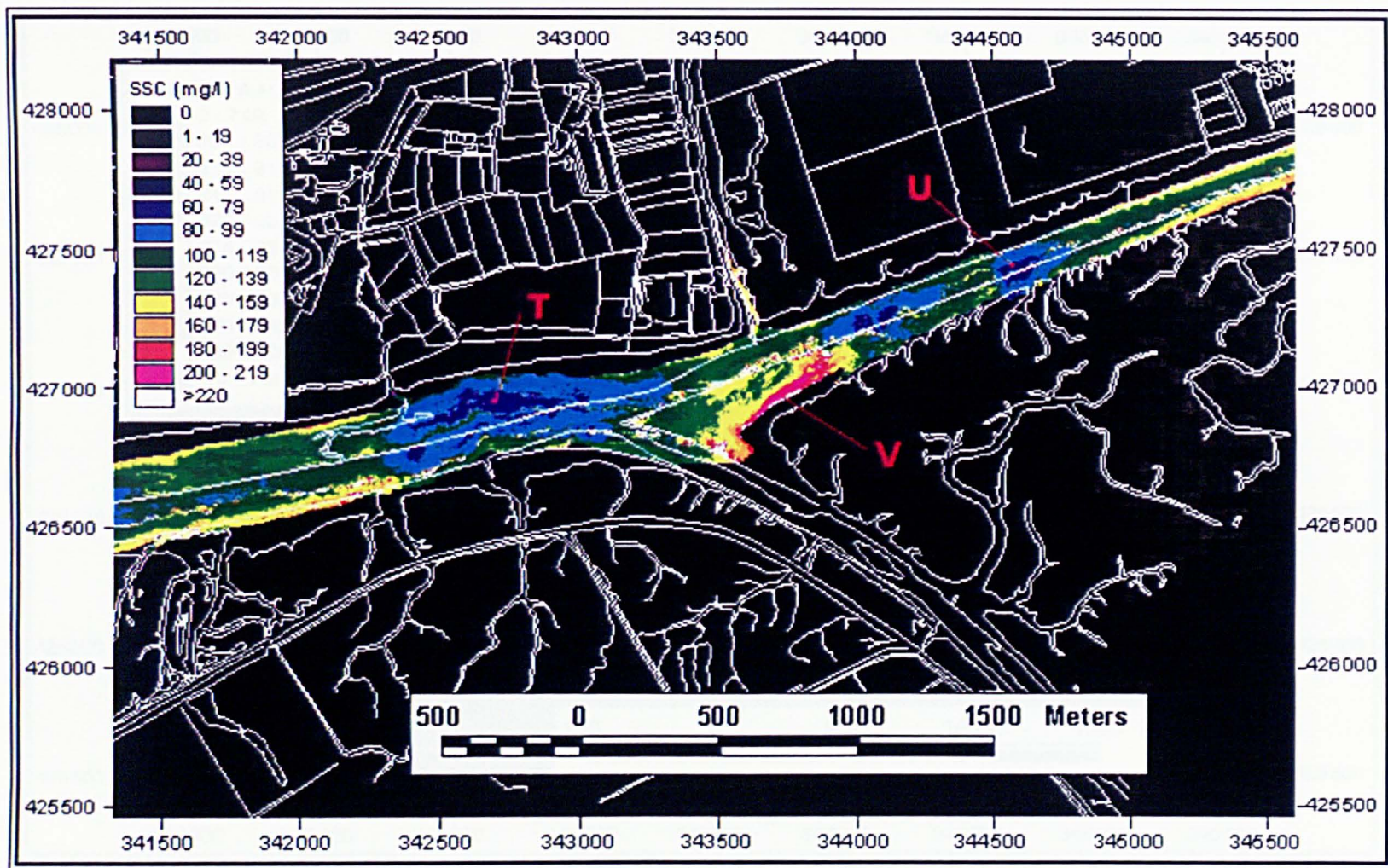


Figure 6.2e(i) CASI image calibrated to suspended sediment concentration, (mg/l), of the confluence area, 09:20, 20-7-97.

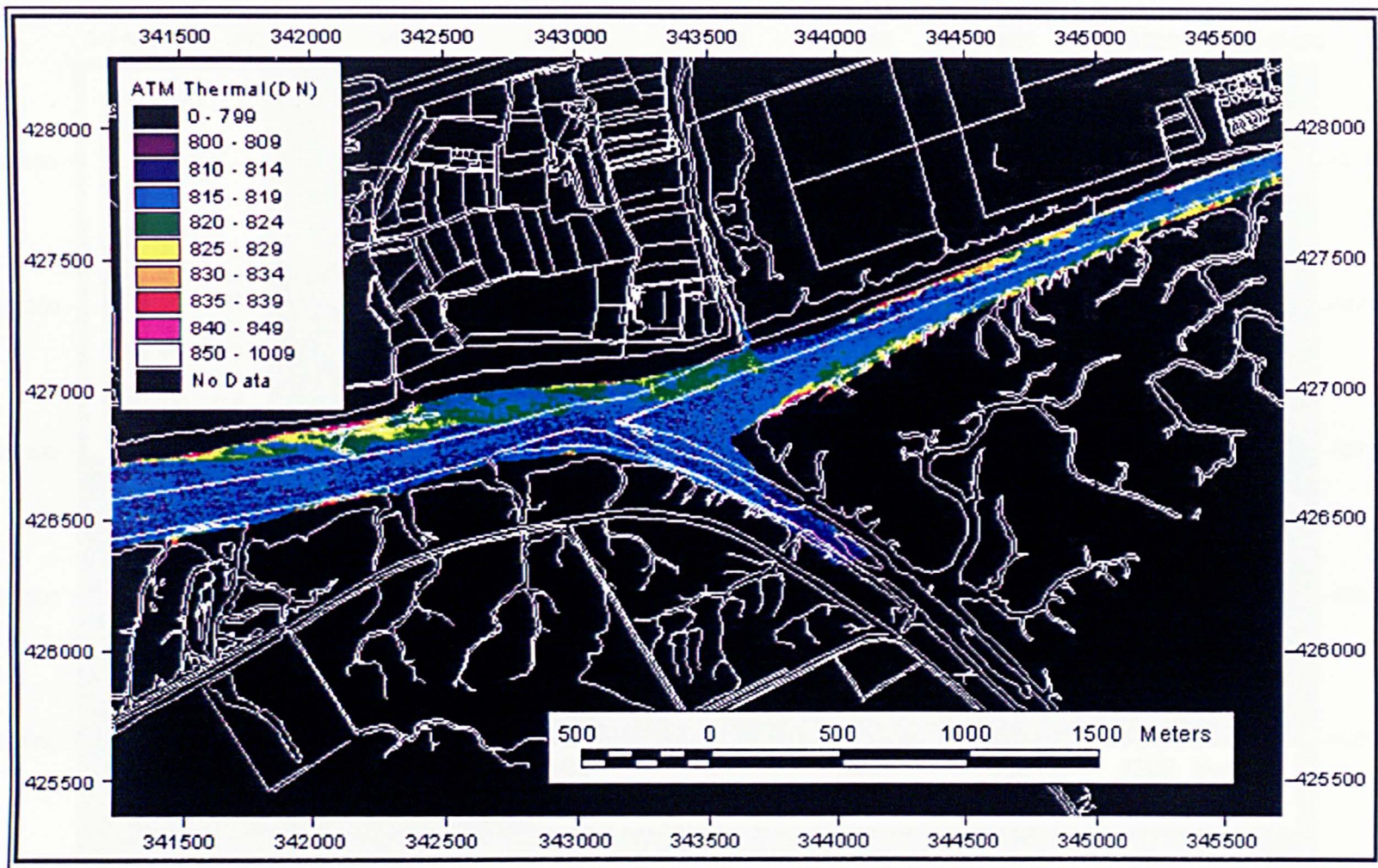


Figure 6.2e(ii) ATM thermal data of the confluence area, 09:20, 20-7-97.

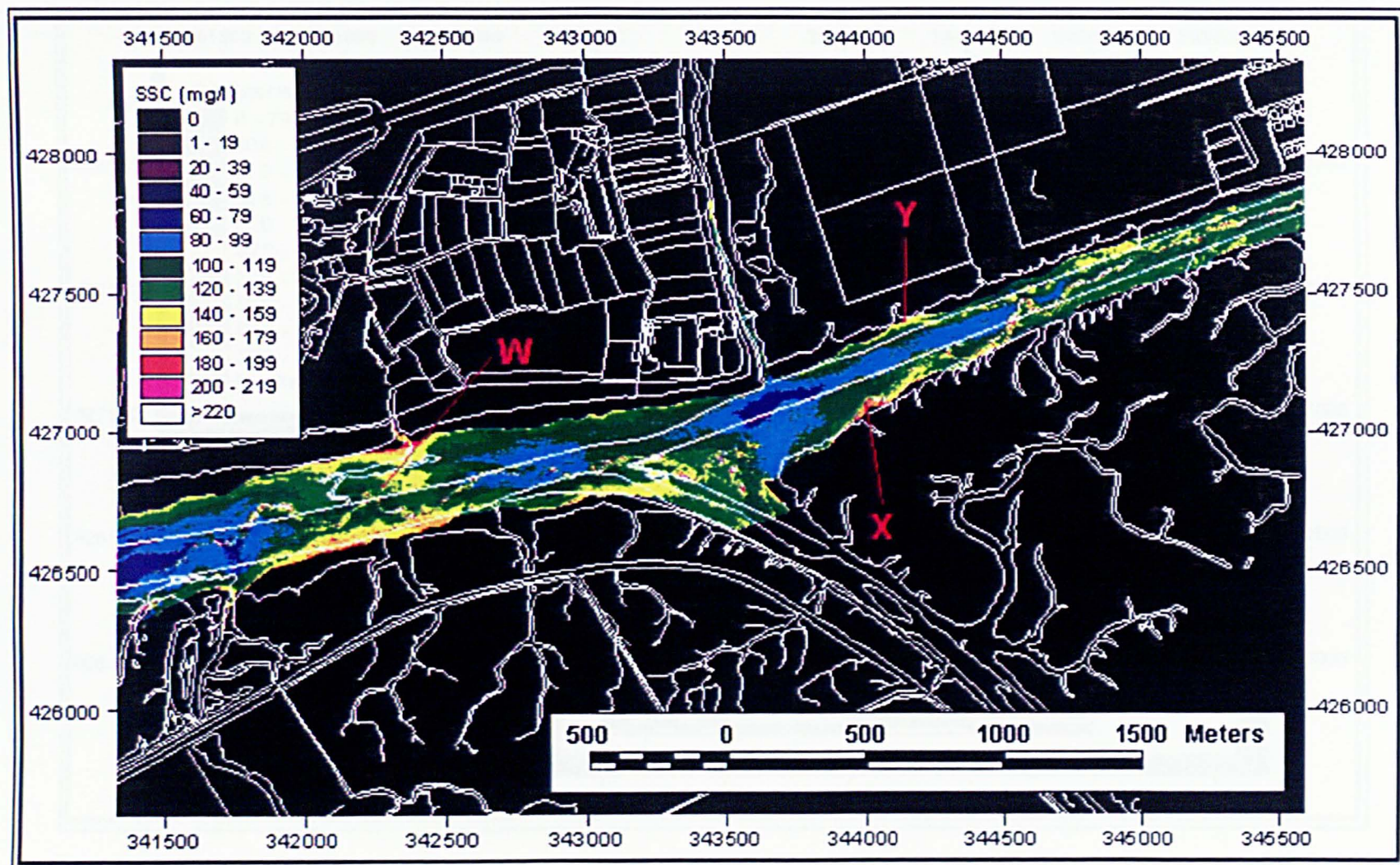


Figure 6.2f(i) CASI image calibrated to suspended sediment concentration, (mg/l), of the confluence area, 09:37, 20-7-97.

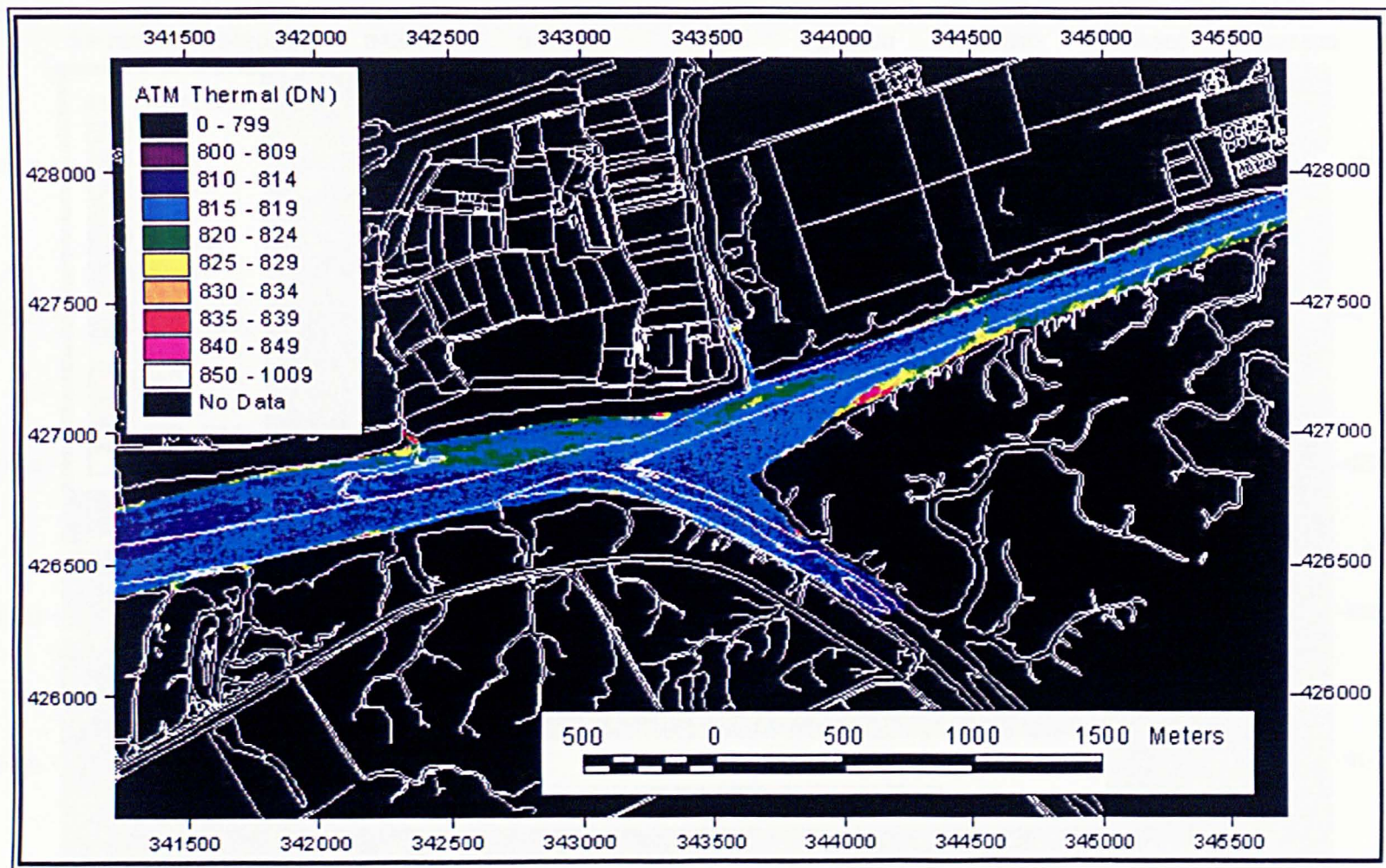


Figure 6.2f(ii) ATM thermal data of the confluence area, 09:37, 20-7-97.

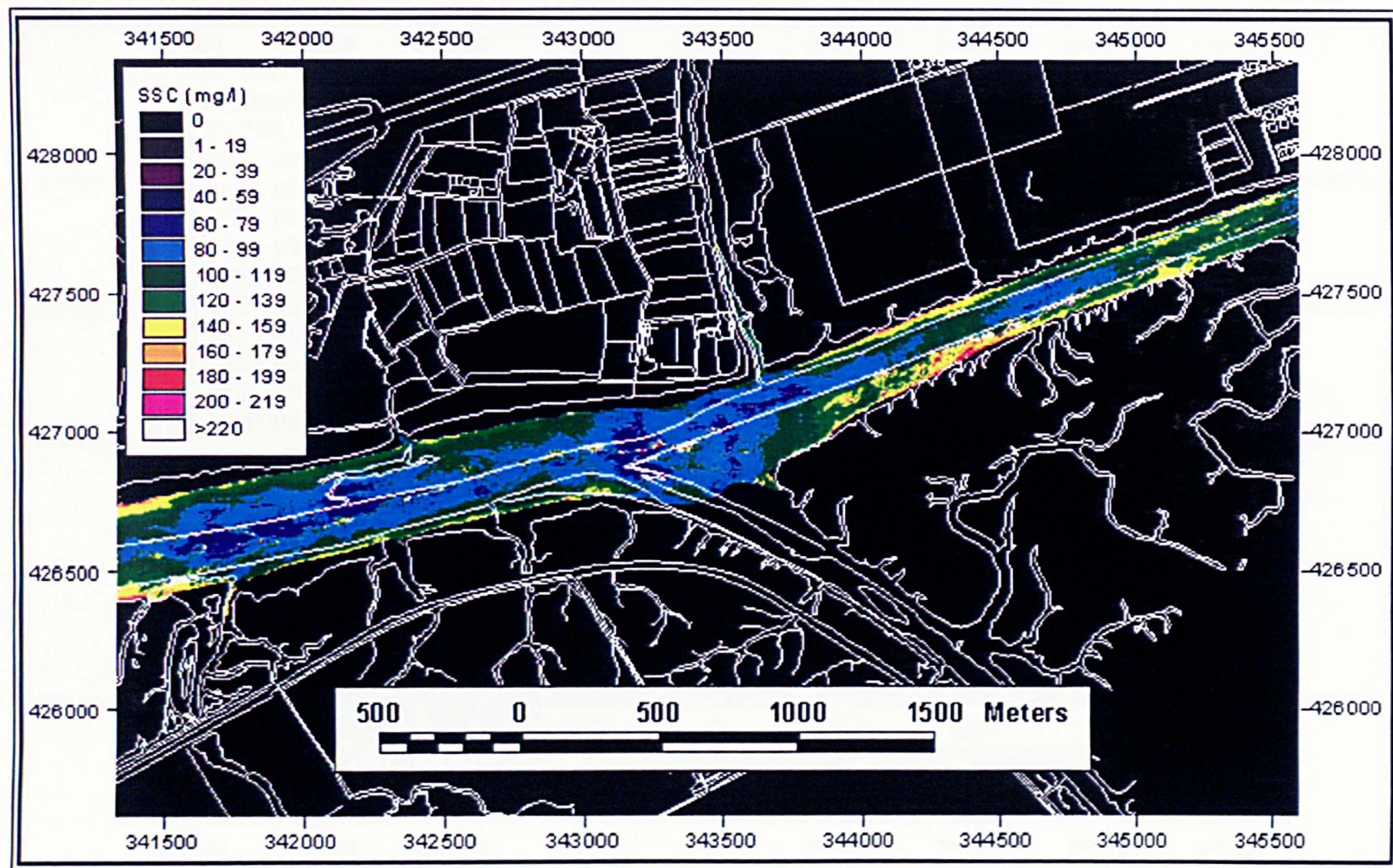


Figure 6.2g(i) CASI image calibrated to suspended sediment concentration, (mg/l), of the confluence area, 09:55, 20-7-97.

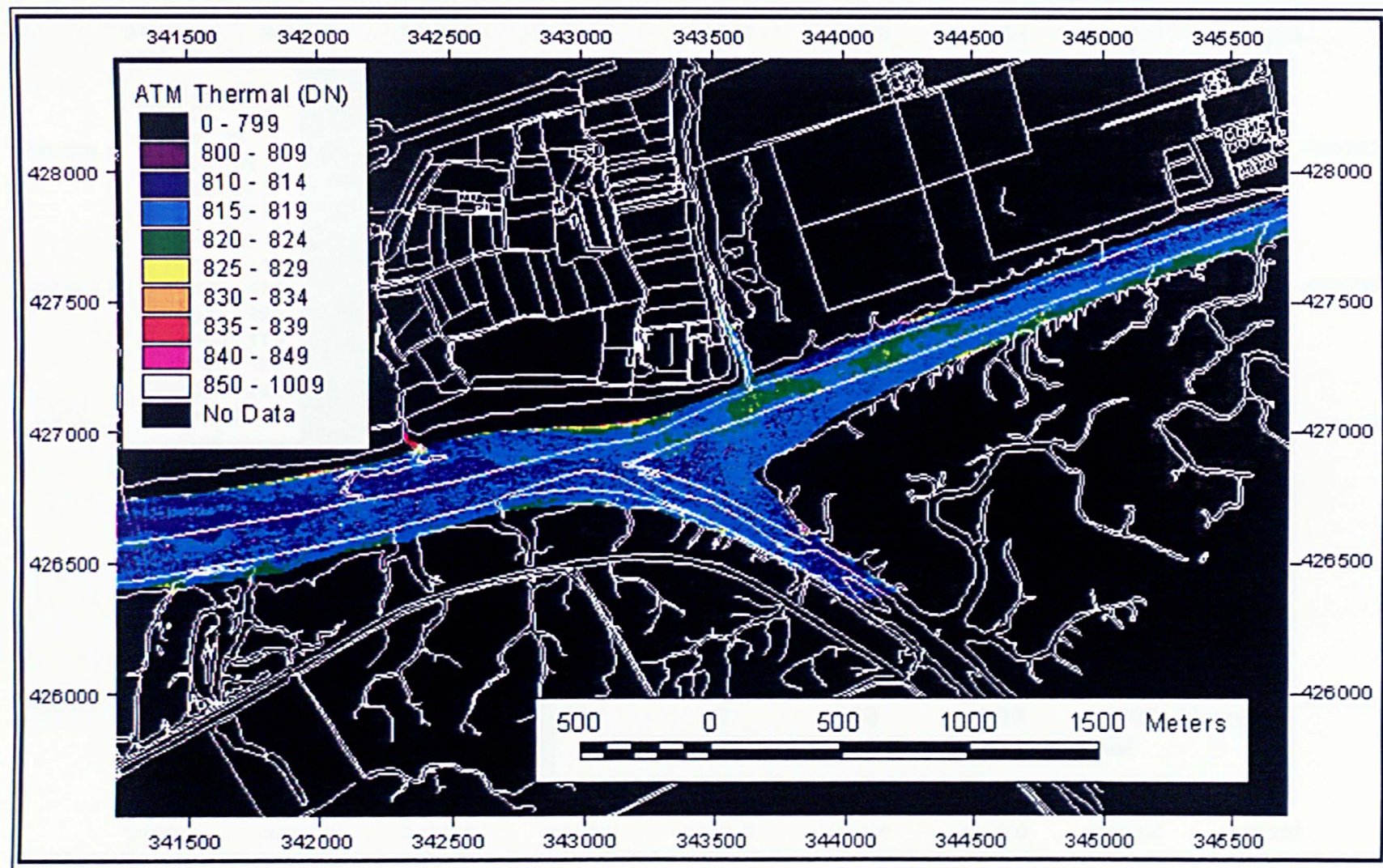


Figure 6.2g(ii) ATM thermal data of the confluence area, 09:55, 20-7-97.

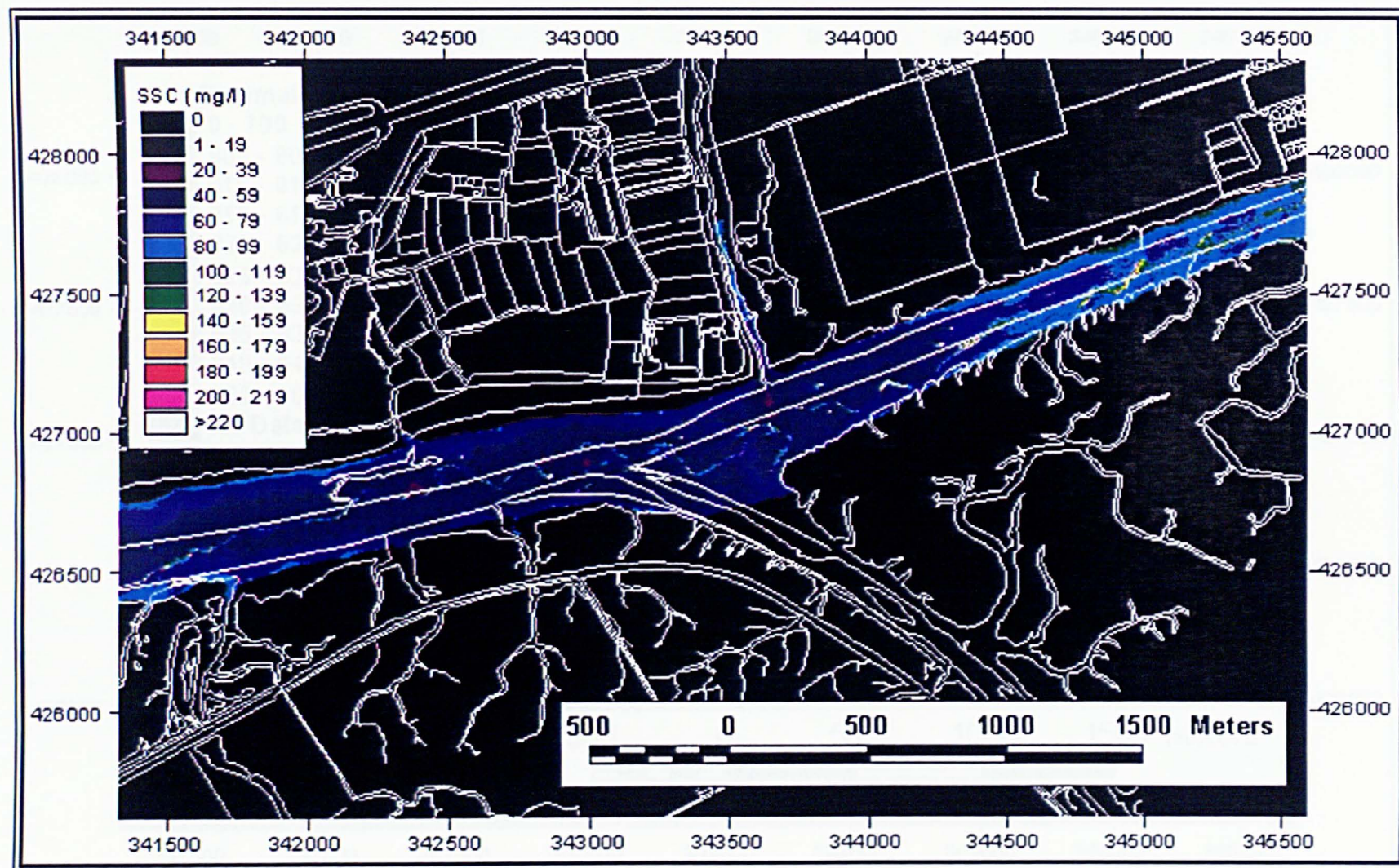


Figure 6.2h(i) CASI image calibrated to suspended sediment concentration, (mg/l), of the confluence area, 11:11, 20-7-97.

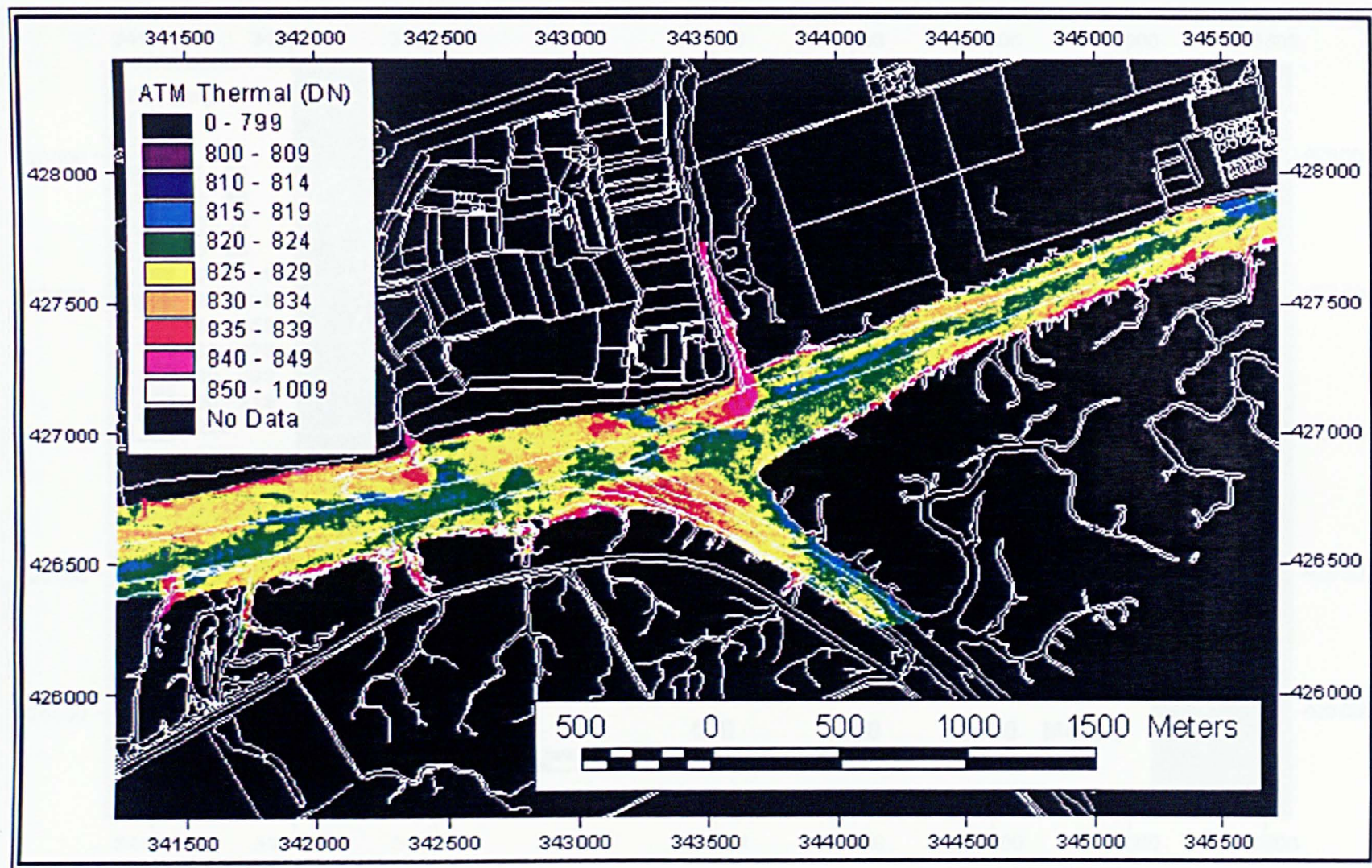


Figure 6.2h(ii) ATM thermal data of the confluence area, 11:11, 20-7-97.

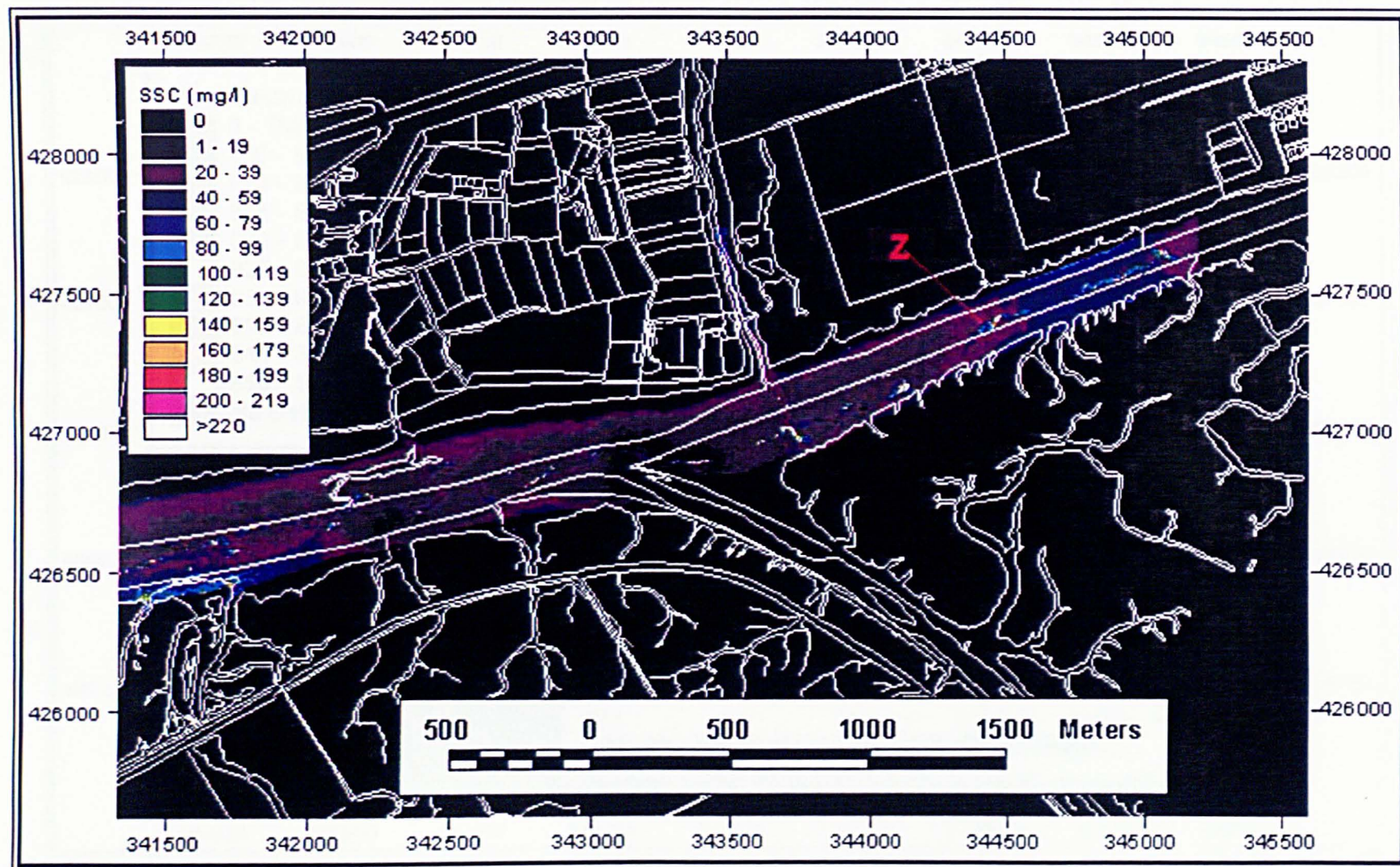


Figure 6.2i(i) CASI image calibrated to suspended sediment concentration, (mg/l), of the confluence area, 11:25, 20-7-97.

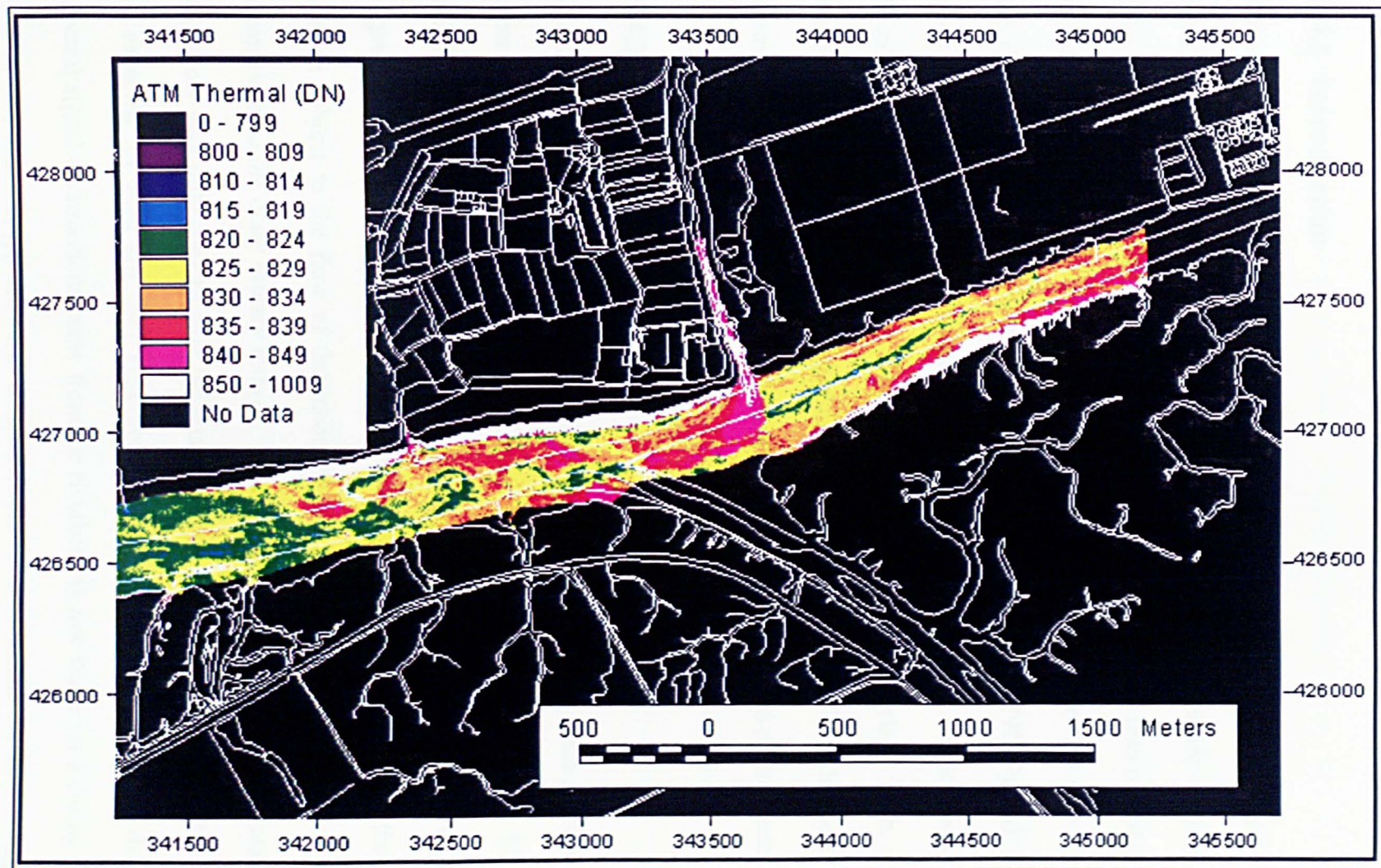


Figure 6.2i(ii) ATM thermal data of the confluence area, 11:25, 20-7-97.

## **6.4 THE SPRINGFIELDS DISCHARGE AREA: SAVICK BROOK**

### **6.4.1 Introduction**

This stretch of the river is spatially the most simple, as it is very straight and the intertidal areas outside the training walls on either side of the river are much narrower than for the previous two areas. However, chemically this area is also one of the most important as there are two effluent discharge points in this stretch of the river. There is the discharge from the sewage treatment works (345710E, 427925N) and also the discharge from the BNFL Springfields plant (347180E, 428450N). In addition, Savick Brook has been reported to be a point that accumulates higher levels of  $^{234}\text{Th}$ , which is routinely discharged from BNFL Springfields (Mudge *et al.*, 1997). This section will try to identify why these elevated levels of  $^{234}\text{Th}$  occur in this region of the estuary.

### **6.4.2 08:11 GMT, Figure 6.3a**

The SSC range for this image is 120-200 mg/l. There are two areas showing some geometric distortion due to aircraft roll, these are located at **A** (345850E to 346100E) and **B** (347250E to 347400E), where SSC is increased by approximately 15% and 20% respectively. The tidal bore is situated off Warton Bank, thus this section of the river is not yet subject to the flow of the incoming tide, hence the small range of SSC in comparison to the outer estuary images. This is supported by the thermal data, which also show very little contrast over the image. However, SSC is still greater than would be expected for such low flow conditions. This suggests the possibility that some spectral signal contributions come from the riverbed, as low water on a spring tide the river is very shallow, typically less than 0.5m. In most locations the SSC is higher on the northern side of the channel, which may be the outflow from Preston docks.

### **6.4.3 08:30 GMT, Figure 6.3b**

The SSC range for this image is similar to the last and ranges from 100 to 240 mg/l. However, the upper values are affected by aircraft roll thus the real SSC range is closer to 100 to 180 mg/l. There are three areas of aircraft roll, **C**, (347050E to 347180E), **D**, (347750E to 347900E) and **E**, (348280E to 348400E) giving errors of +9%, +5% and +20% respectively. The bore has yet to pass and the SSC values are higher than would normally be expected for low tide. As with Figure 6.3a, the suspended sediments are distributed relatively evenly over the image with no distinctive patterns.

### **6.4.4 08:45 GMT, Figure 6.3c**

The SSC range of this image is difficult to determine as large areas of the image are badly affected by aircraft roll. The true range is likely to be similar to the previous two images (Figures 6.3a and 6.3b), but the upper value of the range cannot be accurately determined. The value was estimated by looking at the sediment patterns for the previous two images, which showed little variation in SSC where the tide had not yet reached. However, on this image the tidal bore can be found stretching across the whole width of the river at **F**, (346295E). The highest values caused by roll are to the east of this and it would be expected that the highest SSC would be in the turbulent water following the tidal bore, which is approximately 190 mg/l.

The SSC rises from 145 mg/l to 190 mg/l in the turbulent waters that follow the tidal bore, however there is no thermal boundary marking the location of the bore. The low SSC feature at the eastern end of the image is a continuation of the feature seen in the previous two images.

#### **6.4.5 09:02 GMT, Figure 6.3d**

The SSC range for this image is probably 100 mg/l to 200 mg/l. Again, the upper limit is subject to roll effects and estimated from other areas of the image. The area of the image seriously affected by aircraft roll is at **G** (347530E to 348275E) increasing SSC by up to 30%. There is also a 10% increase in SSC at **H**, (346300E to 346530E). Three-quarters of this section of the channel is now being influenced by the flood tide. The tidal bore is not visible on the imagery but aerial photographs show that the bore is now at **I**, (348555E).

The lowest SSC values are east of the bore with the higher SSC values found in the turbulent water following the bore. The exact magnitude of the increase in SSC due to the bore cannot be determined due to roll problems. However, the ATM image data still show that there is no thermal structure in the river.

#### **6.4.6 09:20 GMT, Figure 6.3e**

The SSC range for this image is 100 mg/l to 240 mg/l. The highest values are found in a large stretch of the river around the Springfields discharge point. There are also high SSC values of over 190 mg/l around the creek entering the river channel at **J**, (346030E, 427900N). In the west of the image, there is an intrusion of lower SSC penetrating as far as the sewage works. The thermal data show that there is a slight decrease in temperature related to this intrusion of lower SSC water at the western edge of the image. There appears to be a pattern of lower SSC in the main channel with higher SSC along the edges as seen in previous images. There is also an increase in temperature at

the very edges of the channel, which corresponds to the increased SSC values in the CASI image.

There is a well-defined linear foam line running along the centre of the channel indicating the presence of an axial convergence front. Aerial photographic evidence suggests that the foam line becomes progressively more faint and finally fades away at **K**, (347400E). This shows that the convergence forms approximately 2 km behind the tidal bore, beginning weakly and getting progressively stronger.

#### **6.4.7 09:37 GMT, Figure 6.3f**

The SSC range for this image is 95 mg/l to 210 mg/l. The image shows some spatial distortion where the river image is not aligned with the map, but there are no coincident changes in SSC. Thus, whilst the NERC GCORR program gives poor geo-correction, the increasing solar elevation angle has kept errors in SSC to a minimum. The water has reached the top of the training walls and begun to inundate the narrow intertidal areas. The lower SSC water has penetrated as far as 346900E. The coincidental thermal image shows that the intruding water is slightly cooler and penetrates to approximately the same point where the foam line disintegrates. The two trends in SSC are increasing SSC upstream and lower SSC in the centre of the main channel. Both suggest that sediment is being resuspended from the intertidal areas within the estuary and negligible amounts are brought in from the Irish Sea. This is further supported by the fact that the maximum SSC for each image series has increased as the area examined progressively moves west to east. The thermal image shows some small areas of warmth along the edges of the river that suggest localised sediment suspension at **M**, (345950E,

427890N) and N, (346260E, 428115N) and a larger area of possible erosion along the southern shore at the eastern end of the image.

The well-developed foam lines again indicate the presence of a strong axial convergence front showing the same trend as the previous image. In the west the foam line is dense and well defined and this gradually decreases towards the east fading out at L (348540E). The line fades approximately 1100m east of the point at which it diminished in the previous image.

#### **6.4.8 09:55 GMT, Figure 6.3g**

The SSC range for this image is 60 mg/l to 220 mg/l, the lower limit of the range is less than for previous images indicating that some settling has occurred. The lower SSC values that are found at the west of the image increase towards the east, the same trend seen in temperature in the thermal image. The SSC are always lower in the centre of the channel and then increase towards the edges. There is evidence that the sediment suspended at the water's edge is being pulled towards the centre of the channel by the convergent currents at O, (346240E, 428020N). The highest SSC are found, along both the north and south banks, to the east of Savick Brook. Aerial photographic evidence identifies these features as foam along the shore, thus the maximum SSC in this area may be less than 200 mg/l.

The foam lines are dense and linear running down the centre of the main channel and become more complex at the area of higher SSC where a second foam line develops joining the main foam line at P, (349035E, 428940N). This suggests further evidence

of sediment and foam being pulled from the shore to the centre of the main channel by the circulatory pattern of the axial convergence front.

#### **6.4.9 11:11 GMT, Figure 6.3h**

The SSC range for this image is 70 mg/l to 100 mg/l. There are two sections of the CASI image missing; these were removed due to there being cloud across the image at these points. The CASI and ATM sensors are not directly adjacent and the thermal ATM data were unaffected. The necessity of re-fuelling the aircraft resulted in a long time gap between images. Current velocity appears to have decreased during this time. This is supported by the disappearance of the patterns associated with sediment erosion, where higher SSC values are found at the water's edge. The decrease in SSC is accompanied by an increase in temperature as seen for other sections of the river.

The foam lines are still present along the length of the image implying that the convergence is still strong enough to prevent the foam dispersing. The sinusoidal pattern that developed in the previous sections of the river is now seen in this section. The aerial photographs provide evidence that this pattern is apparent in the foam lines of the western half of the image but the foam lines in the eastern image are fully intact and more linear. The change between the western sinusoidal and eastern linear foam lines is a gradual process.

The warmer water lies at the edge of the water and suggests a more rapid warming of the water in the shallower areas. The mixing patterns of this warmer water at Q, (345780E, 427800N) show that the direction of flow is to the east, therefore the tide has not yet turned. There is a discrete patch of cooler water in the location of the sewage

works (**R**) that does not appear to originate from a creek. This must be the beginning of the discharge of the sewage effluent on the ebb tide, however, the flow is currently from west to east.

#### **6.4.10 Savick Brook Summary**

1. The overall SSC increases for the first seven images of the series but there is a dramatic decrease in the SSC at 11:11 GMT (Figure 6.3h) suggesting the occurrence of sediment settling.
2. The incoming tide starts to affect this area of the river at 08:44 GMT (Figure 6.3c).
3. Prior to the effects of the incoming tide there is a north south segregation of waters in the eastern extremes of the image nearer the docks, but this is not seen after 09:20 GMT, (Figure 6.3e).
4. For the image series as a whole there is a general trend showing a longitudinal increase in SSC from west to east suggesting that sediment is not brought into the estuary but resuspended from within the estuary.
5. The water level reaches the top of the training wall in Figure 6.3f, after which greater SSC is found over the intertidal areas than in the main river channel. This suggests that the intertidal areas are the main source of suspended sediment.
6. The highest SSC is found along the north and south shores to the west of Savick Brook.
7. The foam lines indicating the presence of an axial convergence start to be seen at 09:20 GMT (Figure 6.3e). The line starts to appear approximately 2km behind the tidal bore. The presence of these foam lines coincides with the location of cooler water entering the estuary. The thermal data at 09:55 GMT (Figure 6.3g) show

evidence for the convergence as sediment is pulled from the shores to the centre of the river channel.

8. At 09:55 GMT (Figure 6.3g) the foam line runs along the length of the image, but is starting to show the sinusoidal patterns associated with the break up of the convergence in the western end of the image.

This section of the estuary is subject to a very short flood tide. Also, at the time sediment settling starts to occur at slack water, this region has higher SSC than the lower reaches of the estuary prior to sediment settling. It is these factors that could be responsible for the elevated  $^{234}\text{Th}$  levels sometimes found in this area as mentioned in Mudge *et al.*, (1997). However, there is another aspect of the tidal cycle that is likely to play a more important role in the occurrence of this phenomenon. This is the variation of maximum tidal heights over the spring–neap cycle. As the maximum tidal elevation diminishes from spring tides to neap tides the sediment deposited during the settling period of the previous high tide will not be fully resuspended and redistributed by the following tide. This will result in a periodic build-up of the locally discharged radionuclides such as  $^{234}\text{Th}$ . However, from this single image series it is difficult to determine an exact mechanism for these occurrences of higher  $^{243}\text{Th}$  concentrations in this area.

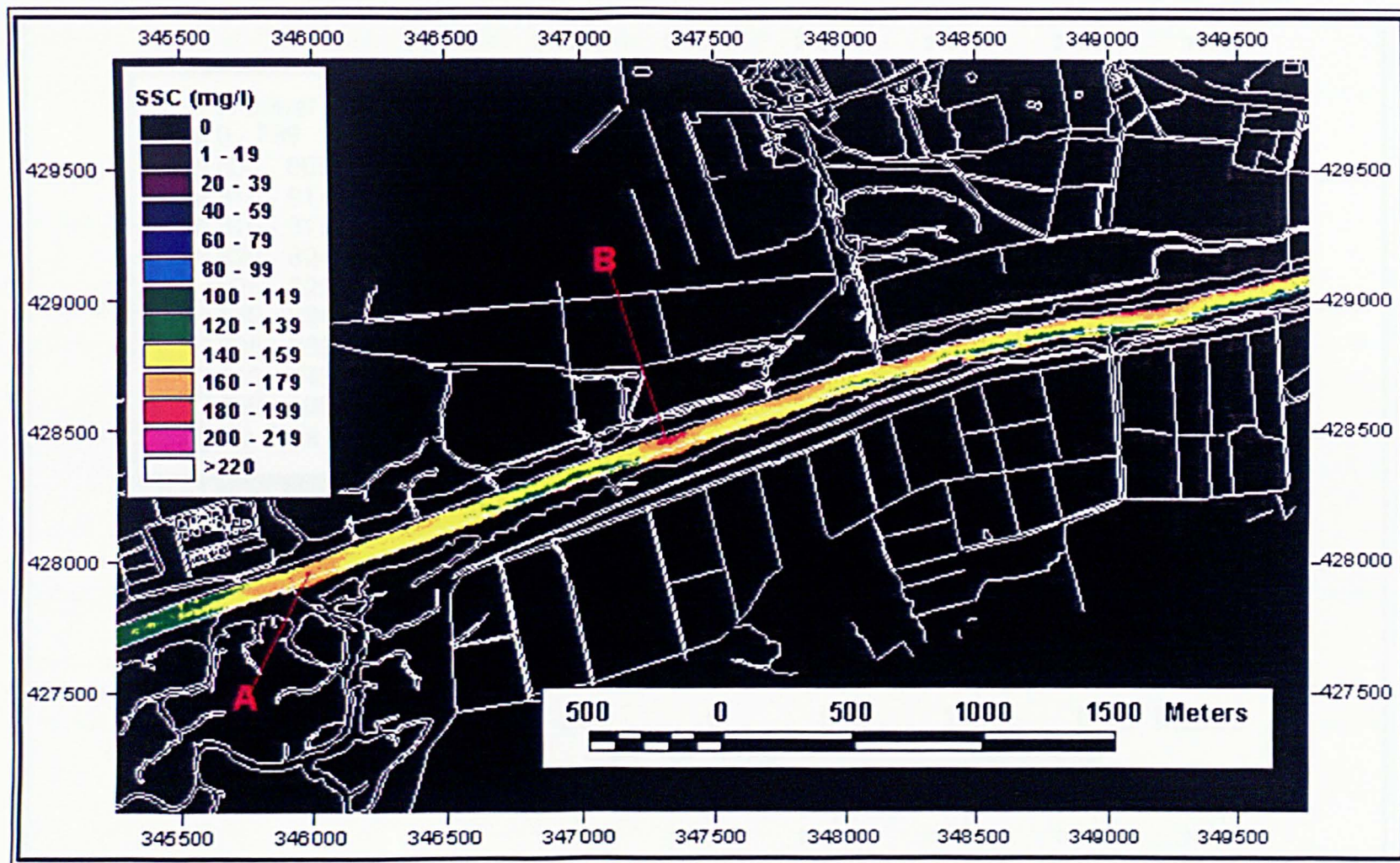


Figure 6.3a(i) CASI image calibrated to suspended sediment concentration, (mg/l), of the Savick Brook area, 08:11, 20-7-97.

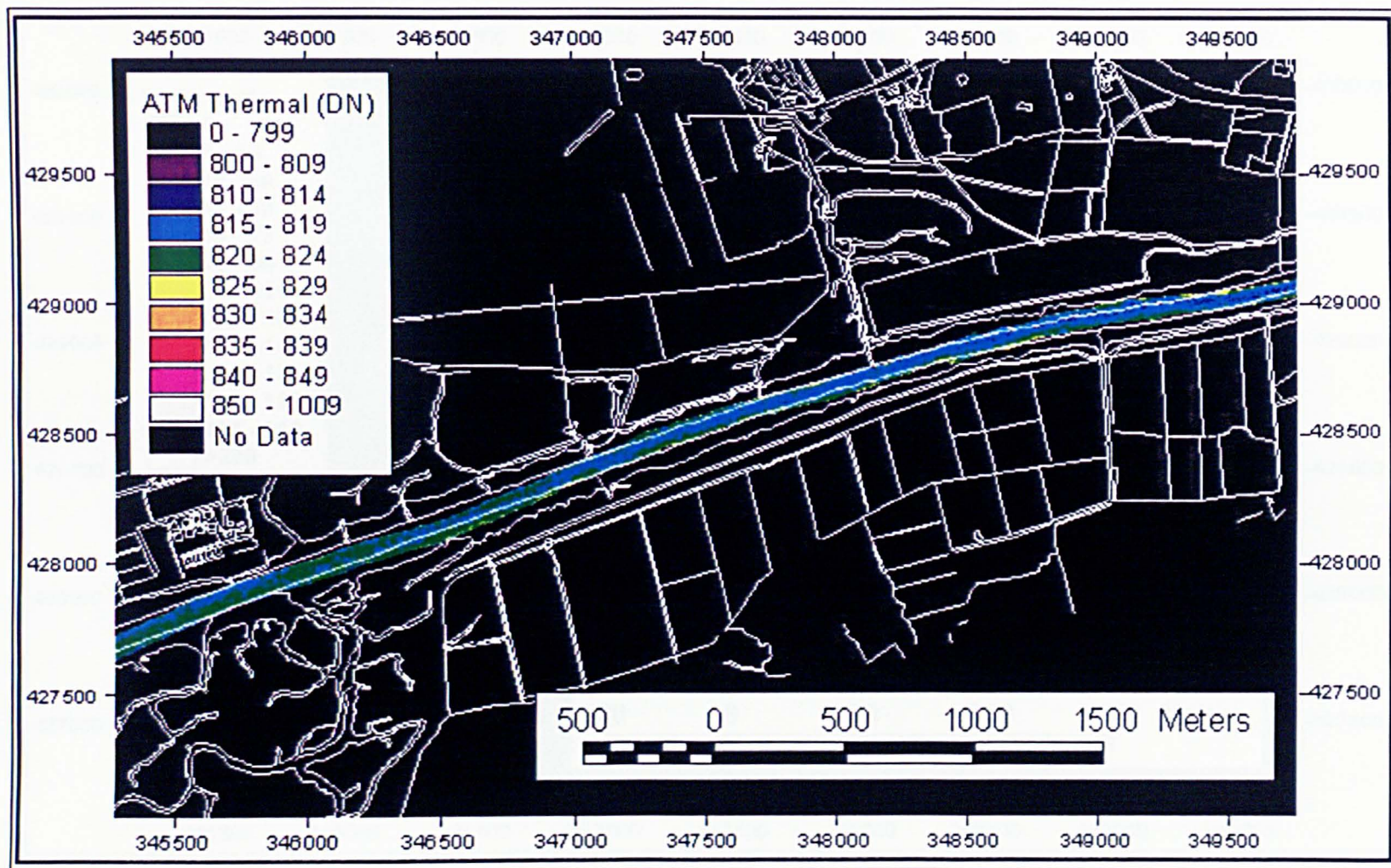


Figure 6.3a(ii) ATM thermal data of the Savick Brook area, 08:11, 20-7-97.

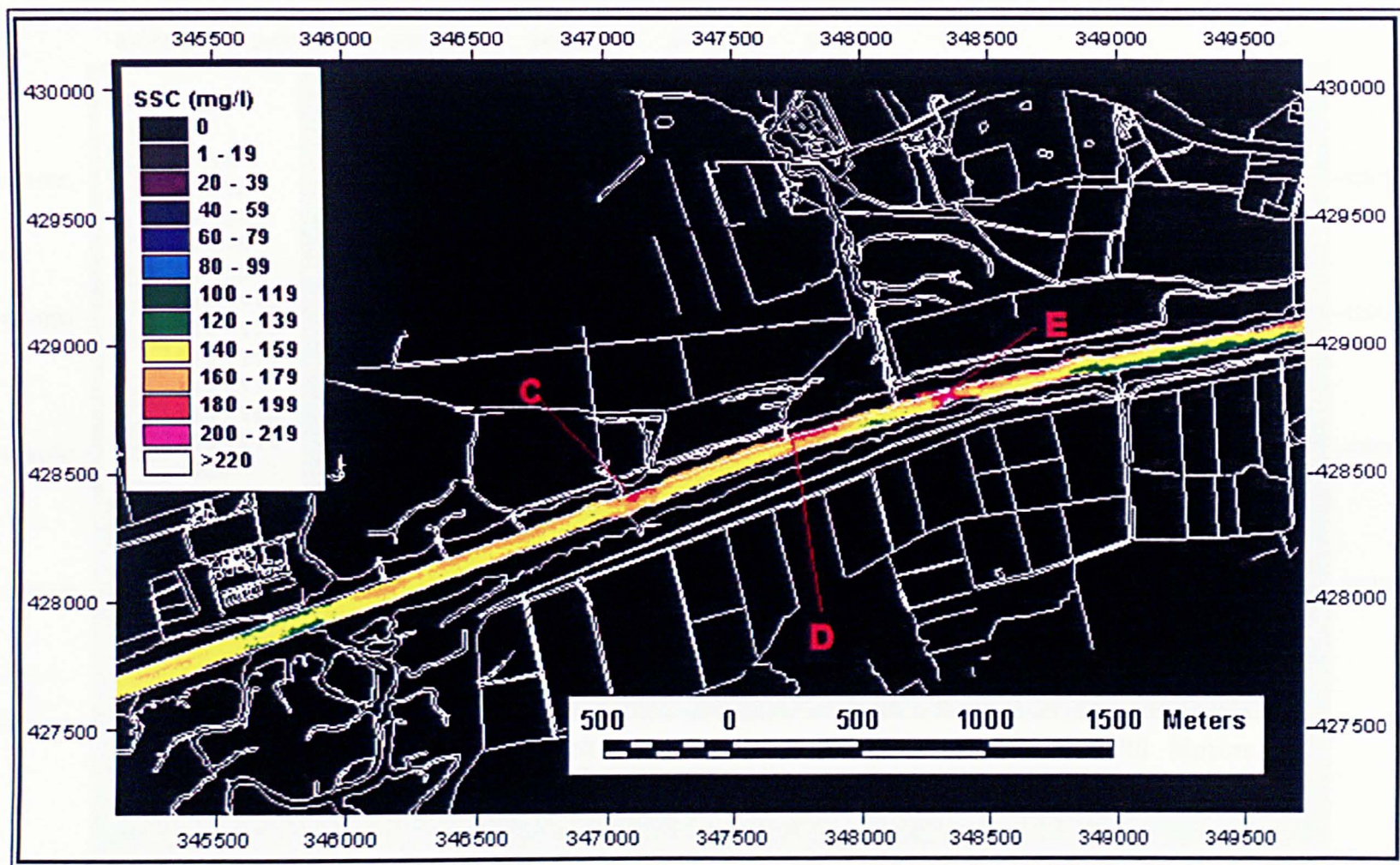


Figure 6.3b(i) CASI image calibrated to suspended sediment concentration, (mg/l), of the Savick Brook area, 08:30, 20-7-97.

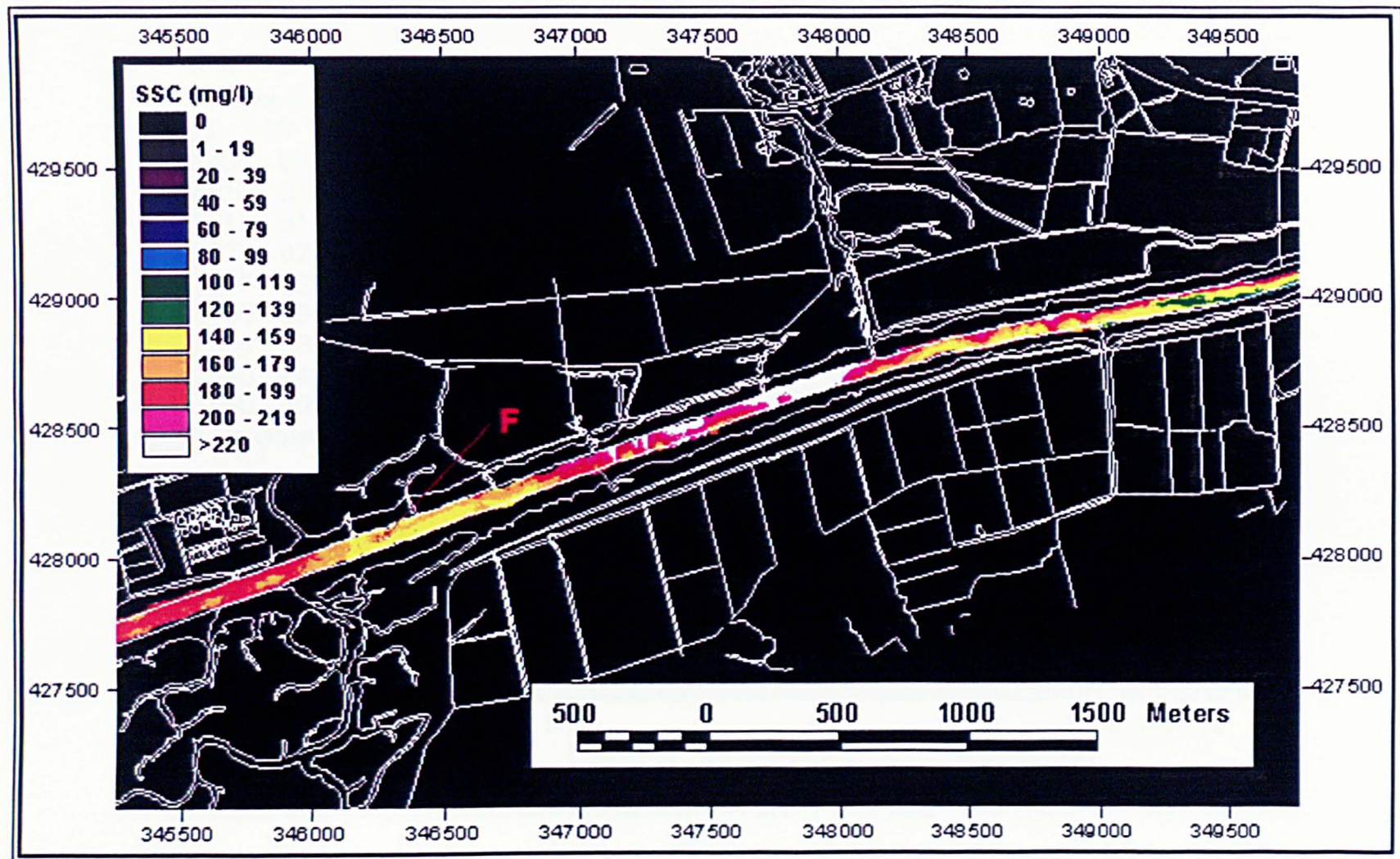


Figure 6.3c(i) CASI image calibrated to suspended sediment concentration, (mg/l), of the Savick Brook area, 08:44, 20-7-97.

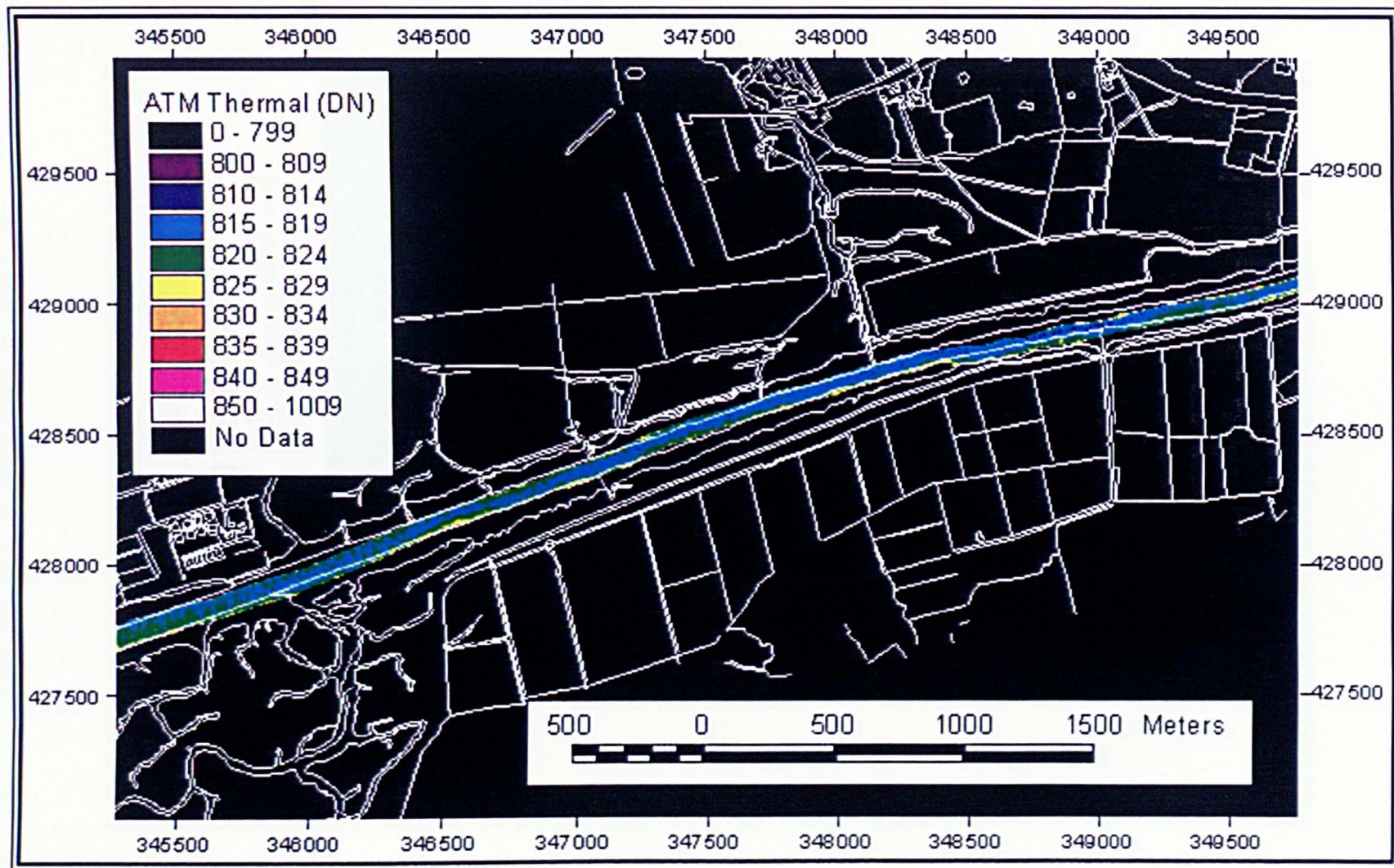


Figure 6.3c(ii) ATM thermal data of the Savick Brook area, 08:44, 20-7-97.

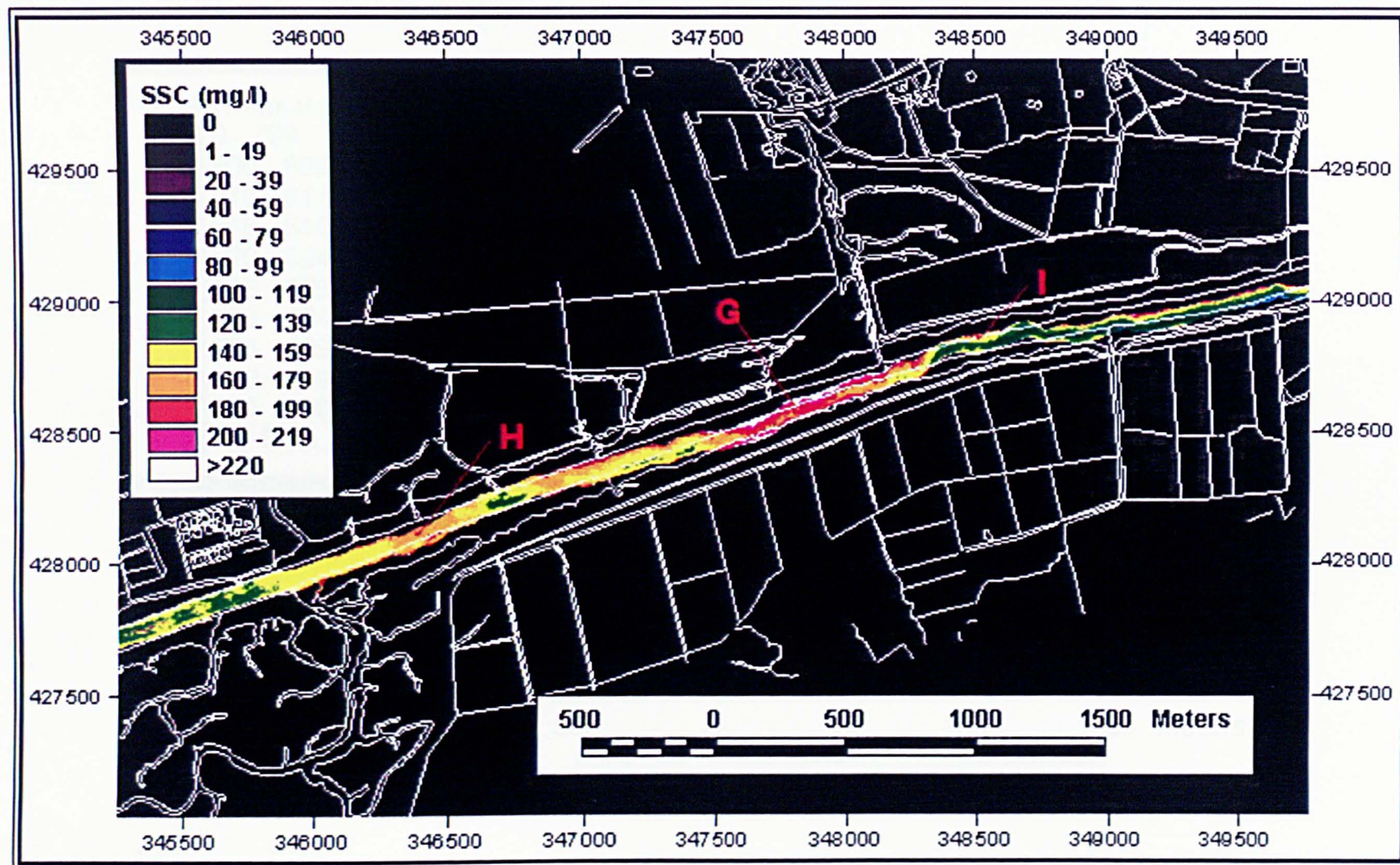


Figure 6.3d(i) CASI image calibrated to suspended sediment concentration, (mg/l), of the Savick Brook area, 09:02, 20-7-97

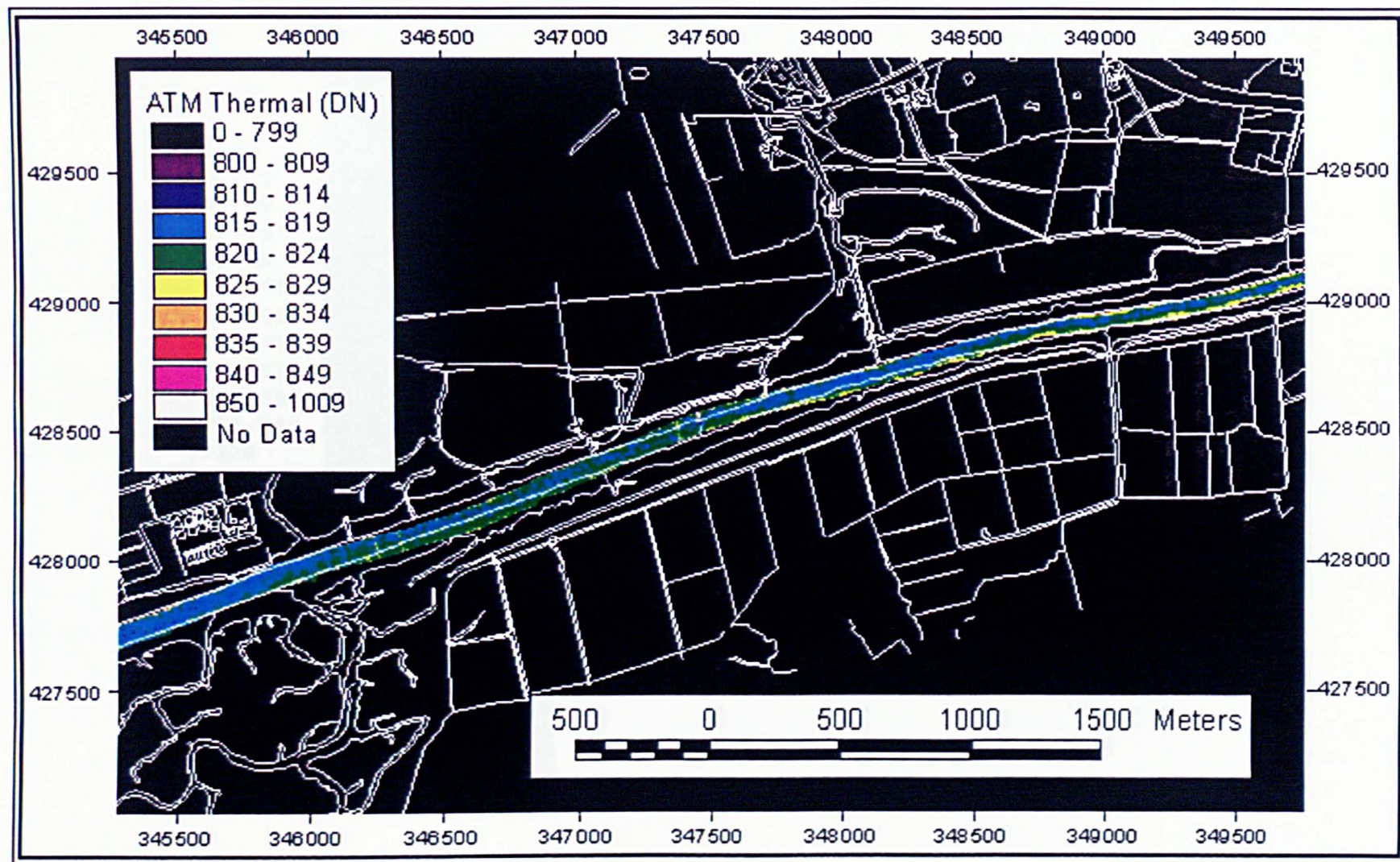


Figure 6.3d(ii) ATM thermal data of the Savick Brook area, 09:02, 20-7-97.

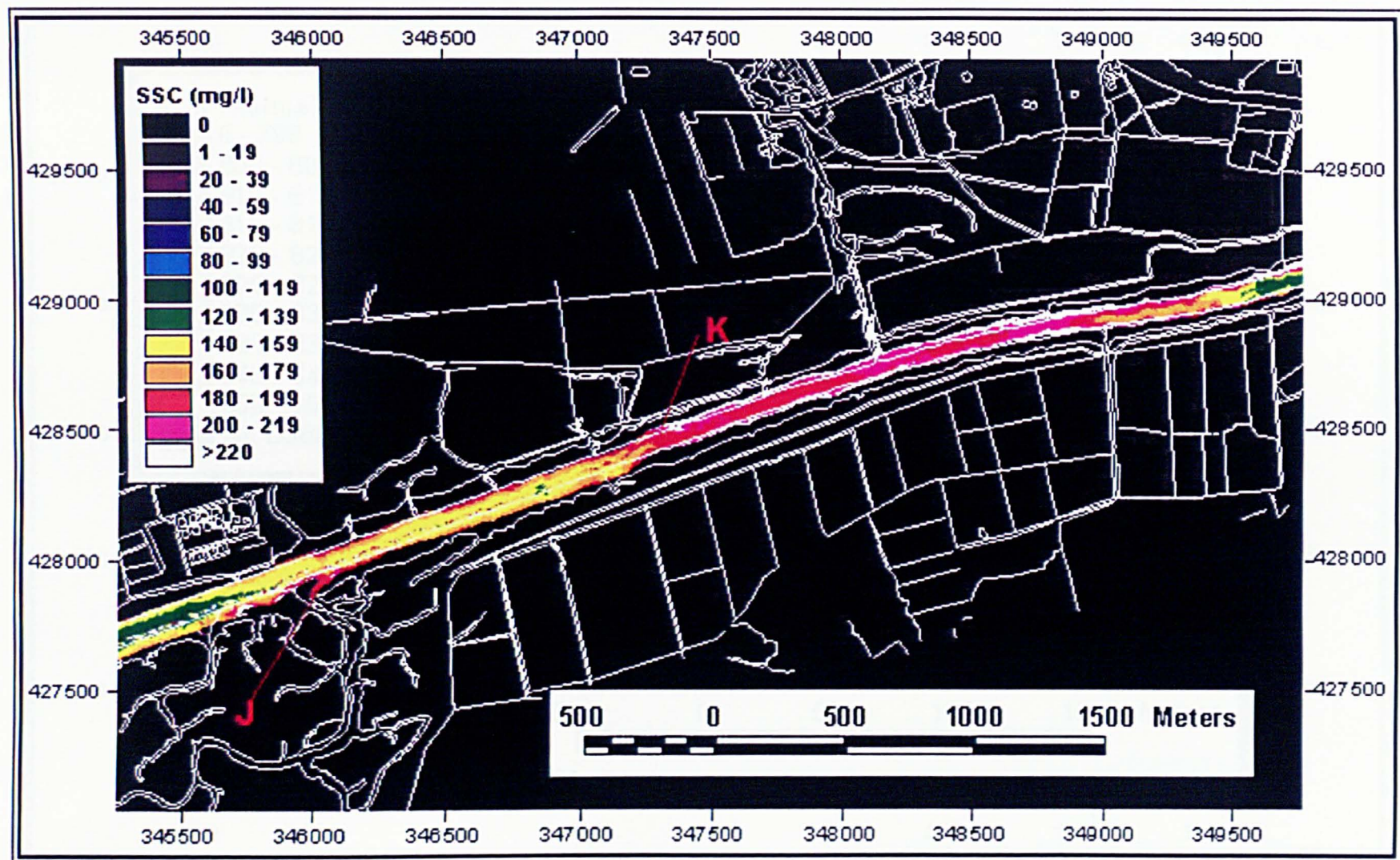


Figure 6.3e(i) CASI image calibrated to suspended sediment concentration, (mg/l), of the Savick Brook area, 09:20, 20-7-97.

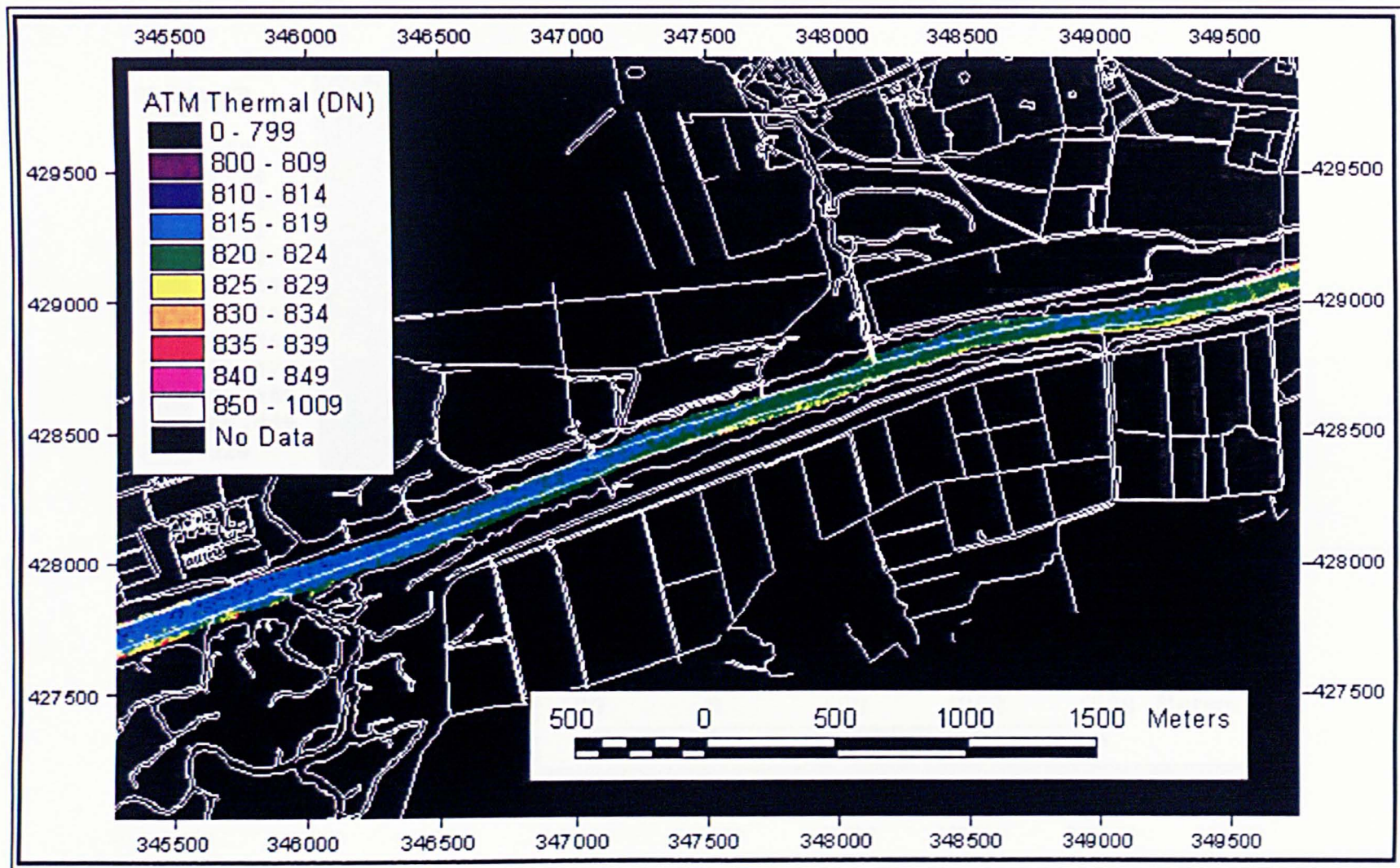


Figure 6.3e(ii) ATM thermal data of the Savick Brook area, 09:20, 20-7-97.

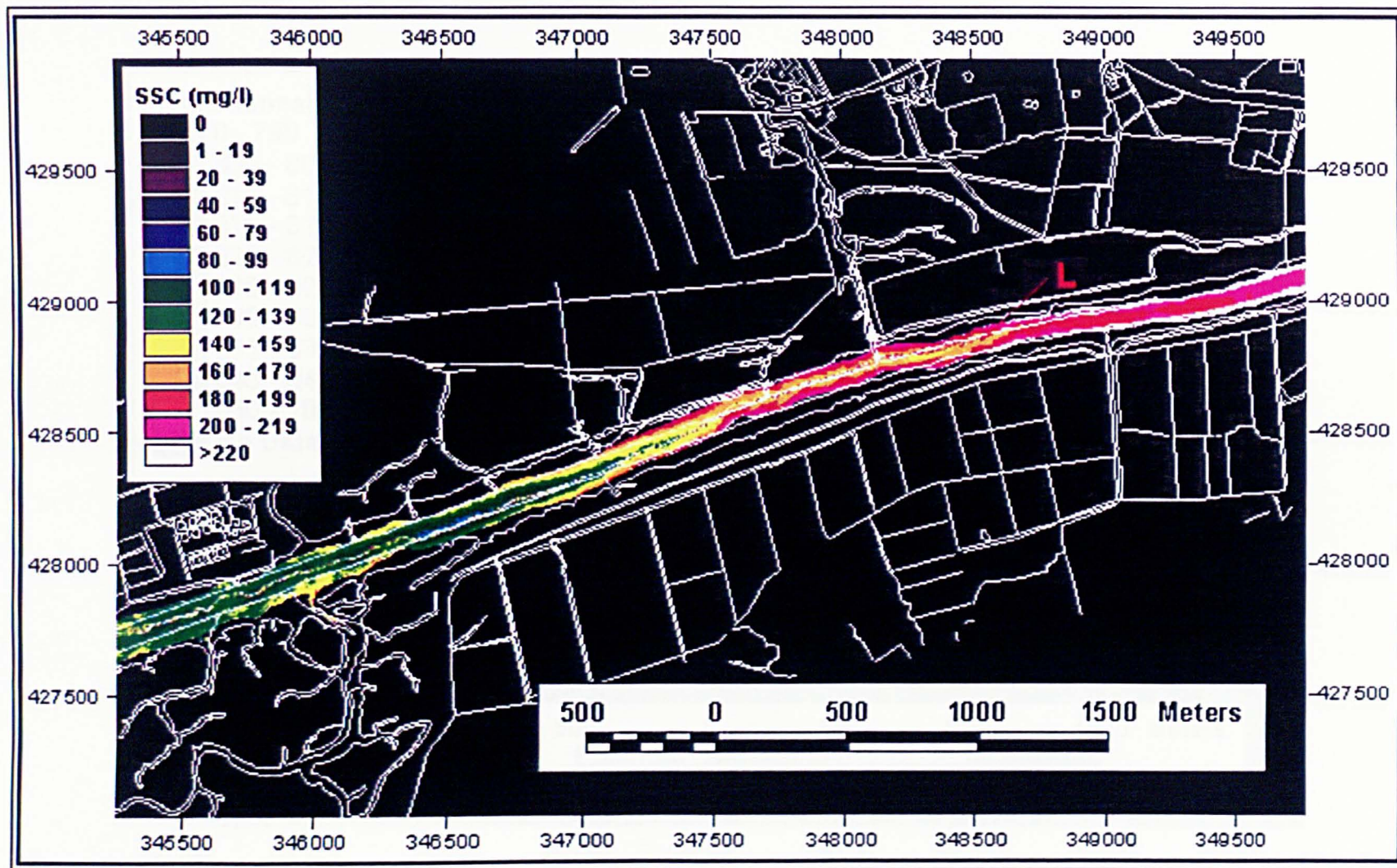


Figure 6.3f(i) CASI image calibrated to suspended sediment concentration, (mg/l), of the Savick Brook area, 09:37, 20-7-97.

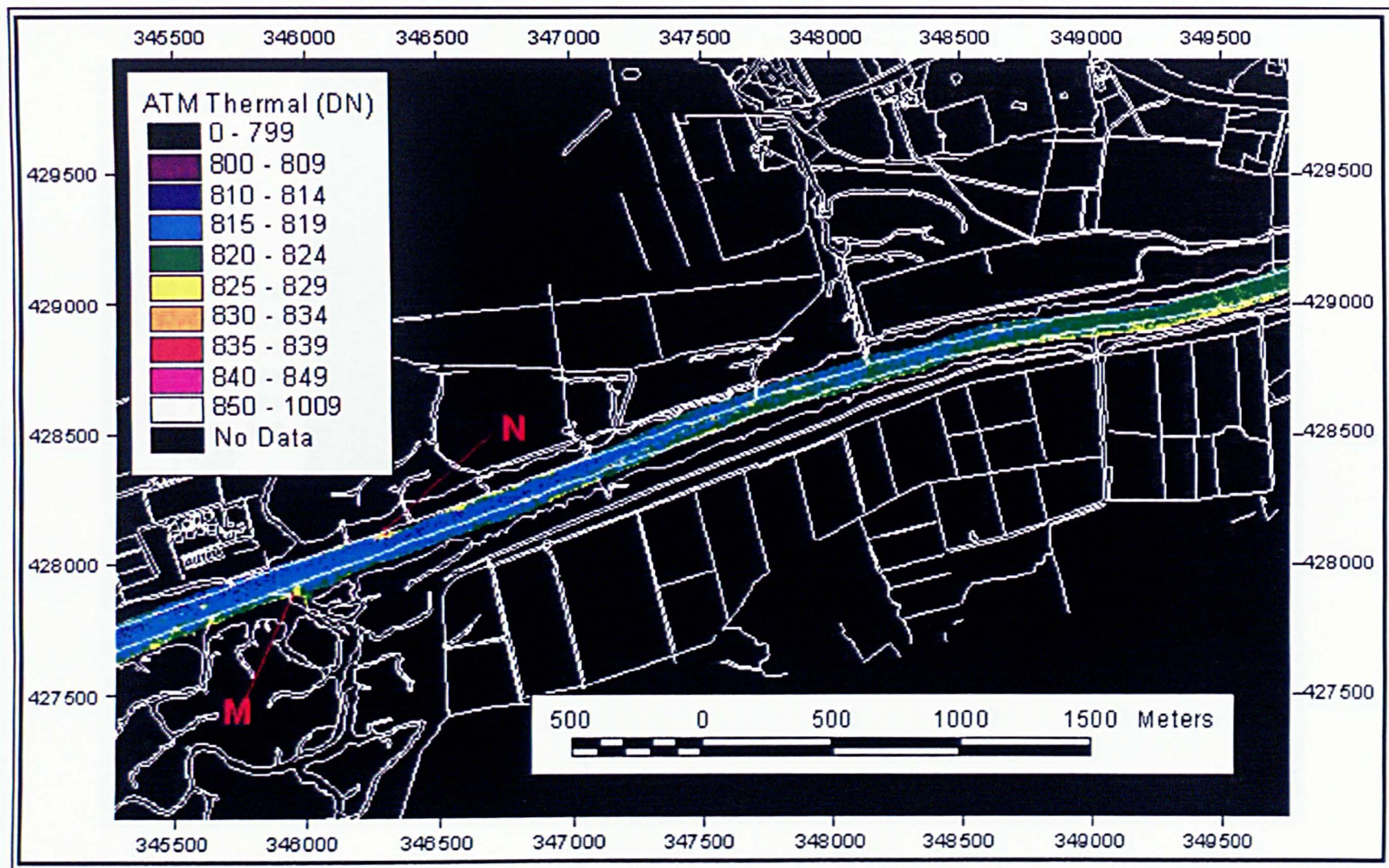


Figure 6.3f(ii) ATM thermal data of the Savick Brook area, 09:37, 20-7-97.

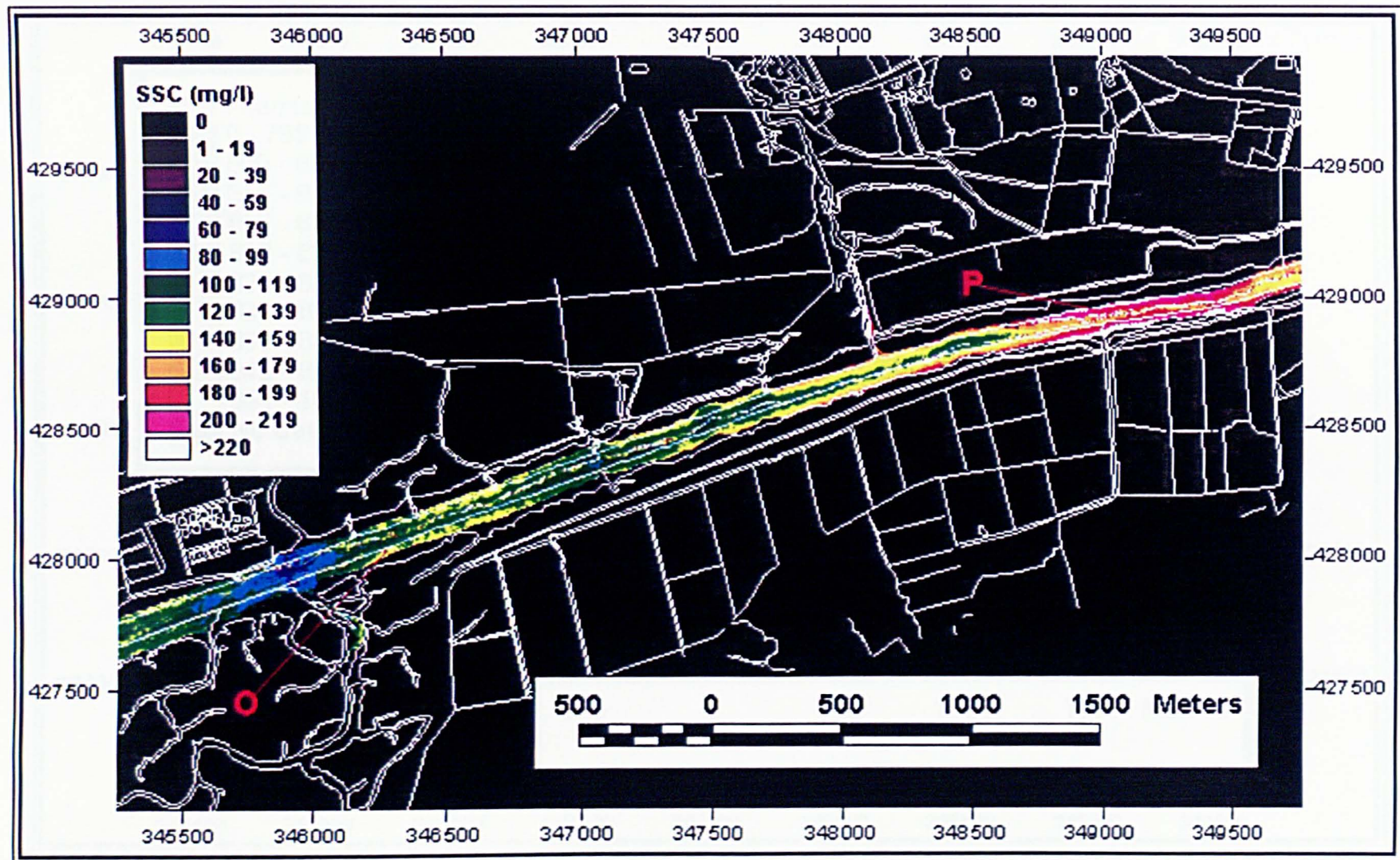


Figure 6.3g(i) CASI image calibrated to suspended sediment concentration, (mg/l), of the Savick Brook area, 09:55, 20-7-97.

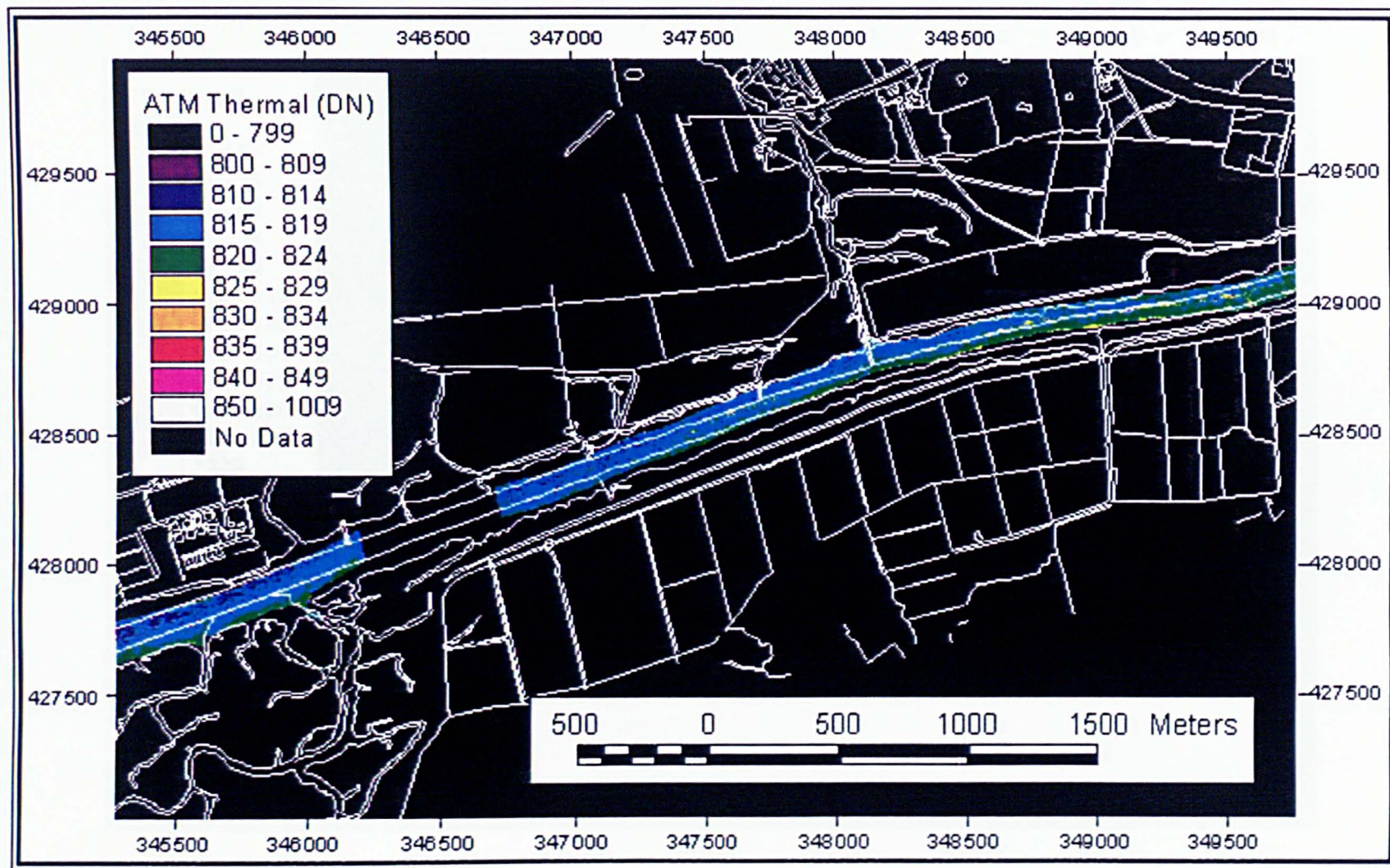


Figure 6.3g(ii) ATM thermal data of the Savick Brook area, 09:55, 20-7-97.

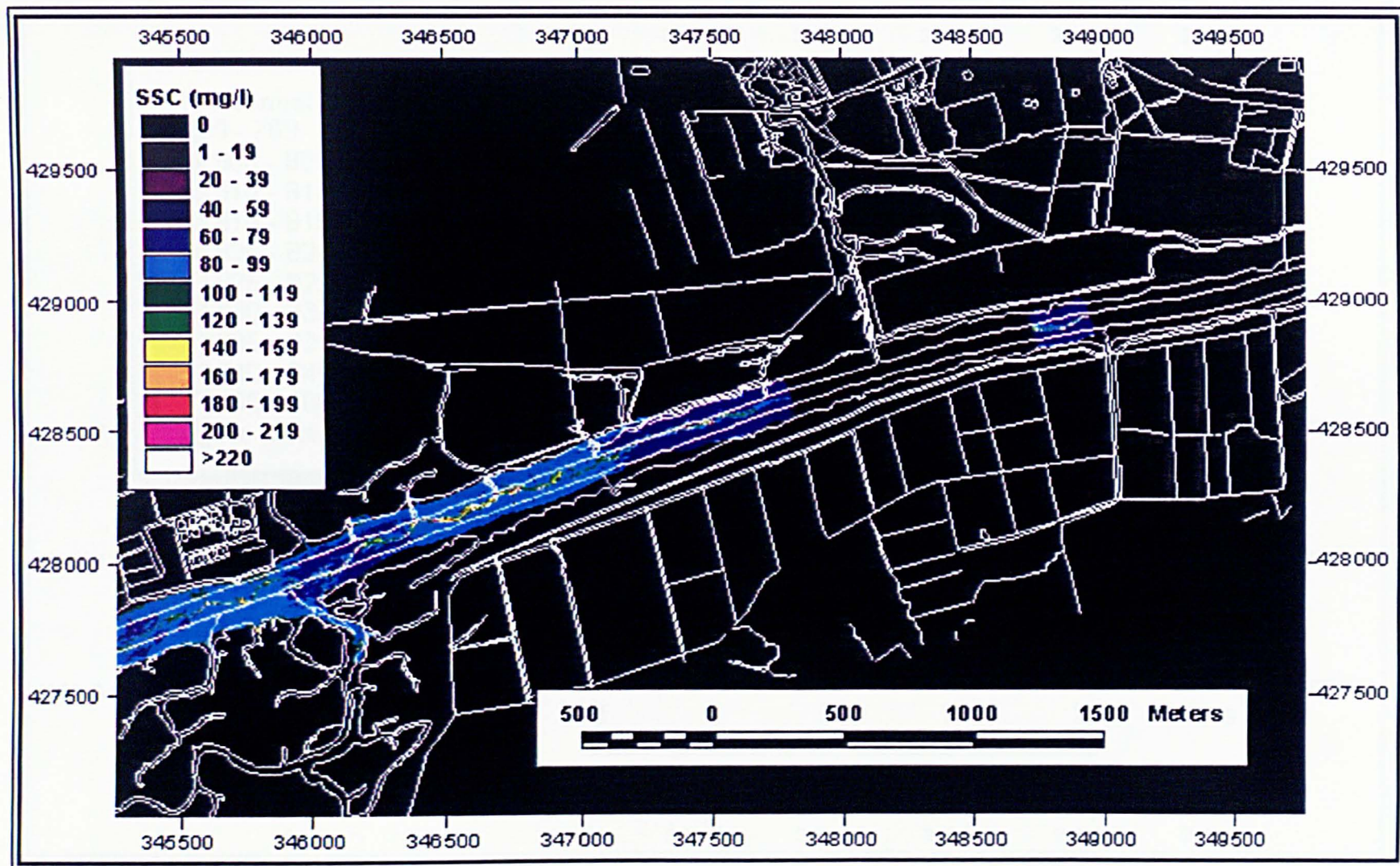


Figure 6.3h(i) CASI image calibrated to suspended sediment concentration, (mg/l), of the Savick Brook area, 11:11, 20-7-97.

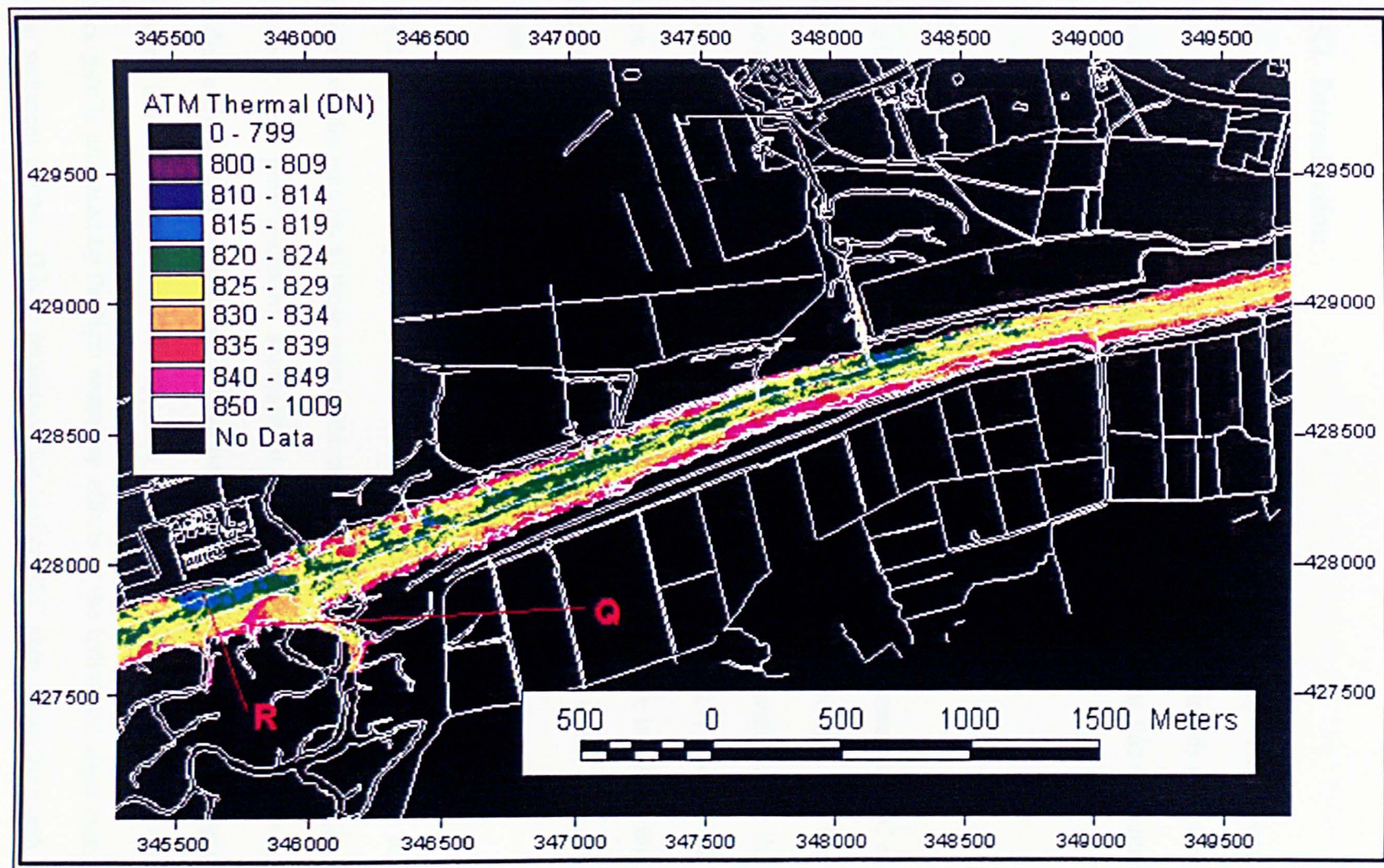


Figure 6.3h(ii) ATM thermal data of the Savick Brook area, 11:11, 20-7-97.

## **6.5 THE DOCKS**

### **6.5.1 Introduction**

This area represents the upstream limit of the imagery for this study. The upper estuary is very important as the very fine sediment is known to settle out in this region and it is known that the finer sediments have the higher associated radionuclide concentrations, as discussed in chapter two.

### **6.5.2 08:11 GMT, Figure 6.4a**

The SSC range for this image is 0 mg/l to 190 mg/l in the river channel but SSC of up to 240 mg/l are found in the outer dock basin. This is due to the presence of a bloom of blue-green algae. There are two sandbanks exposed in this low water image that may affect the flow patterns later in the flood tide, at **A**, (349725E, 429110N) on the north bank and at **B**, (350440E, 429250N). It is known that the tidal bore is off Warton bank, therefore the water along this stretch of the river is still at low water, probably with some ebb flow.

The SSC differs greatly at the dock entrance. West of the dock entrance the SSC exhibit similar patterns to those seen in the east of the previous low water image, which become more pronounced on approach to the dock entrance. Aerial photographic evidence shows that the dock gates have been opened to enable the toxic algae to be drained from the dock basin. The apparent high SSC of the water flowing out of the dock gate is produced by the light scattering effects of the individual algae cells rather than sediment grains. This is producing the higher SSC seen along the north of the channel as far down stream as Savick Brook, 2500m away. This is supported by the

thermal data showing the cooler water from the docks hugging the north bank. Immediately east of the dock entrance the SSC fall dramatically. As the channel is not known to gain in depth at this point it suggests that the bathymetric contributions to the spectral signature can be considered to be minimal.

### **6.5.3 08:30 GMT, Figure 6.4b**

The SSC range for this image is 0 mg/l to 180 mg/l in the river channel but SSC values of up to 240 mg/l are found in the outer dock basin. The image shows some spatial geographic distortions that are not accompanied by sudden variations in SSC of roll effects. This image is not yet subject to the flow of the flood tide as the dock basin is still draining into the river. The water level in the outer dock basin has dropped substantially revealing a sandbank in the northwest corner of the outer basin. The SSC around the dock entrance has dropped since the previous image and there is no obvious water body hugging the northern training wall, probably a result of reduced water flow from the dock basin. Further west, the north-south channel divide of SSC is still evident.

### **6.5.4 08:45 GMT, Figure 6.4c**

The SSC range for this image is 10 mg/l to 200 mg/l in the river channel but SSC values of up to 300 mg/l are found in the outer dock basin. The tidal bore image has not reached this section of the river, therefore the SSC patterns are the same as the two previous images. The water level in the dock basin has further decreased resulting in greater exposure of the dock basin sandbank.

The highest SSC of the river is found on the northern shore along the edge of a sandbank, however, these concentrations are greater than those being discharged from the dock basin. This suggests two possibilities:

1. the flow from the dock is causing some erosion of the sandbank at this location, or
2. there is some spectral contribution from the sandbank where the water is very shallow at the edge.

The area along the edge of the sandbank that is showing higher SSC in the CASI image can be seen to be having a warming effect on the water in the thermal image. This suggests some heat transfer to the water by suspension of warmer deposited sediment from the sandbank, which supports the latter possibility of erosion resulting from the flow of water from the dock basin.

#### **6.5.5 09:02 GMT, Figure 6.4d**

The SSC range for this image is 15mg/l to 200mg/l in the river channel with SSC values of up to 290mg/l found in the outer dock basin. There are some severe geometric distortions, particularly in the 500m stretch west of to the dock entrance, but these are not accompanied by the changes in SSC associated with aircraft roll, indicating reliable SSC data.

The area is not yet subject to the flood tide as the bore is currently 1 km downstream of the western edge of this image. The outer dock basin is still emptying as the sandbank in the corner has again increased in size. The area of erosion associated with the sandbank around 349800E is still showing elevated levels of SSC, however, this time there is no coincidental warming in the thermal image. The thermal image shows cooler

water in this area, which has come from the dock basin, and does not rule out the possibility that flow from the dock basin is causing erosion of the sandbank.

#### **6.5.6 09:20 GMT, Figure 6.4e**

The SSC range for this image is 20 mg/l to 250 mg/l in the river channel with SSC of up to 270 mg/l found in the outer dock basin. This image does suffer some geometric distortion but this is not due to aircraft roll. The ATM imagery is also subject to some geocorrection problems, as the outer dock basin does not fit the overlaid map.

At the eastern end of this image there is a large increase in SSC, this is due to the approach of the flood tide. The tongue of lower SSC from the dock, shown as pale blue, no longer reaches as far downstream as in the previous image. The tidal front has not yet reached the dock entrance and high SSC water is still leaving the outer dock basin and hugging the northern shore. The ATM thermal imagery shows a significant warming of the low SSC water in the eastern half of the image.

#### **6.5.7 09:37 GMT, Figure 6.4f**

The SSC range for this image is 20 mg/l to 230 mg/l in the river channel with SSC of up to 280 mg/l found in the outer dock basin. This image is subject to some large spatial distortions. The two areas where the SSC is increased by aircraft roll are at **C**, (350195E to 350515E) and **D** (351410E to 351555E), other distortions are not subject to SSC errors.

The flood tide has now reached the upper estuary as a well-defined V-shaped tidal boundary can be seen at **E** (351580E). Unusually, the apex of the V is inverted. The

ATM thermal image shows that this intruding water is cooler than the river water. In a normal tidal intrusion the apex of the V is first to intrude as the flow along the riverbanks tends to be slowed by friction. Here the opposite appears to be happening with the water travelling faster along the banks of the river. This is a feature associated with a high inertia flood tide, which can be expected in such a narrow constricted river channel (Largier, 1992). Immediately in front of the tidal intrusion the SSC is increased to 40-60 mg/l for approximately 80m, after which the values are in the usual 20-40 mg/l range. The outer dock basin is starting to refill with water with a lower SSC and algae content. There is a second area of high SSC between the two bridges at the eastern extremes of the image suggesting some flow induced by the incoming tide long before the defined tidal boundary.

#### **6.5.8 09:55 GMT, Figure 6.4g**

The SSC range for this image is 60 mg/l to 240 mg/l. There are errors in the geo-correction of this image as the river does not lie exactly within the training walls on the overlaid map, but there are few errors associated in SSC. There is only one area where the SSC is affected at F, (349570E to 350290E). In this 800m stretch of the river the SSCs are reduced by approximately 5%.

The highest SSC values are found along the stretch of river running parallel to the dock basins. The tidal boundary, now beginning to round the corner of the river near the bridges, is changed from a V-shape to a diagonal line across the river. The highest SSC or turbidity maximum, lies between 300m and 1600m west of this tidal boundary. The SSC gradient across the tidal boundary has decreased from the previous image, which indicates mixing processes are occurring. The SSCs at the lower end of the range have

also increased since the previous image, supporting the suggestion of the occurrence of turbulence and mixing processes before the passing of the tidal front.

Foam lines, indicating the presence of an axial convergence front, are now seen in these upper reaches of the river and a well-defined foam line running as far east as the dock entrance. Aerial photographic evidence shows very faint foam lines east of the lock gate, indicating that the convergent currents are starting to form a faint foam line at 351400E and this continues for the length of the river as far as the weir at approximately 352860E, 428400N.

### **6.5.9 11:11 GMT, Figure 6.4h**

The SSC range of this image is 60 mg/l to 240 mg/l, however the higher values are from a large area of foam and the highest real SSC is probably 140 mg/l, a substantial decrease from the previous image. At least half of the CASI image had to be removed due to cloud obscuring the true SSC.

The foam line that previously ended just west of the dock entrance now passes this point and touches the northern training wall at **G**, (350750E). Using the aerial photographs to interpret the missing CASI data, the foam line then runs along the northern training wall for approximately 270m before moving into the main channel again, where the foam picked up from the northern training wall is unlike that seen previously. It appears to be a fine dust lying on top of the water. This is clearly illustrated at **H**, (351480E, 429330N), showing an erroneously high SSC. The thermal image shows this area as being warmer than the surrounding water; this would suggest the foam was a fine dry dust picked up from the crevices in the training wall.

### **6.5.10 11:25 GMT, Figure 6.4i**

The SSC range for this image is 25 mg/l to 100 mg/l, another overall decrease in SSC. The SSC is spatially very well mixed in the main channel, supported by the thermal data. There are concentrations of up to 200 mg/l in the outer dock basin as the inner dock gates are now open, allowing the algae into the outer basin. There are some spatial distortions but only one stretch shows SSC reduced by 15-20%, at **I**, (349960E to 350180E).

The foam line indicating the presence of the axial convergence front runs up the main channel as far east as the dock entrance, falling short of the position found in the previous image. There are also signs that the convergence is starting to weaken as the sinusoidal patterns found in the previous sections of the river are just starting to form in this section, **J**, (349980E). The large patches of foam that appeared in the previous image also appear in the same location in this image.

### **6.5.11 Docks Summary**

1. Prior to the influence of the flood tide the SSC in the river ranges from 0 to 200 mg/l.
2. The higher SSC values are largely due to the release of water from the outer dock basin, which contain large quantities of blue-green algae. The algae were in such high concentrations that light was scattered by individual phytoplankton cells giving the impression of a high SSC.
3. The water released from the dock flows west down the river, hugging the northern shore of the main channel.

4. The incoming tide is not seen to have any effect on the SSC patterns until 09:20am (Figure 6.4e) when an increase in SSC is seen in the western end of the image.
5. A defined V-shaped boundary marking the tidal intrusion front was visible on the 09:37am image (Figure 6.4f). West of the front the SSC was approximately 160 mg/l. To the east of the tidal intrusion front the SSC were significantly lower at approximately 50 mg/l.
6. In Figure 6.4g, the front has progressed as far east as the first bridge and now takes the form of a diagonal line across the river. The SSC gradient across the front, though still visible is now more gradual than for Figure 6.4f.
7. The first appearance of a foam line, indicating the axial convergence, is seen in Figure 6.4g, at 09:55am. This line reaches as far east as the dock entrance and does not differ greatly in location for the rest of the image series.
8. The axial convergence foam line starts to show signs of breaking down in the last image of the series, as small sinusoidal patterns start to appear.
9. East of the dock entrance, patches of very bright foam or dust are being picked up off the northern training wall, giving areas of erroneously high SSC.
10. In areas not masked by this foam the SSC starts to decrease, showing signs of sediment settling over the last two images.

The most likely reason for the accumulation of fine sediment in this region of the estuary can be seen in the 09:55GMT image (Figure 6.4g). This is the last image taken prior to the start of the sediment settling process. At this time, this upper section of the estuary is subject to the highest SSC seen in any area of the estuary. This is to be expected because the water entering the outer estuary is known to be low in SSC; therefore the source of suspended sediment is from within the estuary. This suggests

that as the tide progresses further up the estuary the greater the amount of sediment that will have been resuspended. As the flood tide is relatively short for the upper estuary settling will occur soon after the maximum SSC values are reached. The sediment accumulating around the upper estuary is particularly fine and thus carries a relatively high load of radionuclides. The fact that this area is a sink for the very fine sediment may also be linked to the long slow ebb tide that is a feature of this area, as this would not be powerful enough to erode cohesive sediments.

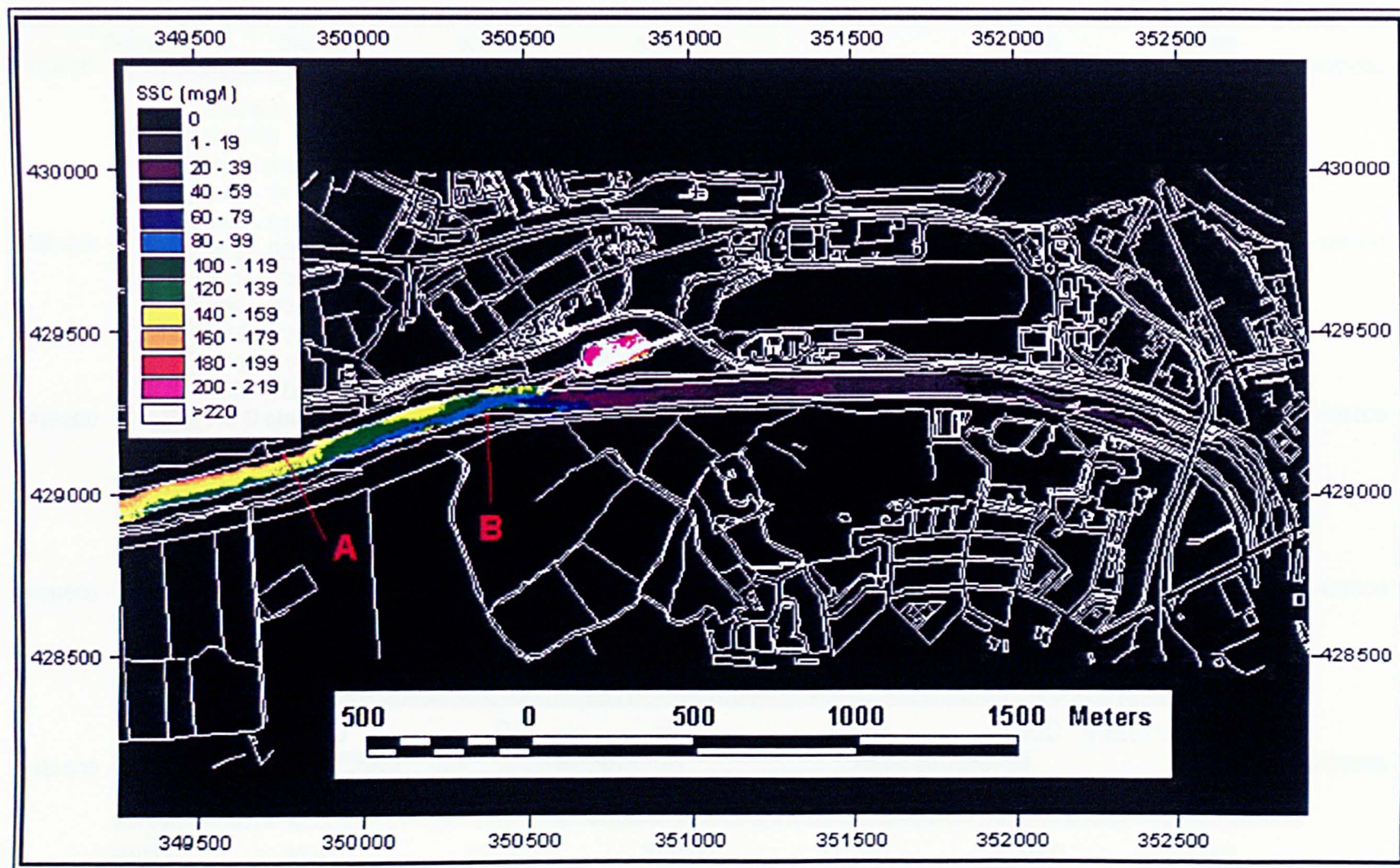


Figure 6.4a(i) CASI image calibrated to suspended sediment concentration, (mg/l), of the Preston Dock area, 08:11, 20-7-97.

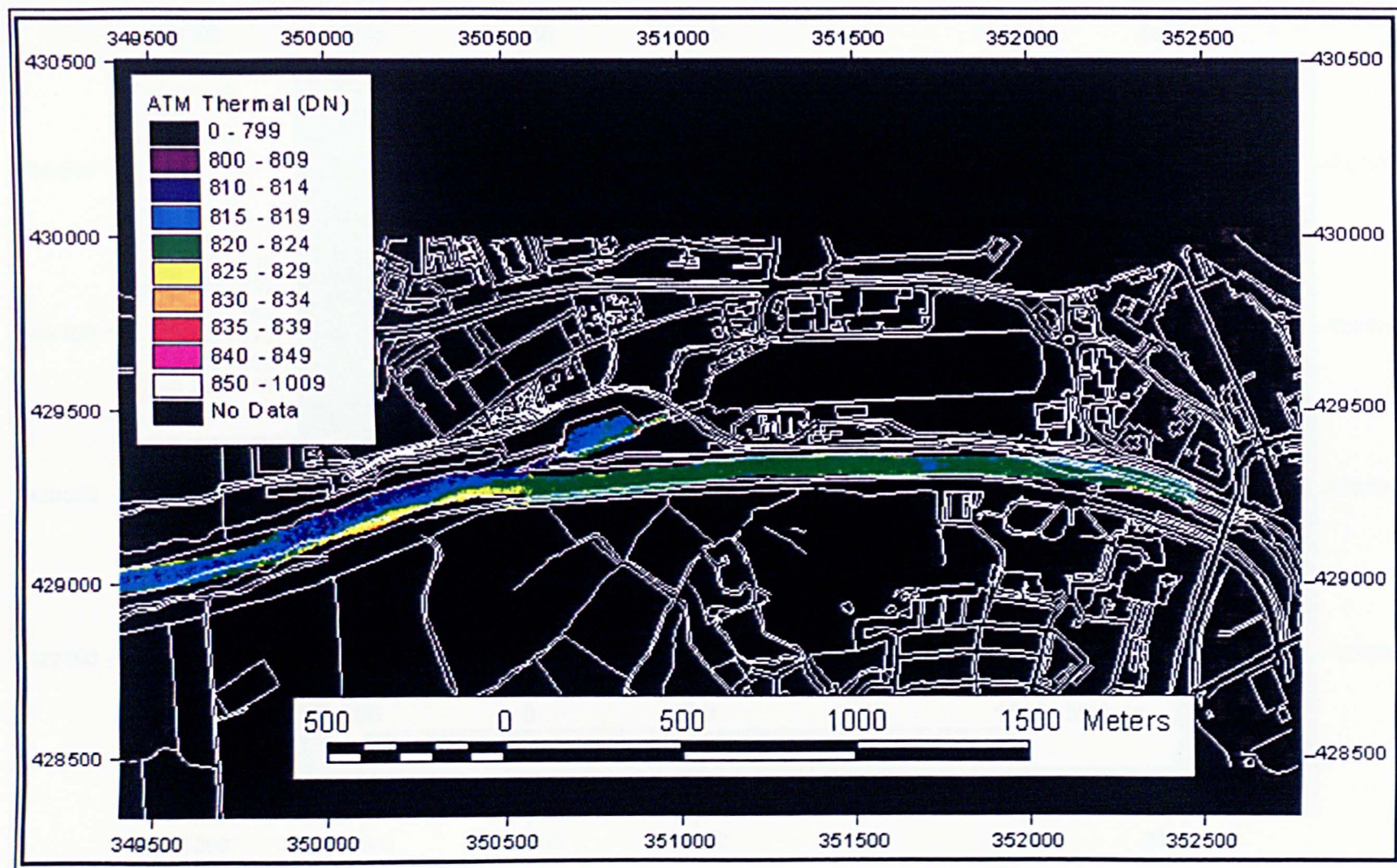


Figure 6.4a(ii) ATM thermal data of the Preston Dock area, 08:11, 20-7-97.

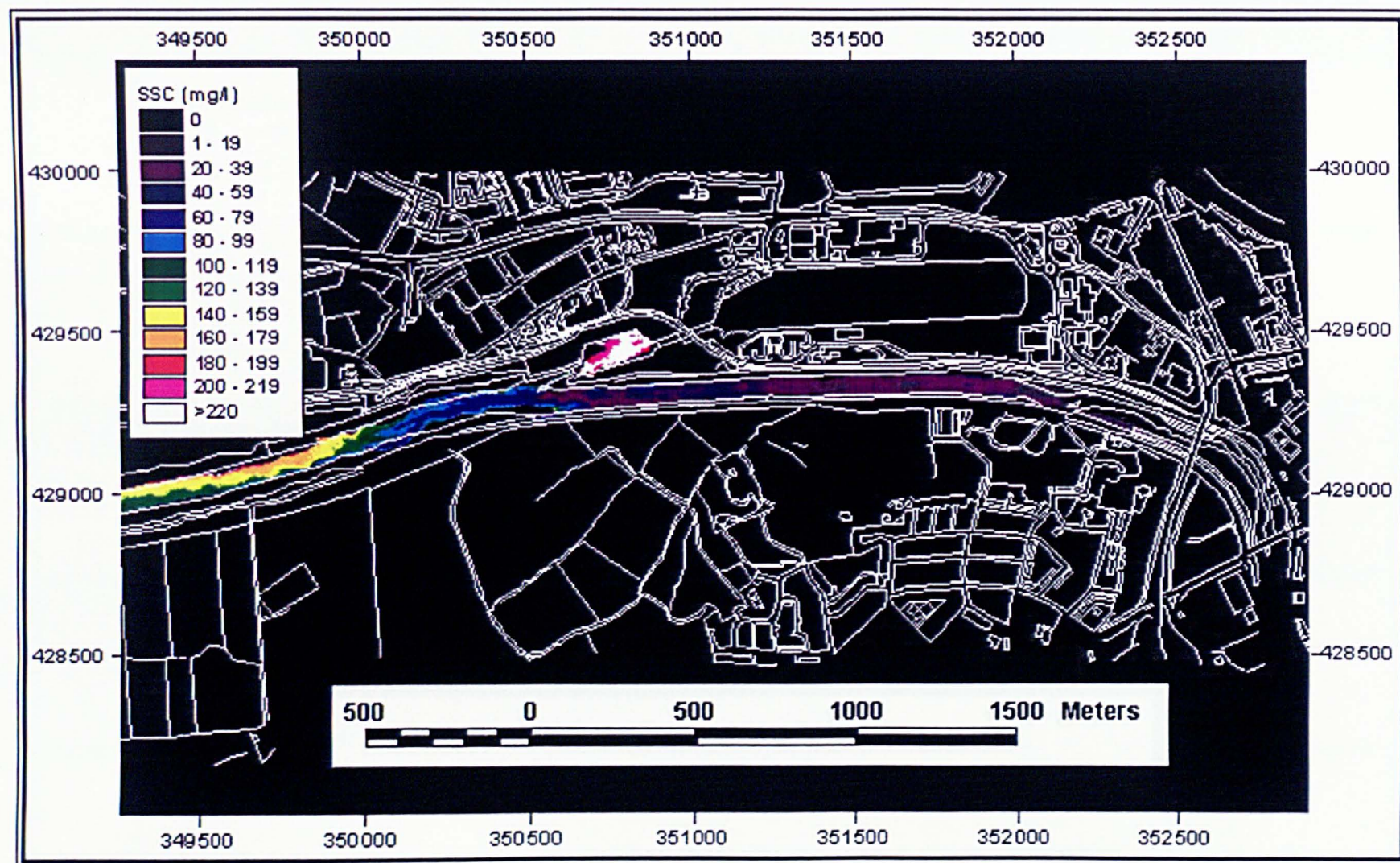


Figure 6.4b(i) CASI image calibrated to suspended sediment concentration, (mg/l), of the Preston Dock area, 08:30, 20-7-97.

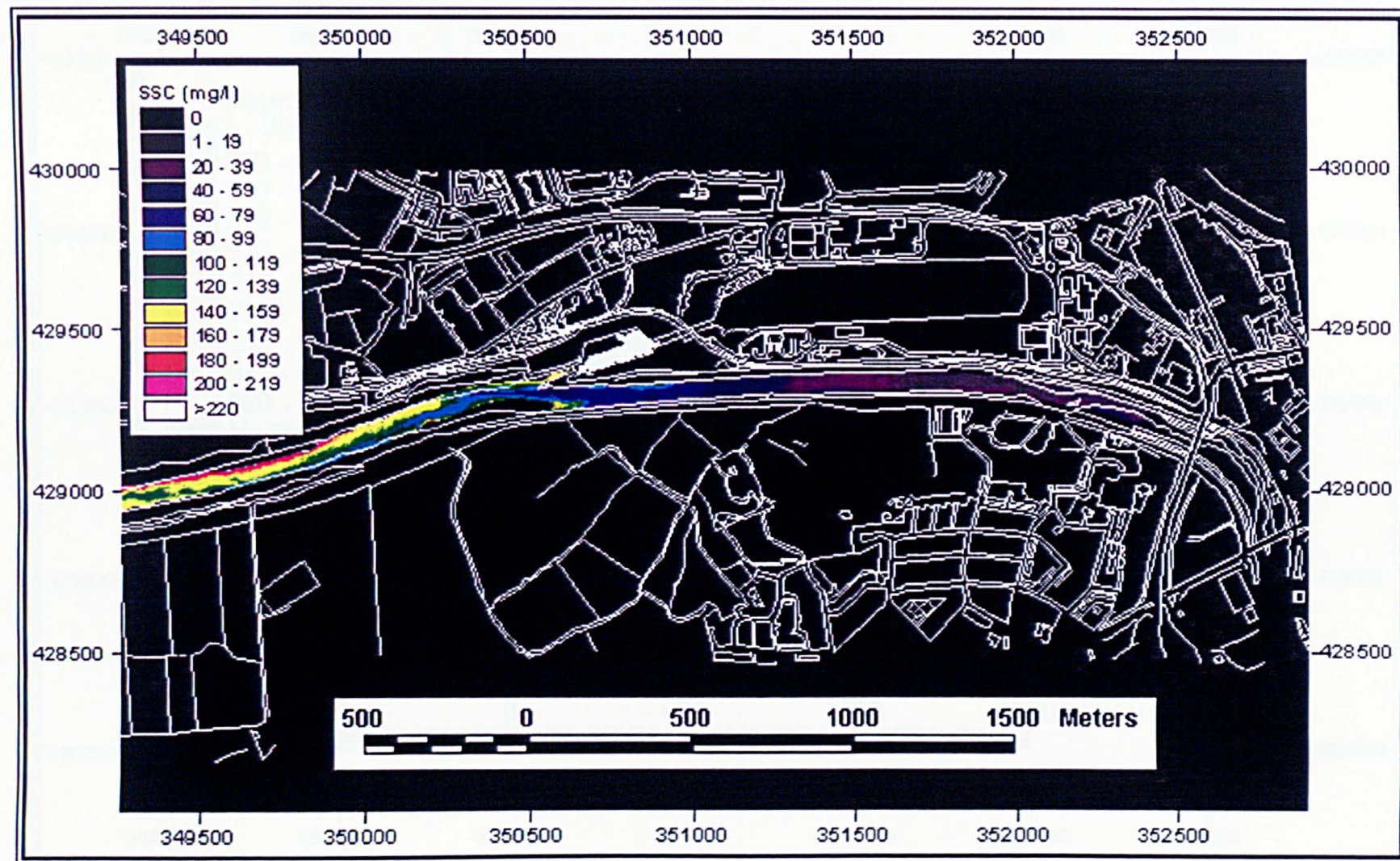


Figure 6.4c(i) CASI image calibrated to suspended sediment concentration, (mg/l), of the Preston Dock area, 08:44, 20-7-97.

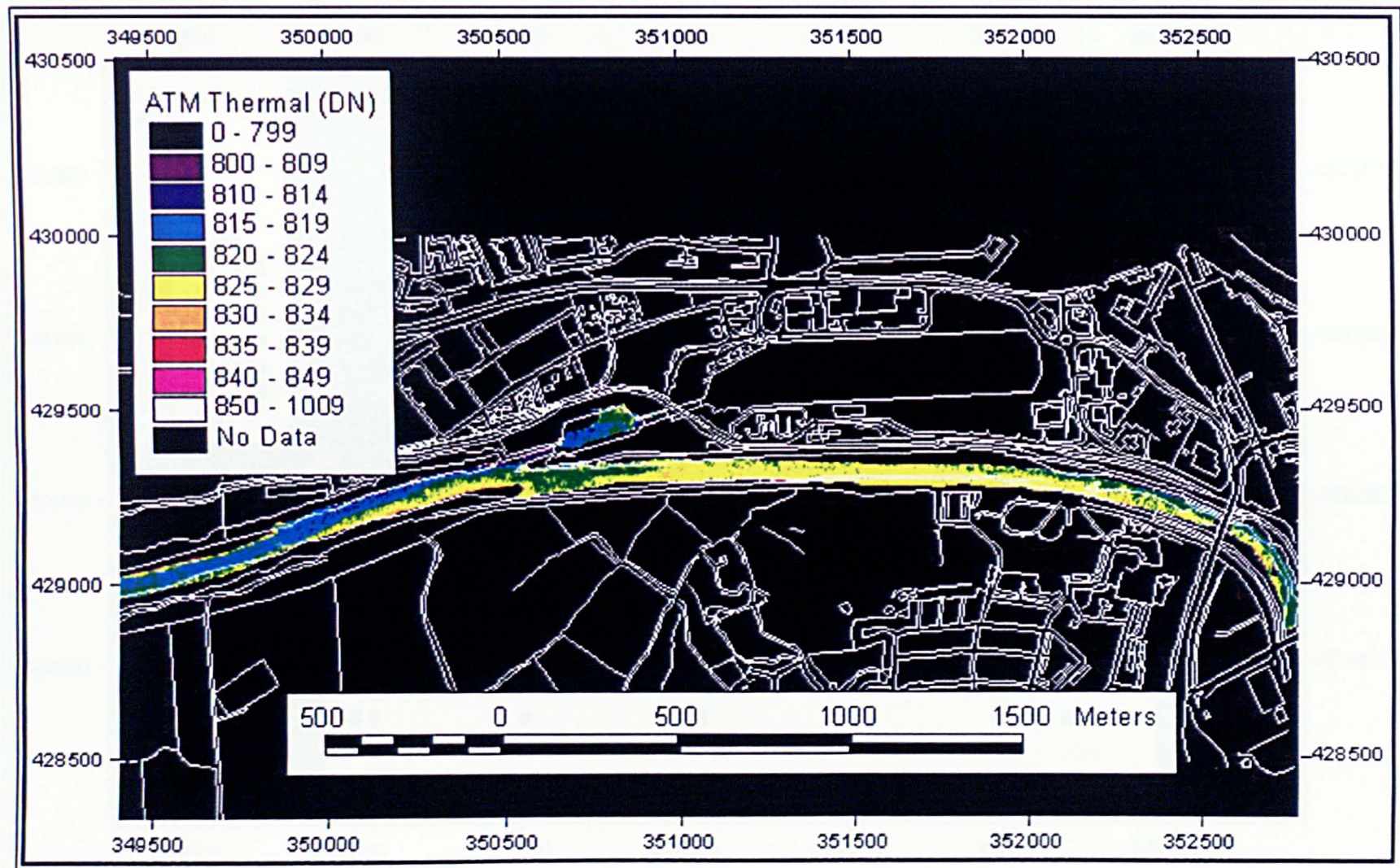


Figure 6.4c(ii) ATM thermal data of the Preston Dock area, 08:44, 20-7-97.

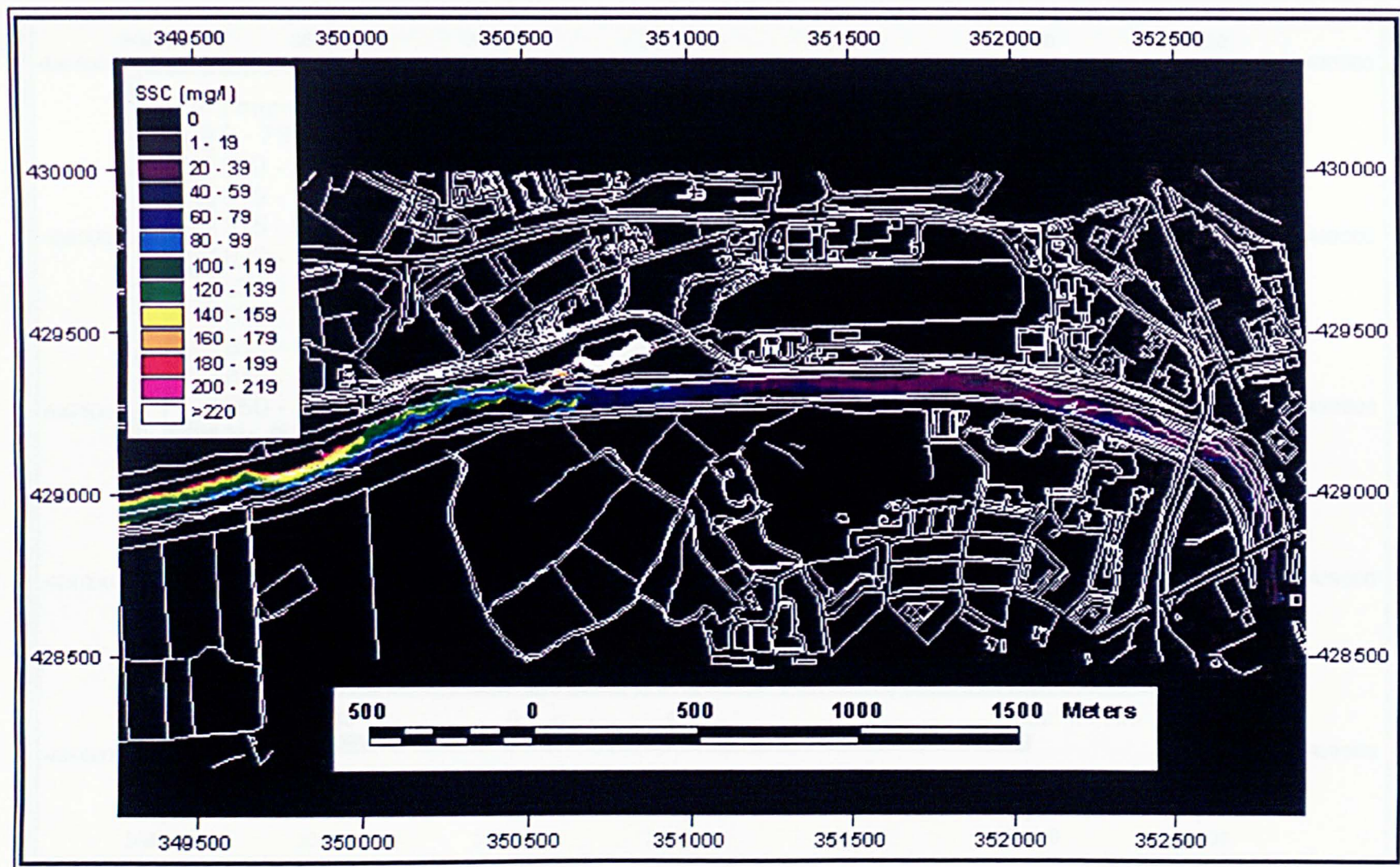


Figure 6.4d(i) CASI image calibrated to suspended sediment concentration, (mg/l), of the Preston Dock area, 09:02, 20-7-97.

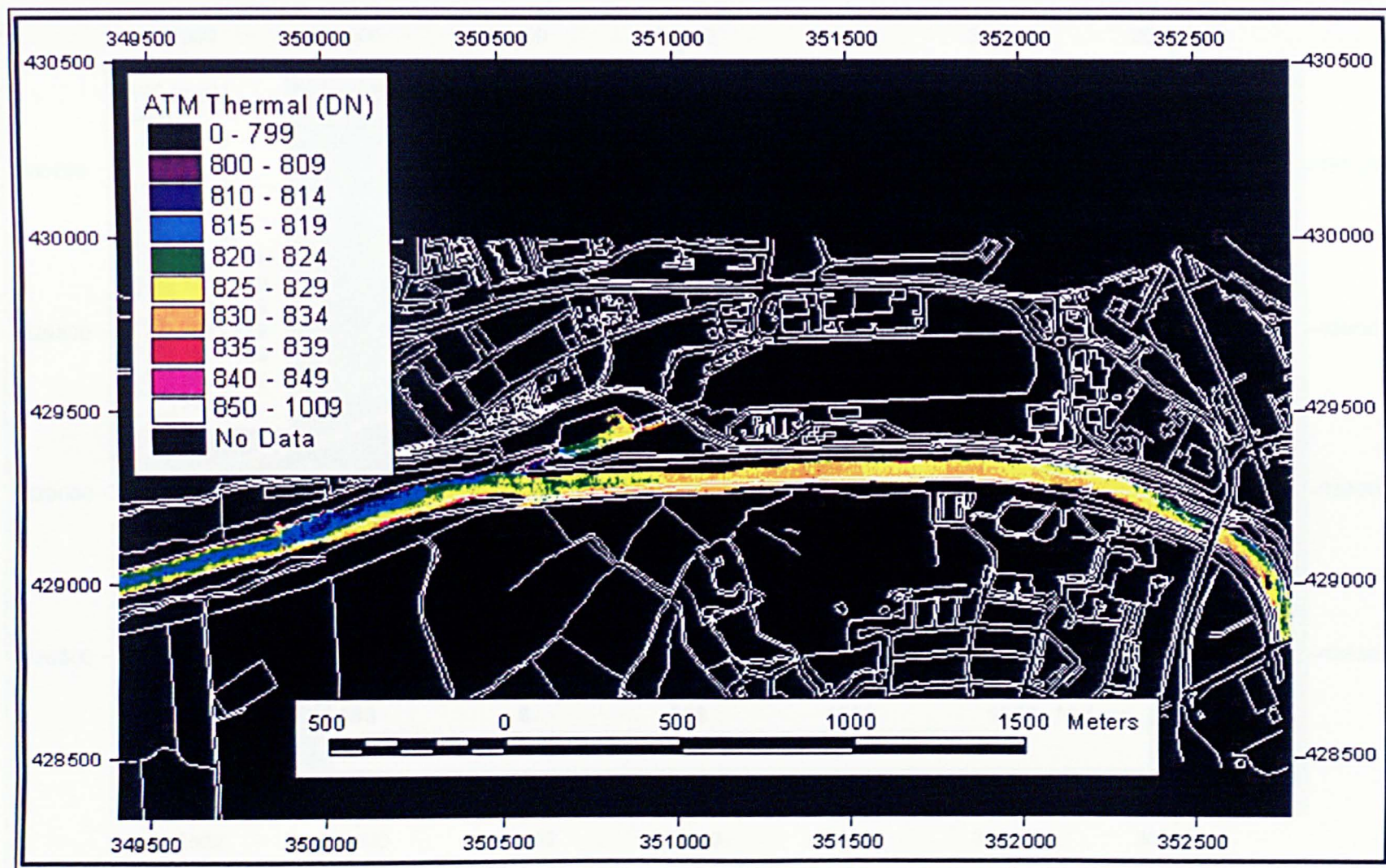


Figure 6.4d(ii) ATM thermal data of the Preston Dock area, 09:02, 20-7-97.

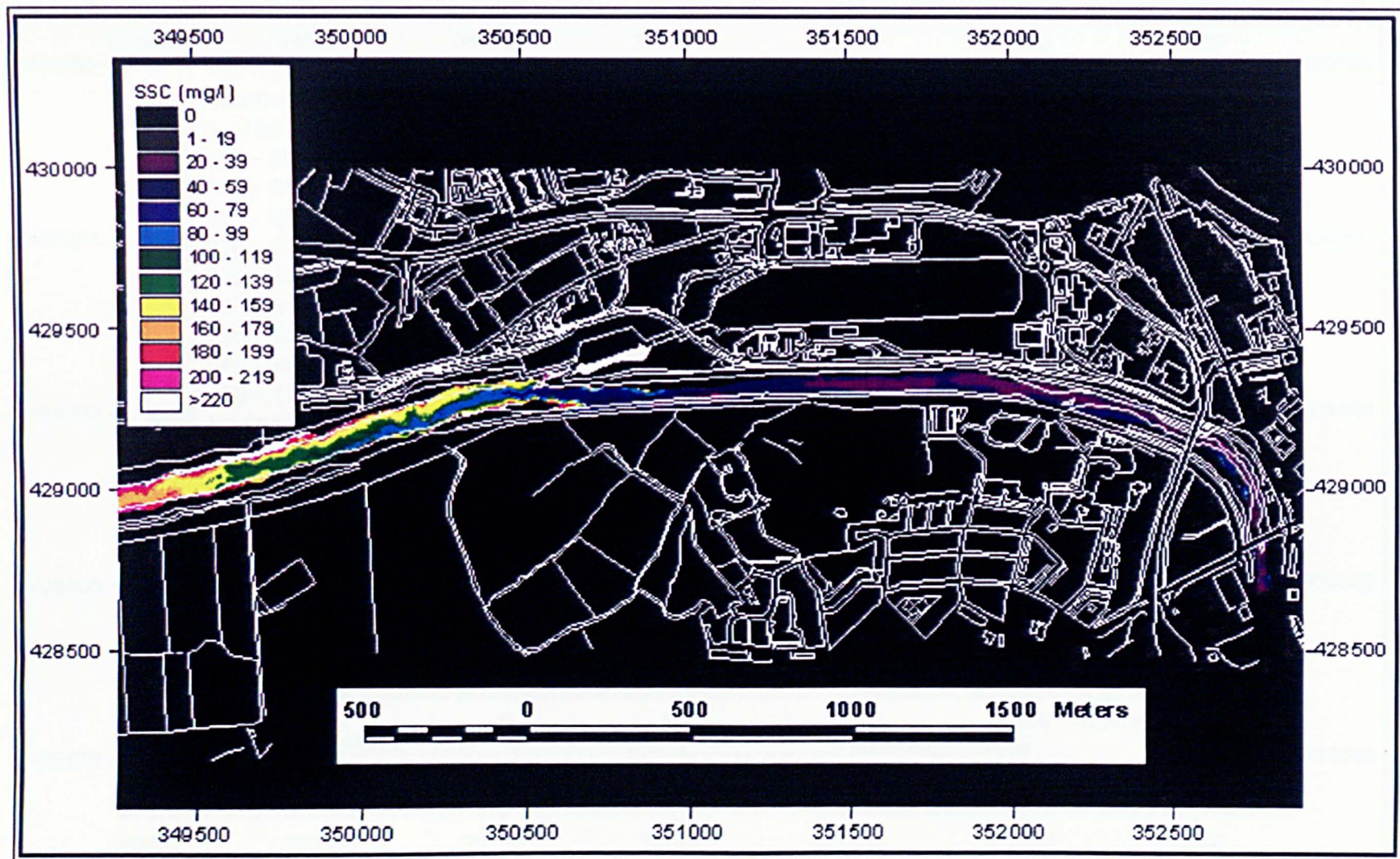


Figure 6.4e(i) CASI image calibrated to suspended sediment concentration, (mg/l), of the Preston Dock area, 09:20, 20-7-97.

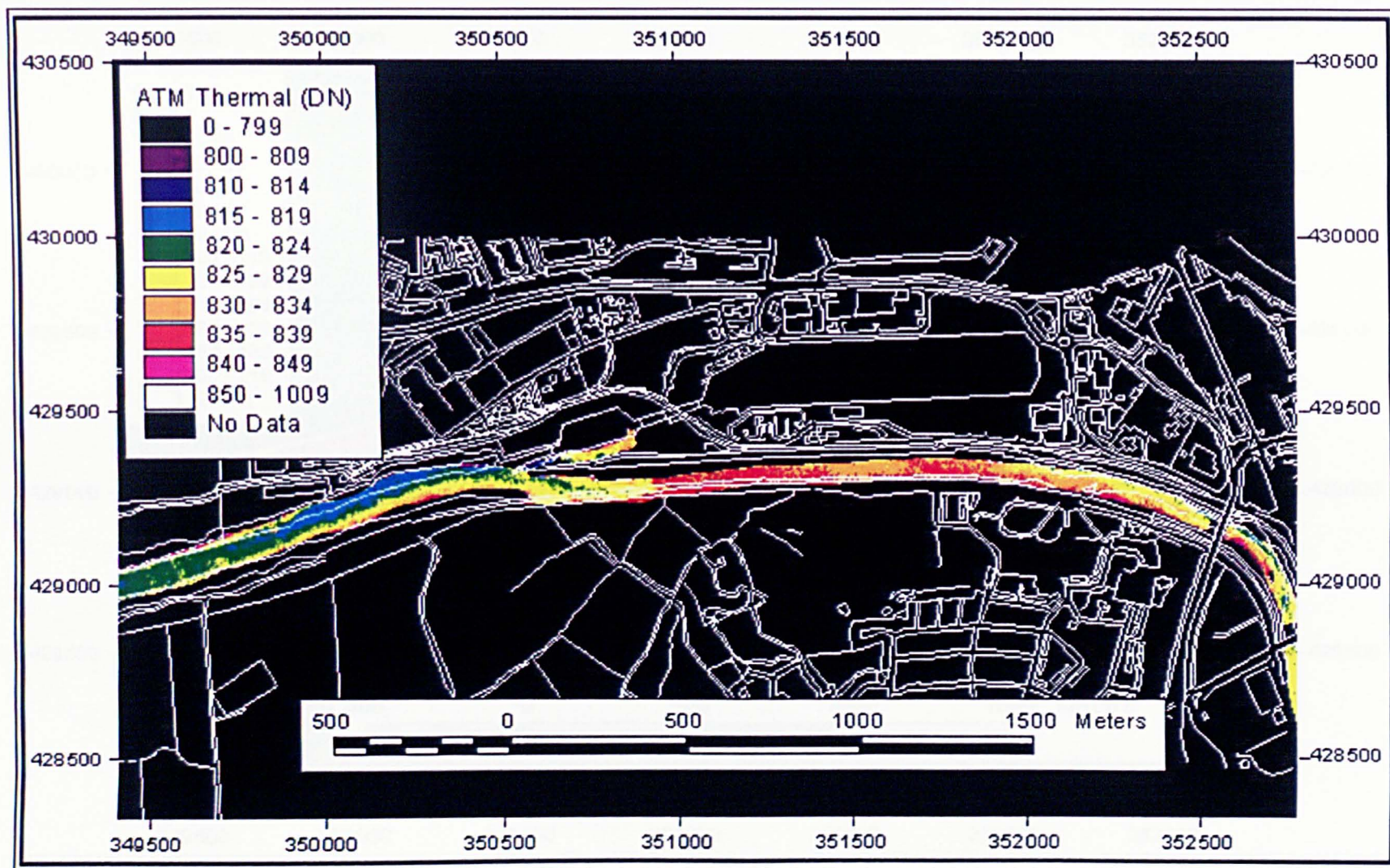


Figure 6.4e(ii) ATM thermal data of the Preston Dock area, 09:20, 20-7-97.

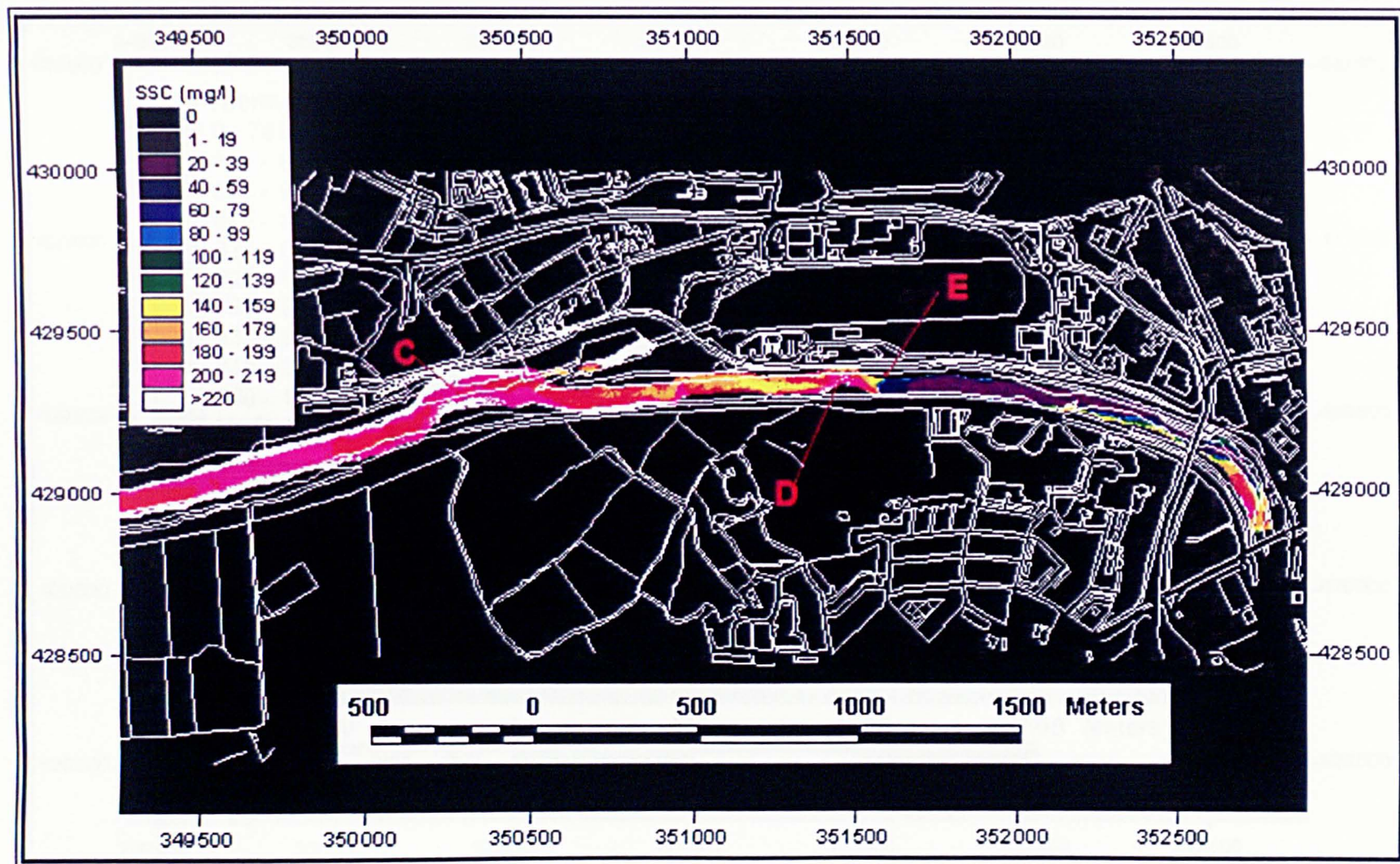


Figure 6.4f(i) CASI image calibrated to suspended sediment concentration, (mg/l), of the Preston Dock area, 09:37, 20-7-97.

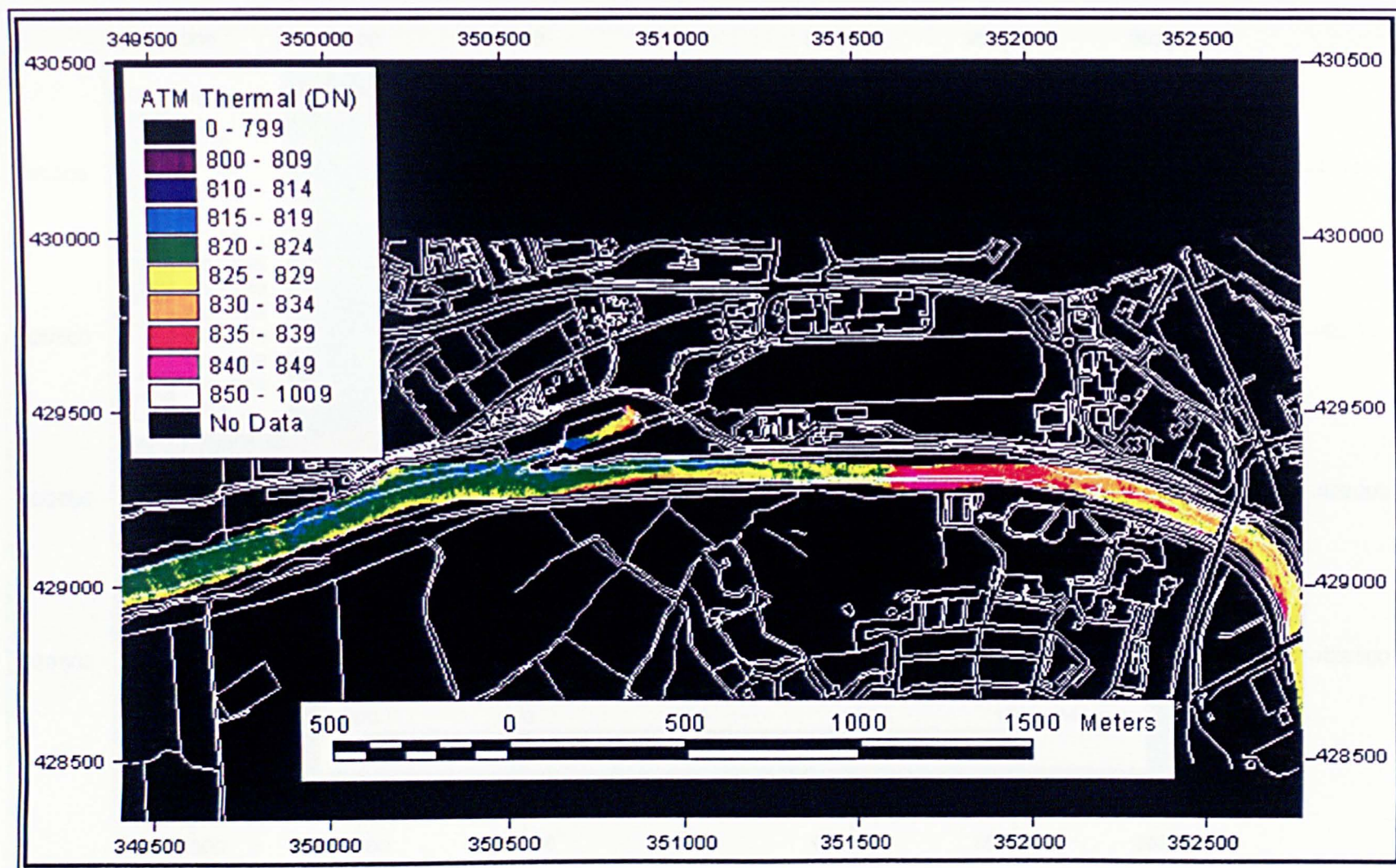


Figure 6.4f(ii) ATM thermal data of the Preston Dock area, 09:37, 20-7-97.

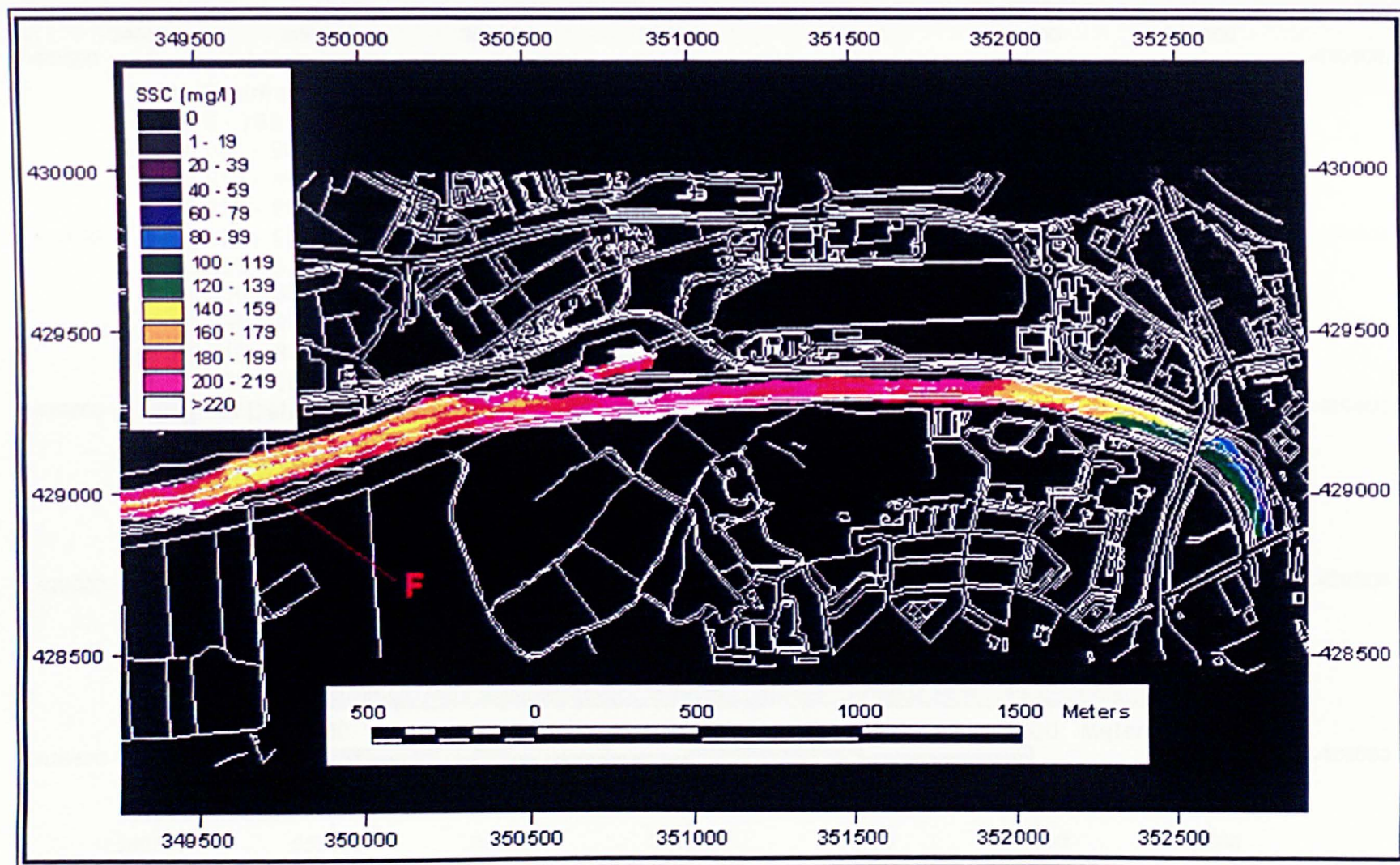


Figure 6.4g(i) CASI image calibrated to suspended sediment concentration, (mg/l), of the Preston Dock area, 09:55, 20-7-97.

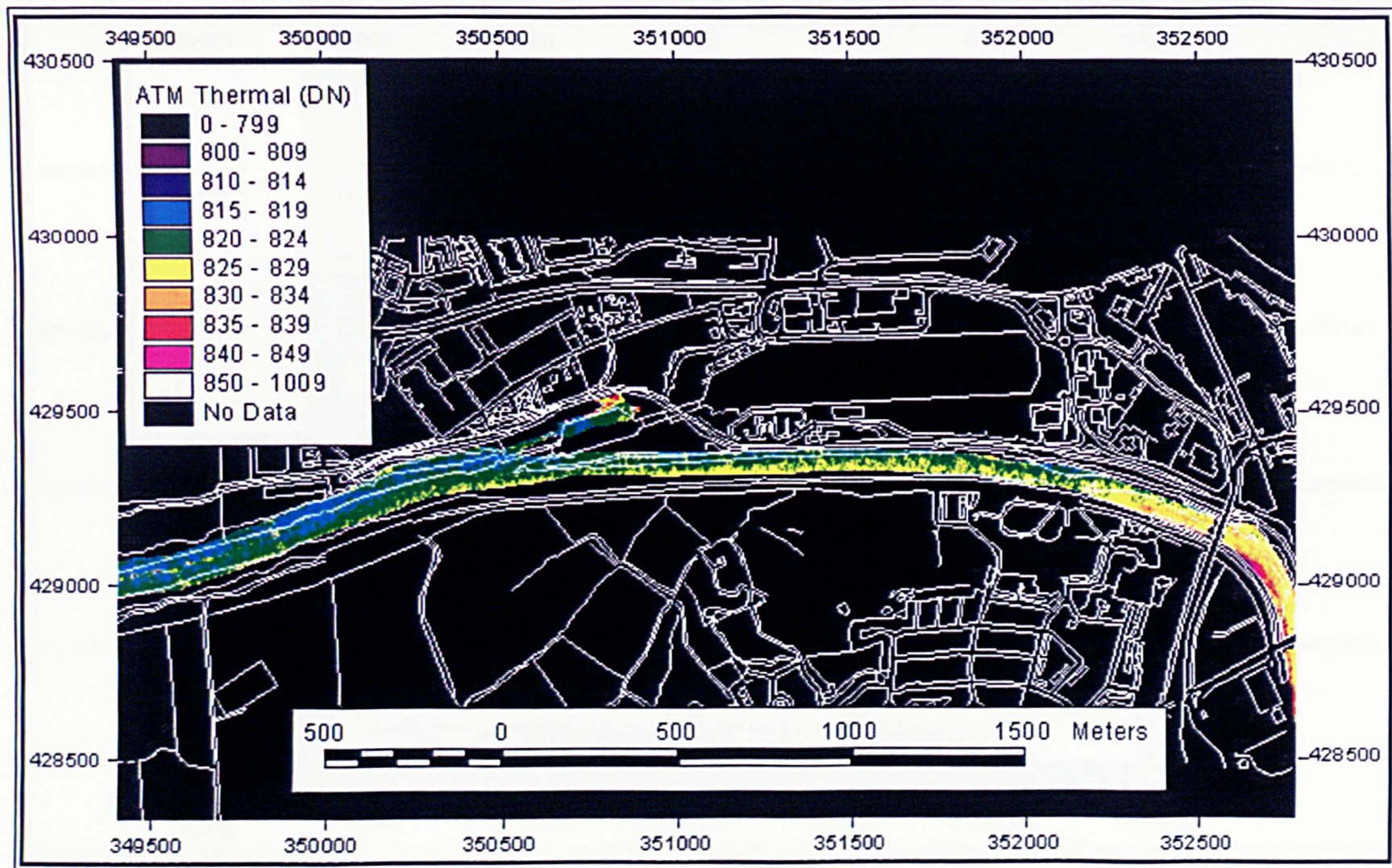


Figure 6.4g(ii) ATM thermal data of the Preston Dock area, 09:55, 20-7-97.

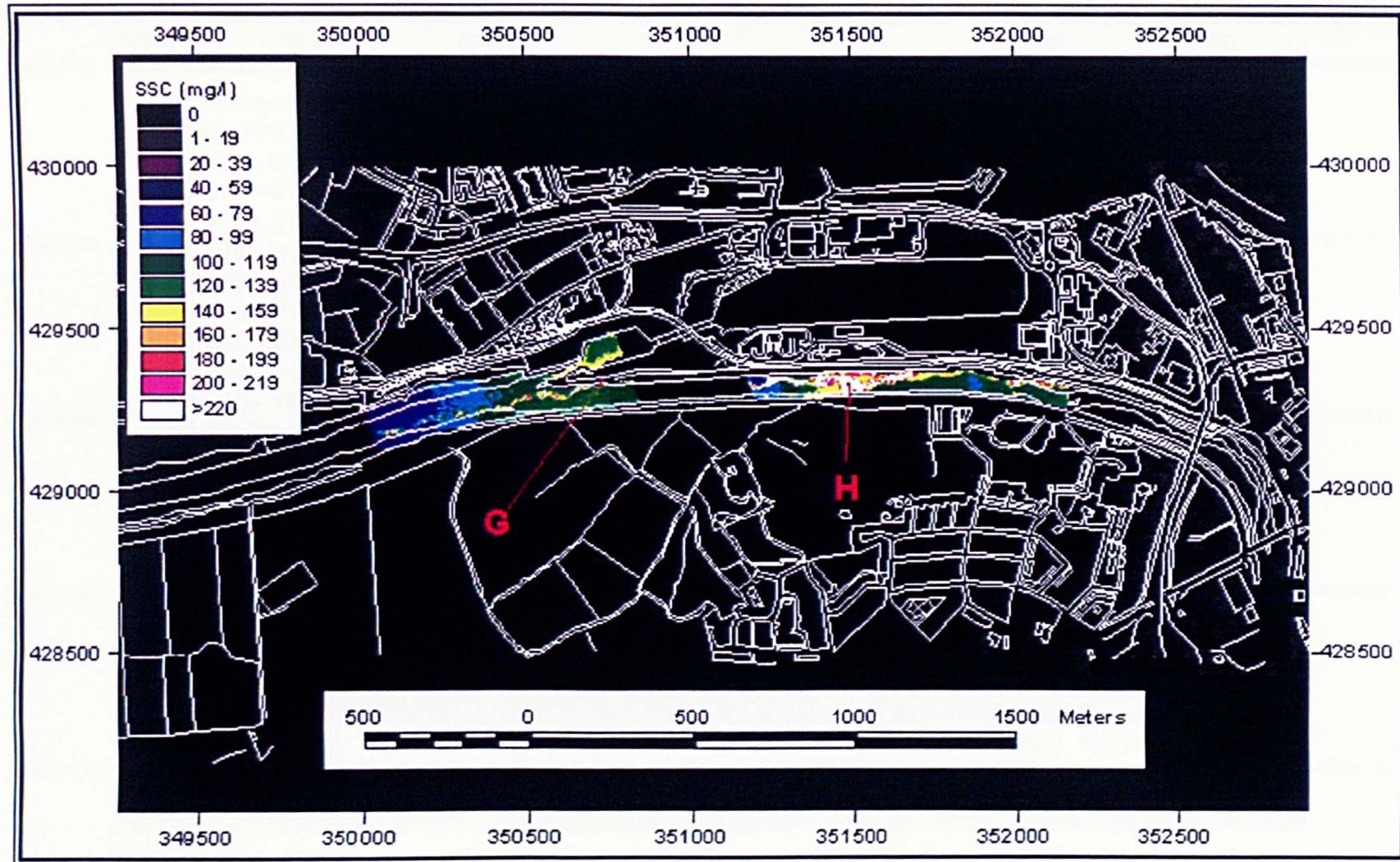


Figure 6.4h(i) CASI image calibrated to suspended sediment concentration, (mg/l), of the Preston Dock area, 11:11, 20-7-97.

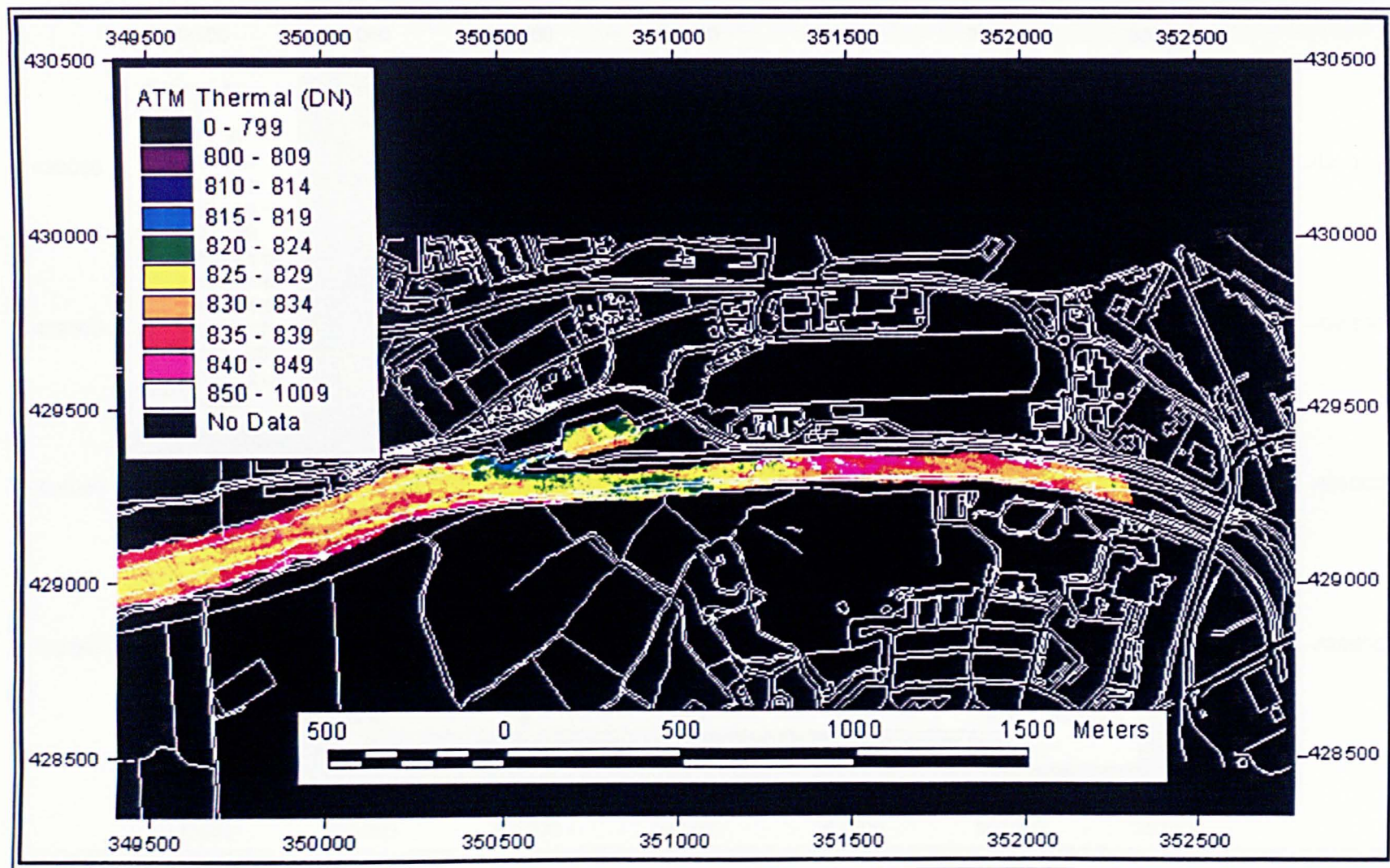


Figure 6.4h(ii) ATM thermal data of the Preston Dock area, 11:11, 20-7-97.

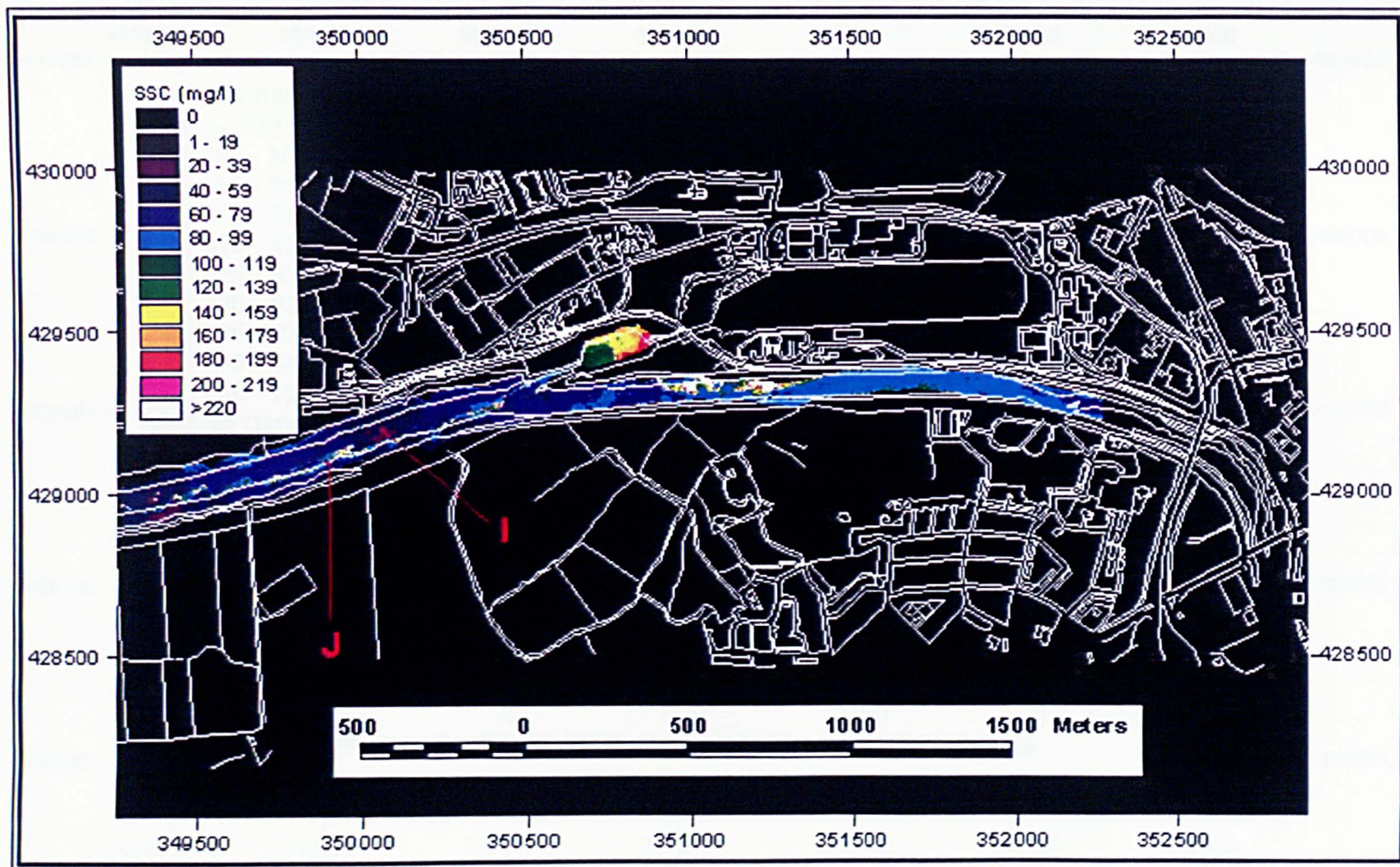


Figure 6.4i(i) CASI image calibrated to suspended sediment concentration, (mg/l), of the Preston Dock area, 011:25, 20-7-97.

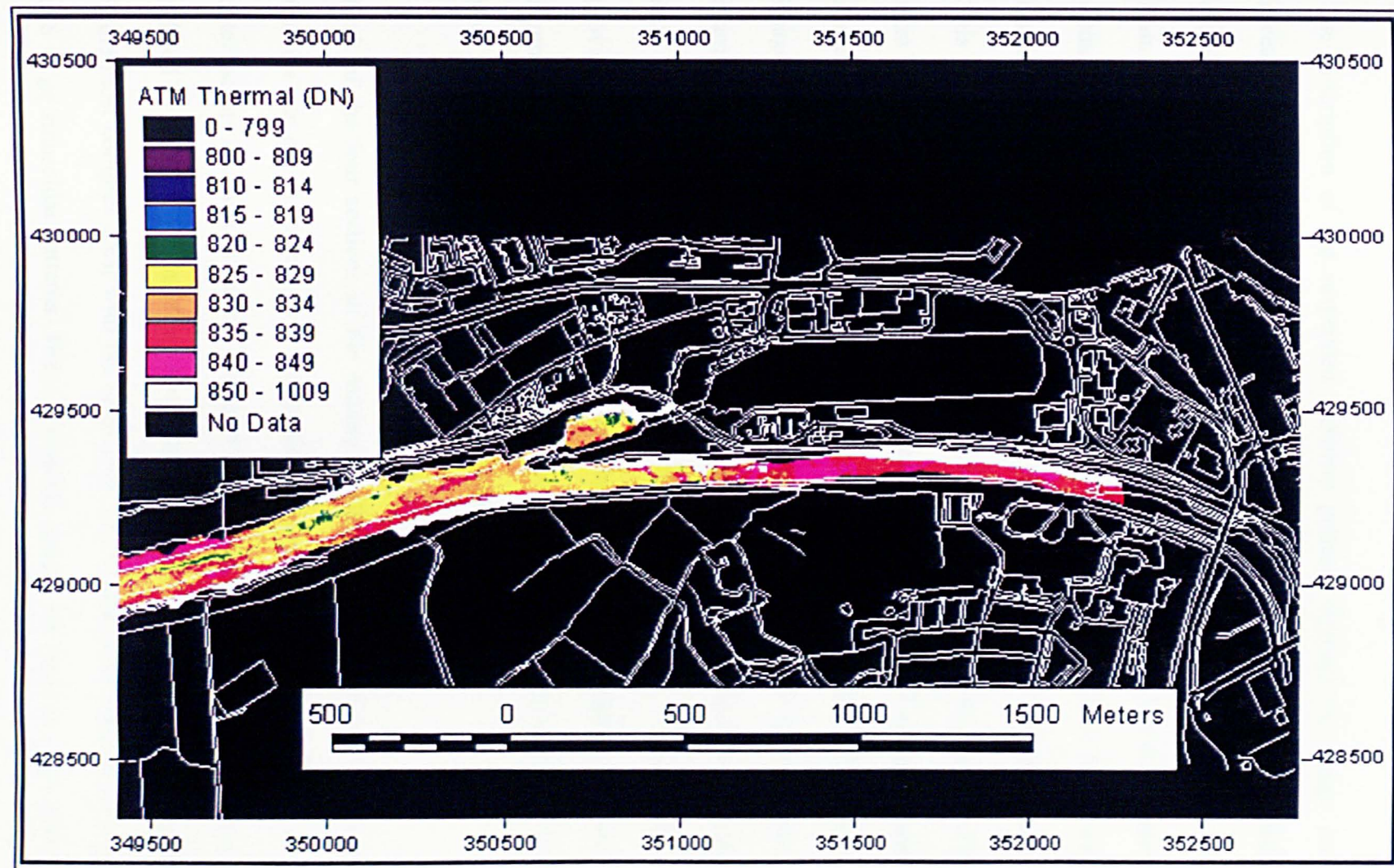


Figure 6.4i(ii) ATM thermal data of the Preston Dock area, 011:25, 20-7-97.

## 6.6 CHAPTER SUMMARY

The description of the suspended sediment patterns through the image series has revealed trends that occur throughout all sections of the estuary in addition to trends that are characteristic of a specific location within the estuary. One of the most important features of the estuary, as a whole, is that the images show that the water entering the estuary is low in suspended sediment. This confirms that the SSCs found within the estuary are almost entirely due to sediment being resuspended from within the estuary. This is further supported by the fact that all the images show a trend of higher SSC from west to east in each image section. This could only occur if sediment was being suspended from within the confines of the estuary. For the length of the estuary, the images show that the SSC are lower in the main channel than over the mud flats, as the intertidal areas are the source of the suspended sediment. As the water inundates the mud flats the sediment is suspended by the advancing water, evidence for this is provided by the fact that the SSC is always higher towards the edge of the water. This is most likely a result of the action of small wind generated waves, which are known to have a large erosive power in shallow tidal areas (Black, 1998).

Each of the four sections of the estuary detailed in chapter six also displays some features that are characteristic to that particular geographical section. For example, the outer estuary is characterised by V-shaped intrusions of low SSC water, which are often defined by lines of foam marking the boundary between water bodies. The confluence is the most complex area, with the foam lines of the axial convergence disintegrating into large sinusoidal patterns. These sinusoidal patterns are seen in other parts of the estuary but not as clearly as just west of the confluence. Areas of sediment suspension

vary with the flood tide as one source is exhausted so another becomes more dominant. This is particularly apparent in the confluence section, as erosion progresses along Longton Marsh. The very straight canalised section of the estuary from the sewage treatment works to east of Savick Brook is the stretch that shows the highest SSC and a very well defined axial convergence front. The upper estuary, around the docks, shows very low SSC but on arrival of the flood tide there is a V-shape intrusion with a very steep SSC gradient that is not seen elsewhere in the estuary.

The description of the trends and mechanisms within the estuary highlights some of the areas that require further investigation. In the following chapter areas will be studied in closer detail, assessing changes over time for a given location with the passing of the tidal bore. The data extracted from the images will then be compared to data from other sources to assess similarities and differences between the data sets. The image data will be used to try to answer some of the questions raised in this chapter. For example:

- Does the presence of microphytobenthos inhibit erosion in all the areas where the algae is present? This possible effect needs to be investigated by locating algal material on the aerial photography and reviewing the imagery for areas where erosion would be expected but is not occurring.
- How does the strength of the convergence vary throughout the flood tide? Can this be estimated from the imagery and used to help interpret sediment erosion mechanisms?

Finally the imagery will be used to calculate approximate suspended sediment and suspended  $^{137}\text{Cs}$  budgets at the various stages of the flood tide.

## **CHAPTER 7: SEDIMENT MOVEMENT IN THE RIBBLE ESTUARY**

### **7.1 INTRODUCTION**

Chapter six has introduced the calibrated suspended sediment images and qualitative analysis has revealed several questions that this chapter will examine in more detail.

The questions have been divided into two main subject areas:

1. Erosion of the intertidal sediments. The information acquired on erosion aims to identify the main sources of suspended sediment in the estuary and relate these sources to the intertidal sediment distribution based on image data collected two months prior to the flood tide image acquisition used here and mapped by Rainey, (1999). The possible effects of microphytobenthos as an erosion inhibitor will also be investigated.
2. Sediment transport and hydrodynamics of the estuary. This will include the importance of the tidal bore in sediment resuspension and the effects of estuarine fronts, in particular axial convergence, on the subsequent sediment transport.

The image data will then be compared to the results of the most recent model of the Ribble estuary, using identical flood tide conditions, to assess the similarities, contrasts and the compatibility between the two data sets. A combination of data from the two sources will then be used to calculate the total loads for suspended sediment and  $^{137}\text{Cs}$  over the flood tide and estimate net sediment and  $^{137}\text{Cs}$  budgets for the whole estuary.

## **7.2 EROSION OF INTERTIDAL AREAS**

### **Introduction**

The image data set comprises nine images collected during a single spring flood tide. The first seven images are almost evenly spaced at approximately fifteen minutes intervals. There is then an interruption of an hour and twenty minutes as a result of aircraft refuelling. This data set provides a series of snap-shots of the suspended sediment distribution within the estuary, providing a data set far superior to any current spatial data set available for the Ribble estuary. The data should enable mechanistic interpretations of the important regions of sediment supply and controls on the transportation of suspended sediment.

### **7.2.1 Identification of sources of sediment supply**

Prior to examining the images for areas of sediment supply it is necessary to consider the possible mechanisms of sediment contribution to the estuary. Sediment sources can therefore be grouped into two categories:

1. External sediment supply: where sediment is brought into the estuary from the Irish Sea.
2. Within estuary supply, which can be further divided into:
  - (i) Continuous sediment supply: where sediment is input to the water column throughout the entire flood tide.
  - (ii) Longitudinally transitional sediment supply: where areas of sediment supply become exhausted and are replaced by an adjacent supply.
  - (iii) Minimal sediment supply: where very little sediment is resuspended throughout the flood tide.

### **External sediment supply**

The extent of sediment input into the estuary from the Irish Sea is difficult to estimate from this series of images, primarily due to the restricted image area. To assess input from the Irish Sea images would be required covering the far outer reaches of the estuary to differentiate SSC derived from sources in the outer estuary to sources derived from the Irish Sea itself. However, the imagery reveals that in this instance the water entering the estuary contains low SSC indicating that, for this particular flood tide, little sediment is derived directly from the Irish Sea, typically <40mg/l. This situation must clearly vary according to weather and tidal conditions as mineralogical data shows that sediment entering the estuary is of a marine origin. This section will therefore focus on examples of within estuary supply of SSC.

### **Areas of continuous sediment supply throughout the flood tide**

Figures 7.1a to 7.1h show the first eight images for the outer estuary. These images focus on the extreme west of Warton Bank, where Lytham Creek flows into the main estuary channel. On the north shore, the area identified by the yellow box, exhibits consistently higher SSC than the immediate surrounding area throughout the majority of the flood tide. The initial increase in SSC (Figure 7.1a) occurs immediately behind a line of foam created as the water washes over a sandbank. In Figure 7.1b the SSC has significantly increased and appears to be generated by the flow of water around the sandbank. The sandbank is no longer visible in Figure 7.1c, however the SSCs on the north shore are still much higher than for the surrounding areas. In Figures 7.1d to 7.1g the higher concentrations of suspended sediment of that area, in comparison to that of the surrounding areas, are not so distinct. However, the concentrations are still

consistently greater than for the eastern extreme of this image. Figure 7.1h shows that sediment has stopped eroding from this area by 11:11 GMT, at slack water.

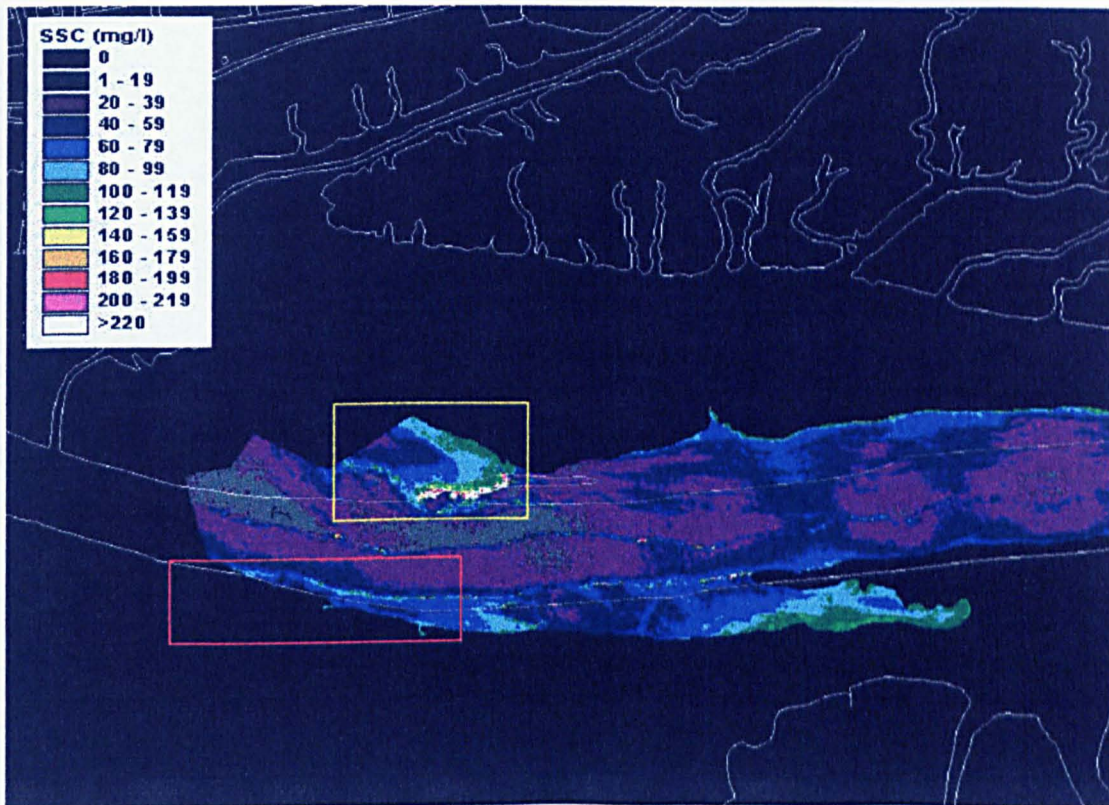


Figure 7.1a Lytham Creek, 0811 GMT, 20-7-97.

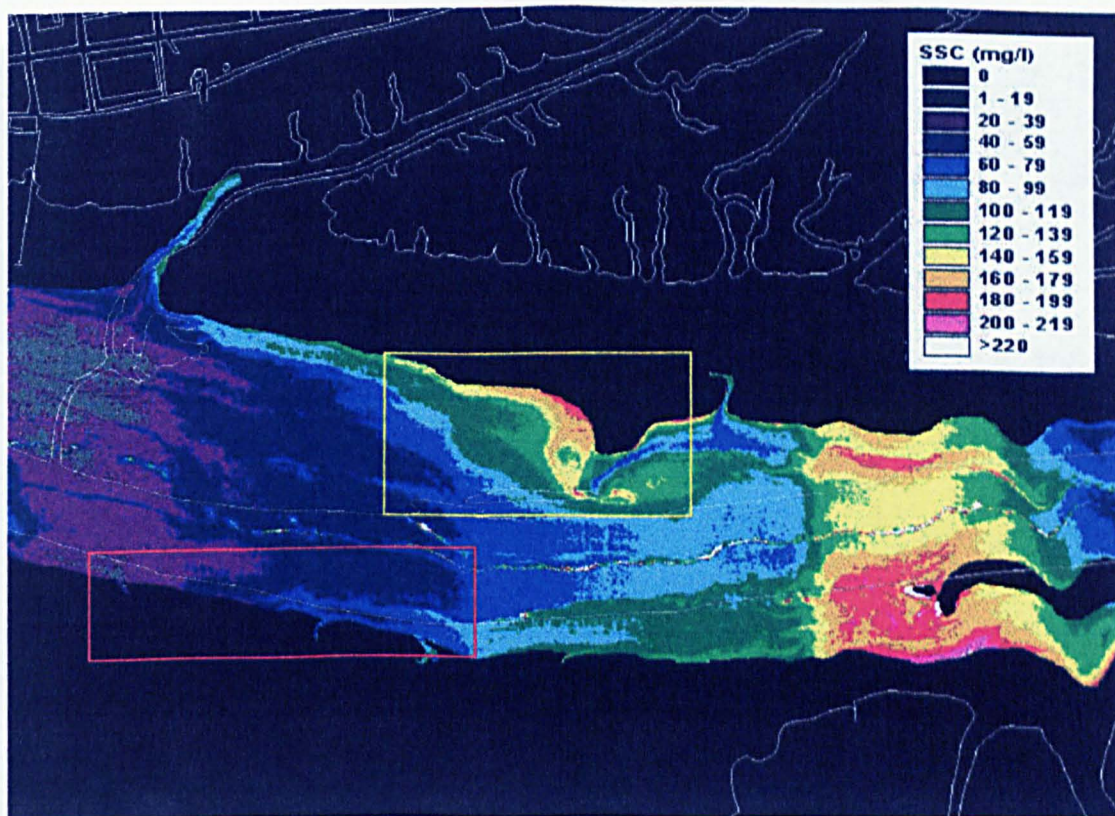


Figure 7.1b Lytham Creek, 0830 GMT, 20-7-97.

Figure 7.1c Lytham Creek, 0845 GMT, 20-7-97.

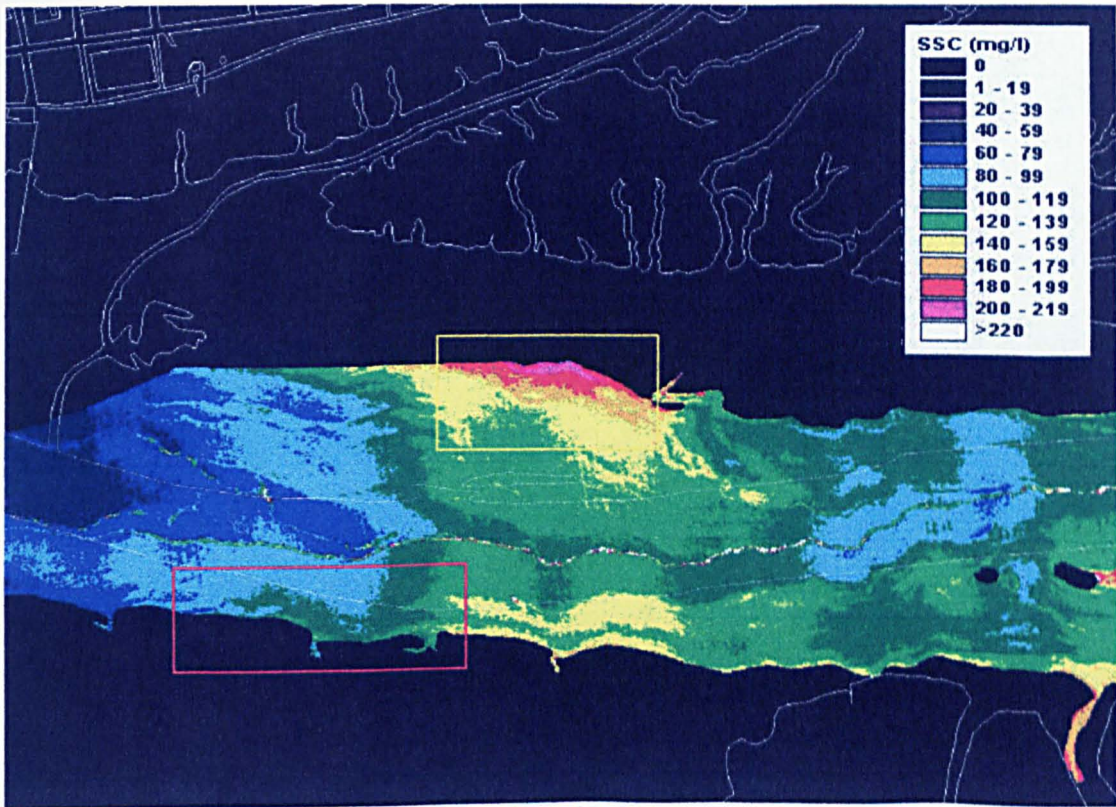


Figure 7.1c Lytham Creek, 0844 GMT, 20-7-97.

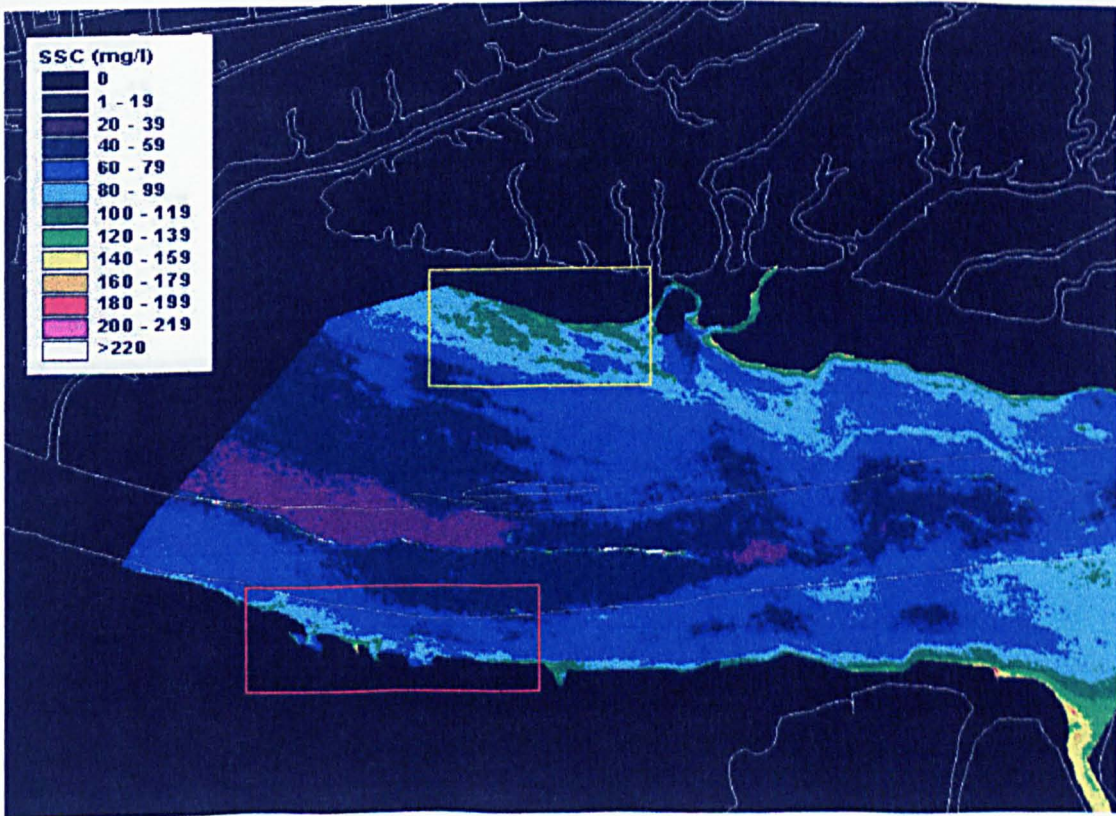


Figure 7.1d Lytham Creek, 0902 GMT, 20-7-97.

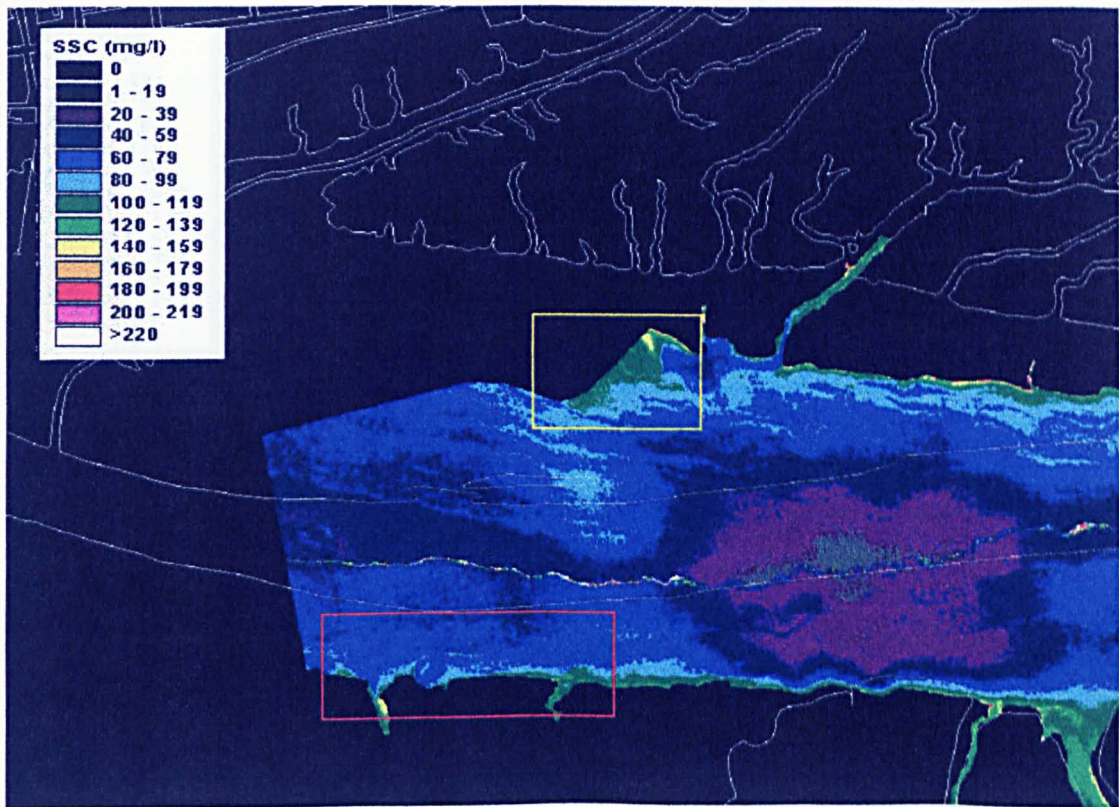


Figure 7.1e Lytham Creek, 0920 GMT, 20-7-97.

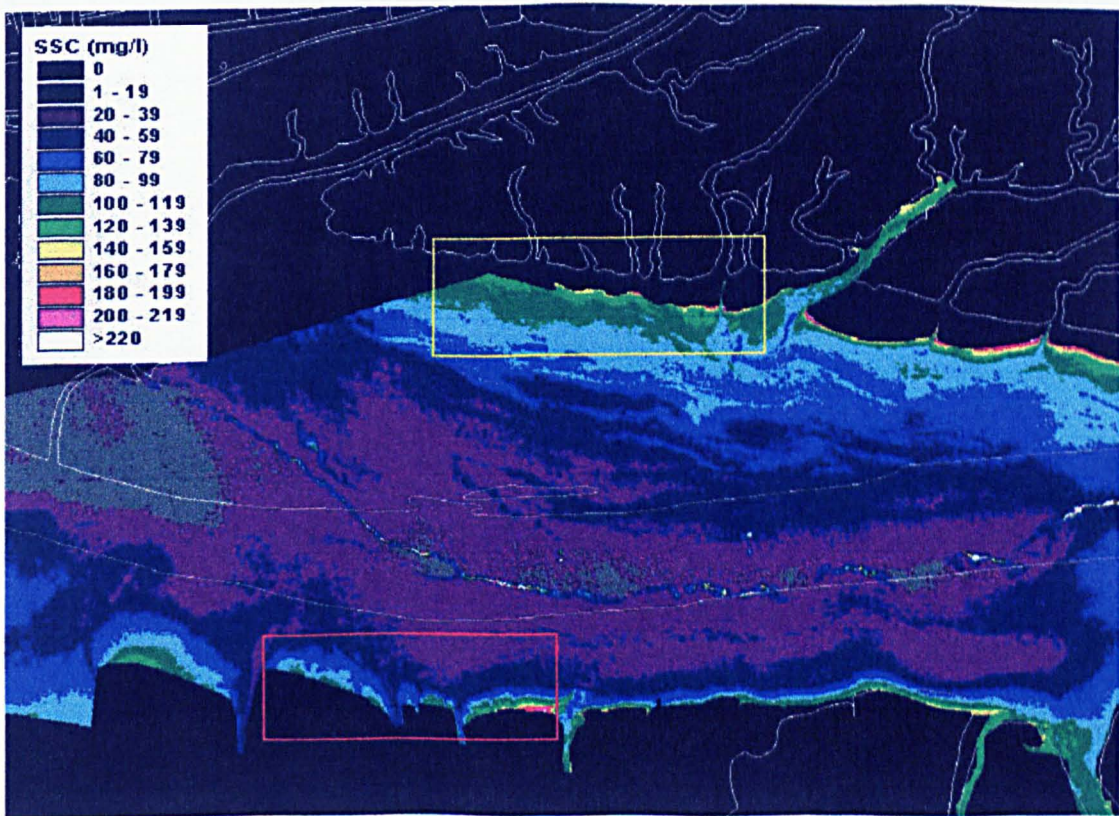


Figure 7.1f Lytham Creek, 0937 GMT, 20-7-97.

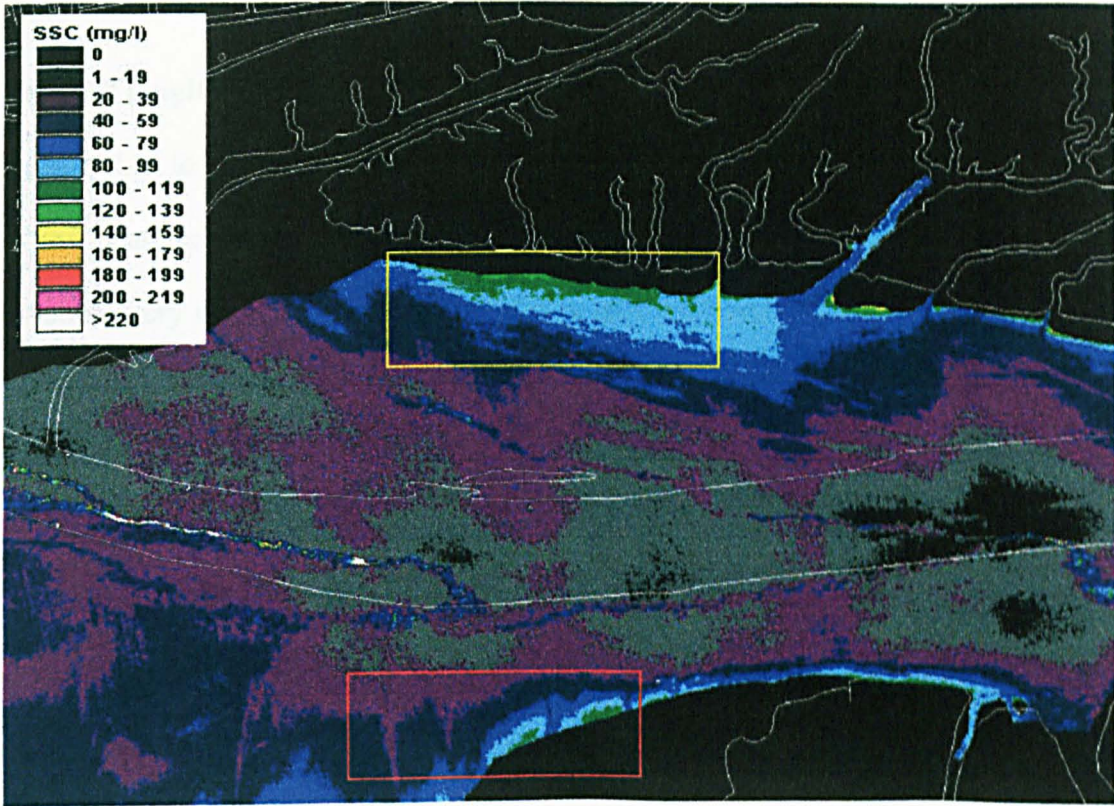


Figure 7.1g Lytham Creek, 0955 GMT, 20-7-97.

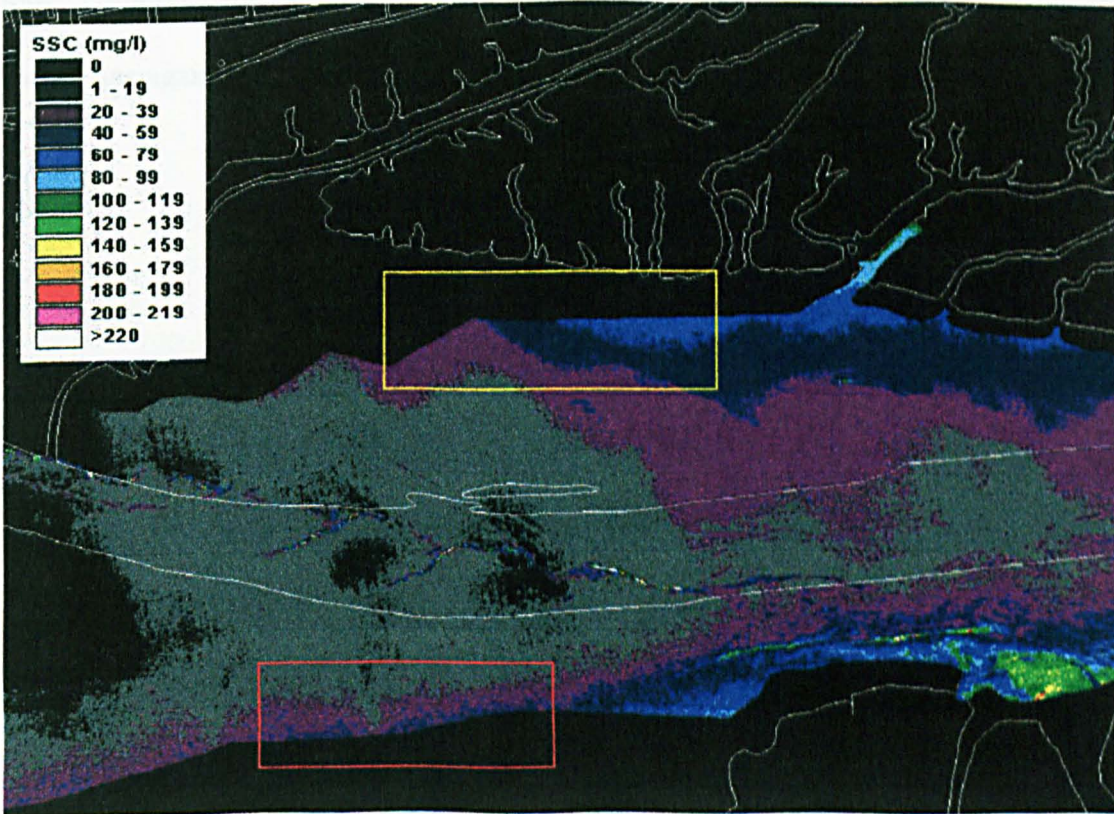


Figure 7.1h Lytham Creek, 1111 GMT, 20-7-97.

### **Areas of longitudinally transitional sediment supply**

Figures 7.2a to 7.2e show a series of five consecutive images of Longton Bank, just east of the confluence. The area of interest is outlined by the yellow box. These images illustrate very clearly the progressive nature of a transitional sediment source. Figure 7.2a shows that just after inundation of the Longton Bank mudflats there is some increase in SSC along the western stretch of the mudflat. As the water flow increases, Figure 7.2b shows that this western end of Longton Bank is providing a large quantity of suspended sediment to the water column. As such a large amount of sediment is being eroded. This sediment source is soon exhausted and a new source of sediment becomes dominant. This is shown in Figure 7.2c and 7.2d, here Longton Bank is still the source of the suspended sediment, but the area of maximum sediment concentration is migrating eastwards. Figure 7.2e shows that despite a significant drop in overall SSC, Longton bank is still providing some suspended sediment. The position of this source has again migrated further eastwards.

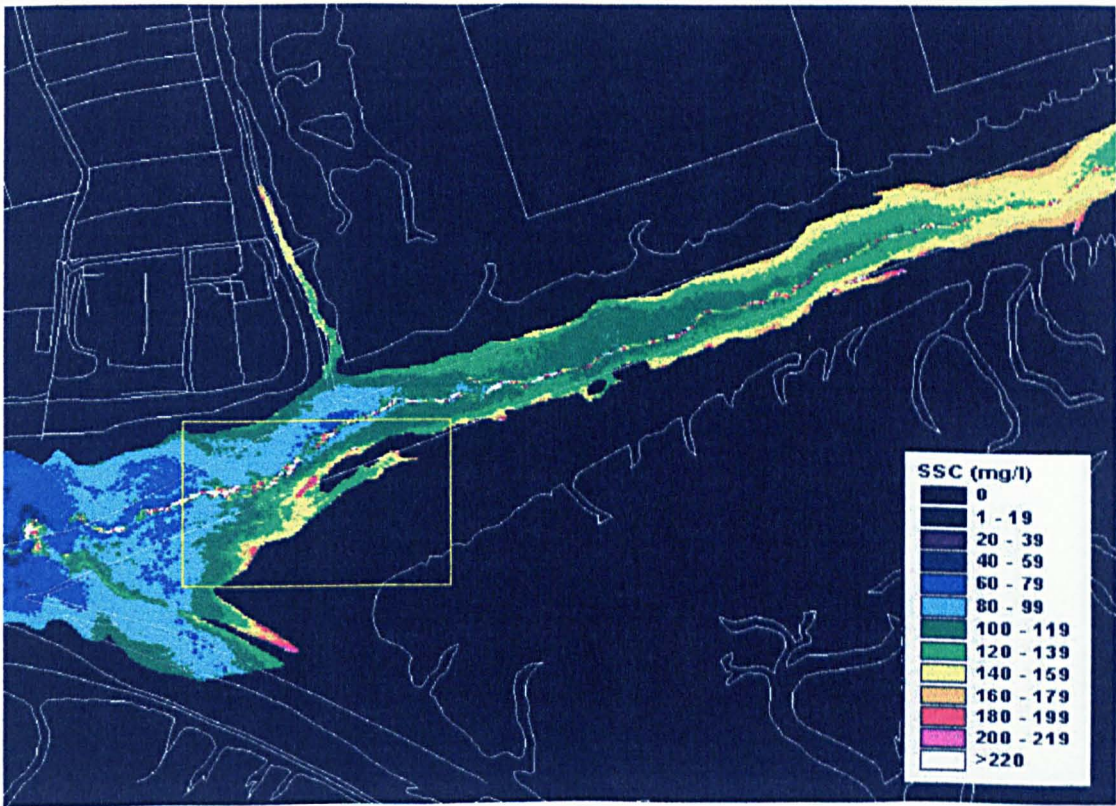


Figure 7.2a Longton Bank, 0902 GMT, 20-7-97.

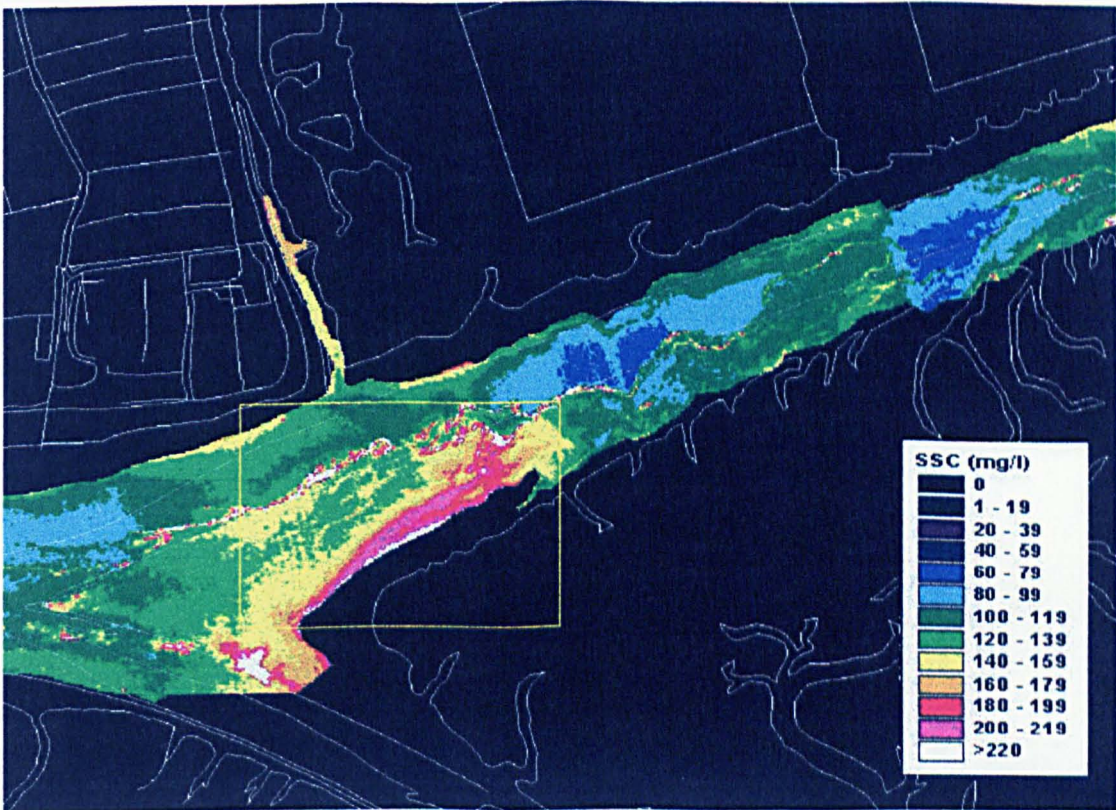


Figure 7.2b Longton Bank, 0920 GMT, 20-7-97.

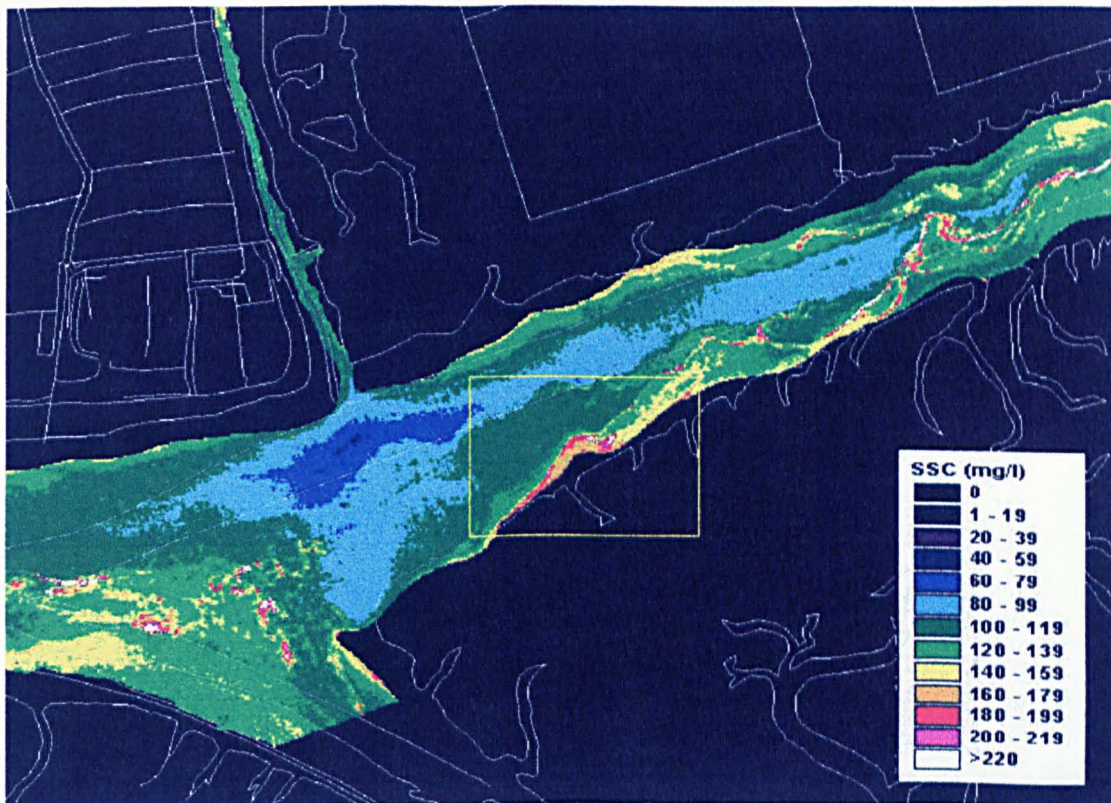


Figure 7.2c Longton Bank, 0937 GMT, 20-7-97.

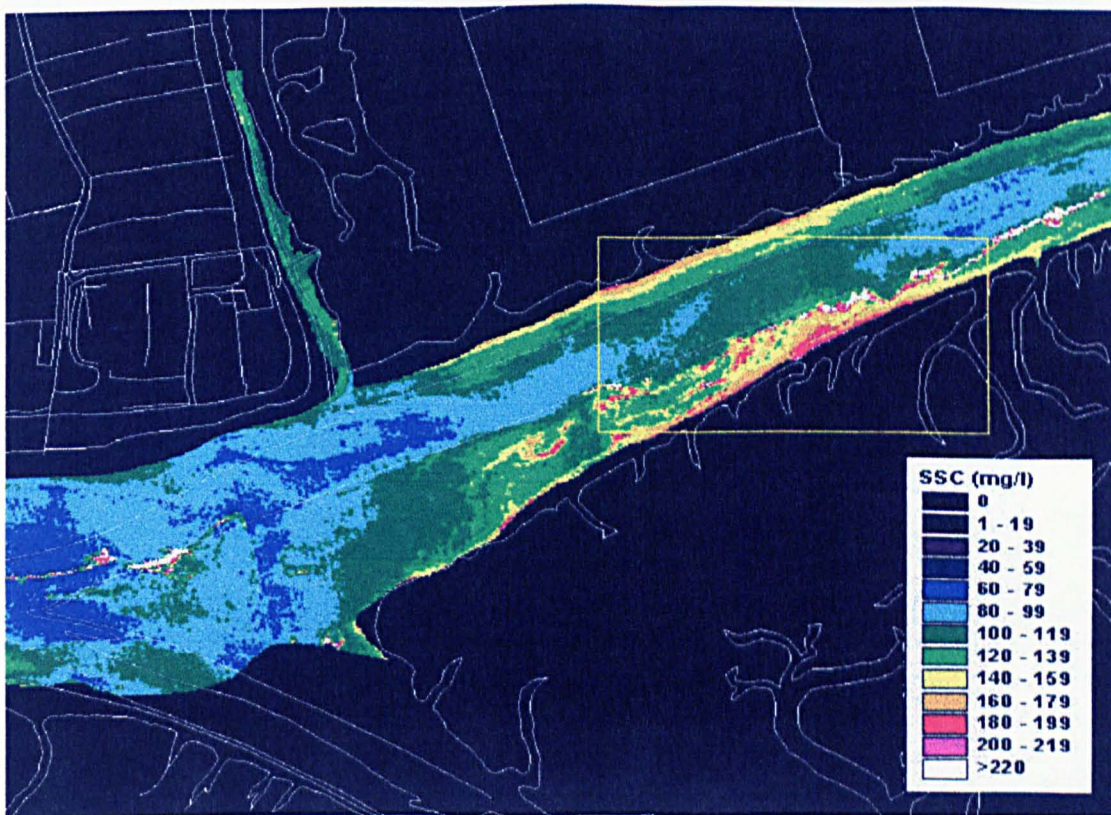


Figure 7.2d Longton Bank, 0955 GMT, 20-7-97.

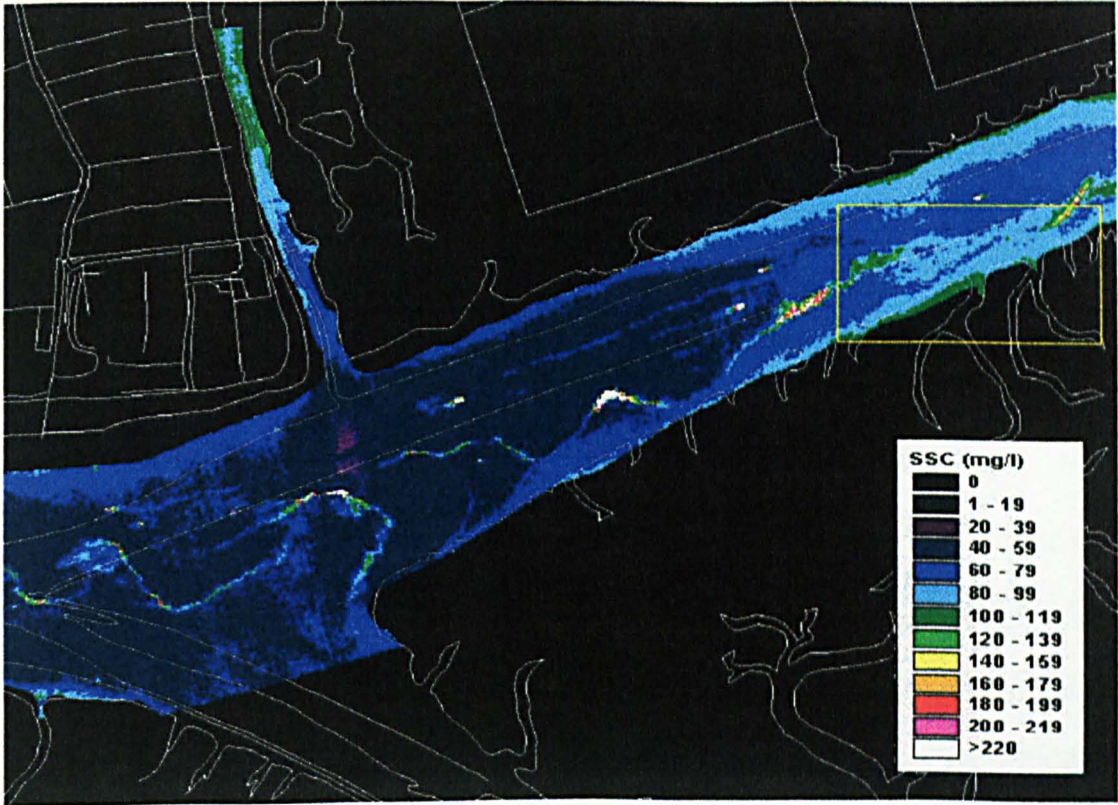


Figure 7.2e Longton Bank, 1111 GMT, 20-7-97.

Sediment transport

Summary

From the above changes it can be seen that the sediment transport is significantly reduced within the river channel. This is due to the fact that the river channel is significantly narrower and shallower than it was in 1990. Conversely, a lack of sediment transport is evident in the area of the river over a horizontal area and indicates a significant reduction in sediment transport area with reduced erosion potential.

Clearly current velocity and magnitude are significantly reduced in the river channel and this is likely to contribute to the reduction in sediment transport and erosion and entrenchment. The above changes in the river channel are likely to contribute to the reduction in sediment transport and erosion and entrenchment (1990), to interpret which results in a significant reduction in sediment transport.

### **Areas of Minimal Sediment Supply**

An area of minimal sediment erosion can be seen in Figure 7.1a to 7.1h. The area of interest is on the south shore of the outer estuary and is contained within the red box. The water entering the estuary from the Irish Sea can be seen to be low in SSC. This SSC does not increase on contact with the southern intertidal area as observed elsewhere. Sediment does not begin to be resuspended until the mouth of the large creek located at the eastern end of this image. There is a further possible reason for reduced sediment supply in this location. The image descriptions of chapter six revealed that the axial convergence front in the outer estuary moves to the south edge of the channel during the flood tide. For this to occur, the currents must be dominant in the northern half of the estuary. This implies that the current velocity on the south side of the estuary may be less than for the north side, which would result in reduced sediment erosion.

### **Summary**

From the above examples we can conclude that the imagery can clearly identify areas of sediment erosion within the outer estuary by locating areas of sudden increase in SSC. Conversely, a lack of suspended sediment at the waters edge, where there is water flow over a intertidal area and sediment would be expected to be resuspended, can suggest an area with reduced erosion potential.

Clearly current velocity and strength of the axial convergence is important in sediment erosion and entrainment. The following section aims to focus on areas with similar tidal flow conditions but differences in SSC and sediment properties, as mapped by Rainey, (1999), to interpret which enable or inhibit sediment erosion and entrainment.

### 7.2.2 Controls on sediment supply

Figure 7.3 shows the abundance imagery for clay content of the intertidal sediment produced from imagery collected approximately two months before the flood tide image set used here. To expose the maximum amount of intertidal mud, the image was taken at low water for a spring tide. Given the absence of extreme weather conditions, an assumption is made here that little variation in the suspended sediment distribution has occurred in the intervening two months period

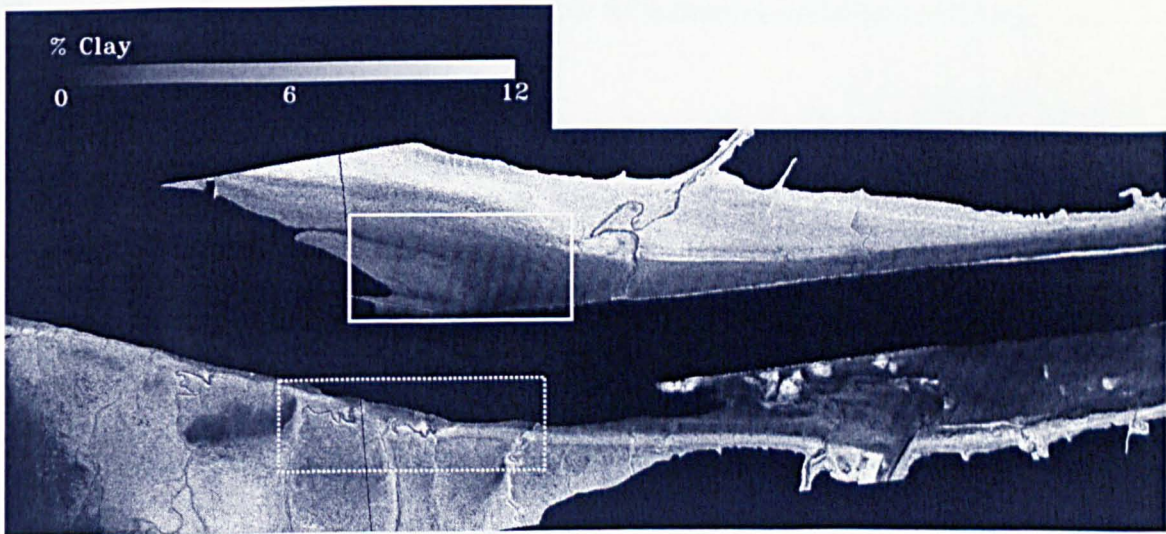


**Figure 7.3** A map of the percentage clay abundance produced from 31-5-1997, taken from Rainey, (1999). The white and dashed boxes correspond with the yellow and red boxes of Figure 7.1.

It can be seen that the area of intertidal mudflats producing a constant source of high SSC, bounded by the white box, corresponds to an area of sediment that is lower in clay and therefore less cohesive than that near the main channel further east along the estuary. The initial high SSC (Figures 7.1a and 7.1b) are from an area where the sand next to the main channel grades to the clay rich sediment bordering the saltmarsh. The sediment between the two extremes of large grain size and strongly cohesive mud is

probably predominantly silt. This is possibly the type of sediment that is most easily eroded and therefore an important sediment source.

However, the area that corresponds to the minimal erosion of Figure 7.1, bounded by the dashed box, is an area that has only slightly higher clay content. On examination of Figure 7.4, it is this area that is relatively high in microphytobenthos cover compared to the areas that are eroding more and it is known that large communities of algae on mudflats do inhibit erosion.

There are two factors that may be responsible for this reduced sediment supply:

1. The presence of microphytobenthos
2. A less dominant flow, suggested by the southwards migration of the axial convergence.

In reality it is likely to be a combination of these two factors.

The microphytobenthos abundance of the area immediately east of the large creek on the north shore is very high, (A in Figure 7.4), this also corresponds to an area of low sediment supply in Figure 7.1.

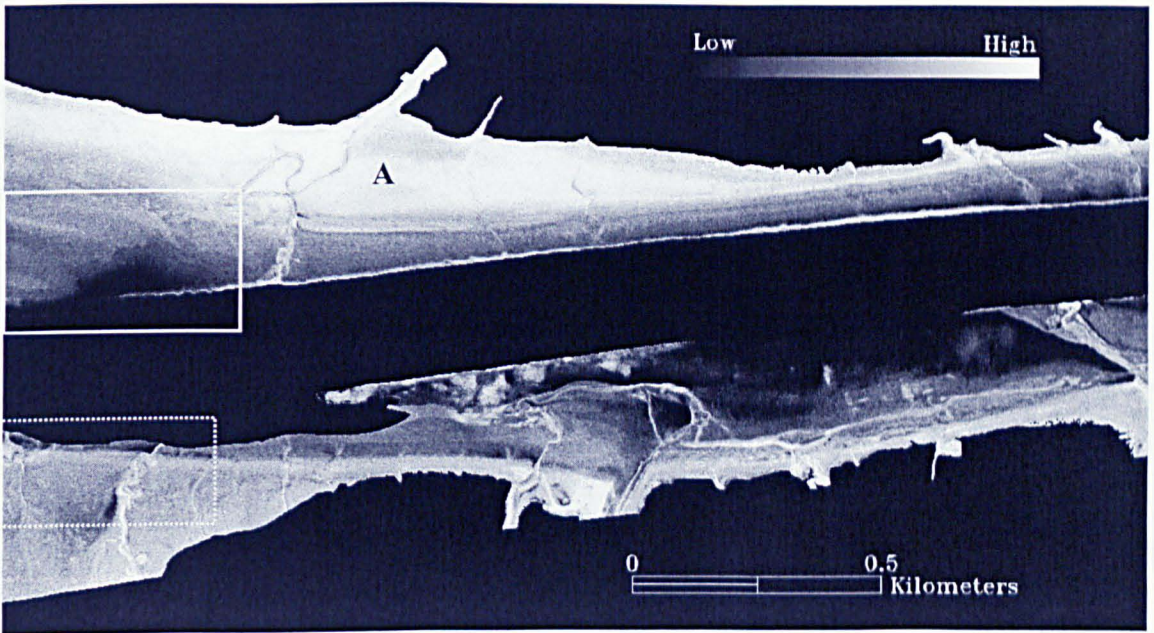


**Figure 7.4** Uncalibrated microphytobenthos relative abundance image produced by the linear unmixing of 31-5-97 imagery, taken from Rainey, (1999). The boxes correspond with the boxes of Figure 7.1.

The transitional areas of erosion, found mainly in the constricted main channel with narrow intertidal areas, may not be related to the underlying sediment in quite the same way as the large intertidal areas of the outer estuary. The area of Figure 7.2 is within the canalised reaches of the outer estuary. Therefore, the reason for the longitudinal migration of the sediment source must be related to the limited quantity of sediment available for erosion. The process that contributes to this knock-on effect of sediment supply is not clear.

Figure 7.5 corresponds to the area shown in Figure 7.2. It is assumed that the sediment that is eroded is the silt dominated sediment as for the outer estuary. In Figure 7.5 there is a sharp transition between the sands and clay rich sediment. This implies that there is a limited source of the intermediate silt dominated sediment. This is perhaps the reason for the initial sediment source being completely eroded and thus progressing along the shore over the course of the flood tide.

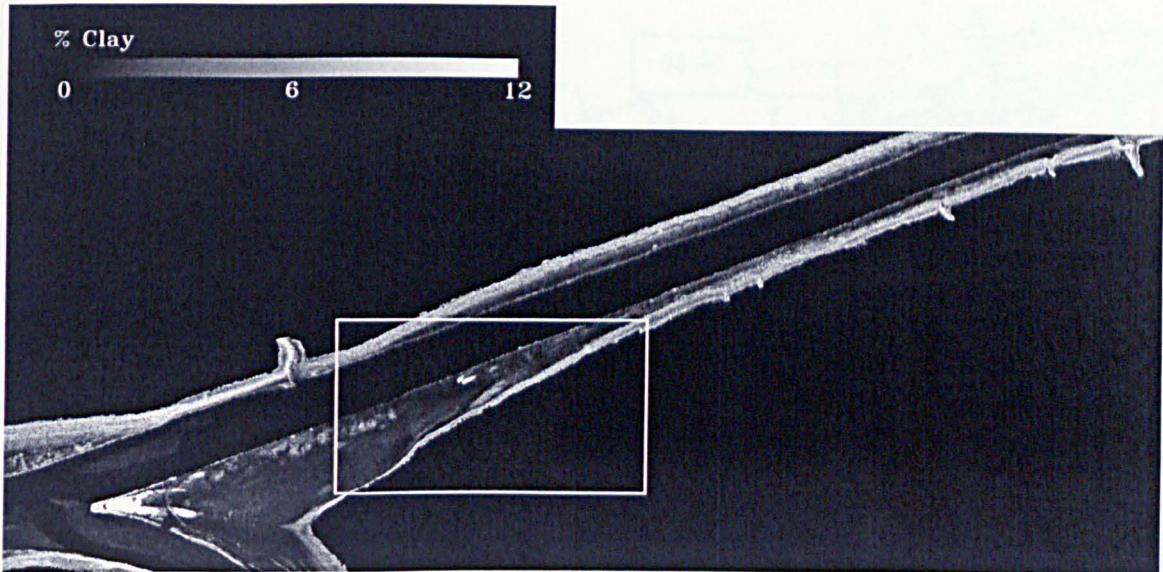


**Figure 7.5** A map of the percentage clay abundance produced from 31-5-1997, taken from Rainey, (1999), corresponding with the area of Figure 7.2.

### 7.3 TRANSPORT OF SUSPENDED SEDIMENT

Having established that the images can be used to identify sources of sediment this section investigates the movement of that suspended sediment within the estuary. To do this the following sections will show some examples of the information that can be obtained on the hydrodynamics of the estuary from the image data.

#### 7.3.1 The importance of the tidal bore in sediment suspension

The flood tide enters the estuary in the form of a tidal bore, an individual wave, approximately 20cm to 30cm high, generated by the decrease in depth of the estuary. The role that the tidal bore plays in the resuspension of sediment is investigated in this section.

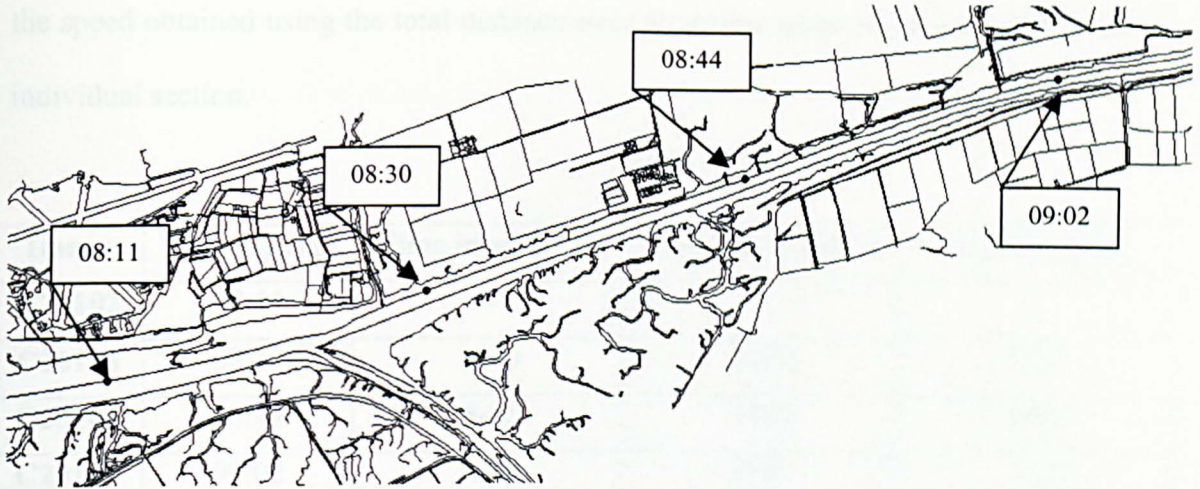


**Figure 7.6** The locations of the tidal bore in the first four images.

The tidal bore was visible on the first four images, and the location of the bore along the north training wall obtained. These locations are given in table 7.1 and shown in Figure 7.6.

Figs.	Position of the tidal bore (OS BNG)		Position 100m to the west (OS BNG)	
	Easting	Northing	Easting	Northing
7.7a	341640	426633	341550	426560
7.7b	343969	427270	343865	427215
7.7c	346285	428120	346190	428040
7.7d	348555	428857	348455	428820

**Table 7.1** The locations of the tidal bore and the point 100m to the west in the centre of the main channel, used to investigate the effect of the passing of the bore on SSC for the first four images.

Using the time taken between subsequent image and the distance between each location of the tidal bore, the speed at which the bore is travelling up the estuary can be calculated. This information is given in table 7.2. It can be seen that over successive sections of the estuary the speed of the tidal bore remains almost constant, and therefore

the speed obtained using the total distance over total time gives a similar value to each individual section.

<b>Image</b>	<b>Time (GMT)</b>	<b>Time interval (s)</b>	<b>Distance (m)</b>	<b>Speed (m/s)</b>
<b>C20102</b>	08:11	-	-	-
<b>C20103</b>	08:30	1140	2470	2.17
<b>C20104</b>	08:44	840	2480	2.95
<b>C20105</b>	09:02	1080	2380	2.20
<b>Total</b>	-	3060	7330	2.40

**Table 7.2** The times and distances used to calculate the speed the tidal bore progresses up the estuary.

To investigate the effect the passing of the tidal bore has on the SSC a point was located in the centre of the main channel 100m behind the bore to represent the SSC in the area that the bore has been observed in the time series. These points have also been identified as not having been influenced by aircraft roll. The SSC were obtained using a 3x3 grid of pixels to give an average concentration and a standard deviation for each point in each image. The variations in SSC over the flood tide at these locations are shown in Figure 7.7a to 7.7d.

Figure 7.7 shows that the variation in SSC with time is markedly different for each location. Figure 7.7a starts at the time at which the bore has just passed and thus starts with a maximum SSC value. Prior to this time the SSC would almost certainly have been much lower. The time distribution reveals that settling occurs within about 30 minutes of the passage of the bore through the channel. After this point, the SSC increases to a second peak, which coincides with the increasing flood tide velocity and the erosion of the intertidal sediments. The SSC then decreases again and a minor third

phase of increase in SSC is seen. This may be associated with a sediment increase related to the inhibition of mixing due to the axial convergence.

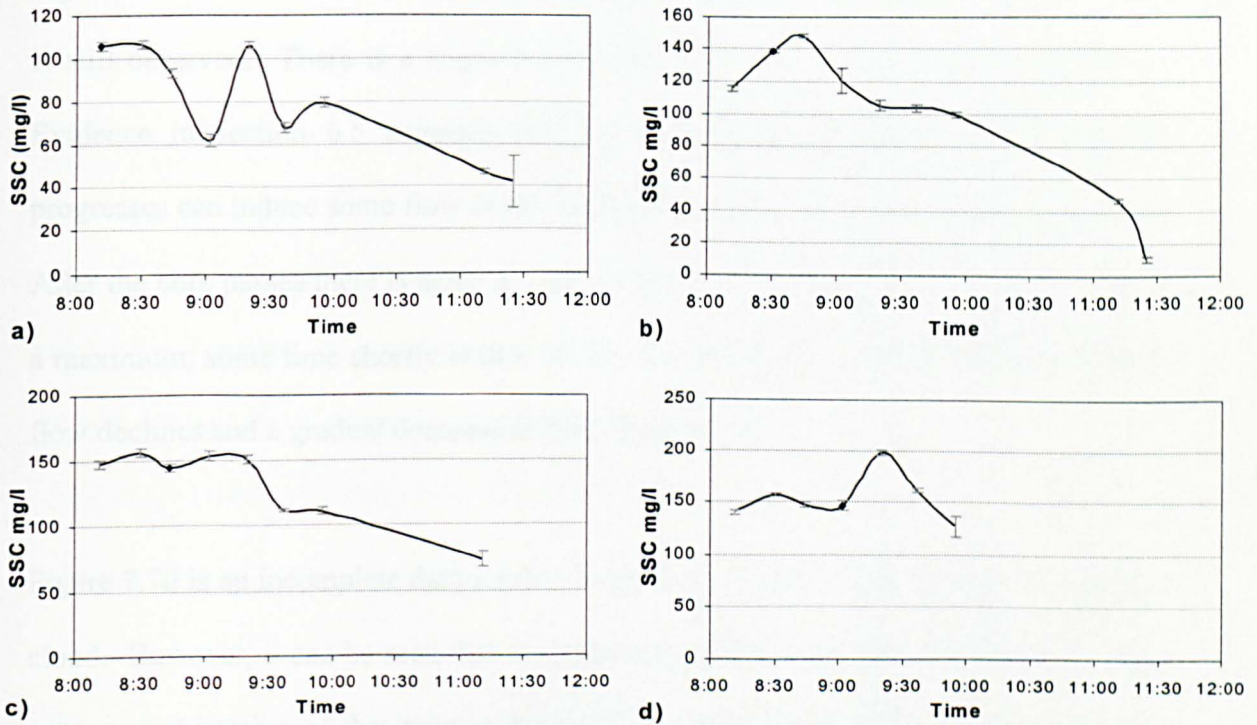


**Figure 7.7** The variation in SSC with time related to the passing of the tidal bore. The sample points, a) to d) are located approximately 100m behind the known bore positions in each image, see table 7.1. On each graph, the point 100m behind the bore is represented as a black diamond. The error bars represent  $\pm$ one standard deviation of a 3x3 grid of pixels.

Figure 7.7b shows a less complex time profile as just two phases of high SSC are observed. The highest SSC occurs some 15 minutes after the passing of the bore, which from the mean speed of the bore, given in table 7.2, approximates to a distance of 2km. This time lag before the high SSC may be due to the inundation of the intertidal areas or the formation of the convergent currents. As the convergent currents carry the higher SSC from the intertidal area to the centre of the channel it is likely to be a result of a combination of both factors. There is then a decline in SSC, but the decrease is less

rapid than in Figure 7.7a. Levels of SSC are then maintained for approximately one hour before the current flow reduces resulting in a corresponding fall in SSC.

Figure 7.7c shows a less marked variation in SSC with time, although a complex pattern is still observed. There is a slight increase in SSC prior to the passage of the bore. Evidence in section 6.5 suggests that the backing up of freshwater as the bore progresses can induce some flow in the confined channel before the arrival of the bore. After the bore passes there is again a time lag of fifteen minutes before the SSC reaches a maximum, some time shortly before 09:30. Once the SSC starts to decrease, current flow declines and a gradual decrease in SSC is observed.

Figure 7.7d is an incomplete data set due to the loss of some CASI data due to wisps of cloud. However, it can be seen that the pattern in variation of SSC with time is a more exaggerated version of that seen in Figure 7.7c. Prior to the arrival of the tidal bore there is a slight increase in SSC, possibly resulting from sediment being suspended by an induced flow. There is then a small decrease as the bore passes followed by a significant increase after a fifteen-minute time lag, after which the SSC declines. As the data set is incomplete, the rate of decline is not known after 10:00.

### **7.3.2 Formation and strength of the axial convergence**

In section 6.4 it was estimated that the foam lines indicating the presence of the axial convergence front appeared approximately 2 kilometres after the passing of the tidal bore. When this distance is measured accurately using ArcView, it can be seen that it varies between approximately two and three kilometres. The exact distances are given in table 2.3.

<b>Image</b>	<b>Distance of foam line from bore</b>
<b>C20102</b>	2133m
<b>C20103</b>	2025m
<b>C20104</b>	2731m
<b>C20105</b>	2921m

**Table 7.3** Distance in meters of the first signs of the axial convergence foam line behind the tidal bore.

From table 7.3 it can be seen that there is a general increase in the distance from the bore to the formation of the foam lines. As the bore progresses along the main channel the area of the intertidal sediment that it has passed over decreases, reducing the amount of debris available for foam line formation. Hence the lack of a foam line may not indicate a lack of convergent current.

Throughout this study no water velocity measurements have been made due to the lack of a stable platform from which they could be made. However, from the images it is possible to deduce some information on the strength of the convergence current in relation to the longitudinal velocity. This information can be inferred from the angle at which the sediments are pulled from the edge of the water to the centre of the main channel. By using the simple geometry of the right-angled triangle we can obtain a ratio of the distance travelled from the shore laterally compared to the distance travelled longitudinally. An example of this is shown in Figure 7.8. As both distances are travelled within the same time it can be used to infer relative velocities.

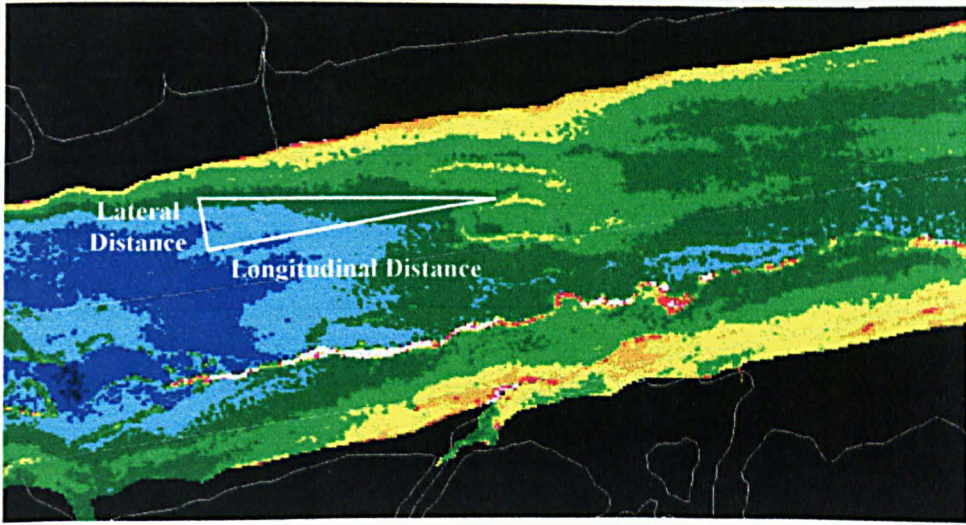


**Figure 7.8** How the angle at which sediment is transported to the centre channel can be used to infer the relative longitudinal and convergence velocities.

Image	Start Point (BNG)	End Point (BNG)	Lateral Distance (m)	Longitudinal Distance (m)	Ratio
C20104	338668,426343	338825,426314	40	154	3.85
C20104	339009,426391	339198,426327	86	186	2.16
C20105	343663,427216	343803,427215	44	130	2.96
C20106	341257,426660	341390,426638	36	125	3.47
C20106	344832,427610	344891,427604	25	53	2.12
C20106	344951,427654	344990,427647	19	33	1.74
C20106	345018,427672	345061,427668	16	28	1.75
C20106	345086,427095	345118,427690	15	24	1.60

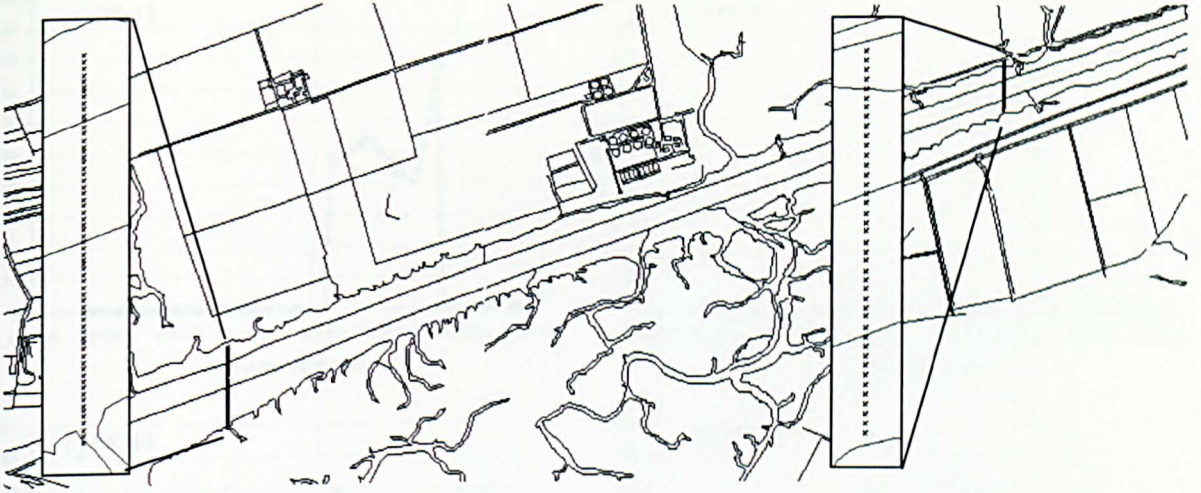
**Table 7.4** The comparative velocity of the convergence current relative to the longitudinal current velocity.

Table 7.4 contains the locations and ratio results of the areas where there is the most marked transport of sediment from the edges of the water to the centre of the main channel north of the axial convergence front. The relative velocity ratios range from 1.60 to 3.85. Whilst the data set is very limited, the data show that the ratio decreases from west to east, signifying that the relative strength of the convergence current

increases up river. It may be that as the river becomes progressively more constrained there are larger distortions in the isohalines, thus creating a stronger convergence current. However, much more data are required before this could be said to be a feature of the estuarine flood tide in the Ribble. Ideally, a comparison between the north and south sides of the convergence would be made. Evidence of the convergent current is difficult to find in the southern half of the channel. This possibly indicates a weaker convergence current south of the front, also indicated by the convergence front being pushed to the south of the channel.

### **7.3.3 Variation in SSC across the convergence front**

The formation of the axial convergence front over the flood tide is the dominating feature of the Ribble estuary; thus the role of this convergence in the transportation of the sediment is particularly important. The convergence forms a boundary that could inhibit the movement of suspended sediment. To investigate if the convergence has any effect on the suspended sediment mixing, transects across the estuary were taken from the images at 1km intervals. The locations of two transects are shown in Figure 7.9. These were chosen to represent transects of similar channel width and intertidal area. Figures 7.10 and 7.11 demonstrate the typical mixed results, even though the transects are geographically similar.



**Figure 7.9** The location of transects used in Figures 7.10 (344000E) and 7.11 (347000E).

Figures 7.10 and 7.11 show the SSC across the width of the estuary at 344000E and 347000E. The series consist of eight of the nine images, the last image has the very low SSCs of slack water and provides no additional information. On each of the graphs the fine grey lines show the position of the main channel.

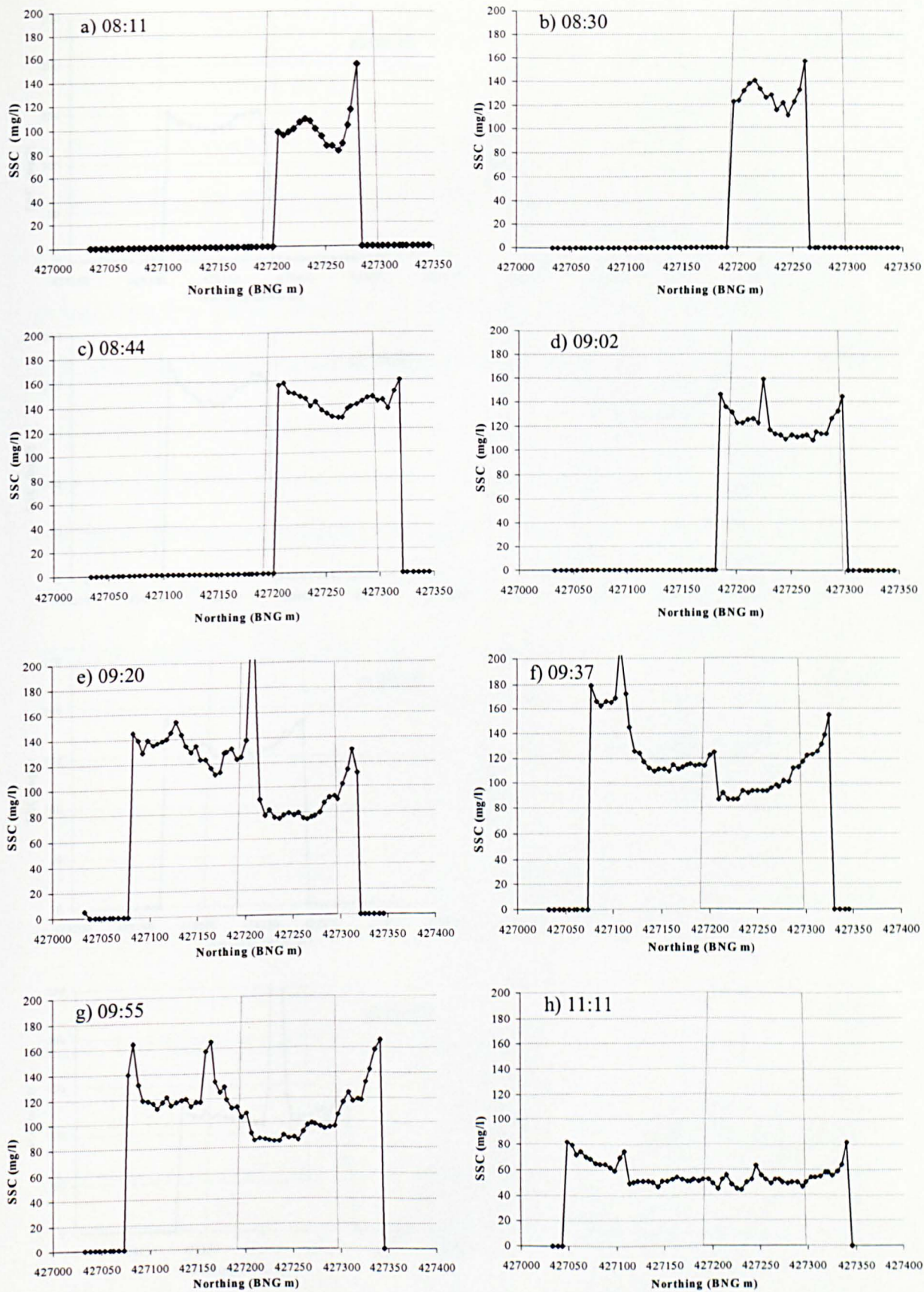


**Figure 7.10** The SSCs for the first eight images of a transect across the estuary at 344000E. The vertical grey lines mark the position of the main channel.

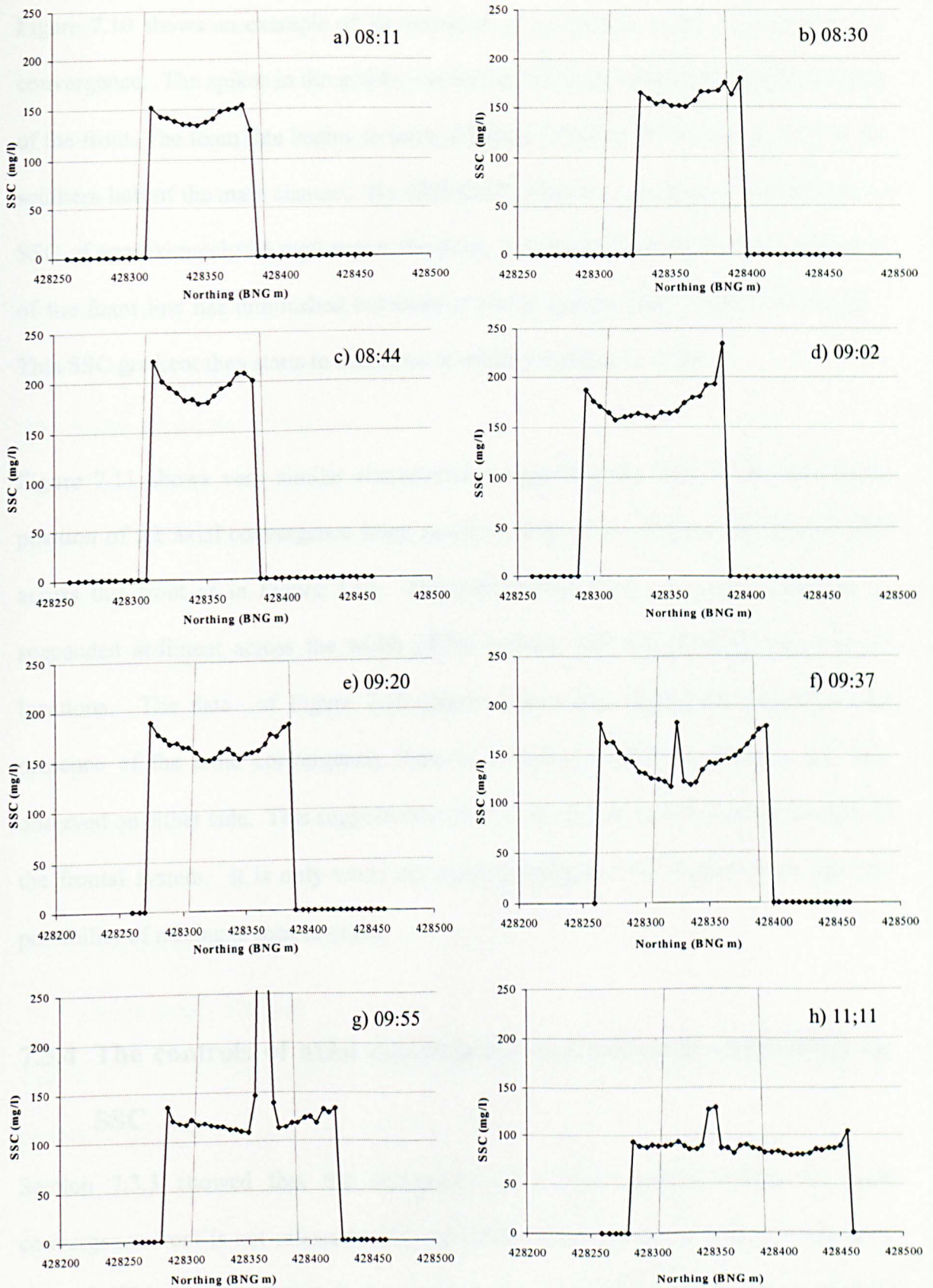


**Figure 7.11** The SSCs for the first eight images of a transect across the estuary at 347000E. The vertical grey lines mark the position of the main channel.

Figure 7.10 shows an example of the presence of a variation in SSC across the axial convergence. The spikes in the graphs, caused by the foam lines, represent the location of the front. The foam line begins to form in Figure 7.10d, at 0902 GMT located in the southern half of the main channel. By 0920 GMT, Figure 7.10e, there is a difference in SSC of approximately 30 mg/l across the front. In Figure 7.10f, 0937 GMT, the spike of the foam line has diminished but there is still a marked SSC gradient of 20 mg/l. This SSC gradient then starts to decrease as sediment begins to settle.

Figure 7.11 shows very similar characteristics regarding the time of formation and position of the axial convergence front, however, there is no obvious variation in SSC across this front as in Figure 7.10. The convergence front can inhibit transport of suspended sediment across the width of the estuary, but this does not occur at all locations. The data of Figure 7.10 clearly shows that during the formation and presence of the axial convergence, there is a marked difference between the SSC observed on either side. This suggests that little or no mixing occurs from either side of the frontal system. It is only when the axial convergence has broken down that the possibility of mixing is seen to occur.

#### **7.3.4 The controls of axial convergence and sediment availability on SSC**

Section 7.3.3 showed that the occurrence of a SSC gradient across the axial convergence front is not related to the size of the intertidal area or width of the main channel. This suggests that it must be related to an inequality of sediment availability between the north and south banks. To investigate this it is necessary to compare the example of the presence of a SSC gradient, Figure 7.10, with the intertidal sediment

distribution map produced by Rainey (1999) for the equivalent area. Assuming the source of suspended sediment is just to the west of the area exhibiting the SSC gradient, the area used in Figure 7.5, it can be seen that there is a major difference between the north and south intertidal banks. On the north shore there is an abundance of generally finer sediments in addition to an extra potential source of sediment from the large creek, Freckleton Brook. On the south shore there is a large area of sand that is unlikely to contribute greatly to the suspended sediment load, which is dominated by particles less than  $63\mu\text{m}$ , as shown in Figure 4.2. However, when a marked SSC gradient is seen across the axial convergence front, it occurs most frequently on the northern side of the channel. From the image series in Figure 6.1 it is seen that the incoming seawater is trapped on the northern side of the front and gradually the front moves from the centre to the south of the channel, implying weaker currents on the southern side of the front. If this is the case then the SSC gradients across the axial convergence front are linked not only to sediment availability but also to the ability of the flow to suspend that sediment.

#### **7.4 COMPARISON OF REMOTE SENSING DATA WITH A SEDIMENT TRANSPORT MODEL**

One of the favoured techniques for studying the behaviour of estuaries is by modelling, calibrated using *in-situ* data and validated with a second set of *in-situ* data. However, there are some drawbacks to using this technique. Models are often over simplified to prevent them becoming too computationally complex, for example by restricting a model to two dimensions or by simplifying the channel shape. Secondly, models are calibrated and validated using spot sample data and these types of data can be spatially

unrepresentative. For this reason it would be useful to assess the use of spatially representative remote sensing data as an aid to model calibration and validation.

#### **7.4.1 The model**

Westlakes Scientific Consulting Ltd is currently in the process of developing a two dimensional model of the Ribble estuary, which includes the river Douglas, (Gleizon 1999). As the haline stratification shows varying patterns throughout the flood-ebb and spring-neap cycles, the model chosen was non-depth-averaged to demonstrate these variations. Therefore, the model is laterally averaged and the estuary assumed to be well mixed across the channel as a result of it being narrow and constrained by training walls. The model operates within a fixed grid of co-ordinates with a scale of 250m longitudinally and 0.2m in depth. The models contains modules for:

1. Hydrodynamics (vertical and longitudinal) including velocity, salinity, temperature and density.
2. Non-cohesive sediment erosion, transport and deposition.
3. Cohesive sediment erosion, transport and deposition.
4. Stokes' Drift for long term sediment movement by residual currents.

Data used to calibrate the model were collected from stable platforms specially built for this purpose. Continuous measurements were collected for water levels, velocity, salinity, and temperature and SSC via turbidity. The VERSE model has not yet been fully calibrated and validated to date but, for the purposes of this investigation, predicted SSC data were produced to enable a limited comparison to be made with the SSC data derived through the remote sensing technique. The output of the model for the same tide used within this study is illustrated graphically in appendix C.

#### **7.4.2 Comparability of remote sensing and model data**

Both the image and model data sets are two-dimensional, the model illustrating longitudinal variations with depth and the image data showing lateral variations of the surface. This incongruity means that the data cannot be compared directly. In addition to differences in the perspective taken of the estuary, there are also large differences in scale. The model has a very coarse longitudinal resolution, 250m, one hundred times larger than the 2.5m scale of the imagery. However, the depth information provided by the model has a resolution of 0.2m. To allow a direct comparison of the surface SSC of both data sets, the image data had to be considerably degraded to give a laterally averaged value over a distance of 250m to provide a one dimensional data set.

The image data were cut into 250m cells and mean and standard deviation SSC values calculated. For each image, the mean SSC from the imagery and the surface SSC value from the model were plotted against model cell number. Figure 7.12 shows the comparison between these one and two-dimensional data sets.

It can be seen that the model consistently underestimates the SSC derived from the imagery. This underestimation of SSC by the model may be a result of the inability of the model to account for lateral variation in SSC. For example, most of the images shown in chapter six show that the SSC in the centre of the channel is lower than the SSC over the intertidal area, which is subsequently lower than the SSC at the edge of the water. If the model is predicting the SSC for the centre of the channel only, this could explain why the model shows a consistent underestimation of SSC. It is also evident that the real variations in SSC are much more irregular than suggested by the

model. It is possible that the alternate high and low values seen in the image data could be a result of the effects of aircraft roll discussed in the initial image descriptions in chapter 6, however, this may also result from the large lateral variations in SSC.

The error bars of plus or minus one standard deviation indicate the even when taking the lower values of the image SSC into account, the model is still generally underestimating the SSC.

If the image data are visually smoothed, the shapes of the two data sets are similar. In most cases the actual and predicted maximum SSC occur in approximately the same location. This is particularly evident in the 08:44 image. As time progresses the position of the actual maximum SSC appears to be positioned further west than the predicted maximum.

In reality the data sources are not directly comparable, as it is not practical to have to substantially degrade the image data, but the data sets are complementary, as the CASI imagery data do not provide any information regarding depth distribution of SSC. However, using the suspended sediment depth profiles from the model with the real surface data from the imagery could result in errors. If the information on the sediment of the substrate is not accurate, then the variation in sediment concentration with depth will be flawed.

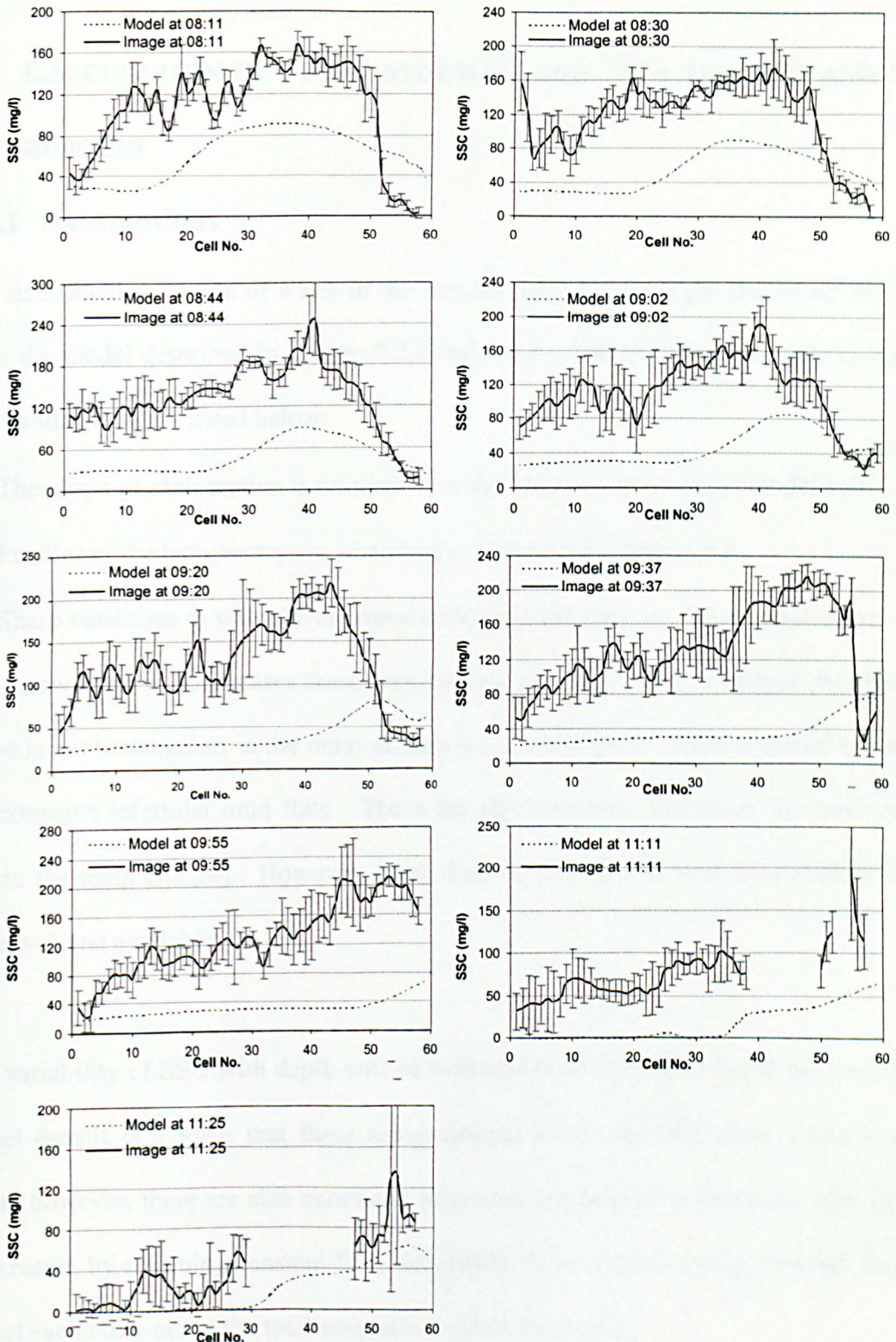


**Figure 7.12** A comparison of CASI data with surface SSC data from the latest two-dimensional model of the Ribble estuary run for the identical tidal and freshwater flow conditions. Error bars represent  $\pm 1$  standard deviation indicating lateral variation in SSC.

## **7.5 CALCULATION OF TOTAL SEDIMENT AND <sup>137</sup>Cs LOADING AND NET BUDGETS**

### **7.5.1 Assumptions**

The data for the volume of water in the estuary during each flight line were obtained from the model described in section 7.2.1 and 7.4.1. The assumptions made to derive this volume data are listed below:

- The shape of each section is uniform over the 250m distance of the model cell.
- Profiles of the bathymetry are smoothed to reduce calculation time.
- Sharp variations in water level produced by the tidal bore are not accounted for.

It is known that in most cases these assumptions are not true, for example the channel shape is not rectangular; in the outer estuary it is a rectangular central channel bordered by extensive intertidal mud flats. There are also localised variations in water depth within the main channel. However, these data do provide the best approximation for water volume available.

The variability of SSC with depth will be assumed to be constant. From the numerical model data it is evident that there are occasions where the SSC does increase with depth, however, there are also occasions where the concentration decreases with depth. As a result, by assuming constant SSC with depth, these extremes may, to some degree, cancel each other out in the total suspended sediment budget.

## 7.5.2 Budget of suspended sediment and <sup>137</sup>Cs in suspension

The information required to calculate the total concentration of sediment in suspension for each flight line, using cells 1 to 59 of the model, corresponding to the area covered by the imagery, is given in table 7.5.

The data for the SSC of cells 1 to 59 were obtained from the images using ERDAS, corner co-ordinates of upper left 338325E, 429617N and lower right 352520E, 425885N. The <sup>137</sup>Cs data were calculated from the image SSC using the equation given in table 4.3, where <sup>137</sup>Cs in becquerels per litre is equal to 0.0003 times the SSC in milligrams per litre.

Time (GMT)	Water Vol. (m <sup>3</sup> ) = [Y]	Vol. of top 1m (m <sup>3</sup> ) = [X]	SSC in top 1m (mg) = [A <sub>SSC</sub> ]	<sup>137</sup> Cs in top 1m (Bq) = [A <sub>Cs</sub> ]
0811	4528208	1575444000	5445466788000	1633640000
0830	7182383	2661478000	6356173894000	1906852500
0844	9254535	2475006000	6919910688000	2075973125
0902	11859330	2672753000	6109251781000	1832775625
0920	15093153	3094228000	6206414069000	1861924375
0937	18471116	3450662000	6140081219000	1842024375
0955	20150853	3488600000	5538477256000	1661543125
1111	20108531	3755572000	3408471563000	1022541250
1125	18300018	3783522000	1981509944000	594453125

**Table 7.5** The information used to calculate the quantity of sediment and associated <sup>137</sup>Cs in suspension for each flight line and over the course of the flood tide.

The total suspended sediment loading for one flight line was calculated using the ratio of the top one-meter depth to the total. This assumes a rectangular channel but eliminates the need to use an averaged SSC. The stages of the calculation are presented below:

1. The area of one pixel of a 2.5m resolution is  $6.25\text{m}^2$
2. The volume of that pixel to 1m depth is  $6.25\text{m}^3$  or 6250 litres
3. The volume of the top 1m of the image is the number of pixels multiplied by 6250 litres, denoted as **X** in equation 7.1.
4. From the model we know the total volume for each flight line, denoted as **Y** in equation 7.1.
5. The quantity of sediment, in milligrams, contained within the top 1m of the estuary is calculated from the sum of the pixels for each image (mg/l or Bq/l) multiplied by the volume of that pixel to one meter depth, 6250 litres, denoted as **A** in equation 7.1.

$$\mathbf{X/Y = A/B}$$

Therefore **B** gives the total SSC in the Ribble estuary for each flight line:

$$\mathbf{B = (Y/X) \times A} \quad \mathbf{[7.1]}$$

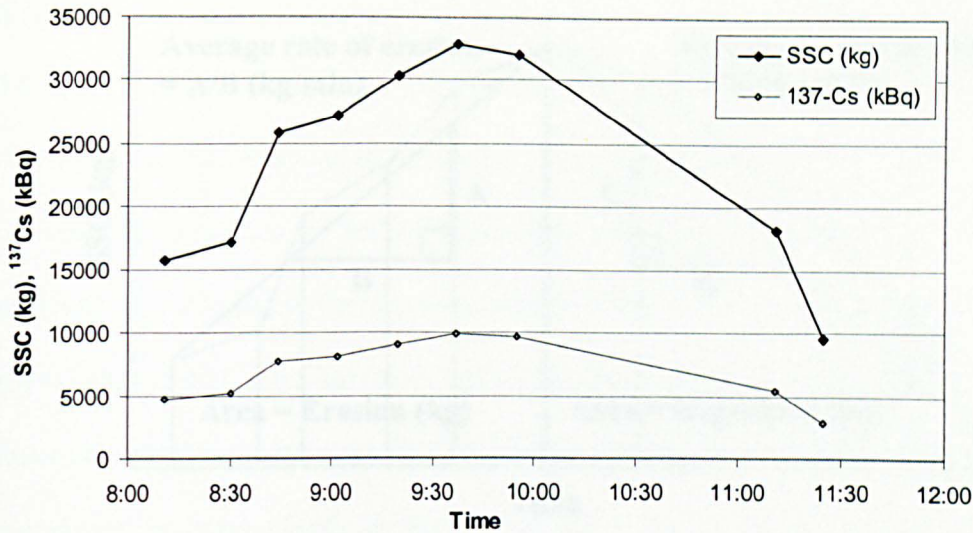
The results for both total suspended sediment load and associated  $^{137}\text{Cs}$  in suspension during each flight line are given in table 7.6.

Image	Time	B <sub>SSC</sub> =SSC (kg)	B <sub>Cs</sub> = <sup>137</sup> Cs(kBq)
C20102	08:11	15652	4696
C20103	08:30	17153	5146
C20104	08:44	25875	7762
C20105	09:02	27108	8132
C20106	09:20	30274	9082
C20107	09:37	32867	9860
C20108	09:55	31991	9597
C20110	11:11	18250	5475
C20111	11:25	9584	2875

**Table 7.6** The total suspended sediment load and associated <sup>137</sup>Cs load for each flight line

### 7.5.3 Interpretation and validity

By plotting the total sediment load and the quantity of associated <sup>137</sup>Cs against time, as in Figure 7.13, it can be seen that the increase in sediment and <sup>137</sup>Cs load is not a smooth curve. There appears to be a pulse of sediment in the 08:44GMT image. This may be associated with the beginning of the inundation of the major intertidal areas of the estuary, increasing the rate at which sediment is supplied to the water column. The total suspended sediment load of the estuary increases until 09:37 indicating erosion, after which it starts to decrease indicating deposition through settling.



**Figure 7.13** The variation in total suspended sediment and associated <sup>137</sup>Cs loading for each flight line with time.

To quantify erosion and deposition the area under the graph of Figure 7.13 was calculated using the trapezium rule to calculate the sum of the trapeziums forming the curve. (The sum of the first five trapeziums represent the erosion phase and the sum of the remaining three trapeziums represent the deposition phase.) The average rate of erosion and deposition was also calculated. The results are presented in table 7.7.

	SSC	<sup>137</sup> Cs
<b>Area representing erosion</b>	7076389 kg	2120217 kBq
<b>Average rate of erosion, E.</b>	82179 kg/min	24654 kBq/min
<b>Area representing deposition</b>	10594292 kg	3178287 kBq
<b>Average rate of deposition, D.</b>	98095 kg/min	29429 kBq/min
<b>((D-E) / D) x 100%</b>	19%	19%

**Table 7.7** Information derived from the images on the erosion and deposition of the flood tide for model cells 1 to 59.

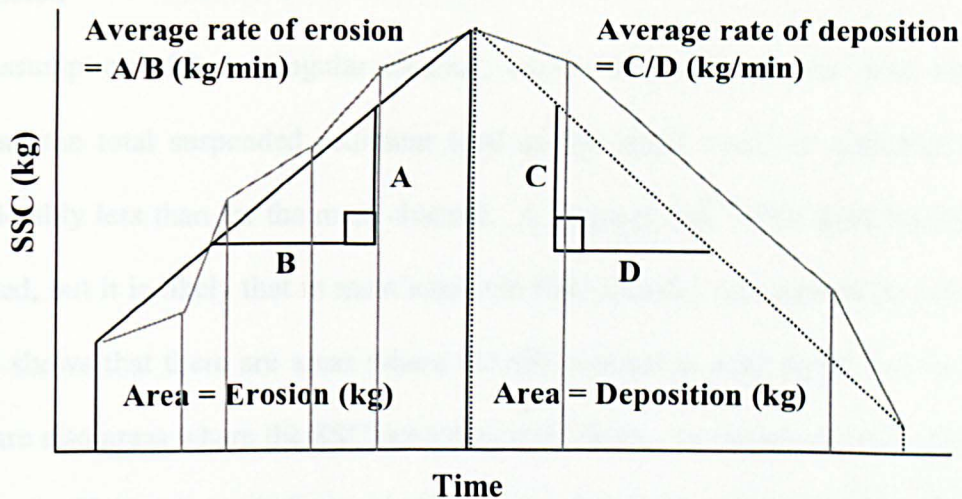


**Figure 7.14** A schematic representation of the trapeziums, areas and gradients used in the calculation of net deposition from the image data.

To determine whether there is net erosion or deposition it is necessary to compare the areas representing erosion and deposition. However, the time spent sampling in the erosion phase was less than that for the deposition phase, thus a direct comparison of areas will result in a bias towards deposition as this phase was sampled for a longer period of time. Dividing the difference between the deposition and erosion rates by the erosion rate provides us with a comparison between the amount of erosion and deposition corrected for this time bias, (Figure 7.14). This tells us that there is 19% more deposition than erosion in the section of the estuary for cells 1 to 59 during this flood tide, representing  $2.01 \times 10^6$  kg of sediment and 604 MBq of associated  $^{137}\text{Cs}$  for the whole estuary from Lytham to Preston. The result is also consistent with the fact that the estuary is known to be accumulating silt. These values are only valid for this individual tide and will vary considerably between spring-neap and seasonal cycles.

## **Discussion**

The assumption of a rectangular channel, which is clearly not the case, may over estimate the total suspended sediment load as the depth over the intertidal areas is considerably less than for the main channel. A constant SSC with depth has also been assumed, but it is likely that in most areas the SSC actually increases with depth. The model shows that there are areas where the SSC increases with depth and conversely there are also areas where the SSC decreases with depth. In the areas where there is an increase in SSC with depth the bed load is likely to consist of larger sand grains, which roll and bounce along the bed. This type of sediment is not as important in the accumulation of  $^{137}\text{Cs}$ , as sand is known to carry a lower concentration of  $^{137}\text{Cs}$ . This increase in SSC with depth would result in the calculation underestimating the total sediment load. Therefore it is likely that the two assumptions will produce errors, but to some degree these may cancel each other out. There is also a possibility of some errors being introduced through the elevated SSC produced by the foam lines of the axial convergence. The question is whether a flood tide sediment load calculated using these assumptions is valid. In the absence of any other data of this type calculated using suspended sediment and  $^{137}\text{Cs}$  concentrations of such spatial integrity, the answer must be that these results represent a very good first estimate.

## **7.6 SUMMARY**

This chapter has presented the advantages of using remote sensing for gaining real information on estuarine behaviour. The image data calibrated for SSC can be used to located sources of erosion and with the aid of a map of intertidal sediment type (Rainey, 1999) this can be related to sediment grain size and stability. The tidal bore has been shown to play an important role as a source of sediment suspension before the

inundation of the intertidal mud flats. The development of the axial convergence front has been shown to follow the tidal bore. This forms approximately 2 to 3 km behind the bore and there is some evidence to suggest that this may vary systematically with estuarine location, but needs further investigation. Once the axial convergence has formed the image data show that it plays an important role in inhibiting sediment transport, particularly where the sources of sediment are unequally distributed between the north and south banks. This can result in SSC gradients of 30 mg/l in just 5m. The data are difficult to compare directly to the data produced by modelling the estuary as the dimensions and resolutions of the data sets differ. To compare the laterally averaged surface concentrations directly, the image data had to be significantly degraded. Degrading the image data showed that the model consistently underestimated SSCs, probably a result of the assumptions that had to be made to simplify the calculations. However, the image and model data sets are complementary as the model provides depth profile information but contains no information on lateral suspended sediment patterns. Using the water volume provided by the model data, it has been possible to calculate total sediment and associated  $^{137}\text{Cs}$  loading for each flight line. This allows the identification of the times and relative magnitudes of the erosion and deposition phases of the tide.

## **CHAPTER 8 DISCUSSION & CONCLUSIONS**

### **8.1 THE NEED FOR A SPATIAL AND TEMPORAL APPROACH TO MONITORING RADIONUCLIDES IN THE RIBBLE ESTUARY**

The extensive saltmarsh formation and land reclamation shows that the Ribble estuary is accumulating sediment, and associated sediment bound radionuclides, derived from authorised BNFL Sellafield discharges over the past forty years. In addition to the radionuclides from BNFL Sellafield, the Ribble is relatively unique in that it is subject to a second discharge of isotopically different radionuclides directly into the estuary from BNFL Springfields. These sediments and associated radionuclides represent the main radioactive source to the houseboat dwellers in the Douglas, identified as the critical group for the Ribble, (Hunt and Smith 1999). Hence monitoring of the estuary is of primary importance to BNFL who need to understand the mechanism controlling the long-term fate of the radionuclides. This is especially important given the current reduced discharges from BNFL. The reduced radionuclide concentrations in the water column trigger the release of radionuclides from the sediments in an attempt to maintain a chemical equilibrium; thus the sediment sinks could represent future sources of radionuclides.

Spot sampling has been the standard method for estuarine monitoring. This approach tends to be labour intensive, time consuming and more importantly, spatially unrepresentative. As estuaries are subject to tidal flows, the time taken to perform sampling often means that the data are averaged over time and are therefore temporally unrepresentative, especially when the hydrodynamic mechanisms of the estuary are considered. To overcome some of these shortcomings in the sampling methodologies,

modelling approaches have been developed to predict the behaviour of sediments in estuaries. However, this predictive approach tends to be built, calibrated and validated using spot sample data from a few isolated locations.

It is therefore clear that the improvement in the understanding of the behaviour of estuaries is hindered by the lack of spatially and temporally representative data. The use of airborne remote sensing therefore offers the potential solution to the dilemma of obtaining spatially and temporally accurate data.

## **8.2 DEVELOPMENT OF A TIME SERIES APPROACH TO FLOOD TIDE MONITORING**

This project was designed to develop a method for gaining spatially representative data of the distribution of SSC within the Ribble estuary. A time series of multiple images was used to assess the mechanisms controlling the movement and fate of sediment over a spring flood tide and more specifically:

1. Mapping the concentrations of suspended sediment and identifying sediment and hence radionuclide sources.
2. Evaluating the hydrodynamic controls on sediment entrainment and transport.
3. Quantifying sediment and radionuclide budgets for the estuary.

The proposed method was based on the outcome of previous studies on remote sensing of suspended sediment, which repeatedly showed that there was a systematic increase in reflectance with an increase in SSC. However, the form of this relationship tended to be highly site and method specific. Studies on the Ribble estuary have focused on the accumulation of radionuclides. Thus a hypothesis was introduced to illustrate a

systematic relationship between SSC and the adsorbed radionuclide concentration. From this, SSC could act as a surrogate for the concentration of a given radionuclide. This hypothesis was proven by this research and is discussed in more detail in section 8.2.1.

### **8.2.1 Characterisation of SSC**

Fundamental to most quantitative remote sensing applications is the understanding of the physical and optical properties of the target to be investigated. However this becomes a logistical problem when working with a system which is highly dynamic. Initial investigations of the SSC and reflectance characteristics were limited to a period two hours either side of high water. However, sampling trips were designed to establish the possible variation in SSC properties with time and location. The results showed that there was not a statistically significant difference in sediment grain size properties between the stationary data and the estuary wide data. However, sampling performed over the complete flood tide, used to calibrate the imagery, showed that the sediment was from a different population. The data show a noisy trend of the percentage of sand decreasing and silt increasing throughout the flood tide. This suggests that some settling of the larger particles occurs very soon after the initial suspension by the tidal bore, which is characterised by high turbulence and accelerated velocities, and before the period two hours before high water.

Spectral characterisation of the suspended sediments in the field was also problematic given traditional sampling techniques, resulting in a relationship exhibiting scatter. For this reason, laboratory experiments were performed to investigate:

1. The relationship between SSC and reflectance.

2. The effect of varying clay and sand content on the SSC reflectance relationship.
3. The effect of salinity on the SSC reflectance relationship.
4. The optimal CASI bands for quantitatively mapping SSC.

The laboratory equipment was designed to minimise internal reflectance and settling. The set-up was tested by using a turbidity meter to assess the behaviour of the suspended sediments, and was proven to be suitable for the reflectance experiments. The laboratory experiments were successful in demonstrating a well-defined ln-linear relationship between SSC and reflectance, with  $R^2 > 0.9$  for all wavelengths above 650nm, correlations similar to most other controlled laboratory studies. The necessity to transform the data to a natural logarithm was in agreement with a study by Chen *et al.*, (1991). The nature of the relationship appears to depend on sediment type and range of SSC used and has varied between previous studies.

From this it was necessary to investigate the effect of a variation in clay content on the SSC reflectance relationship, as it is the clay particles that carry the majority of the  $^{137}\text{Cs}$ . An increase in  $<2 \mu\text{m}$  particles did result in a reduction in the sensitivity of the relationship at very high SSC, seen in the graph as higher clay content sediment approaching an asymptote. Had the SSC values in the imagery been greater than 500 mg/l this would need to be considered, however at less than 300 mg/l the SSC was not high enough for the effect to be significant. Laboratory experiments assessing the effect of the increased sand content, in the early stages of the tide, on the reflectance show that 15% of particles greater than  $63\mu\text{m}$  reduces the reflectance by around ten percent. As all the laboratory data were recorded on particles mainly  $<63 \mu\text{m}$ , laboratory reflectance would be slightly higher than *in-situ* reflectance, depending on illumination conditions.

Thus, for the imagery, the reflectance of the earlier samples, with a higher percentage greater than  $63\mu\text{m}$ , would be underestimating the SSC and the later samples would be more accurate. This may be the cause of some of the scatter in the calibration relationship. If, in the event of ground truth data loss, the images were to be calibrated using a laboratory relationship, defined using  $<63\mu\text{m}$  sediment, the reflectance would have to be corrected prior to image calibration.

In the estuary salinity varies considerably over a flood tide. There are two much referenced papers that have mapped salinity in estuaries using spectral properties (Khorram 1982 and Rimmer *et al.*, 1987). However, no laboratory data have been published to show the existence or absence of a systematic variation in the reflectance of a given SSC with a variation in salinity. Results from the laboratory experiments described here show that there is clearly no systematic relationship between reflectance and salinity for clear or sediment laden waters. This questions the validity of the above two studies. The study by Rimmer *et al.*, (1987), used a salinity range of less than 1‰, between 33‰ and 34‰, representing the upper limit of UK saline waters. The salinity gradient used in the experiments was 0‰ to 30‰, over which no systematic relationship was found. It is hard to accept that the multiple regression of ATM data, used in the study by Rimmer *et al.*, (1987), could be sensitive enough to determine salinity to 0.1‰ in environmental conditions when no systematic relationship is seen in controlled laboratory conditions. The study by Khorram, (1982), was carried out in low SSC waters, (CASE I), over a more realistic salinity gradient. In this environment it is possible that the results are valid, however the data may actually represent measurements of dissolved organic matter, which is inversely correlated to salinity.

The choice of wavebands used to collect the CASI data was strongly influenced by the results obtained from the laboratory studies described here, in addition to those from previous studies. The wavebands, given in table 4.13, were chosen to allow the data to yield the maximum quantity of water quality information. The first three bands were chosen to allow the quantification of dissolved organic matter and bands six to eight allow the quantification of chlorophyll by solar stimulated fluorescence (Gower and Borstad, 1990). Some bands were included to enable atmospheric effects to be studied, band 11 for oxygen absorption and band 14 for water vapour absorption. The remaining bands, up to the maximum 17 bands, were fitted into the region of 700nm to 900nm, which is most suitable for quantification of SSC.

The main variables within the Ribble estuary, such as grain size, sediment composition and salinity are seen to have little effect on the reflectance properties of the suspended sediment and the necessary relationships do exist. This demonstrates that airborne remote sensing is an appropriate method for the quantification of SSC and  $^{137}\text{Cs}$ , and allows a spatial investigation of the mobilisation of sediment over a flood tide.

## **8.2.2 Processing of time series image data**

### **Geo-correction**

The rationale behind the processing of the image data was to eliminate all sources of error prior to image calibration using the ground truth data. The first correction applied was the automated NERC GCORR program to apply the GPS corrections for aircraft roll, pitch, yaw and position. This resulted in three types of error being visible in the CASI images:

1. Spatial distortion.

2. Roll distortion introducing sudden changes in SSC.
3. Small distortions without sudden changes in SSC.

Where spatial distortions result in the image not fitting the digitised map, this is most likely to be a result of the basic errors of the civilian GPS system and was corrected for by fixing the image to the digitised map using ground control points. The roll accompanied by changes in SSC is a result of the change in geometry of the sensor, target and light source. This is difficult to correct for without additional ground truth information and data on aircraft attitude. It has become evident that this is one of the main sources of error in the use of airborne remote sensing platforms.

The very small distortions in the image that are not accompanied by changes in SSC cannot be due to aircraft roll as the geometry remains constant and these are too small to be smoothed using the manual geo-correction techniques used to eliminate other spatial distortions. As the errors are purely spatial not effecting SSC, this implies that this type of error results from problems in the GPS data. As it is the small sudden aircraft motions that are being missed, it suggests that the positional update frequency of the GPS is too low for the correction of the CASI imagery. As the ATM is a whiskbroom sensor it is not susceptible to this problem. It is interesting to note here that the published data on the accuracy of the NERC integrated data system (Wilson 1995) uses the ATM sensor. The Environment Agency produces CASI data but does not use multiple GPS systems. They use a separate gyro system to monitor the motion of the aircraft around its centre of gravity, which is later combined with GPS data. This is an older, well-established technique not subject to the teething problems of the NERC IDS system used in this study.

## **Atmospheric correction and image normalisation**

Correction to the image to remove atmospheric effects must also take place prior to image calibration. As the data were to be calibrated using ground truth data, a haze correction was not necessary. Pathlength effects were investigated but were found to be insignificant at the longer wavelengths that were selected to quantify SSC; hence application of the proposed correction was not required. The main problem resulting from using multiple images is normalisation of illumination conditions. The importance of the correction for solar elevation angle was clearly illustrated when the effect of variations in the solar elevation angle were investigated. As the images were taken over a single flood tide the atmosphere was assumed to be consistent over the three-hour period thus any resulting variation in reflectance must be a result of change in solar elevation angle. Once the variations were quantified, corrections could be applied. The correction for solar elevation angle made a significant improvement of the goodness of fit for the regression between radiance and SSC. The  $R^2$  improved from 0.54, before correction, to 0.76, indicating a successful correction technique. The remaining scatter could result from a variety of sources. Errors due to grain size variations, as discussed earlier, are one possibility. Another possible source of scatter could result from spatial variations in SSC, which is generally patchy, resulting in unrepresentative SSC samples. A mean of three replicate SSC samples was used to compensate to some extent for this possibility. Another possibility of scatter results from the difference in sampling scales. The SSC samples represent just a very small volume at one point in time, whereas the CASI radiance was obtained using a mean value of a 3 x 3 grid of pixels. Using a grid of multiple pixels is a technique commonly used in remote sensing to gain information on variability, but the radiance value obtained represents an area of approximately

56m<sup>2</sup>. The solar elevation correction technique used here would not be valid to normalise images taken on different days, as the assumption that the atmosphere remains unchanged between images would be invalid. After correction the images were then calibrated using the coincidental ground truth data producing what is possibly the first time series data set of this kind and certainly the first for the Ribble estuary.

### **8.3 APPLICATION OF IMAGE DATA TO THE RIBBLE ESTUARY**

There were three main areas for which the image data were required to collect information. The following section will discuss the results derived from the imagery.

#### **8.3.1 Identification of sediment sources**

The time series data were animated to aid interpretation over the temporal scale. The animations were then used to visually identify particular sediment supply characteristics over the flood tide. These were then grouped into the categories, used in section 7.2.1.

1. External sediment supply
2. In estuary: Continuous sediment supply
3. In estuary: Longitudinally transitional sediment supply
4. In estuary: Minimal sediment supply

From the images it was evident that the concentration of suspended sediment entering the estuary from the Irish Sea was very low. However, Brown (1996) used mineralogical data to show that the sediment of the intertidal areas is almost totally of marine origin and not fluvial origin. The SSC range for the ground truth data was much lower than previously sampled, despite being a spring tide. This suggests that the SSC entering the estuary can be much higher than is observed in these images. However,

this would be expected to be strongly dependent on the seasonal cycle. Winter images, or perhaps images collected after a summer storm, may show much higher quantities of sediment entering the estuary from the Irish Sea.

The area used to illustrate a continuous sediment supply to the estuary over the flood tide is in the outer estuary, Figures 7.1a to 7.1h. The initial supply of SSC appears to be generated by turbulent flow around a sandbank. However, after inundation of the bank, there is still a larger amount of sediment being supplied than for similar areas to the immediate south and east. The difference in behaviour was linked to two possible causes:

1. Intertidal sediment properties.
2. Microphytobenthos cover.

Comparing the properties of the intertidal sediment using the map recently produced by Rainey (1999) it could be seen that the area to the south had a higher clay content and would be more cohesive. This cohesiveness, coupled with the possibility of a lower flow velocity implied by the convergence being pushed south by the dominant northern flow, would result in less sediment being suspended from the southern shore compared to the northern shore. The area directly to the east of the high SSC supply showed a higher clay content, increasing the cohesive properties of the sediment but also, and perhaps more importantly, a much higher level of microphytobenthos (A, Figure 7.4). As microphytobenthos is known to inhibit erosion this will further reduce the potential supply of sediment from the area adjacent to the continuous sediment supply. The fact that living organisms play such an important role in the inhibition of sediment erosion

emphasises the potential seasonal variability of the sedimentation in the Ribble estuary as different species dominate at different times of the year.

The longitudinally transitional sediment erosion appears to occur on the narrow intertidal areas where sediment supplies are more limited and is potentially a more interesting puzzle. The question that must be asked is why the sediment does not erode simultaneously along the length of the intertidal area, giving a lateral migration as seen in the outer estuary, as opposed to the longitudinal migration seen here. The process for this is not known, but there is the possibility that again it is the microphytobenthos that play an important role in the mechanism of the erosion. It is possible that a covering of microphytobenthos is inhibiting the overall erosion. The weakest points of the algal mat will be at the edges and the flow will be strongest at the leading edge rather than edge parallel to the main channel. This could result in the erosion mechanism being analogous to the peeling off of a label, that is the erosion must start at the edge and work along the bank as erosion cannot start in the middle. There are no published data on the relative microphytobenthos abundance for Longton Marsh therefore the actual mechanism would require further *in-situ* investigation.

### **8.3.2 Hydrodynamic controls on sediment transport**

In chapters six and seven the imagery showed that there are two main features of the flood tide hydrodynamics. These are the initial influx of the tide creating the tidal bore and the axial convergence flow that forms after the passing of the tidal bore. The sandbanks within the main channel and the confluence area further complicate these hydrodynamic features. The imagery can be used to infer the mechanisms of sediment transport from the surface SSC patters but it must be remembered that the imagery will

only be truly representative of the surface of the water. However, as the estuary is known to be vertically well mixed on a flood tide (Burton *et al.*, 1995), assumptions relating to a relatively constant SSC with depth can be made.

### **The tidal bore**

The tidal bore enters the estuary and progresses at an approximately constant speed of 2.4 m/s. As the speed of a wave is related to the depth (Open University, 1991) this implies that the water depth within the estuary channel is approximately constant over the distance that the bore was observed. The imagery has shown that there is an initial increase in SSC in the turbulent water following the tidal bore, however the pattern of the variation in SSC with time following the bore varies over the length of the estuary. Off Warton Bank, (Figure 7.7a), after the initial increase in SSC, there is a decrease of 40 mg/l, followed by a second increase in SSC. This may be related to the larger grain sizes found early in the flood tide settling quickly before the sediments suspended off the intertidal areas reach the main channel via convergent flows. Further up the estuary, this pattern changes to one of an initial increase following the passing of the bore after which the SSC decreases more steadily. However, the image SSC values used to establish these patterns were sampled from the centre of the main channel, where the SSC is generally lower and some of the more complex suspension patterns related to the intertidal mudflats are not seen.

### **The axial convergence**

The axial convergence is seen to form approximately 2km west of the point at which the bore passes and this distance appears to increase as the bore progresses up the estuary. This may be a result of a change of the velocity of the water flow relating to the

narrowing of the channel and the intertidal areas. However, it may also be a result of using the visibility of foam lines to identify the presence of an axial convergence. As the area of the intertidal mud decreases eastwards along the estuary, the delay in the visibility of the foam line may be due to the reduced amount of debris available. So, the convergence may always form exactly the same distance behind the bore but it is the production of the foam line that is taking longer. To accurately determine the presence of a convergence would require another more complex *in-situ* technique, such as the salinity probe bridge used by Nunes and Simpson, (1985) or the Acoustic Doppler Current Profiler (ADCP) used by Robinson-Swift *et al.*, (1996).

Once the axial convergence is established the images were used to try to gain some information on the strength of the convergence. As no velocity data were collected, the relative velocity of the lateral flow could be estimated only as a ratio with the longitudinal flow. This information could be obtained using the simple geometry of the right-angled triangle and the sediment patterns. The limited data available showed that the strength of the lateral flow appeared to increase along the channel, west to east. This may be related to the decreasing width of the channel or increasing flow velocity. To establish if this trend is a constant feature of the flood tide would require more data to confirm the trend followed by further investigation using *in-situ* velocity data.

Over the flood tide it was evident that the position of the axial convergence front was moving south, implying the flow in the north of the channel is dominating over the flow in the south of the channel. Towards the end of the flood tide this asymmetry of the convergence produced the interesting situation of promoting a simultaneous trapping and supplying of sediment from the creeks. The creeks draining into the north of the

channel were still backed up by the dominant flow, whereas the creek draining into the south of the main channel were supplying sediment to the main channel as the flow in the south was too weak to prevent drainage of the creeks. This illustrates that in the latter stages of the flood tide it is not only the sediment properties or microphytobenthos that are influencing the supply of sediment to the main channel.

A steep SSC gradient was frequently seen across the convergence front as the presence of the front inhibited mixing between the northern and southern water bodies. Examples of transects are shown in section 7.3.3, deliberately choosing areas of similar channel width and intertidal area just 3 km apart. This illustrated that factors other than the geographical location were responsible for the gradients in SSC, therefore the obvious factor was inequality in sediment supply or current velocity. The previous paragraph details the possibility of a weaker flow in the south of the channel and Rainey (1999) details the characteristics of the intertidal sediment. On the narrower intertidal areas around the sewage works the patterns of intertidal sediment distribution are relatively uniform for the north and south shores and the trends for each shore are similar with an increase in percentage clay content with distance from the main channel. This provides further evidence to the concept of higher flow to the north of the convergence front.

### **8.3.3 Model Validation**

The latest two-dimensional model of the Ribble estuary is VERSE, produced by Westlakes Scientific Consulting Ltd and is described in sections 2.2.3 and 7.4.1. The model covers the length and depth of the estuary, but not lateral information. One of the main limitations of this model is that it cannot predict cross channel values for

suspended sediment concentration. A uniform suspended sediment concentration across the width of the channel is unrealistic, as there is known to be a strong axial convergence effectively splitting the channel in two. Also, on inundation of the mudflats the availability of sediment for resuspension will vary across the channel, as the intertidal areas on each side of the main channel are rarely equal.

The most useful information this study can provide for modellers is whether the two data sets can be combined in a more useful format than the one-dimensional results shown in Figure 7.12. The model relies on being told where the cohesive and non-cohesive sediments are located and at the time the equivalent flood tide results were produced for this study, the intertidal mapping (Rainey 1999) was not complete. If this new intertidal mapping can provide accurate substrate data that can be incorporated into the model, this removes one of the potential limitations of the model. The images produced for this study could introduce information on the lateral surface pattern that the model lacks. The combination of the three data sets effectively provides a complete three-dimensional picture of the Ribble estuary. However, to provide enough lateral information to provide a true picture of the Ribble would require flights to assess variations within all three temporal cycles of the estuary:

1. The flood-ebb cycle
2. The spring-neap cycle
3. The seasonal cycle.

Thus, although the information gained through direct comparison of the data sets is limited the three data sets are not mutually exclusive. None of the three data sets can replace another. However, together they have the potential to combine to produce a complete three-dimensional assessment of the Ribble estuary.

### 8.3.4 Sediment and radionuclide budgets

The images were used to calculate sediment and  $^{137}\text{Cs}$  budgets for the flood tide. This was achieved by calculating the total SSC or  $^{137}\text{Cs}$  for each flight line, which was then plotted against time (Figure 7.13). The area under this graph represented the total sediment ( $^{137}\text{Cs}$ ) suspended over the flood tide. The shape of the graph showed when the erosion and deposition phases occurred. The validity of the method used is discussed in section 7.5.3.

The main revelation was that the deposition phase started much earlier than expected, 1.5 hours before high water (11:07 GMT). This represents a large proportion of the flood tide, which is already reduced in time due to the effects of tidal asymmetry. This settling is almost certainly a result of a reduction in the velocity of the flood tide, but there is also the long period of slack water after high water where more deposition will occur. The ebb tide is known to be longer and slower than the flood tide, again an effect of the tidal asymmetry. This will result in the flow having less erosive power and therefore being unable to resuspend all the sediment deposited at high water. The consequence of this is that the figures of  $2.01 \times 10^6$  kg containing 604MBq of  $^{137}\text{Cs}$ , as calculated from Figure 7.13, probably represent a reasonable estimate.

Brown (1996) calculated the inventory of  $^{137}\text{Cs}$  for the Ribble estuary (including saltmarsh and intertidal sediments) to be 10TBq. A supply rate of 604MBq per flood tide would achieve this inventory in 20 to 25 years. This figure is substantially less than the 45 years for which BNFL Sellafield has been discharging, however, there are several reasons for this. The discharges of  $^{137}\text{Cs}$  have decreased with time, thus the

concentrations of  $^{137}\text{Cs}$  adsorbed onto the sediment will have varied over the 45 years. Also, this result assumes all flood tides will deposit 604MBq of  $^{137}\text{Cs}$ , which is clearly not likely to be true. Neap tides will deposit less  $^{137}\text{Cs}$  and this will increase the time required to accumulate 10TBq of  $^{137}\text{Cs}$ . Finally, the 604MBq does not account for a complete tidal cycle, just the flood tide. If we assume the ebb tide removes some of the  $^{137}\text{Cs}$  back out past Lytham, the figure of 604MBq is an overestimation, resulting in an increase in the time required to accumulate 10TBq of  $^{137}\text{Cs}$ .

#### **8.4 MAIN CONTRIBUTIONS OF THIS THESIS**

Although the systematic relationship between SSC and the concentration of adsorbed  $^{137}\text{Cs}$  was assumed to exist, this study represents the first conclusive evidence of the relationship. As it is known that a systematic relationship between other radionuclides and sediments exist, it can be assumed that relationships between other radionuclides and SSC also exist. The fact that they were not established within this study was a result of limited sample size. A technique such as *in-situ* centrifugation would be required to harvest enough suspended sediment to establish the evidence for the other radionuclides known to be present in the estuary.

The laboratory experiments investigating the effect of a NaCl salinity gradient on the reflectance of SSC in a controlled environment are the first published data of this kind. The results have shown that variation in salinity has no systematic effect on reflectance of SSC, which then brings into question the validity of previous papers on salinity mapping using remote sensing.

The pre-processing correction techniques used on the imagery are standard techniques that can be repeated using any image processing software. The exception is the empirical solar elevation angle correction method developed within this study. This is a logical, post processing correction technique that can be applied to any time series data set without prior knowledge of the exact solar elevation.

The linear regression used to calibrate the imagery is valid for the Ribble estuary sediment. However, as this sediment is known to be almost totally of marine origin this calibration may represent a single SSC algorithm that is valid for the Irish Sea and all the Irish Sea estuaries, particularly as this is a relatively enclosed sea. This results in an algorithm that is potentially valid for an area that is much greater than most other airborne remote sensing SSC algorithms, which are known to be very site specific.

This project demonstrates how image data have been applied to various aspects of the estuarine flood tide to gain useful quantitative information on sediment supply and transport. This has resulted in data providing useful estimates of sediment and, more importantly,  $^{137}\text{Cs}$  budgets for the spring flood tide. This is the first time this kind of information has been derived using image data.

## **8.5 REFINEMENTS IN METHODOLOGY**

Despite the success of this study there are several areas where improvements in the methodology could be made. One of the major limitations was the small data set used to calibrate the images. Ideally, two data sets should be collected using two boats, one used for relationship definition and the second for relationship validation. This would have enabled an estimation of the magnitude of the errors, however, this would have

been prohibitively expensive for this study. The ground truth data for SSC and  $^{137}\text{Cs}$  would be improved with more replicates. This would allow a better understanding of variability in SSC and temporal stability of the  $^{137}\text{Cs}$  concentrations. However, despite the need for replicate samples being limited by the capacity of the boat, the reduced data sets still showed good relationships, particularly between SSC and  $^{137}\text{Cs}$ .

The *in-situ* and laboratory spectral work was performed using whichever spectrometers were available from the NERC EPFS. Ideally, all spectral work should have been performed with the same spectrometer and under the same lighting conditions, with the best combination being either spectrometer used in direct natural light (sunshine). The need for this was clearly demonstrated by the comparison of the various spectrometers and illumination conditions in section 4.3.6.

The time of remote sensing data acquisition was earlier than originally desired. Had the high tide fallen two to three hours later the flights would all have been performed between 1100 and 1400 GMT. If this had been the case, the solar elevation angle correction would not have been necessary. In the event of the earlier flights the correction obviously worked well, however it is always preferable to alter the raw data as little as possible to avoid the possibility of adding any further errors into the data. The earlier flights were used as the possibility of perfect weather and ideally timed high tides occurring simultaneously could not be relied upon and opportunities must be seized as and when they arise, even if some compromise has to be made.

A further possibility of an improvement to the image calibration would be to develop a correction technique for adjusting the radiance for variations in grain size. As there is a

possible trend of the percentage  $>63\mu\text{m}$  decreasing with time this may be able to be applied on a temporal basis, as was the solar elevation angle correction. However, more data collection over the complete flood tide would be required to confirm the relationship is real before this could be attempted.

The budget calculations are derived using the water volume from the VERSE model, but this model makes assumptions regarding the shape of the channel that reduce the accuracy of the volume data. A second remote sensing technique, light detection and ranging (LIDAR) could be used to produce a digital terrain model (DTM) to 0.01m accuracy. Using GIS software to ‘virtually’ flood the estuary to the required depth above ODN a more precise volume would be obtained. This would greatly improve the sediment and  $^{137}\text{Cs}$  budget estimates.

## **8.6 FINAL CONCLUSIONS OF THE REASEARCH**

This project has successfully met the need for a spatially representative investigation of the Ribble estuary using a combination of *in-situ* and laboratory data to develop a method of remote sensing SSC. The SSC was then used as a surrogate for  $^{137}\text{Cs}$  using a well-defined relationship established *in-situ*. The images were used to provide useful quantitative data on the behaviour of the estuary.

The major conclusions of this research are:

1. An understanding of the influence of suspended sediment particle size and concentration on the spectral properties of the waters of the Ribble estuary. Particularly the importance of SSC range and clay content in defining the relationship and demonstrating the necessity for ground truth data.

2. The establishment of a well-defined linear relationship between the SSC and the associated  $^{137}\text{Cs}$  concentration for the Ribble estuary, which is shown to be relatively temporally stable.
3. The development of a protocol for the processing of airborne CASI data to reflect SSC and  $^{137}\text{Cs}$  concentrations, correcting for the spatial and temporal effects of image collection. This could also be combined with field experiments including sediment traps and erosion pegs. This would provide more quantitative information on the effects of sediment stabilisation by microphytobenthos.
4. The production of SSC and  $^{137}\text{Cs}$  maps, which can be used to identify sediment sources and the hydrodynamic controls on sediment transportation processes. The data can also be used to aid the interpretation of VERSE model data.
5. The calculation of erosion and deposition phases of the flood tide allowing the computation of sediment and  $^{137}\text{Cs}$  budgets for the estuarine flood tide. This demonstrates a net deposition of  $2.01 \times 10^6 \text{kg}$  of sediment, with an associated  $^{137}\text{Cs}$  concentration of 604MBq.

Overall it has been clearly shown that the technique of remote sensing is able to overcome such difficulties as placing spot samples in a spatial and temporal context, thus reducing errors due to interpolation. The method developed within this study has shown that remote sensing does have the capability to be used to gain spatially and temporally representative data of the Ribble estuary and has produced an unrivalled data set with which to assess the Ribble estuary.

## **8.7 FURTHER WORK**

This method of estuarine monitoring has been shown to work well and provide useful quantitative information. However, there are several logical progressions for future applications of this technique or data.

1. To extend the investigation to the temporal cycles of the Ribble estuary, such as, the ebb tide, the spring-neap tidal cycle and seasonal cycles.
2. To apply the method without modification to other Irish Sea estuaries undergoing the same siltation problems as the Ribble estuary. Using high-resolution satellite data, available from the new generation of satellites currently nearing launch, the method could also be applied to the Irish Sea as a whole. This would be particularly useful to estimate quantities of sediment transported out of the Irish Sea to the northeast Atlantic.
3. To obtain quantitative sediment and  $^{137}\text{Cs}$  budget data from the image series on a smaller spatial scale, providing information on which areas of the estuary that are more active in erosion and deposition.
4. To utilise the full potential of the band set to provide additional water quality information. For example, the water flowing out of the docks could also be studied using chlorophyll analysis by solar stimulated fluorescence (Gower and Borstad, 1990) to provide information on the processes involved in the downstream mixing of the released water.

5. Finally, to establish the relationship between SSC and other particle reactive pollutants for distribution mapping and budget calculation.

This research has fulfilled the original aim and answered many questions, however, our understanding of the estuarine environment is still far from complete. It is therefore essential to continue scientific research into the estuarine environment to enable management plans to be established for our resource-rich estuaries.

## REFERENCES

- Aranuvachapun, S. and Le Bond, P.H. 1981. Turbidity of coastal waters determined from Landsat. *Remote Sensing of the Environment*. **11**(2), pp 112-113.
- Assinder, D.J; Kelly, M. and Aston S.R. 1985. Tidal variations in dissolved and particulate phase radionuclide activities in the Esk estuary, England, and their distribution coefficients and particulate activity fractions. *Journal of Environmental Radioactivity*. **2**, pp 1-22.
- Assinder, D.J; Yamamoto, M; Kim, C.K; Seki, R; Takaku, D; Yamauch, Y; Komura, K; Veno, K. and Bourne, G.S. 1991. Neptunium in intertidal, coastal and estuarine sediments in the Irish Sea. *Journal of Environmental Radioactivity*. **14**, pp 135-145.
- Assinder, D.J., Mudge, S.M. and Bourne, G.S. 1997. Radiological assessment of the Ribble estuary I :- Distribution of radionuclides in surface sediments. *Journal of Environmental Radioactivity*, **36** (1), pp 1-19.
- Aston, S.R; Assinder, D.J; Stanners, D.A. and Rae, J.E. 1981. Plutonium occurrence and phase distribution in sediments of the Wyre estuary, N.W. England. *Marine Pollution Bulletin*. **12** (9), pp 308-314.
- Atkins, W.S. 1993. The Ribble estuary model. BNFL final report.
- Bagheri, S; Stein, M.. and Dios, R. 1998. Utility of hyperspectral data for bathymetric mapping in a tidal estuary. *International Journal of Remote Sensing*. **19** (6), pp 1179-1188.
- Bale, A.J.; Tocher, M.D; Weaver, R; Hudson, S.J. and Aiken, J. 1994. Laboratory measurements of spectral properties of estuarine suspended particles. *Netherlands Journal of Aquatic Ecology*, **28**(3/4), pp 237-244.
- Beresford-Hartwell, P.R., Horsington, R.W., Mamas, C.J.V., Randle, K., Taylor, E.W., West, J.R. and Sokhi, R.S. 1995. Changes in sedimentation and contamination in the Ribble estuary. *Coastal Zone Topics: Process, Ecology and Management*, **1**, pp 14-19.
- Bhargava, D.S and Mariam, D. W. 1990. Spectral reflectance relationships to turbidity generated by different clay materials. *Photogrammetric Engineering and Remote Sensing*. **56** (2), pp 225-229.
- Bhargava, D.S and Mariam, D. W. 1991a. Light penetration depth, turbidity and reflectance related relationships and models. *ISPRS Photogrammetry and Remote Sensing*. **46** , pp 217-230.
- Bhargava, D.S and Mariam, D. W. 1991b. Effects of suspended particle size and concentration on reflectance measurements. *Photogrammetric Engineering and Remote Sensing*. **57** (5), pp 519-529.

- Bierwirth, P.N; Lee, T.J. and Burne, R.V. 1993 Shallow sea floor reflectance and water depth derived by unmixing multispectral imagery. *Photogrammetric Engineering and Remote Sensing*. **59** (3), pp 331-338.
- Black, K.S. 1998. Suspended sediment dynamics and bed erosion in the high shore mudflat region of the Humber estuary. *Marine Pollution Bulletin*, **37** (3-7) pp 122-133.
- Black, K.S., Paterson, D.M. and Cramp, A. (Eds.) 1998. *Sedimentary processes in the intertidal zone*. Geological Society London, Special Publication.
- BNFL 1993. Annual report on radioactive discharges and monitoring of the environment. Report on discharges and environmental monitoring.
- BNFL 1996. Annual report on radioactive discharges and monitoring of the environment. Report on discharges and environmental monitoring.
- BNFL 1998. Annual report on radioactive discharges and monitoring of the environment. Report on discharges and environmental monitoring.
- Bondietti, E.A. 1981. Mobile species of Pu, Am, Cm, Np and Tc in the environment. *Invited paper IAEA-SM-257/42*. pp 81-96.
- Bowden, K.F. 1980. Physical factors : Salinity, temperature, circulation and mixing processes. Chapter two in: *Chemistry and biogeochemistry of estuaries*. Eds: E. Olausson and I. Cato, Pub. J. Wiley and Sons.
- Bowie, S.H. and Plant, J.A. 1983. Natural radioactivity in the environment. Chapter 16 in: *Applied environmental geochemistry*. Pub.: Academic Press. Ed.: Iain Thornton. ISBN 0-12-690640-8.
- Bricaud, A., Morel, A. and Prieur, L. 1981. Absorption by dissolved organic matter of the sea (yellow substance) in the UV and visible domains. *Limnology and Oceanography*, **26**(1), pp 43-53.
- Brown, J. 1996. The behaviour of radionuclides in the Ribble estuary, N.W. England. *PhD Thesis*, Postgraduate Research Institute for Sedimentology, University of Reading.
- Brown, J; Turrell, W.R. and Simpson, J.H. 1991. Aerial surveys of axial convergence fronts in UK estuaries and the implications for pollution. *Marine Pollution Bulletin* **22** (8), pp 397-400.
- Burton, D.J; West, J.R; Horsington, R.W. and Randle, K. 1995. Modelling transport processes in the Ribble Estuary. *Environment International*. **21** (2), pp 131-141.
- Bryant, R; Tyler, A; Gilvear, D; McDonald, P; Teasdale, I. and Ferrier, G. 1995. A preliminary investigation into VNIR spectral characteristics of intertidal sediments. *International Journal of Remote Sensing*. **17** (2), pp 405-412.
- Campbell, J.B. 1996 Introduction to Remote Sensing : Second Edition. Published by Taylor and Francis (London). ISBN 0-7484-0663-8.

Chavez, P.S. jnr. 1988. An improved dark object subtraction technique for atmospheric scattering correction of multi-spectral data. *Remote Sensing of the Environment* **24**, pp 459-479.

Chen,Z; Hansom, J.D. and Curran, P-J 1991. The form of the relationship between suspended sediment concentration and spectral reflectance: Its implications for the use of Daedalus 1268 data. *International Journal of Remote Sensing*. **12** (1), pp 215-222.

Chen,Z; Curran, P-J and Hansom, J.D. 1992. Derivative reflectance spectroscopy to estimate suspended solids concentration. *Remote Sensing of the Environment*. **40** (1), pp 67-77.

Choubey, V.K. and Subramanian, V. 1991. Spectral response of suspended sediments in water under controlled conditions. *Journal of Hydrology*. **122**, pp 301-308.

Choubey, V.K. and Subramanian, V. 1992. Estimation of suspended solids using Indian remote sensing satellite-1A data : a case study from Central India. *International Journal of Remote Sensing*. **13** (8), pp 1473-1486.

Clifton, J., McDonald, P., Plater, A. and Oldfield, F. 1999. An investigation into the efficiency of particle size separation using Stokes' Law. *Earth Surface Process Landforms*, **24** (8), pp 725-730.

Collins, M. and Pattiaratchi, C. 1984. Identification of suspended sediment in coastal waters using ATM data. *International Journal of Remote Sensing*. **5** (4), pp 635-657.

Cook, G.T; Baxter, M.S; Duncan, H.J. and Malcolmson, R. 1984a. Geochemical association of Pu and gamma- emitting radionuclides in Caithness soils and marine particles. *Journal of Environmental Radioactivity*. **1**, pp 119-131.

Cook, G.T; Baxter, M.S; Duncan, H.J; Toole, J.and Malcolmson, R. 1984b. Geochemical associations of Plutonium in the Caithness environment. *Nuclear Instruments and Methods in Physics Research*. **223**, pp 517-522.

Cook, G.T., MacKenzie, A.B., McDonald, P. and Jones, S.R. 1997. Remobilisation of Sellafield derived radionuclides and transport from the North East Irish Sea. *Journal of Environmental Radioactivity*. **35** (3) pp 227-241.

Davis, K. S. and Shaw, G. 1993. Fixation of <sup>137</sup>Cs by soils and sediments in the Esk estuary, Cumbria, UK. *The Science of the Total Environment*. **132**, pp 71-92.

Dyer, K.R. 1973. Estuaries: A physical introduction. Pub. John Wiley and Sons. ISBN 0-471-22905-9.

Dyer, K.R. 1979. Chapter 1: Estuaries and Estuarine Sedimentation. in *Estuarine Hydrography and Sedimentation* : Estuarine and Brackish-water sciences association handbook. Ed: K.R. Dyer. Pub: Cambridge Universtiy Press. ISBN 0-521-29496-7 pp 1-14.

- Eisenbud, M. and Gesell, T. 1997. Environmental radioactivity from natural, industrial and military sources. Pub: Academic press, ISBN 0-12-235154-1.
- Ellis, S. and Mellor, A. 1995. Soil constituents and Properties. In: *Soils and Environment* Pub: Routledge. ISBN 0-415-06888-6.
- Environment Agency. 1997. The river Ribble fact file.
- Fairbridge, R.W. 1980. The estuary : Its definition and geodynamic cycle. Chapter 1 in : *Chemistry and biogeochemistry of estuaries*. Eds. E. Olausson and I. Cato. Pub. John Wiley & sons. ISBN 0-471-27679-0.
- Ferrier, G. 1995. A field study of the variability in the suspended sediment concentration - reflectance relationship. *International Journal of Remote Sensing*. **16** (14), pp 2713-2720.
- Francis, C.W. and Brinkley, F.S. 1976. Preferential adsorption of  $^{137}\text{Cs}$  to micaceous minerals in freshwater sediment. *Nature*, **260**, pp 511-513.
- Gilabert, M.A.; Conese, C. and Maselli, F. 1994. An atmospheric correction method for the automatic retrieval of surface reflectances from TM images. *International Journal of Remote Sensing*. **15** (10), pp 2065-2086.
- Gillham, R.W.; Cherry, J.A. and Lindsay, L.E. 1980. Caesium distribution coefficients in unconsolidated geological materials. *Health Physics*, **39**, pp 637-649.
- Gippel, C.J. 1989. The use of turbidimeters in suspended sediment research. *Hydrobiologia* **176/177**, pp 465-480.
- Gleizon, P. 1999. A vertically resolving model of sediment and radionuclide transport for the Ribble estuary. *Proceedings of the 6<sup>th</sup> SRP International Symposium, Southport. 14-18 June*. pp 291-294.
- Goodin, D.G.; Han, L.; Fraser, R.N.; Rundquist, D.C.; Stebbins, W.A. and Schalles, J.F. 1993. Analysis of suspended solids in water using remotely sensed high resolution derivative spectra. *Photogrammetric Engineering and Remote Sensing*. **59** (4), pp 505-510.
- Gower, J.F.R., Lin, S. and Borstad, G.A. 1984. The information content of different optical spectral ranges for remote chlorophyll estimation in coastal waters. *International Journal of Remote Sensing*, **5**(2), pp 349-364.
- Gower, J.F.R., Borstad, G.A. 1990. Mapping phytoplankton by solar stimulated fluorescence using an imaging spectrometer. *International Journal of Remote Sensing*, **11**(2), pp 313-320.
- Hamilton-Taylor, J.; Kelly, M.; Mudge, S. and Bradshaw, K. 1987. Rapid remobilisation of Plutonium from estuarine sediments. *Journal of Environmental Radioactivity*, **5**, pp 409-423.

- Han, L. and Rundquist, D.C. 1996. Spectral characterisation of suspended sediments generated from two texture classes of clay soil. *International Journal of Remote Sensing*. 17 (3), pp 643-649.
- Han, L. 1997. Spectral reflectance with varying suspended sediment concentrations in clear and algal laden waters. *Photogrammetric Engineering and Remote Sensing*, 63(6), pp 701-705.
- Harrington, J.A.; Schiebe, F. and Nix, J.F. 1992. Remote sensing of Lake Chicot, Arkansas: Monitoring suspended sediments, turbidity and Secchi depth with Landsat TM data. *Remote Sensing of the Environment*, 39, pp 15-27.
- Hill, A.E., Brown, J. and Fernaud, L. 1997. The summer gyre in the western Irish Sea: Shelf sea paradigms and management implications. *Estuarine coastal and Shelf Science*. 44 (Supp A) pp 83-95.
- Hird, A.B., Rimmer, D.L. and Livens, F.R. 1995. Total caesium fixing potentials of acid organic soils. *Journal of Environmental Radioactivity* 26, pp 103-118.
- Hudson, S.J; Moore, G.F; Bale, A.J; Dyer, K.R. and Aiken, J. 1994 An operational approach to determining suspended sediment distributions in the Humber estuary by airborne multi-spectral imagery. *Proceedings of the first Airborne Remote Sensing Conference and Exhibition*, Strasbourg, France. 11-15 Sept 1994.
- Hunt, G.J. and Smith, B.D. 1999. Radiological impact of actinides discharged to the Irish Sea. *Journal of Environmental Radioactivity*, 44 pp 389-403.
- Hursthouse, A.S.; Baxter, M.S.; Livens, F.R. and Duncan, H.J. 1991. The transfer of Sellafield derived <sup>237</sup>Np to and within the terrestrial environment. *Journal of Environmental Radioactivity*, 14, pp 147-174.
- IAEA. 1985. Sediment  $K_d$ s and concentration factors for radionuclides in the marine environment. *IAEA Technical Report Series No. 247*
- Ivanovich, M. and Harman, R.S. 1982. Uranium series disequilibrium; Applications to environmental problems. *Clarendon Press, Oxford*
- Jensen, J.R. 1986. Introductory digital image processing : a remote sensing perspective. Chapter 6 - Atmospheric effects. Pub. Prentice and Hall. *ISBN 0-13-500828-X-025*.
- Kershaw, P.J., Pentreath, R.J., Woodhead, D.S. and Hunt, G.J. 1992. A review of radioactivity in the Irish Sea: A report prepared for the marine pollution monitoring management group. *MAFF Aquatic Monitoring Report No. 32*. ISSN 0142-2499.
- Khorram, S. 1982. Remote sensing of salinity in the San Francisco Bay delta. *Remote sensing of the Environment*. 12, pp 15-22.
- Knoll, G.F. 1989. Radiation Detection and Measurement. Pub. John Wiley and sons. *ISBN 0-471-61761-X*.

Krauskopf, K.B. and Bird, D.K. 1995. Introduction to geochemistry Third Edition. Pub: McGraw-Hill. ISBN 0-07-035820-6.

Largier, J.L. 1992. "Tidal intrusion fronts" *Estuaries*, **15** (1), pp 26-39.

Lillesand, T.M and Kiefer, R.W. 1994. Remote sensing and image interpretation. 3<sup>rd</sup> Ed. Pub. John Wiley and Son.

Livens, F.R. and Baxter, M.S. 1988. Particle size and radionuclide levels in some west Cumbrian soils. *The Science of the Total Environment*. **70**, pp 1-17.

Lyon, J.G.; Lunetta, R.S. and Williams, D.C. 1992. Evaluating bottom sediment types and water depth of the St. Mary's river - Michigan. *Photogrammetric Engineering and Remote Sensing*. **58** (7), pp 951-956.

Lyons, M.G. 1997 The dynamics of suspended sediment transport in the Ribble estuary. *Water, Air and Soil Pollution*, **99** (1-4) pp 141-148.

MacFarlane, N. and Robinson, I.S. 1984. Atmospheric correction of Landsat MSS data for a multi-date suspended sediment algorithm. *International Journal of Remote Sensing*. **5** (3), pp 561-576.

MacKenzie, A.B.; Scott, R.D.; Allan, R.L.; Ben Shaban, Y.A.; Cook, G.T. and Pulford, I.D. 1994. Sediment radionuclide profiles : Implications for mechanisms of Sellafield waste dispersal in the Irish Sea. *Journal of Environmental Radioactivity*. **23**, pp 39-69.

Mamas, C.J.V.; Earwaker, L.G.; Sokhi, R.S.; Randle, K.; Beresford-Hartwell, P.R. and West, J.R. 1995. An estimation of sedimentation rates along the Ribble estuary, Lancashire, UK, based on radiocaesium profiles preserved in intertidal sediments. *Environment International* **21**(2), pp 151-165.

Mantovani, J.E., Cabral, A.P. 1992. Tank depth determination for water radiometric measurements. *International Journal of Remote Sensing*. **13** (4), pp 2727-2733.

McCave, I.N. 1979. Suspended sediment pp131-185 in: *Estuarine Hydrography and Sedimentation: Estuarine and Brackish-water sciences association handbook*. Editor K.R. Dyer. Cambridge University Press. ISBN 0-521-29496-7.

McDonald, P. and Jones, S.R. 1995. The behaviour of radionuclides in the coastal and estuarine environments of the Irish Sea. In: *Biogeochemistry of intertidal sediments*. Cambridge environmental chemistry series No, 9. Eds.: Jickells, T.D and Rae, J.E.

McDowell, D.M. and O'Connor, B.A. 1977. Hydraulic Behaviour in Estuaries. The MacMillan Press Ltd. ISBN 0-333-12231-3.

Mudge, S.M.; Assinder, D.J. and Bourne, G.S. 1994. A survey of radioactivity in the Ribble Estuary. Part 1: Activity concentrations and estuary dynamics. *HMIP Environmental Series Report No.2*.

Mudge, S.M.; Assinder, D.J. and Bourne, G.S. 1994. A survey of radioactivity in the Ribble Estuary. Part 2 : Radiological assessment. *HMIP Environmental Series Report No.3*

Mudge, S.M., Bourne, G.S. and Assinder, D.J., 1997. Radiological assessment of the Ribble estuary II :- "Beta and Gamma dose rates and doses to critical groups. *Journal of Environmental Radioactivity*, **36** (1), pp 21-41.

Muller-Karger, F.E. 1992. Remote sensing of marine pollution, a challenge for the 1990's. *Marine Pollution Bulletin*. **25** (1/4), pp 54-60.

Novo, E.M.M.; Hansom, J.D. and Curran P.J. 1989. The effect of sediment type on the relationship between reflectance and suspended sediment concentration. *International Journal of Remote Sensing*, **10** (7), pp 1283-1289.

Novo, E.M.M.; Steffen, C.A. and Braga, C.Z.F. 1991. Results of a laboratory experiment relating spectral reflectance to total suspended solids. *Remote Sensing of the Environment*. **36** (1), pp 67-72.

Nunes, R.A. and Simpson, J.H. 1985. Axial convergence in a well-mixed estuary. *Estuarine, Coastal and Shelf Science*, **20**, pp 637-649.

Olausson, E. and Cato, I. (Eds.) *Chemistry and biogeochemistry of estuaries*. Pub. John Wiley & sons. ISBN 0-471-27679-0.

Open University. 1989. Seawater: its composition, properties and behaviour. Ed. Open University Team. Pub. The Open University and Pergamon Press. ISBN 0-08-036367-9.

Open University. 1991. Waves, Tides and Shallow Water Processes. Ed. Gerry Bearman. Pub. The Open University and Pergamon Press. ISBN 0-08-036371-7.

Pritchard, D.W. 1989. Estuarine classification - a help or a hinderance? Chapter 1 in: *Estuarine Circulation*. Eds. Neilson, B.J., Kuo, A. and Brubaker, J. Pub. Humana Press Inc.. ISBN 0-89603-155-1. pp 1-38.

Paterson, D.M. Yates, M.G., Wiltshire, K.H., McGroarty, S. Miles, A. Eastwood, J.E.A., Blackburn, J. & Davidson, I. 1998. Microbiological mediation of spectral reflectance from intertidal cohesive sediments. *J. Limnol. Oceanog.* **43**(6), pp 1207-1221.

Paterson, D.M. 1999. The fine-structure and properties of the sediment interface. In: *The benthic boundary layer: Transport Processes and biogeochemistry*. Eds.: Boudreau, B.B. and Jorgensen, B.B. Pub.: Open University Press.

Rahman, H. and Dedieu, G. 1994. SMAC : a simplified method for atmospheric correction of satellite measurements in the solar spectrum. *International Journal of Remote Sensing*. **15** (1), pp 123-143.

- Rainey, M.P. 1999. Airborne remote sensing of estuarine intertidal radionuclide concentrations. *PhD Thesis*, University of Stirling.
- Rainey, M.P., Tyler, A.N., Bryant, R.G., Gilvear, D.J. and McDonald P. 2000. The influence of surface interstitial moisture on the spectral characteristics of intertidal sediments: Implications for airborne image acquisition and processing. *International Journal of Remote Sensing* **21**(16) pp 3025-3038.
- Richter, R. 1990. A fast atmospheric correction algorithm applied to Landsat TM images. *International Journal of Remote Sensing*, **11** (1), pp 159-166.
- Rimmer, J.C.; Collins, M.B. and Pattiaratchi, C.B. 1987. Mapping of water quality in coastal waters using Airborne Thematic Mapper data. *International Journal of Remote Sensing*, **8** (1), pp 85-102.
- Robinson-Swift, M.; Fredriksson, D.W. and Celikkol, B. 1996. Structure of an axial convergence zone from acoustic doppler current profile measurements. *Estuarine, Coastal and Shelf Science*, **43**, pp 109-122.
- Sanderson, D.C.W; Allyson, J.D. and Tyler, A.N. 1993a. Rapid quantification and mapping of radiometric data for anthropogenic and technologically enhanced natural nuclides. *Application of uranium exploration data and techniques in environmental studies*. IAEA-TECDOC-827 pp 197-216
- Sanderson, D.C.W; Allyson, J.D; Tyler, A.N. and Scott, E.M. 1993b. Environmental applications of airborne gamma spectroscopy. *Application of uranium exploration data and techniques in environmental studies*. IAEA-TECDOC-827 pp 71-91
- Sanderson, D.C.W; Allyson, J.D; Tyler, A.N. 1993c. An aerial gamma ray survey of Springfields and the Ribble estuary in September 1992. *Scottish Universities Research and Reactor Centre, Report 9301*.
- Schulz, R.K. 1965. Soil chemistry of radionuclides. *Health Physics*, **11**, pp 1317-1324.
- Scott, M.R. 1982. The chemistry of U and Th series nuclides in rivers. In: *Uranium series disequilibrium : Applications to environmental problems* Eds. Ivanovich, M. and Harmon, R.S. Pub. Clarendon Press. ISBN 0-19-854423-5 Chapter 8, pp 181-199.
- Sholkovitz, E.R. 1983. The geochemistry of Plutonium in fresh and marine water environments. *Earth Science Reviews*, **19** , pp 95-161.
- Simpson, J.H. and Turrell, W.R. 1986. Convergent fronts in the circulation of tidal estuaries. In: *Estuarine Variability*. Ed.: Wolfe, D.A., Pub.: Academic Press. ISBN 0-12-761890-2.
- Singh, S.M. 1994. Parameterisation of a single scattering atmospheric correction algorithm using 5S code. *International Journal of Remote Sensing*. **15** (1), pp 191-196.
- Tassan, S. 1994. Removal of the effect of sunglitter from Thematic Mapper imagery of the sea. *International Journal of Remote Sensing*. **15** (3), pp 719-723.

- Topliss, B.J. 1986. Spectral variations in upwelling radiant intensity and turbid coastal waters. *Estuarine Coastal and Shelf Science*, **22** (4), pp 395-414.
- Topliss, B.J.; Almos, C.L. and Hill, P.R. 1990. Algorithms for remote sensing of high concentration, inorganic suspended sediment. *International Journal of Remote Sensing*, **11** (6), pp 947-966.
- Turner, A.; Millward, G.E. and Tyler, A.O. 1994. The distribution and chemical composition of particles in a macro-tidal estuary. *Estuarine Coastal and Shelf Science*, **38**, pp 1-17.
- Turrell, W.R., Brown, J. and Simpson, J.H. 1996. Salt intrusion and secondary flow in a shallow, well mixed estuary. *Estuarine Coastal and Shelf Science*, **42**, pp 153-169.
- Tyler A.N. 1994. Environmental influences on gamma ray spectrometry. *PhD Thesis*. University of Glasgow.
- Tyler, A.N. 1999. Monitoring anthropogenic radioactivity in saltmarsh environments through *in-situ* gamma ray spectrometry. *Journal of Environmental Radioactivity*, **45**, pp 235-252.
- Uncles, R.J. 1981. A note on tidal asymmetry in the Severn Estuary. *Estuarine Coastal and Shelf Science*, **13** pp 419-432.
- West, J.R. and Cotton, P. 1981. The measurement of diffusion coefficients in the Conwy estuary. *Estuarine, Coastal and Shelf Science*. **12** pp 232-336.
- Wilson, A.K. 1994. The NERC integrated ATM and CASI GPS system. *Proceedings of the first international airborne remote sensing conference and exhibition: applications, technology and science*. **2**, pp 249-259.
- Wilson, A.K. 1995. The NERC airborne remote sensing user handbook, version 1.0.

## APPENDIX A

### OPERATION OF THE ASD FR<sup>®</sup> SPECTRORADIOMETER

1. Change directory to **C:\FR\** and type **FR 632 2** to start software
2. Select **Spectrum Save** menu and define data directory (e.g. c:\Ribble), base filename (e.g. test) and starting spectrum number (default is .000) to give files c:\Ribble\test.000 to c:\Ribble\test.nnn.
3. Select **Adjust Configuration** menu and define the number of scan to average for spectrum, dark current (DC) and white reference. It is recommended that the same number is used for all three, usually 10.
4. Define the fore-optic used via the offered options on the toolbar.
5. Position sensor over the barium sulphate reference panel and optimise using (**Ctrl-O**) or the optimise button on the toolbar, this optimises the gain settings and integration times.
6. Perform a dark current measurement if necessary using the toolbar or the shortcut key **F3**. This is done approximately every 15 minutes throughout the sampling period and requires the user to press any key twice, once to initiate the measurement and once to confirm completion.
7. To take a spectrum of the reference panel, position the sensor over the panel and press the **Spacebar**. Make a note on the log-sheet of the spectrum number and that this is a reference panel spectrum.
8. To take a spectrum of the target, position the sensor over the target and press the **Spacebar** once for each replicate spectrum that is required. Make a note on the log-sheet of the spectrum numbers and the target name.
9. At each sample site repeat steps 7 and 8.

At the end of each day the files are downloaded using an external floppy disk drive for transfer to a PC for processing.

## OPERATION OF THE GER 1500 SPECTRORADIOMETER

### Stand Alone Mode:

In the scrolling menu, parameters are selected using the up and down arrows on the control panel, then altered using the edit key. The selected parameter will flash and is then toggled to the correct option, the edit button sets the selected parameter.

1. Select the next scan number to be displayed using the **mem.** parameter.
2. Select **average** to set the number of scans to be averaged for a collected spectrum. This is obtained using the formula  $2^{(x-1)}$ , thus a averaging value of 5 gives us  $2^4 = 16$ , this is the recommended value.
3. Select **Intsp** to set the integration speed. The up and down arrows are used to set fixed values or **A** can be selected to give an automated integration speed which selects the optimum value. The automated integration speed is the recommended setting.
4. Select **trg** to choose the trigger options from the choice of **lsr** = laser only, **scan** = scan only or **both** = laser on when trigger is pressed and scan on trigger release. Scan only is the recommended option.
5. Select **optic** to choose optic settings from the choice of five.
  - (i) Std =  $\sim 4^\circ \times 5^\circ$
  - (ii) Fibre optic = not available for NERC EPFS GER1500
  - (iii)  $15^\circ$  FOV
  - (iv) Cosine diffuser
  - (v) Unity = raw 16-bit digital number

Unity is the recommended option.

1. Collect spectra using the red trigger by facing the sun while standing behind the sensor head – DO NOT POINT SENSOR AT YOUR FEET. The first scan defaults to a reference panel scan the user must remember to toggle between REFERENCE and TARGET scans.
2. Download the data via the comm2, to the serial port of the PC.

Alternatively data can be collected via the PC using the PC software to select the set-up options described above. Data is the processed as detailed in paragraph 3.3.1.

## **OPERATION OF THE MALVERN MASTERSIZER: PARTICLE SIZING BY LASER DIFFRACTION**

1. Enter notes on the sample in the box provided and make a written record. This needs to be done as the sample information is not exported when the data is transferred to an Excel spreadsheet.
2. Select a background reading, which once done will go directly to sample measurement.
3. When prompted add the sample until lens obscuration reaches between 8% and 15%.
4. To collect the data press the spacebar and then the disk icon to save.
5. Open the drain and rinse with one litre of distilled water.
6. Close the drain and fill the sample well with distilled water until the level is above the inlet to the instrument.
7. Set the stirrer and pump speeds at two levels down from the maximum and cover the sensor with your finger tips so that the distilled water is passing through the machine for a minimum of ten seconds.
8. Open the drain and wait for the “ready” light to come on.
9. Close the drain and fill with distilled water until the level just covers the sensor, the instrument is now ready for the next sample.

Repeat steps one to nine for each sample. The data is then exported to Microsoft Excel for further analysis.

## APPENDIX B

The grain size distributions and mean Grain Size (MGS) for sediment samples taken on the 6<sup>th</sup> June, 3<sup>rd</sup> and 4<sup>th</sup> of August 1996 and 20<sup>th</sup> July 1997.

Site I.D.	Date	% clay ( $<2\mu\text{m}$ )	% Silt ( $2-64\mu\text{m}$ )	% Sand ( $>64\mu\text{m}$ )	MGS ( $\mu\text{m}$ )
1	6-6-96	10.156	67.54	22.30	78.98
2	6-6-96	4.31	85.66	10.03	30.67
3	6-6-96	3.98	77.45	18.57	40.00
4	6-6-96	4.71	85.56	9.73	28.83
5	6-6-96	5.12	87.30	7.57	26.65
7	6-6-96	3.62	74.50	21.88	43.33
8	6-6-96	4.90	80.11	14.99	35.31
9	6-6-96	13.45	60.14	26.41	80.78
10	6-6-96	3.78	84.55	11.67	33.17
11	6-6-96	13.05	51.00	35.95	124.76
13	6-6-96	3.76	81.37	14.88	43.63
1	3-8-96	7.44	85.65	6.92	22.59
2	3-8-96	7.39	85.98	6.63	22.08
3	3-8-96	7.86	88.14	4.01	18.69
4	3-8-96	7.34	86.57	6.08	21.59
5	3-8-96	7.99	85.10	6.91	21.71
6	3-8-96	7.71	86.21	6.09	21.94
9	3-8-96	11.68	80.73	7.59	20.18
10	3-8-96	7.45	86.53	6.02	21.70
11	3-8-96	9.56	85.76	4.68	18.09
12	3-8-96	6.95	85.55	7.50	23.32
13	3-8-96	6.56	85.90	7.54	24.17
14	3-8-96	7.80	88.49	3.71	17.8
15	3-8-96	7.39	89.51	3.1	17.57
16	3-8-96	5.96	86.92	7.11	24.88
17	3-8-96	6.35	87.62	6.03	22.92

Site I.D.	Date	% clay ( $<2\mu\text{m}$ )	% Silt ( $2-64\mu\text{m}$ )	% Sand ( $>64\mu\text{m}$ )	MGS ( $\mu\text{m}$ )
1S	4-8-96	6.51	86.91	6.58	24.04
1N	4-8-96	6.97	89.46	3.57	19.64
2S	4-8-96	5.49	84.71	9.80	29.21
2N	4-8-96	6.25	86.89	6.86	24.73
4S	4-8-96	6.80	84.26	8.93	26.22
4N	4-8-96	6.44	86.37	7.19	24.33
6S	4-8-96	9.35	85.20	5.45	19.25
6N	4-8-96	10.93	79.13	9.94	24.02
7S	4-8-96	8.79	85.51	5.70	19.11
7N	4-8-96	9.52	84.49	5.99	20.20
11N	4-8-96	5.47	85.55	8.98	28.07
12N	4-8-96	6.93	86.70	6.37	22.86
1	20-7-97	1.55	54.87	43.58	69.87
2	20-7-97	2.15	61.62	36.22	60.79
3	20-7-97	2.25	70.26	27.49	51.98
4	20-7-97	1.94	53.11	44.95	74.00
5	20-7-97	3.11	74.47	22.42	46.45
6	20-7-97	2.68	66.18	31.14	54.30
7	20-7-97	3.38	74.01	22.6	44.52
8	20-7-97	2.72	68.67	28.62	51.62
9	20-7-97	2.71	67.51	29.78	54.81
10	20-7-97	4.70	78.25	17.04	41.74
11	20-7-97	4.38	84.00	11.62	33.53
12	20-7-97	2.90	66.91	30.20	53.56
13	20-7-97	4.31	75.57	20.12	43.24
14	20-7-97	3.00	57.78	39.22	71.52
15	20-7-97	3.98	78.09	18.02	39.37
16	20-7-97	3.09	72.95	23.96	46.55
17	20-7-97	3.51	74.79	21.70	45.49
18	20-7-97	3.16	73.60	23.23	49.34

<b>Site I.D.</b>	<b>Date</b>	<b>% clay (&lt;2µm)</b>	<b>% Silt (2-64µm)</b>	<b>% Sand (&gt;64µm)</b>	<b>MGS (µm)</b>
19	20-7-97	3.59	76.81	19.61	43.61
20	20-7-97	3.69	75.57	20.74	43.76
21	20-7-97	3.45	75.75	20.79	46.08
22	20-7-97	2.98	80.03	16.99	41.01
23	20-7-97	2.91	81.78	15.31	41.17

**APPENDIX C**  
**VERSE Model Output For SSC, 20<sup>th</sup> July 1997.**

